CAL-2064

National Aeronautics and Space Administration

# FINAL TECHNICAL REPORT FOR NASA GRANT NAGW-1887

**Submitted to:**

National Aeronautics and Space Administration
Astronomy and Relativity Branch
Astrophysics Division, Code EZ
Attention of Dr. Edward Weiler
NASA Headquarters
Washington, DC 20546



**Submitted by:**

The Trustees of Columbia University
in the City of New York
Box 20, Low Memorial Library
New York, New York 10027

**Prepared by:**

Columbia Astrophysics Laboratory
Departments of Astronomy and Physics
Columbia University
538 West 120$^{th}$ Street
New York, New York 10027

**Title of Research:**

**"Pre-Phase A Development of a Far-Ultraviolet Photometric- and Spectroscopic-Survey Small-Explorer Experiment"**

**Principal Investigator:**

Christopher Martin
Associate Professor of Physics

**Period Covered byRreport:**

1 November 1991 – 31 October 1992

# Final Technical Report for NAGW-1887

The scientific results of the awarded proposal entitled, "Pre-Phase A: Development of a Far-Ultraviolet Photometric- and Spectroscopic-Survey Small-Explorer Experiment," have led to the recent submission of the proposal entitled, "Joint Ultraviolet Nightsky Observer: A Far-Ultraviolet Sky-Survey Explorer," for consideration by NASA's Small-Class Explorer Missions Program (OSSA 2-92). The scientific results obtained from NAGW-1887 are specifically addressed in Appendix A of the proposal.

FOR CONSIDERATION BY NASA'S SMALL-CLASS EXPLORER MISSIONS PROGRAM (OSSA 2-92)

# JUNO

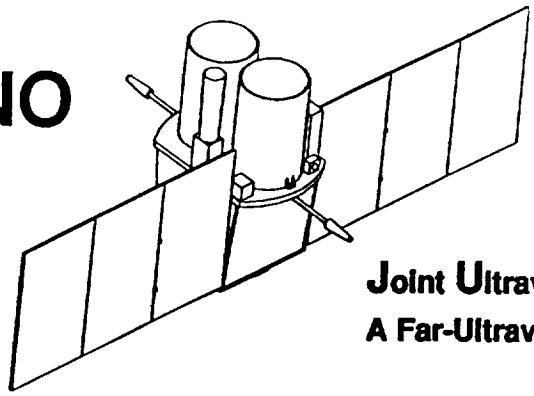

## Joint Ultraviolet Nightsky Observer
## A Far-Ultraviolet Sky-Survey Explorer

### Section I: Investigation & Technical Plan

**Submitted to:**

Astrophysics Division
Code SZ (Attn. AO OSSA 2-92)
Office of Space Science and Applications
National Aeronautics and Space Administration
Washington, DC 20546

**Submitted by:**

The Trustees of Columbia University
in the City of New York
Box 20 Low Memorial Library
New York, NY 10027

**Period of Research:**

| | | |
|---|---|---|
| Phase I: | Definition Phase: | 1 July 1993 – 30 April 1994 |
| Phase II: | Bridge Phase: | 1 May 1994 – 31 July 1994 |
| Phase III: | Development Phase: | 1 August 1994 – 31 July 1997 |
| Phase IV: | Mission Operations & Data Analysis Phase: | 1 August 1997 – 31 July 2000 |

**United States Team**

**Principal Investigator:**

Christopher Martin
Associate Professor of Physics
Columbia University

**Project Scientist:**

Peter G. Friedman
Associate Research Scientist
Columbia University

**Co-Investigators:**

*Columbia University*

Arlin P.S. Crotts, Asst. Prof. of Astronomy
Jules P. Halpern, Research Scientist
David J. Helfand, Prof. of Astronomy
Joseph Patterson, Assoc. Prof. of Astronomy
R. Michael Rich, Asst. Prof. of Astronomy
Jacqueline van Gorkom, Assoc. Prof. of Astronomy

*Space Telescope Science Institute*

Michael Shara, Astronomer

**Italy Team**

**Principal Investigator:**

Francesco Paresce
Senior Astronomer
Space Telescope Science Institute

**Project Scientist:**

Luciana Bianchi
Research Associate
Space Telescope Science Institute

**Co-Investigators:**

*Osservatorio Astronomico di Torino*

Attilio Ferrari, Prof. of Astronomy
Mario Gai, Research Astronomer

FOR CONSIDERATION BY NASA'S SMALL-CLASS EXPLORER MISSIONS PROGRAM (OSSA 2-92)

# JUNO

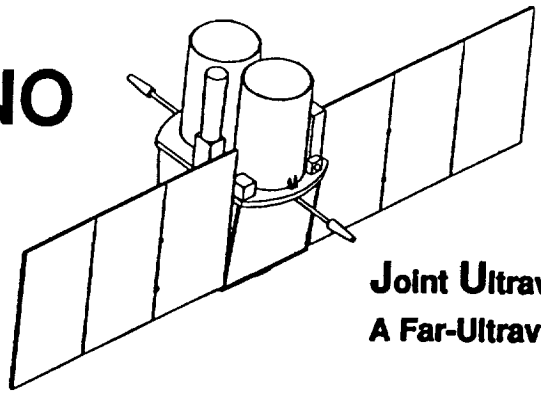

## Joint Ultraviolet Nightsky Observer
### A Far-Ultraviolet Sky-Survey Explorer

**Submitted to:**

Astrophysics Division
Code SZ (Attn. AO OSSA 2-92)
Office of Space Science and Applications
National Aeronautics and Space Administration
Washington, DC 20546

**Submitted by:**

The Trustees of Columbia University
in the City of New York
Box 20 Low Memorial Library
New York, NY 10027

**Prepared by:**

Columbia Astrophysics Laboratory
Departments of Astronomy & Physics
Columbia University
538 West 120$^{th}$ Street
New York, NY 10027

**Total Estimated Costs:**

See Cost Section

**Principal Investigators:**

Christopher Martin
Columbia Astrophysics Laboratory
538 West 120$^{th}$ Street
New York, NY 10027
Tel: (212) 854-7490
Fax: (212) 316-9504
e-mail: dcm@cuphyd.bitnet

Francesco Paresce
Space Telescope Science Institute
3700 San Martin Dr.
Baltimroe, MD 21218
Tel: (410) 338-4328
Fax: (410) 338-2617
e-mail: paresce@stsci.bitnet

FOR CONSIDERATION BY NASA'S SMALL-CLASS EXPLORER MISSIONS PROGRAM (OSSA 2-92)

# JUNO

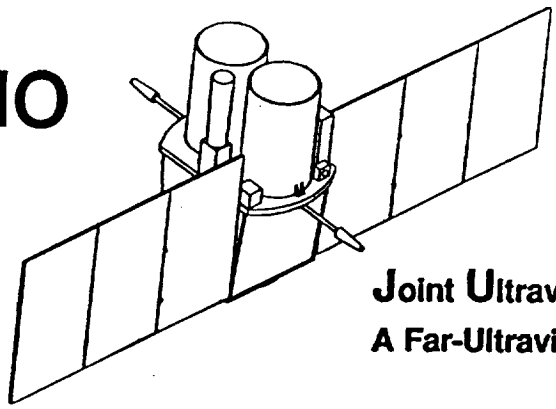

## Joint Ultraviolet Nightsky Observer
## A Far-Ultraviolet Sky-Survey Explorer

ENDORSEMENTS:

Christopher Martin, Principal Investigator
for the U.S.
Associate Professor of Physics
Columbia University
(212) 854-7490
e-mail: dcm@cuphyd.bitnet

Francesco Paresce, Principal Investigator
for Italy
Senior Astronomer
Space Telescope Science Institute
(410) 338-4328
e:mail: paresce@stsci.bitnet

James H. Applegate
Co-Director,
Columbia Astrophysics Laboratory &
Chair, Dept. of Astronomy
(212) 854-6834

Shoji Nagamiya
Co-Director,
Columbia Astrophysics Laboratory &
Chair, Dept. of Physics
(212) 854-3366

Beth H. Israel, Associate Director
Office of Projects & Grants
Columbia University
(212) 854-6851

# Table of Contents
## I. Investigation & Technical Plan

## Table I – SMEX Technical Checklist

| Item | Value | Ref | Supplier | Development Status |
|---|---|---|---|---|
| | *Instrument Information* | | | |
| Payload Size: | | | | |
| Telescopes(2) | 45 cm (DIAM) × 70 cm (LEN) | §4.1 | | |
| Electronics(2) | 37 × 10.7 × 20.6 cm | §D, Figure D.3 | SNL | Concept |
| Payload Shape | 2 right cyl, 1 box | Fig. 4.1, 4.3 | | |
| Payload Mass: | | | | |
| Telescope | 40.5/46.3 kg | §D, Table B.11.1 | | Includes |
| Electronics | 24.5 kg | §D, Table B.11.1 | | 15% Contingency |
| TOTAL | 111.2 kg | §D, Table B.11.1 | | |
| Telescope 1 Mass Center | 25.6 cm from S/M I/F | | HDOS | |
| Telescope 2 Mass Center | 30.9 cm from S/M I/F | | HDOS | |
| Mechanical I/F with S/C | 3-pt/tel on S/C I/F plate | §4.1,4.6, Fig. 4.1,4.3 | | |
| Connector Locations | On S/C I/F plate near E-box | Figure 4.3 | | |
| Thermal Paths | S/M-Tel I/F isolated<br>S/M-E Box I/F conductive | | | |
| Field of View | 5.0°cone | §4 | | |
| Payload Power | | | | |
| Nom-Orbit Averaged | 60.7 W | Table B.11.2, D.2 | | Includes |
| Nom-Night[OBS] | 96 W (43%) | Table B.11.2, D.2 | | 20% Contingency |
| Nom-Day[STDBY] | 24 W (54%) | Table B.11.2, D.2 | | |
| Stdby | 24 W | Table B.11.2, D.2 | | |
| Basic Functional Description | | §4, Table 4.1 | | |
| Telescope | 3-mirror f/2.75, 5°fov | §4.1 | HDOS | like VUE |
| Prisms | 6×12 cm diam × 2°wedge | §4.2, A.3 | prototype vibrated | |
| Filters | $BaF_2$, $SiO_2$ | §4.2 | CAL/Acton | Flight proven |
| Detector | MCP+Delay-line readout | §4.3 | CAL | prototype proven, vibrated |
| Preamplifiers | | §D.1 | standard | |
| Timing System | CFD+TAC | §D.1 | CAL | proven design |
| ADC | AD671 | §D.2 | Analog Devices | |
| Processor | RTX2010 | §D.2 | Harris | ACE/EOS/Cassini |
| Mass Memory | HM628512 | §D.3 | Dense Pac/Mosaic | like SXRP |
| DPU | | §D.2 | SNL | Concept |
| Basic Operational Description | | §3-5, Tab. 4.1,5.1 | | |
| Power Interface | 28V±2% from S/C | §B.8 | | |
| Telemetry I/F | MS1553B 2.5Mb/s | §B.9, §D.4 | | |
| Command I/F | ESA OBDH Std | §B.10, §D.8 | | |

## Table I – SMEX Technical Checklist (cont.)

| Item | Value | Ref |
|---|---|---|
| | *Spacecraft Accomodation Requirements* | |
| Preferred Launch Orientation | Vertical | Figure 4.3 |
| Instrument Location Constraints | Near/Coaxial with STR | Figure 4.3 |
| Alignment to Axis | $\pm$5 arcminutes | §3,4,5 |
| Baffling | Telescopes are baffled | §4, Figure 4.1 |
| Temperature Limits: | | |
| Operation – Telescopes | 25$\pm$3C | §4, B.5 |
| Operation – E-box | 20$\pm$15C | §4, B.5 |
| Survival – Telescopes | ?? | §4, B.5 |
| Survival – E-box | 20$\pm$40C | §4, B.5 |
| S/C Data Processing: on-board | NONE | |
| S/C Data Processing: ground | NONE | |
| Telemetry: | | |
| type | S-band | |
| quantity | 2 | §3, §B.9 |
| sample rate | 2.92 Mbps | |
| time tagging | DPU, yes | |
| format | 32-bit/photon | §D.3 |
| Commands: | | |
| type | Discrete, digital serial | §D |
| quantity | 2, 50 | |
| function | On/Off, OBS/STDBY, Programming | |
| timing constraints/frequency | OBS/STDBY synched with orbit | |
| Timing: | | |
| resolution | 32 $\mu$sec | |
| accuracy | 100 msec | |
| transfer method | S/C clock, T/M synch | §D |
| Environmental sensitivities: | | |
| electrical cleanliness | Detector/Preamps RFI sensitive | |
| magnetic fields | Detector sensitive | |
| contamination | Telescopes are sensitive | |
| Data collection & storage: | | |
| volume | 1.25Gbits/orbit | §3,5 |
| | 15 Gbits/day | |
| | 8.2 Tbit total mission | |
| rate | 833 kbits/s (observing) | §3.4, A.4 |
| rate | 220 kbits/s (orbit average) | §3.4, A.4 |
| D/L freq.& rate | 1 dump @ 2.5Mb/s $\times$ 500 sec every orbit | §3,5,B.8 |
| bit error rate | $10^{-6}$ | |
| GF Support: | | |
| equipment | shipping containers | |
| services | S/C Launch | Vol II |
| | P/L Environmental testing | |
| | U.S. communications to POC | |
| facilities | P/L Environmental test | |

## Table I – SMEX Technical Checklist (cont.)

| Item | Value | Ref |
|---|---|---|
| | *Mission Requirements* | |
| Science Operational Scenarios | | §3,5,A.4 |
| S/C Pointing | | |
| Where | All-Sky | §3,5,A.4 |
| Which Axis | y-axis | Figure 4.3 |
| When | AS: 1 new pointing per orbit | |
| When | DS/SS: 10-50 orbits/pointing | |
| Accuracy | $10'$ | §3,4 |
| Stability | $10'$ ($\pm$ $5'$) | §3, A.4, B.7 |
| Viewing Requirements (Observing) | Tel/Sun Angle $>$ 100°(OBS) | §5, Table 5.1 |
| | Sun-Horizon $<$-15° | |
| | Zenith Angle $<$70° | |
| Sun avoidance | Tel/Sun Angle $>$ 30°(STB) | §5, Table 5.1 |
| Attitude Determination | | |
| When/accuracy | On-orbit/$30''$ | §A.4 |
| When/accuracy | Ground/$<5''$/s | §3, A.4 |
| Orbit Determination | | |
| In-Track | | |
| Across-Track | | |
| Altitude | $\pm$25 km | |
| Frequency | 1/day | |
| Mission Lifetime | | |
| Required | 18 months | §3, B.1 |
| Desired | 24 months | §3, B.1 |
| Launch Window | NONE | |
| Orbit | | |
| Required | 600$\pm$70 km, 0°$\pm$0.2 | §B.1 |
| Desired | 600$\pm$35 km, 0°$\pm$0.1 | §B.1 |
| Unacceptable | $<$600 km | §B.1 |

## Acronym Glossary

14N, 14 – λ1400 JUNO narrow band
16N – λ1600 JUNO synthetic narrow band
16W, 16 – λ1600 JUNO wide band
18N, 18 – λ1800 JUNO narrow band
ADC – Analog-to-Digital Convertor
ADCS – Attitude Determination and Control System
ALS - Alenia-Spazio (Italian Aerospace Company)
ANS – Astronomical Netherlands Satellite
AS - All-sky Survey
ASI - Italian Space Agency
BOL – Beginning of Life
BPL – Bright Pixel List
CAL – Columbia Astrophysics Laboratory
CFD – Constant Fraction Discriminator
CIFS – Consorzio Interuniversitario per la Fisica Spaziale
CRA – Centro Ricerche Aerospaizale
CSS – Coarse Sun Sensor
CTU – Central Terminal Unit
CVs – Cataclysmic Variables
DOD – Depth of Discharge
DPU – Digital Processing Unit
DS – Deep Survey
EOL – End of Life
EUVE - Extreme Ultraviolet Explorer
FIFO – First In First Out memory
FOCAS – Faint Object Classification and Analysis System
FOV – Field of View
GPU – Gyro Package Unit
GSSS – Guide Star Survey System
HB – Horizontal Branch
HDL - Helical Delay-Line detector
HDOS - Hughes-Danbury Optical Systems
HUT – Hopkins Ultraviolet Telescope
IGM – Intergalactic Medium
IMF – Initial Mass Function
IPI – Italian Principal Investigator
IRAF – Image Reduction and Analysis Facility
IRAS - Infrared Astronomy Satellite
IUE – International Ultraviolet Explorer
JUNO - Joint Ultraviolet Nightsky Observer

LLS – Lyman Limit System
LMXRB – Low Mass X-ray Binary
MAMA – Multi-Anode Microchannel Array
MCP – Microchannel Plate
MGM – Magnetometer
MGT – Magneto Torquers
MIC – MCP Intensified CCD
MLI – Multilayer Insulation
MM – Mass Memory
MOC – Mission Operations Center
MOM – Missions Operations Manager
MS – Main Sequence
NASA – National Aeronautics and Space Administration
NUVIEWS – Narrow-band Ultraviolet Imaging Experiment for Wide-field Surveys
OAO – Orbiting Astronomical Observatory
OATO - Osservatorio Astronomico Torino
OBDH – On-Board Data Handling
OFHC – Oxygen-Free High Conductivity
PAF – Payload Attach Fitting
PAIP – Performance Assurance and Implementation Program
PAR – Performance Assurance Requirements
PCDU – Power Control and Distribution Unit
P/L – Payload
PNN - Planetary Nebula Nucleus
POC – Payload Operations Center
POSS - Palomar Sky Survey
RAS – Rapid Analysis Station
ROSAT – Roentgen Satellite
RW – Reaction Wheel
S/C – Spacecraft
SAA – South Atlantic Anomaly
Sd – Subdwarf
SDL - Serpentine Delay-Line detector
SDRAS – Science Data Reduction and Analysis System
SEL – Single Event Latchup
SEU – Single Event Upset
SIRTF – Space Infrared Telescope Facility
SM/SVM – Service Module
SNL – Sandia National Laboratory
SOC – Science Operations Center
SS – Spectroscopic Survey

STR – Star Tracker
SXRP – Stellar X-Ray Polarimeter
TAC – Time-to-Analog Convertor
TOS – Telescope Operations Station
UART – Universal Asynchronous Receiver Transmitter
UIT – Ultraviolet Imaging Telescope
USPI – U.S. Principal Investigator
UVX – Ultraviolet Experiment on Shuttle
WD – White Dwarf

# 1. SUMMARY

We propose to perform a far ultraviolet photometric and spectroscopic survey covering the $\lambda\lambda$ 1300-2000 band with a sensitivity comparable to that of the Palomar Sky Survey (**Figure 1.1**). This survey will proceed in three phases: an all-sky survey in three bands to 18-19.5$^m$, deep surveys of selected targets of interest in the same bands to 21-22$^m$, and a spectroscopic survey of 2% of the sky to 18$^m$ with a resolution of 3-20Å . This mission, the Joint Ultraviolet Nightsky Observer (JUNO), can be performed by a Small-Explorer-class satellite.

The mission promises to increase by a factor of 1000 the number of known active galactic nuclei, quasars, active galaxies, white dwarfs, cataclysmic variables, and evolved stars. Low to moderate resolution spectra will be obtained for more than 50,000 objects, including thousands of QSOs and Seyferts, thousands of post main sequence stars, and tens of thousands of galaxies to a redshift of 0.2. The surveys will provide fundamental new data on the luminosity functions, temperature distributions, evolutionary histories, spatial distributions, and time variability of these objects. Each phase of the mission will support and compliment the other phases. The JUNO surveys will result in substantive progress on these major, unresolved astrophysical issues:

- The nature of the energy source in QSOs and active galactic nuclei;
- The luminosity function and evolution of QSOs and AGN;
- The correlation of AGN with galaxies, clusters and large scale structures in general;
- The nature, history, and global behavior of star formation in field and cluster galaxies;
- The nature of the faint blue galaxies, and the existence of young galaxies;
- The origin of the UV excess in elliptical galaxies and globular clusters;
- The ionization of the intergalactic medium;
- The luminosity function and evolution of post-main sequence stars;
- Interacting binary evolution;
- Galactic and extragalactic origins of the far ultraviolet background.

The JUNO mission is a collaboration between the Consorzio Interuniversitario per la Fisica Spaziale (CIFS) of Italy and the Columbia Astrophysics Laboratory (CAL). NASA and the Italian Space Agency (ASI) have a long history of successful bilateral space missions. Each country will contribute 50% of the total cost of the mission, and will share equally the resulting data. ASI/CIFS will be fully responsible for the construction of the spacecraft, which will be contracted to Alenia-Spazio (ALS) in Torino. CAL will develop the payload, in partnership with Sandia National Laboratory (SNL) for digital electronics design and flight electronics fabrication, and contracting with Hughes-Danbury Optical Systems (HDOS) for mirror and telescope fabrication. JUNO will be launched into a 600 km, equatorial orbit by Pegasus. ASI/CRA will provide ground station coverage for the 18 month mission at the *equatorial* San Marco ground station and both CAL and CIFS will support science operations and data analysis. We will perform near-real-time optical identification of JUNO sources using the digitized POSSI/II plates for initial classification. The resulting all-sky map will remain a fundamental resource for astronomy well into the next century, and we plan to make the results of the survey available to the community on CDROM. We also propose that a portion of the deep and spectroscopic surveys be devoted to a Guest Observer Program.

The Palomar Sky Survey has served as the fundamental resource for research in optical astronomy for over thirty years. The IRAS, EUVE, and ROSAT satellites provide a similar database for the infrared, extreme ultraviolet, and X-ray regimes. *The mission proposed here will provide a catalog with an order of magnitude more sources than any of these space-borne experiments, and, more importantly, will fill in the crucial missing piece of the spectrum so that our knowledge of the sky from 100$\mu$m to 10Å is complete.*

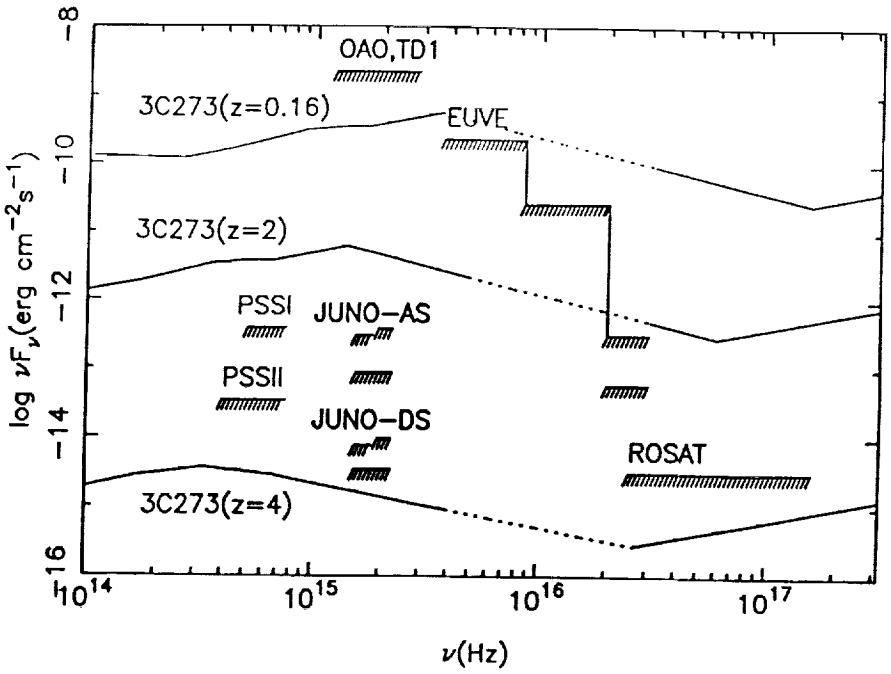


**Figure 1.1** Sensitivity of JUNO compared with other UV, optical, and x-ray surveys.

## 2. SCIENTIFIC OBJECTIVES

The importance of the far UV band for astrophysical studies has been aptly demonstrated by the productive tenure of the IUE Observatory and the breathtaking discoveries of the Hubble Space Telescope. A variety of astronomical objects radiate a large fraction of their luminosities in this band. At the same time, the numerous atomic and molecular resonance and forbidden transitions of abundant elements which appear in the far UV make it a key regime in multispectral studies. HST and FUSE are designed to perform detailed imaging and spectroscopic studies in the far UV. No mission has yet exploited the powerful source selection potential of this band to discriminate objects of great astrophysical interest. Survey missions have been performed (OAO, ANS), but these were limited by non-imaging detectors to the brightest sources (m<10). A deep far UV survey would play a major role in finding candidates for study by HST and FUSE.

The JUNO mission will perform three complementary surveys.

- *An all-sky survey (AS) to a limiting magnitude of ~18$^m$-19.5$^m$ in three bands at λ1400(**14**), λ1600(**16**) and λ1800(**18**).*

  The all-sky survey will yield large numbers of sources and the greatest sensitivity to rare objects. Accurate positions will permit straightforward optical identification using presently available digitized northern and southern sky surveys. The derived UV and UV-V colors and UV magnitudes will permit efficient preliminary source classification, and yield initial information about temperature, gravity, spectral slope, and/or stellar populations.

- *Deep surveys (DS) of selected targets to 21$^m$-22.5$^m$ in the three bands.*

  The deep surveys will probe selected targets that in many cases have well defined extinctions and distances, leading directly to HR diagrams and luminosity functions. Deep galaxy number-count surveys will bridge the all-sky survey with HST faint surveys. The DS will verify the completeness of the all-sky survey.

- *A spectroscopic survey (SS) to 17-18.5$^m$ over ~2% of the sky, with $\Delta\lambda \sim 3 - 20$Å. Two-thirds of the spectroscopic survey will extend over a continuous 90 degree arc at high Galactic latitudes.*

  The spectroscopic survey will permit a detailed look at a smaller, but still substantial and varied sample of objects as well as providing important basic data for the interpretation of the photometric surveys. It will furnish detailed information about temperature, gravity, continuum slope, redshift, ionization,

metallicity, stellar population and extinction in hundreds to thousands of sources in each class.

The scientific objectives of the JUNO mission have a common theme: there are a set of major, unsolved astrophysical problems which cannot be addressed without the information carried by far UV emission and absorption, by the statistical power which complete surveys provide, and/or by the discovery of the rarest objects in a class. The JUNO far UV surveys will increase by a factor of 100-1000 the numbers of known quasars, active galaxies, white dwarfs, cataclysmic variables, and evolved stars. JUNO will have the unique ability to obtain integrated far-UV spectra of nearby galaxies, the only sample of unevolved galaxies against which very high redshift galaxies (z>3) can be compared. The spectroscopic and photometric surveys will be the most comprehensive data set ever utilized in attempts to understand the far-UV rising flux in late, metal rich E/S0 galaxy populations (FD92). The database will make possible a systematic investigation of the post-main sequence evolution of low mass stars. It will be sensitive to rare objects and stages of evolution in both stars and active galactic nuclei, detecting thousands of cataclysmic variables, including 500 eclipsing systems, thousands of white dwarfs in close binaries, and hundreds of interacting binary systems. Extinction at high and low latitudes will be accurately determined using several methods. We summarize in the following sections three of the major investigations that this mission will carry out: on QSOs, on white dwarfs, and on the far UV background. In Table 2.1 we list over fifty additional investigations than will be made possible by the JUNO database. We present the scientific rationale for many of these investigations in Appendix C.

### 2.1 Quasi-Stellar Objects

Quasi-stellar objects are likely to be fueled by the accretion of gas onto a supermassive black hole at the nucleus of a galaxy. This model is widely accepted not on the basis of convincing observational proof, but because it is the only plausible explanation. These questions must be tackled: Is the source of energy accretion, or black hole rotation and the Blandford-Znajec process? What is the structure of the accretion disk? How is gas supplied to the disk? What is the source of viscosity? How is the gravitational energy transferred to non-thermal particles and radiation? Why do QSO counts die out at $z > 3$ and $z < 1$? Do QSOs evolve in luminosity or in number, or both, and what controls the evolution? What evolutionary stages precede and follow the QSO period? What is the spatial distribution of QSOs, and how does it relate to their formation and evolution?

The JUNO mission will make an unequaled contribution to the study of QSOs by providing an enormous ($> 10^5$), homogeneous, magnitude-limited, minimally-biased, *all-sky* photometric sample of QSOs. Moreover, it will provide a very large (4000) catalog of QSOs with redshifts, luminosities, and low-resolution spectral properties. In each case, the observations will be performed in the spectral band most sensitive to the accretion disk luminosity, with the greatest diagnostic power for disk properties, at the peak of the optical-UV energy distribution, and with the fewest contaminating background sources and associated biases. It is *only* with such a sample that the fundamental problems of the QSO luminosity function, evolution, spatial distribution, and relationship to lower luminosity AGN can be attacked.

*The Structure of the QSO Accretion Disk.* JUNO will play a critical role in measuring the EUV spectrum of QSOs, which may be dominated by the accretion disk (**Figure 2.1**). The accretion disk structure depends on the ratio of the accretion rate to the Eddington luminosity limit (R84; B85). In low rate systems, ions can couple to electrons resulting in an ion torus which may collimate relativistic particle beams and give a radio loud QSO. At intermediate accretion rates, a classical thin disk may form (SS73), in which the local viscosity adjusts itself so that gravitational energy released at each disk radius is dissipated by thermal radiation. Such a disk will radiate predominantly in the extreme and far UV. If the accretion rate exceeds the Eddington limit, a radiatively supported accretion torus may be produced, again furnishing a preferred axis for radiation collimation and particle acceleration. A radiative torus will also be a copious far and extreme UV emitter. The $10^9$K accretion disk corona can comptonize the thermal radiation and produce a power law component in the hard x- to $\gamma$-ray region. A typical QSO has a $\sim \nu^0 - \nu^{-1}$ spectrum into the far

UV, and a break occuring near rest $\lambda 1200$. This flat spectrum component has been identified with thermal radiation from the accretion disk (S78; MS82). Based on very limited IUE data, at shorter wavelengths the continuum steepens to $\nu^{-2} - \nu^{-4}$ due to a combination of $e^-$ scattering in the disk corona and cumulative Lyman limit absorption by intervening clouds.

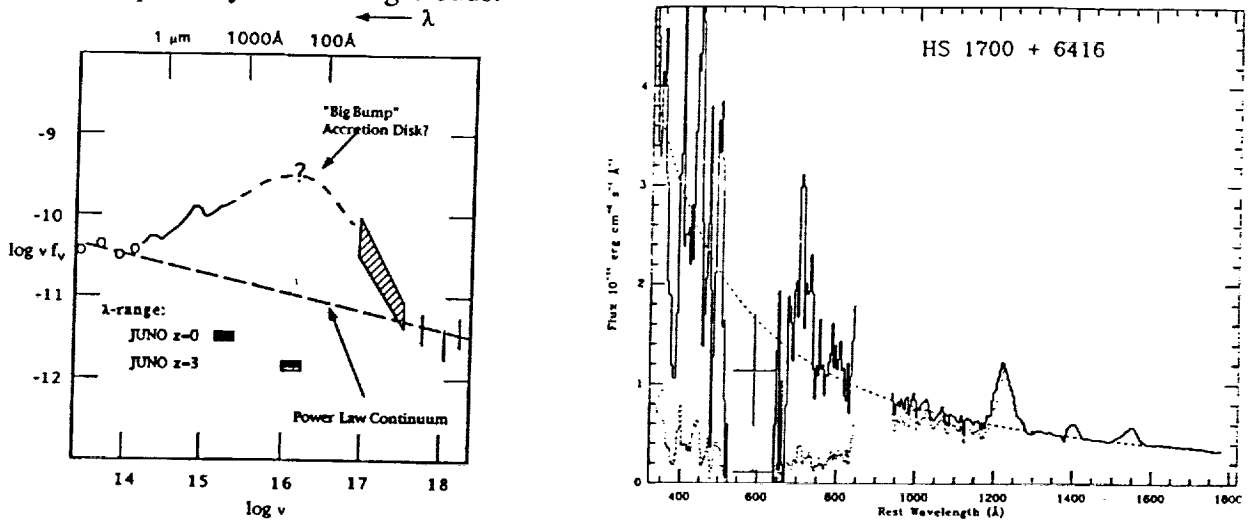


Figure 2.1 (a) QSO energy distribution. (b) HS1700+6416 z=2.73 QSO spectrum. Dashed: raw data; Solid: IGM absorption corrected.

*EUV Spectrum & Luminosity Function of QSOs.* The EUV luminosity and spectrum of QSOs is of great interest for several reasons: (1) the spectral shape will test accretion disk models, particularly in the inner disk where $e^-$ scattering becomes important; (2) the turnover energy is a measure of the black hole mass; (3) there is suggestive spectral evidence in the UV and soft x-ray bands for a large "hidden" luminosity in the EUV; (4) there is "missing energy" required to explain the ionization of the broad line region; (5) the degree to which QSOs can ionize the IGM depends on their EUV luminosity function; (6) remnant black-hole demographics depend on the unknown EUV luminosity function. Because of Lyman limit absorption, only one QSO has been discovered which is visible to a rest wavelength of <300Å(HS1700+6416, R89). With conservative assumptions, our UV model, discussed in §3, 4.5, and A.4, predicts a QSO redshift distribution shown in **Figure 2.2.** At least 14,000(5,000) QSOs with $z > 2$ and 3000(600) QSOs with $z > 2.5$ will be discovered in the AS(DS). A successful accounting for the stochastic absorption of LLS requires a large sample of high $z$ QSOs. High $z$ QSOs will also provide background sources for the HeII Gunn-Peterson test, a critical dicriminant among IGM models.

*QSO Luminosity Function and Evolution.* The QSO evolution problem can only be addressed using large *homogeneous* samples, with well determined statistical properties and no significant biases. One of the major goals of the JUNO mission is to make possible an unbiased measurement of the QSO luminosity function. The luminosity function furnishes a global and fundamental constraint on models for the QSO central engine. The far UV luminosity function may be especially significant if the emission is indeed dominated by the accretion disk. A measurement of the far UV luminosity function will characterize the QSO continuum spectrum in the band where the accretion disk spectrum peaks. This is critical for determining whether the UV bump is produced by the accretion disk or by non-thermal processes. QSOs exhibit strong redshift evolution. They appear to increase rapidly in number (or luminosity) in the interval $3.5 > z > 2.5$, and then decrease sharply for $z < 2.5$. JUNO will study the death phase of QSOs. At this time, despite considerable efforts, we do not even know whether QSOs evolve in density, luminosity, or a combination of the two (e.g., HFC92). Clearly, the evolutionary history of QSOs is of fundamental importance. The turn-on timescale may be governed by the collapse time of the central black hole, or by the generation of fuel. The falloff almost certainly reflects depletion of either accreting matter (if gravitational

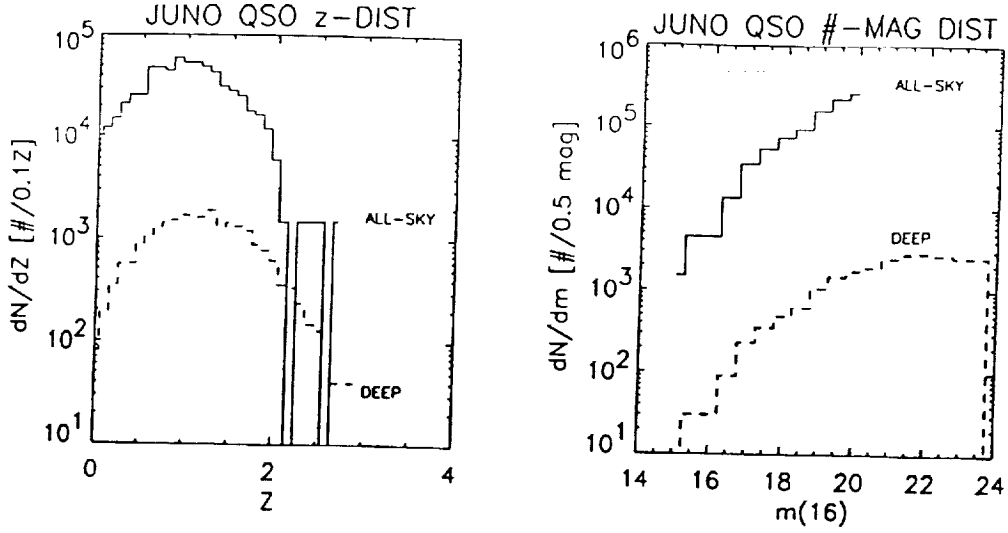


**Figure 2.2** Predicted number/redshift (Left) and number/magnitude (Right) distribution of JUNO QSOs.

energy is responsible) or black hole angular momentum (Blandford-Znajec process). Placement of a QSO on the $z - L$ diagram is only the first step. A single $(z, L)$ point may be populated by QSOs with a distribution of physical parameters. For example, if two parameters, black hole mass (M) and accretion rate ($\dot{M}$) determine $L$, a $(z, L)$ point is shared by low M/high $\dot{M}$ objects and their inverse. With the small existing samples it is impossible to investigate QSO properties other than luminosity in the context of evolutionary models. The JUNO photometric survey will measure QSO colors, which is sensitive to the thermal/nonthermal ratio. The spectroscopic survey will determine kinematics and ionization in the BLR, which may be directly related to the disk. It will be possible to compile evolutionary laws for subsamples organized by these observables.

*The Spatial Distribution of QSOs.* The distribution of QSOs in space is poorly determined, but of central importance (Sh9?). There are many relevant questions. First, are QSOs preferentially located in clusters? The effects of the ram pressure of the intercluster gas, or more frequent galaxy-galaxy interactions, or differences in the original morphological distribution could be manifested in an increased (or decreased) probability of QSO activity or increase in lifetime. Are QSOs more likely to be found near other galaxies? Collisions might then be important. Is there a relationship between galaxy density and the level and evolution of activity? Finally, are QSOs over- or underrepresented in large scale structural features, such as voids, ridges, and superclusters?

Answering these and related questions requires large, homogeneous samples of QSOs with well determined statistical properties, occupying contiguous parts of the sky, and with comparable limiting magnitudes. The JUNO mission will obtain such a sample, and will measure:

- # of QSOs: $10^6$ (AS), $10^5$ (DS), $10^4$ (SS: Figure 2.3) with accurate extinction (cf. §A.4.2)
- Angular correlation functions $\theta_{QSO-QSO}$, $\theta_{QSO-Clust}$, $\theta_{QSO-Gal}$ (AS, DS)
- Spatial correlation functions $\xi_{QSO-QSO}$, $\xi_{QSO-Clust}$, $\xi_{QSO-Gal}$, $\xi_{QSO-LLS}$ (SS).
- Bias parameter $b_{QSO}/b_{Gal}$.
- Large-scale structure on 0.05-1 Gpc scale sensitive to $\Delta\rho/\rho \sim 1$ on 75 Mpc $h^{-1}$ scales. (SS)

*The Intergalactic Medium: Lyman Limit Systems (LLS).* The JUNO spectroscopy survey will provide a minimally-biased survey of Lyman limit systems (LLS) in the redshift interval $0.5 < z < 1.1$. LLS are in an interesting range of column density, since it is at this point that a transition is observed between low column clouds that show no correlated metal lines, and high column density systems that almost always have associated metal lines. The onset of self shielding here should create a break in the $dN/dN_H$ distribution as well. Approximately $10^3$ QSOs with redshifts >0.5 will provide background continuum spectra to map out these systems in three dimensions. We estimate that in this redshift interval, ~1 detectable Lyman limit system will appear in each spectrum. **Figure 2.3** illustrates simulated spectra for several cases. With the

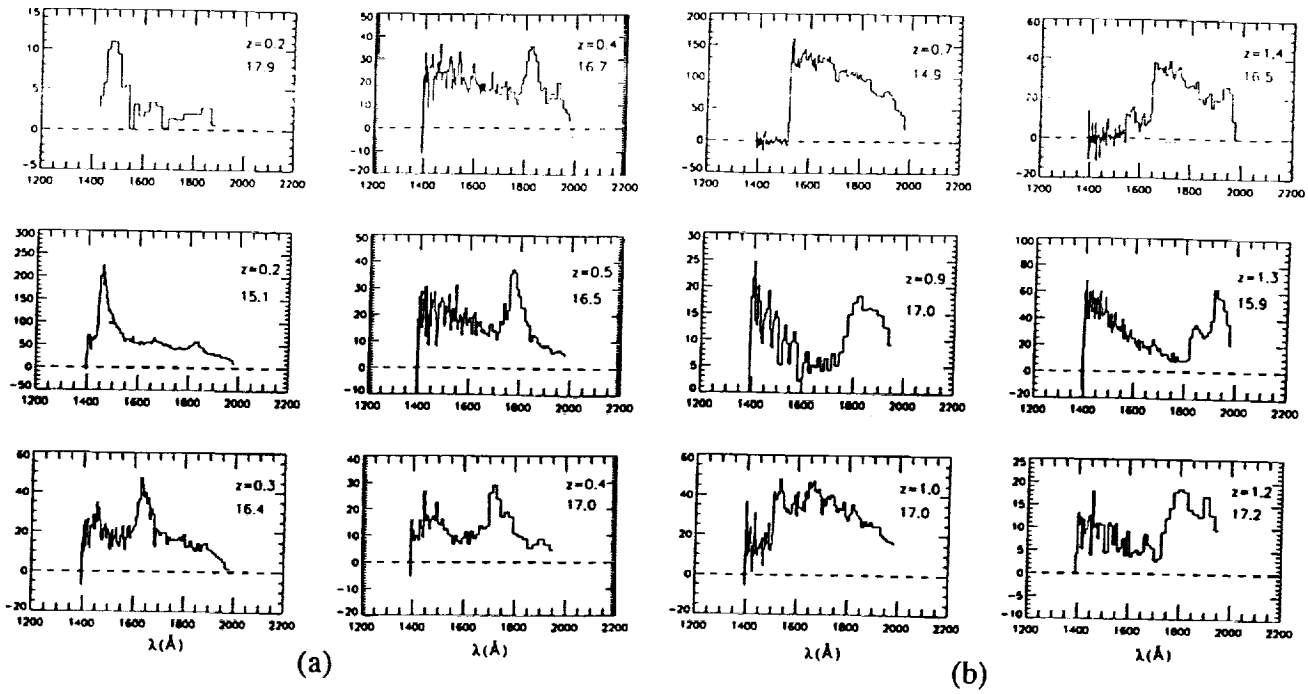


**Figure 2.3** (a) The JUNO QSO $z$-survey. (b) QSO LLS survey. QSO $z$ and FUV magnitudes shown.

LLS survey, we will investigate the large scale structure of the strongly absorbing systems over a region of $400 \times 500 \times 70h^{-3}$ Mpc$^3$. More than 20% of this volume will overlap the QSO redshift survey region. The study of Lyman limit systems may represent an important way to trace galaxy evolution, as well as the evolution of the intergalactic medium. Observations suggest that LLS may include evolving, possibly collapsing galaxy halos, irregular galaxies in orbit around larger systems that may be tidally disrupted, or delayed dynamical evolution of late-type galaxies. The discovery of strong evolution in Ly$\alpha$ clouds in the $z < 2$ range by HST (B92;TI92), and in the population of faint blue galaxies (T88;BES88), has made the question of LLS $z < 2$ evolution even more compelling.

## 2.2 White Dwarfs

A far UV survey is an excellent starting point for exploring low mass post-main sequence evolution. This is aptly illustrated by **Figure 2.4**, which shows the location of known classes of post-MS star on an HR diagram, and theoretical evolutionary tracks to the white dwarf stage. Superimposed on this diagram (from VL87), are the detection limits for the JUNO surveys. The observational goal is to populate this diagram (accurately) with enough objects to furnish statistically sound conclusions about the lifetime of each state and its relationship to others, and to determine whether stellar parameters other than $T_{eff}$ and luminosity (such as He and metal abundance, or prior mass loss) are required to identify the state and its associated remnant mass. The JUNO mission will find the stars with complete and unbiased surveys, and provide essential data for their spectral typing. In many cases, the survey data will be sufficient to identify and type stars, and therefore to derive HR diagrams and draw important conclusions.

With its UV sensitivity, sky coverage, and spectroscopy survey, the JUNO mission is ideally suited to the study of white dwarfs (WD). These stars dominate the stellar faint number counts at moderate and high Galactic latitudes. The combination of UV-V flux ratios and optically determined Balmer line profiles will yield accurate $T$ and $g$ values, along with radii, distances and luminosities. Approximate temperatures can be derived from photometry for $T < 40,000$K and used to select regions of particular interest, such as the hottest stars, the DB gap, and those objects near the crystallization temperature. Many variable WD's will be discovered. White dwarfs in binaries can be selected photometrically over the whole sky.

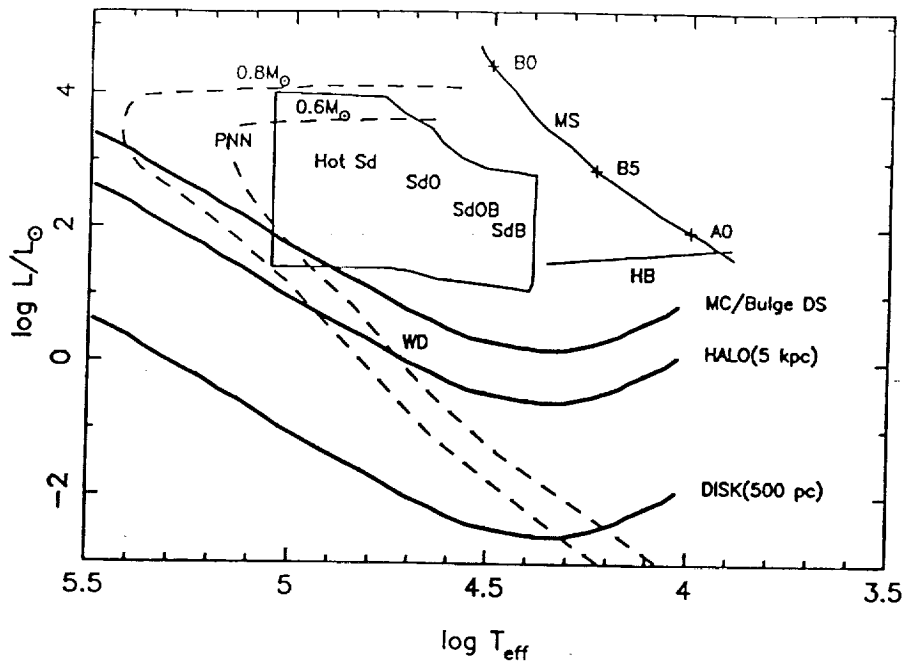


**Figure 2.4** HR diagram for post main sequence stars. Approximate observed locations of Planetary Nebula Nuclei (PNN), subdwarfs (SdB, SdO, SdOB, Hot Sd), horizontal branch (HB) and white dwarfs (WD) are shown. Also shown are the JUNO survey limits for the deep surveys of the Magellenic Clouds and galactic bulge, the all-sky surveys of the galactic halo to 5 kpc, and the "thick disk" to 500 pc.

*White Dwarf Luminosity Function and Neutrino Cooling.* Better definition of the luminosity function, in particular at high temperatures, is of fundamental importance to understanding the origin and evolution of white dwarfs. With a total sample of >200,000 stars to draw upon, we will be able to determine the luminosity function with unprecedented precision. In this way, we will test theories of neutrino cooling, crystalization, dependence on mass and composition. The study of the luminosity function of the hottest white dwarfs can establish constraints on neutrino cooling. Our current understanding of the hot WD luminosity function is limited by the lack of objects: no WD has been found with a temperature >70,000K. We can estimate from the WD birthrate of $6\times10^{-13}yr^{-1}pc^{-3}$ and cooling models of LV74 (which incorporate neutrino cooling), that the AS should locate >5000 stars with temperatures T>70,000K, if WD's are formed at significantly higher temperatures. Understanding of the cooling law and luminosity function are critical for using WD as a measure of the age and star formation history of the Galaxy.

*White Dwarf Luminosity Function in Disk, Halo, Globular Clusters.* With a large sample of objects in two colors, the temperature can be determined as well as the distance. The scale height of white dwarfs can be established with good accuracy; current estimates vary from 150 to 500 pc. The scale height is indicative of the average age of the population. In fact, by measuring the dependence of the luminosity function on height, we can constrain the history of stellar birthrate over the age of the galaxy. It will be important to compare the WD luminosity function in the disk and halo, obtained by JUNO, with that in globular clusters, which will be derived largely from HST surveys. This could reveal differences in the WD birthrate in each population that reflects distinct star formation histories or initial mass functions.

*White Dwarfs in Binaries.* A white dwarf (or subdwarf) that is a member of a binary with a late-type companion will appear in the photometric survey with a *14-18* color that is characteristic of the WD temperature, and a 18-V color that depends on the companion spectral type. From the colors alone, it will be possible to derive a complete white dwarf-late type binary frequency distribution. Eclipsing systems will make up ~10%. Follow-on photometry and radial velocity studies will allow us to derive a definitive

mass distribution and mass-radius law. Comparison to the known distributions of non-degenerate binaries will yield basic data on the turnoff mass, progenitor populations, and the effects of mass loss. By searching for short period detached binaries, we will determine the applicability of common envelope evolution and other evolutionary paths to cataclysmic variables and Type I supernovae.

### 2.3 Far UV Background and the Re-ionization of the Universe

An all-sky survey with the sensitivity and angular resolution of JUNO will profoundly advance the study of the cosmic far UV background in three areas:

*Global distribution of CIV* $\lambda$1549 *line.* The synthetic **16N** band (cf. §3.1) will provide an all-sky map of diffuse CIV (MB90) with S/N=10 in 1° bins. The global (anti)correlation with low- and intermediate velocity-N(HI), dust, soft X-ray background, H$\alpha$, and radio continuum will provide a powerful test of models for the production, distribution, and energetics of the hot ISM in the Galaxy. Comparison of large- and small-scale structure in the soft X-ray background (S92) to that in the CIV will lend insight into the physical relationship between the $10^6$K and $10^5$K phases. At high Galactic latitudes, galactic fountain, mixing layer, and "galactic chromosphere" models can be tested. In the Galactic plane, the existence and morphology of late-stage radiative supernova remnants willoffer essential clues to the origin and filling factor the hot ISM.

*Distribution and life cycle of dust.* Continuum maps of dust-scattered diffuse starlight will map the distribution of dust cirrus at high latitudes, with S/N=10 in $\sim$30″ bins. These can be directly correlated with IRAS and HI maps to derive the dust albedo and phase function. The universality of these quantities will be tested in regions that could be expected to harbor dust in different phases of evolution, such as low, intermediate, and high-velocity gas. We will also search for enhancements that may be produced by fluorescence in PAH molecules.

*Extragalactic and ionizing backgrounds.* An all-sky imaging survey with the sensitivity and angular resolution of JUNO is the most powerful way to measure the extragalactic UV background. It is essential to determine and eliminate the major foreground contribution of the Galaxy, which as COBE aptly demonstrated *requires* an all-sky survey. The power spectrum and **14-18** color of small-scale fluctuations (and cross-correlation with optical galaxy counts) in the all-sky and deep-survey images will place strong constraints on the extragalactic sources of the background, and on the star formation history of the universe over $0 < z < 1$ (MB89). In particular, the contribution of strongly evolving faint blue galaxies (T88, BES88, C90) will be measured. Finally, it may be possible in the deep surveys to measure the $z = 0$ remnant of the $z = 3$ ionizing background. Fluctuations (at 16″) in a high $z$ background are amplified by stochastic IGM absorption (J92). Our sensitivity to 2% fluctuations yields a limiting flux of $J_{-21} < 2 \times 10^{-3}$, a factor of 3-50 below current estimates (e.g.. MO91).

### 2.4 Additional Scientific Objectives

We summarize in Table 2.1 over fifty investigations that will be based upon the JUNO database. We show for each the number of objects made available by the JUNO surveys, and the methods we will use to identify the sources and carry out the investigation. Detailed discussion of many of these studies can be found in Appendix C.

## 3. INVESTIGATIVE APPROACH

The JUNO far ultraviolet survey will progress in three stages: an all-sky, two color photometric survey at a magnitude level comparable to the first Palomar Sky Survey, a deep survey of selected areas, and an objective prism survey of 2% of the sky. The surveys will be performed by two 33 cm telescopes with 4.8° fields of view and a photon counting microchannel plate detector. The photometric surveys will be in two 200Å wide bands, at $\lambda$1400 and $\lambda$1800, and one wide band, $\lambda\lambda$1600 with 16 arcsecond resolution,

# Table 2.1
## Science Investigations Summary

| Investigation | Survey* | Objects | Δλ(Å) | Method* |
|---|---|---|---|---|
| **Cosmology and IGM** | | | | |
| 1. QSO $\theta_{qq}$, $\theta_{qg}$, $\theta_{qc}$ | A,D | $10^6$ | | a |
| 2. QSO $\xi_{qq}$, $xi_{qg}$, $xi_{qc}$ | A,D,S | $10^3$-$10^4$ | | a,n |
| 3. Galaxy redshift survey | S | 5000 | 3-15 | k,q |
| 4. Intergalactic D and He | S | 100 | 10-20 | a,k,d |
| 5. Primordial abundance background | A,D,S | 400,000 | - | a,k |
| 6. Lyman limit survey: IGM evolution | S | 1000 | 20 | k,n |
| 7. Helium Gunn-Peterson survey | A,D | 300 | - | d,q |
| 8. Ionizing Source for IGM: fluctuations & holes | D | | | t |
| 9. Extragalactic far UV background | A | | | h |
| **Galaxies** | | | | |
| 10. Nature & redshift of faint blue galaxies/dwarfs | | | | |
| 11. Far UV s.e.d.s: spirals | S | 1000 | 3-15 | k,j,l |
| 12. Far UV s.e.d.s: ellipticals | S | 50 | 3-15 | k,j,l |
| 13. Spiral photometry survey | P,D | $10^5$ | - | q,i,f,m |
| 14. Elliptical photometry survey | P,D | 1000 | - | q,i,f,m |
| 15. MC and M31 globular cluster photometric survey | P,D | 200 | - | f,a,i |
| 16. MC stellar populations | D,S | $10^4$ | 3-15 | e,l,f |
| 17. SF history in Milky Way: WDs | P,D | 100 | - | d,n,m |
| 18. Morphology-density relation | P,D | $10^5$ | - | a,q |
| 19. BO effect in clusters and field | P,D | $10^5$ | - | a,q,f,g |
| 20. Background QSOs for galactic halos | P,D | $10^6$ | - | d,q |
| 21. Damped Lα systems | S | - | 3-15 | k |
| 22. Starburst galaxy survey | P,D,S | $10^4$ | 3-15 | k,a,q,f |
| 19. Potential discovery of young galaxies | P,S | ? | 3-15 | k,a,q |
| 23. Cluster cooling flows | S,P | 100 | 3-15 | f,l,s |
| **Accreting Binary Stars** | | | | |
| 24. CV's: luminosity function | P,D | 5000 | - | c,b |
| 25. CV's: variability survey | P,D,S | 1000 | - | c,o,k,p |
| 26. CV's: time resolved spectroscopy | S | 200 | 10 | c,l,k,r |
| 27. Low mass x-ray binaries | P,S,D | 10-20 | 10 | d,e,l,n,p |
| **Active Galactic Nuclei** | | | | |
| 28. EUV spectrum of QSOs | | | | |
| 29. Seyferts, LINERS and AGNs | S | 200 | 10 | k,c,o,d |
| 30. QSO LF and evolution | S,P,D | $10^3$-$10^5$ | 10 | k,d,l,n |
| 31. QSO spectrophotometry survey | S | 2000 | 10 | k,l |
| 32. BAL QSOs | S | 30-100 | 10 | k,l |
| 33. QSO spatial distribution | S,P,D | $10^3$-$10^6$ | 10 | d,q,k |
| 34. QSO variability survey | S,P,D | 2000 | - | c,o,d,k |

| Investigation | Survey | Objects | Δλ(Å) | Method |
|---|---|---|---|---|
| **Interstellar Medium** | | | | |
| 35. High *b* extinction map | P | - | - | h,q,g |
| 36. Dust distribution in disk | P | $10^5$ | - | s,g |
| 37. Bubbles and superbubbles in ISM | P | ?? | - | s,g |
| 38. CIV distribution in disk & halo | P | $4\pi$ sr | | s |
| 39. Molecular hydrogen | P,S | 100 | 10 | s |
| 40. Radiative SNR survey | P | 300 | | s |
| **Young Stars** | | | | |
| 41. Spiral arms and OB association IMF | P | $10^4$ | - | s,g |
| 42. Stellar activity survey | S | 1000 | 10 | k,l,r |
| 43. Young star activity | S | 100 | 10 | k,l,r |
| **Evolved Stars** | | | | |
| 44. Wolf-Rayet stars | S,D | 200 | 10 | k,l,r |
| 45. Horizontal branch survey | P,D,S | 66,000 | 5-12 | k,l,d,e |
| 46. Planetary nebula nuclei | P,D,S | 6000 | 10 | b,e,k,r,m,n |
| 47. Subdwarf evolution | S,P,D | 10,000 | 10 | b,e,k,r,m,n |
| 48. WD LF and $\nu$ cooling | P,D | 5000 | - | b,e,k,r,m,n |
| 49. DB temperature gap | S,P | 1000 | 10 | d,e,k,r,n |
| 50. WD LF in disk, halo and globular clusters | D,P | - | - | b,a,d,e |
| 51. WD evolution and variables | P,D | 10,000 | - | c,b,a,d,e |
| 52. WD in open clusters | P,D | 100 | - | e,f |
| 53. WD in binaries | P,D | $10^4$ | - | d,b,c,p |
| 54. WD variables | P,D | $10^3$ | - | c |

Method:

a. Galactic pole color survey
b. Color survey over galactic latitude
c. short term variability search
d. Color-magnitude distribution at poles
e. Color-absolute magnitude distribution
f. Previously catalogued and studied object
g. Number counts
h. Diffuse background light
i. Imaging photometry
j. Spectral synthesis
k. Slice of the universe spectroscopic survey
l. Spectroscopic identification
m. Follow on IR, optical, UV, x-ray photometry
n. Follow on IR, optical, UV, x-ray spectrophotometry
o. Long-term variability search
p. Eclipse survey
q. Extended/stellar on PSS/PSSII
r. Low *b* spectroscopic survey
s. Synthetic band 16N.
t. (Anti-)Correlation with $N_{gal}(J)$

Type
P - All-sky photometric survey at λλ1400, 1800
D - Deep two color surveys at λλ1400, 1800
S - Objective prism survey

$5\sigma$ limiting magnitude of $18 - 19.5^m$, and sensitivity to variability from $10^{-3} - 10^3$ seconds, depending on source strength. The deep surveys will reach $21^m - 22.5^m$. The prism survey will obtain $3 - 20$Å resolution time-resolved spectra of thousands of sources to $17^m - 19.5^m$. We present estimates of the number, photometric accuracy, and classification efficiency of detected sources in each class using realistic models of the UV sky and JUNO mission.

### 3.1 All-sky Survey

*Sky Coverage.* We emphasize here the motivation for an *all-sky* survey. It is always important to find the brightest objects in a class, since follow-up observations are then efficient and detailed. Targets of special interest will be found in all parts of the celestial sphere. In many extragalactic investigations, it will be important to have complete sky coverage, so that the effects of extinction and local galaxy clustering can be assessed. A deep survey will be executed for some parts of the sky, notably areas of particular astronomical interest.

*Wavelength Range.* We choose to limit our wavelength coverage to $\lambda\lambda$1350-2000. There are strong scientific and practical arguments for this restriction. The $\lambda\lambda$1350-2000 band represents a low background "window" surrounded on either side by sources of copious background, such as the zodiacal light, $O_2$ bands, and geocoronal HI lines. Objects of interest are most effectively discriminated from other sources in this band. The $\lambda\lambda$1350-2000 band also contains most of the useful UV lines for spectroscopy (excepting the important $\lambda\lambda$912-1250 region).

*Photometric Bands.* We require at least two bands in the far UV to measure the spectral slope independent of the far UV-visible ratio. To maximize the leverage of the slope measurement while avoiding HI and OI airglow features, we have designed the bands to peak near $\lambda$1400 (**14N**) and $\lambda$1800 (**18N**) (see Figure 3.1). To accomplish this, the detector surface of telescope 1 has been divided (down the center) into two equal regions with different photocathodes, one with an efficiency cutoff at $\lambda$1600 (KBr) and the other with a cutoff at $\lambda$2000 (CsI).

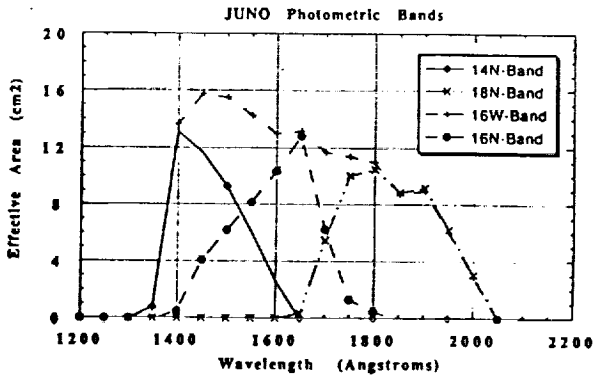


**Figure 3.1** Effective area of photometric bands.

The filter just in front of the detector will consist of a $BaF_2$ crystal over the KBr photocathode, and fused silica over the CsI section. The combination of a $BaF_2$ filter and the KBr photocathode give a sharp cutoff with an effective peak throughput of $> 50\%$.The detector coating process will be only slightly more complex. Telescope 2 will have a single, broad filter covering the $\lambda\lambda 1400 - 2000$ band (**16W**). A third narrow band, at $\lambda$1600 (**16N**), can be creating by subtracting the $\lambda$1400 and $\lambda$1800 fluxes from the wideband flux.

*Sensitivity and Detectable Volume.* To make substantial progress in many of the areas mentioned earlier, we must obtain a 2-3 order of magnitude increase in the number of identified objects of each type. Based on our detailed UV Universe model (cf. §A.4), this requires a limit of $17^m$-$18.5^m$ ($5\sigma$). Table 3.1 and C.1 show the predicted number counts in several classes. POSSI, with $V_{lim} \simeq 19$, will provide optical counterparts for objects with **16-V**>-1, while POSSII will reach $2^m$ deeper, to **16-V**>-3. Sources with **16-V**>-3 will be rare and obvious candidates for immediate follow-up spectrophotometry. For those objects not identified photometrically, spectroscopic identification to V=18-20 will be efficient and routine on 4 m telescopes.

*Angular Resolution.* The angular resolution requirement is determined primarily by the confusion limit for UV separation and optical identification efficiency. It is limited by the desire to maximize the field of

view and survey volume while employing available UV detectors, as well as by the attitude stabilization achievable by a SMEX. We have carried out a detailed analysis of the requirement using our UV model. A summary of the results is presented in **Figure 3.2**, and a more detailed discussion is given in §A.4. We require 16″ resolution and 3″ astrometry to achieve <5% false IDs in the Galactic plane, and to obtain photometry to $0.1^m$ in crowded regions. Resolution and astrometry error budgets are presented in **Table 4.2.**

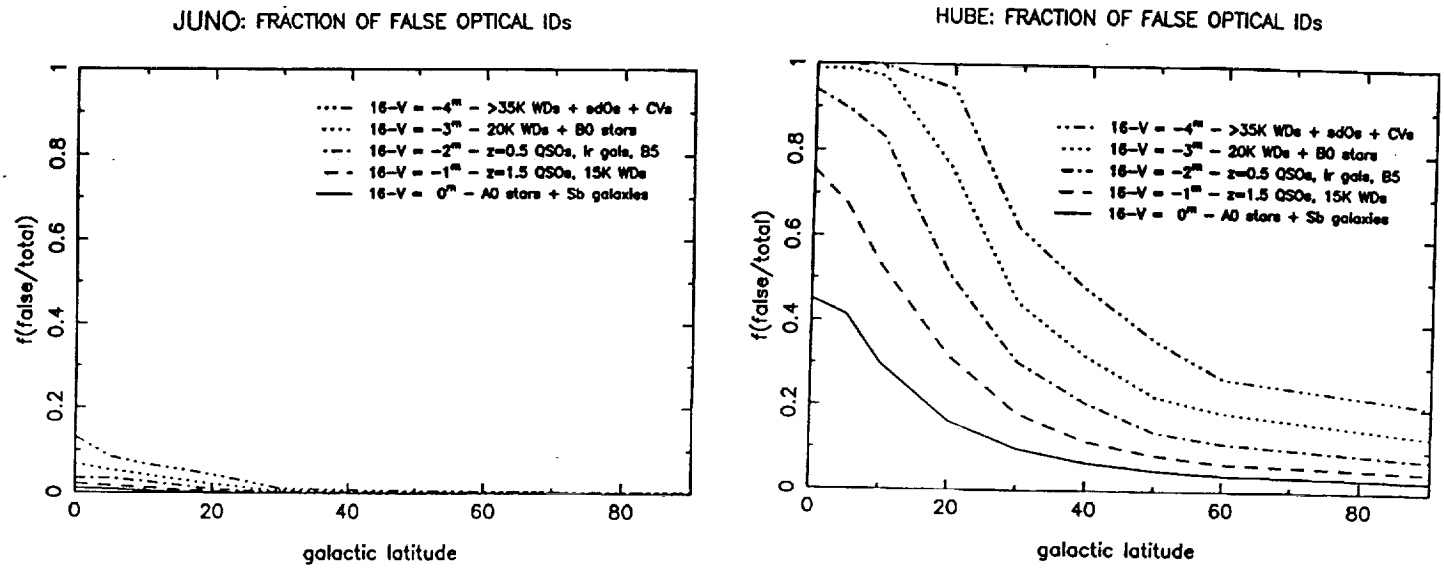


**Figure 3.2** Comparison of JUNO optical ID efficiency with that of another proposed UV survey mission with lower angular resolution (2′), HUBE (K89).

- *The key strategy of the JUNO mission is to make unambiguous optical identifications of the majority of the UV sources all the way into the Galactic plane and in deep high-latitude fields. This can only be done with <5″ error boxes, a fact that we have verified with our optical identification simulation.*

*Source Classification and Characterization.* A fundamental goal of our program is to maximize the information that can be obtained from the all-sky survey, so that a large fraction of the sources can be immediately classified and partially characterized. To do this, we will use some combination of **14-18**, **16-J**, and J-R colors, number-magnitude and color-number-magnitude information, and time variability. We intend to obtain all J and R magnitudes from digitized POSSI and POSSII catalogs that are either available now or planned to be so in 1997. There are three limiting cases: (1) high Galactic latitude survey, (2) low Galactic latitude survey; (3) surveys of previously studied associations. We discuss the latter two in Appendix C.

*High Galactic latitude survey.* We show in **Figure 3.3** the loci of **14-18** and **16-V** colors for several UV-bright sources. Considerable source discrimination will be possible using 14-18, **16-V**, and V-R colors only. For example, the average QSO with $z > 1$ will be distinct from stars. Low $z$ QSOs will be confused with B5-B8 stars and 12-15,000K white dwarfs. We will treat this and similar cases using color-number-magnitude distributions. In **Figure 3.4**, we show color-magnitude plots for a UV model simulation of a single high $b$ pointing. Symbols give source types. QSOs, galaxies, and hot white dwarfs will dominate the far UV faint number counts. We predict $\sim 6$ QSOs deg$^{-2}$ to $18^m$ and 45 to $19.5^m$. Faint galaxies will be more numerous, but can be discriminated from stellar objects using the optical plates (§A.4). The most serious contamination may be compact blue galaxies that appear stellar on the POSSII plates. These will also be confused with white dwarfs, but will be separated using proper motions on POSSI vs. POSSII (cf. §6.3 and §A.4). **Table 3.1** summarizes the classification efficiency of color/magnitude/proper motion

discrimination, based on extensive and realistic simulations using the UV model and actual digitized optical plates (§A.4). QSOs, WD's, and SD's will be classified with high efficiency, and the resulting catalogs will have very high purity.

- *The JUNO QSO catalog, consisting of ~$10^6$ objects over >3/4 of the sky, will be pure at >93% level, according to realistic detection, optical ID, and classification simulations with our UV model.*

**Table 3.1 – Detection & Classification Efficiency: High $b$ Surveys**

| Input Sources ($m_{16}$ <20) | #/3π sr | Detected & Classified Sources: Normal Galaxies | Blue Galaxies | QSOs | WD's | Unclassed | Detection Efficiency (%) |
|---|---|---|---|---|---|---|---|
| Normal Galaxies | 3,100,000 | 2,300,000 | 54,000 | <10,000 | <10,000 | 750,000 | 75% |
| Blue Galaxies | 3,600,000 | 140,000 | 2,600,000 | 20,000 | <10,000 | 880,000 | 72% |
| QSOs | 890,000 | <10,000 | <10,000 | 680,000 | 20,000 | 180,000 | 76% |
| WD's | 190,000 | <10,000 | <10,000 | 12,000 | 123,000 | 53,000 | 65% |
| Other | 100,000 | <10,000 | 1500 | 20,000 | <10,000 | 75,000 | 75% |
| Catalog Purity (%) | | 94% | 98% | 93% | 71% | 6% | |

### 3.2 Deep Survey

As the all-sky survey progresses across the sky, we will occasionally pause and make deep observations of selected areas, including the Galactic bulge (Baade's windows), the north and south Galactic poles, the Magellenic Clouds, M31, M33, M83, the Virgo core, Coma, Hydra, and the Bootes void. A 40,000 s (25 orbit) pointing will reach 21-22.5$^m$. Operationally, this phase of the mission is identical to the all-sky survey. Source confusion and optical identification efficiency is examined in §A.4.

### 3.3 Spectroscopic Survey

In order to provide a substantial increase in the information available on a subset of the UV sources, we will perform a spectroscopic survey of ~2% of the sky (exposures ~50,000) to a magnitude limit comparable to that of the AS (yielding ~$10^4$ spectra), after the AS is complete. An array of six matched prisms mounted on a single panel will be swung into the entrance pupil of Telescope 2, leaving the central 10% of the aperture clear to provide "zero order" reference images. We will also gather long-term variability (6-12 month) data on 1-2% of the sky. The effects of source crowding, discussed in some detail in §A.4 and §F.3, can be effectively eliminated. The spectral resolution requirement is imposed by the desire to resolve broad lines in AGN for kinematic studies and line profiles of luminous stars, to determine redshifts to 100-300 km/s in galaxies and QSOs, and to perform accurate spectral synthesis of galaxies. $CaF_2$ dispersion changes steeply in the far UV: our design has $\Delta\lambda = 3$Å at $\lambda$1300, and $\Delta\lambda = 25$Å at $\lambda$2000. The short$-\lambda$ part, is the location of the strongest stellar absorption features: Si II, Si III, Si IV, OIV, and CIV. With cross-correlation methods, we have verified (§A.4) that velocity centroids to ±100-300 km/s should be possible (for galaxies). Also, this band will provide the greatest sensitivity to Ly$\alpha$ emission line galaxies (and emission line clouds), which should have unresolved lines at $\Delta\lambda = 4$Å. The long$-\lambda$ portion will have resolution sufficient to resolve important lines, make spectral identifications, and search for QSO Lyman limit systems (cf. Figure 2.3).

### 3.4 General Mission Considerations

*Orbital Environment.* The major impact of the orbital environment on the mission is the nighttime photon, particle and detector background. The potential sources of light are geocoronal HI $\lambda$ 1216, OI $\lambda\lambda$1304, 1356, vehicle/ram glow, zodiacal light and the cosmic UV background. We discuss these, along

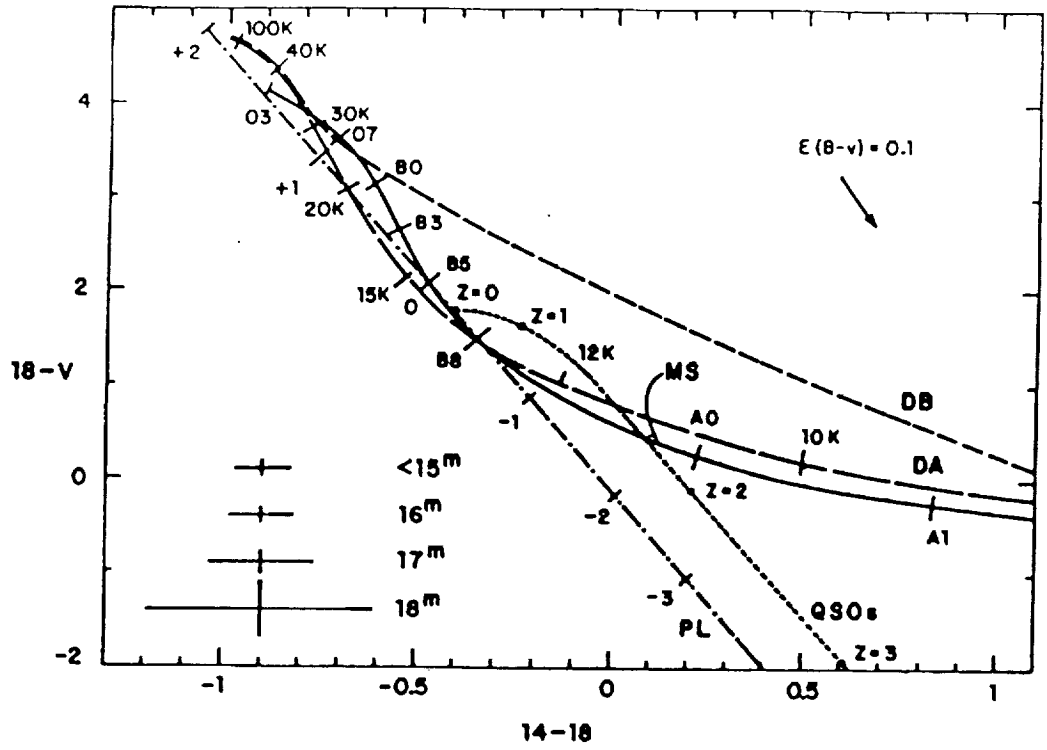


**Figure 3.3** 18-V/14-18 color-color diagram for various sources, with main sequence (*solid line*), hydrogen white dwarfs (*dashed line* labeled DA), helium white dwarfs (*dashed line* labeled DB), power law (*dot-dashed line*), and QSO's (*dotted line*). Main sequence stars are from IUE standard spectra, and white dwarfs from models of W80, W81 Average QSOs spectra for various redshifts have been taken from B84. These include the effects of intervening absorption, which causes a power law break that steepens with redshift. Error bars show $1\sigma$ color errors at various magnitudes, including systematics. The reddening vector is also shown.

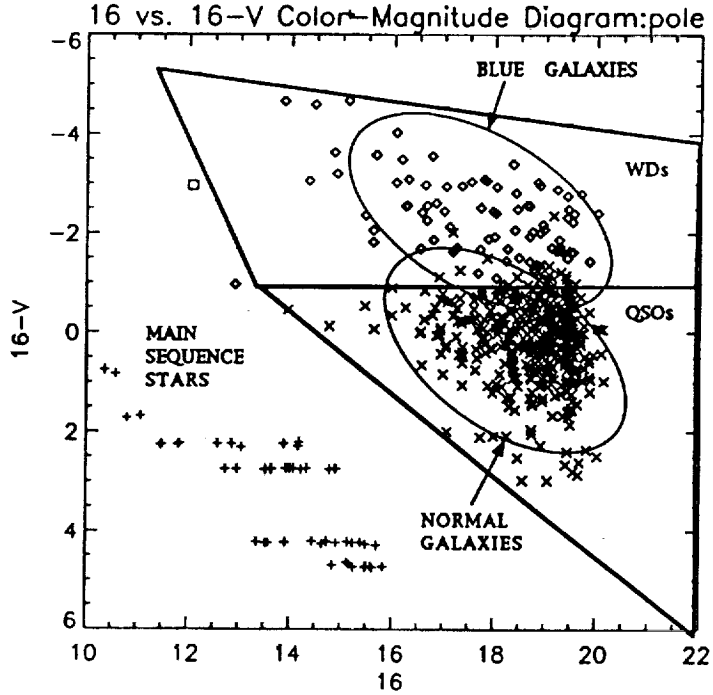


**Figure 3.4** Galactic pole simulation, one JUNO pointing (20 square degrees). Symbols give source type: +MS star, ×QSO, ◇WD, □CV. Galaxies have been shown in outline only for clarity.

Table 3.2 – JUNO Performance Summary

| Survey/Parameter | 14N pole | 14N plane | 18N pole | 18N plane | 16W pole | 16W plane |
|---|---|---|---|---|---|---|
| AS $m_{lim}$ ($\Delta m$ <0.2) | 17 | 16 | 17.5 | 15.8 | 18.5 | 16.7 |
| AS $m_{lim}$/contamination (>90% complete) | 17.8/5% | 16.8/<1% | 18.0/3% | 16.7/<1% | >20.0/5% | 18.5/<1% |
| 0.32 | | | | | | |
| DS $m_{lim}$ ($\Delta m$ <0.2) | 19.5 | | 19.8 | | 20.0 | |
| DS $m_{lim}$ (>90% complete) | 19.5/2% | | 19.7/1% | | 23.5/3% | |
| SS $m_{lim}$ (S/N=10(5)) | - | - | - | - | 16(17) | 15.7(16.7) |
| SS $\Delta v$ (m=16) | - | - | - | - | <2000 km/s | |

with particle induced background and radiation, in detail in §D. With our choice of filters, the dominant source of nightsky background will be the cosmic UV background.

*Attitude Stabilization and Pointing Program.* We will perform the all-sky survey in a sequence of slow-drift scans over ~5° during each orbital night. The slow drift is chosen over a stable pointing to: (1) increase the photometric accuracy by averaging source exposures over a large region of the detector; (2) minimize MCP fatigue from bright stars; and (3) produce a more uniform sky coverage; and (4) provide in-orbit flat fielding and distortion checks. The pointing program is designed to expose the entire sky in 3 bands in 9 months. Spacecraft stabilization will be provided by a 3-axis ADCS (§B.7). Absolute reference will be derived from stellar positions in the telescope data. Gyroscope and thermal drifts will be compensated *ex post facto* using telescope data and the star sensor, a technique we have verified with our UV model (§A.4).

*Dynamic Range, Data Storage, and Transmission.* A far ultraviolet all-sky survey carries with it a significant challenge: processing and transmission of large amounts of data. Many areas of the sky will have numerous bright stars, and even more numerous faint stars. The detector and event processing system must be capable of handling large local and global count rates. Also, the data must be telemetered to the ground at rates consistent with the spacecraft transmitter and ground station equipment. We have considered this question carefully and have adopted the following approach:

1. Detector saturation, which occurs naturally in microchannel plate detectors, will be used to prevent the brightest stars from creating significant event processing dead time. Stars with $m_{16} < 5$ will saturate and therefore not be detected photometrically.
2. Star photons that do not saturate the detector but would saturate the telemetry (approximately $m_{16}$ <10) are extracted by course image accumulation, and telemetered as coordinates and count rates only.
3. All other photon events will be downlinked individually, with detector coordinates and time tags, giving time resolution to <1 msec, and allowing significant ground post- and re-processing. This is critical for optimal *ex post facto* aspect reconstruction and meeting our astrometry requirement.

With the above method, we will require an orbit-averaged telemetered event rate of 260 KHz. By using the Italian ground station at Malinde, we will be able to dump the nighttime orbital data (1.25 Gbits) *every orbit*. Data accumulated during the night will be stored in a 200MB mass memory (§D) and can be dumped in <10 minutes. This is one of the principle motivations for our choice of an *equatorial* orbit.

### 3.5 Mission Performance Summary

The performance of the JUNO instrument and mission was determined from detailed simulations using our UV model. The results are summarized in Table 3.2.

# 4. INSTRUMENT DESCRIPTION

Two 33 cm three-reflection telescopes will perform both the photometric and spectroscopic surveys. At the focus of each, a 65 mm diameter MCP detector with an opaque, solar blind UV sensitive photocathode and a helical delay-line anode readout will provide photon counting detection with good quantum efficiency and 30 $\mu$m spatial resolution. The detectors will be sealed with $CaF_2$ entrance windows, and vented to space through an external valve after launch. System resolution is 16″. For the spectroscopic survey, a prism array will be interposed in the incident beam of one telescope, leaving the central 10% of the aperture to produce a reference "zero order" image. The optics, prisms, and detector will be mounted in a hermetic cavity with a movable dust cover. The externally mounted electronics package provides pulse amplification and timing, A-to-D conversion, bright star recognition and data compression, T/M formatting, storage and retrieval using a 200 MB CMOS RAM. **Figure 4.1** shows the JUNO telescope, and Table 4.1 summarizes its design and spacecraft accommodation requirements.

- *Two telescopes provide complete redundancy in MCP detectors and front-end electronics, high voltage bias supplies, and dust cover mechanisms. Digital electronics and mass memory are designed for graceful degradation.*

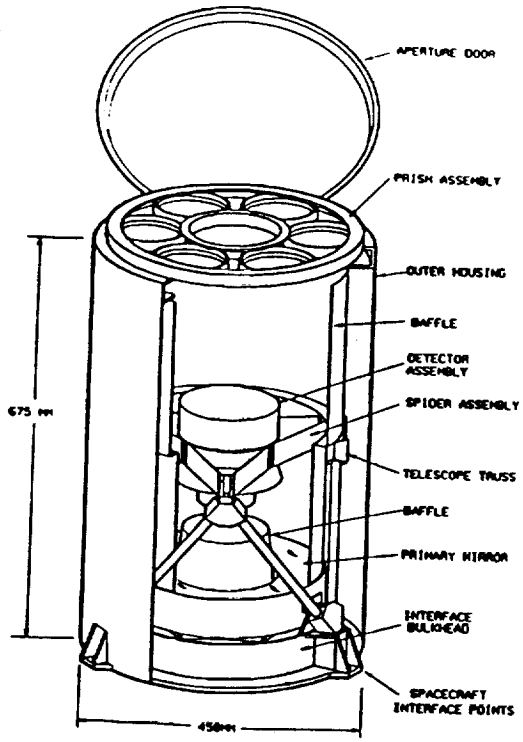


**Figure 4.1** A single JUNO telescope.

**Table 4.1**
**JUNO Payload Characteristics**

| | |
|---|---|
| *Payload Requirements* | |
| # of Telescopes | 2 |
| Telescope Housing Diameter | 45 cm |
| Telescope Housing Length | 70 cm |
| Payload Weight: Telescope | 40 kg |
| Electronics | 25 kg |
| TOTAL | 116 kg |
| Payload Power (Orbit Averaged) | 55 W |
| Payload T/M (Downlink) | 2.5 Mbit/s |
| Payload T/M (Orbit Average) | 260 Kbit/s |
| Mass Memory | 200 Mbytes |
| *Telescope Design* | |
| Primary Aperture | 33 cm |
| Focal Length | 77 cm |
| Plate scale | 0.26 arcsec/$\mu$m |
| Focal ratio | 2.75 |
| Type of telescope | 3 mirror (all hyperboloids) |
| Field of View | 4.8 ° circular |
| Coating | Al+$MgF_2$ |
| Temperature Control | 25±3C bulk, <1°C gradient |
| System Angular Resolution | 16″ (80% included) |
| *Detectors & Filters* | |
| Detector | Microchannel plate |
| Channel Diameter | 12 $\mu$m center-to-center |
| Detector Readout | Delay-line |
| Detector Photocathodes | CsI/KBr |
| Prism | $CaF_2$, 2 ° wedge |
| *Performance Summary* | |
| Telescope 1: Photometry | 1430Å: 1350-1575Å ($BaF_2$+KBr) |
| | 1830Å: 1650-2000Å ($SiO_2$+CsI) |
| Telescope 2: Photometry | 1600Å: 1400-2000Å ($BaF_2$+CsI) |
| Spectroscopy | 1250-2000Å, $\lambda/\Delta\lambda \sim 50-300$ |
| Magnitude Limits | 1400/1800: 18$^m$ |
| | 1600: 19.5$^m$ |
| Maximum data rate | $10^5$ events/s |

## 4.1 Telescope Optics

*Telescope Optical Design.* To maximize the survey volume, we require a telescope which is both fast and well corrected over a wide field of view. We have selected a modified Paul-Baker telescope, consisting of three hyperboloids in a compact, mechanically favorable configuration. A Schmidt telescope, ideal for optical surveys, is not optimal for a UV satellite survey. UV transmitting correctors give poor imaging, the Schmidt requires an expensive and less proven curved MCP detector, and using a reflective corrector

the resulting telescope is three times larger and considerably heavier than the modified Paul-Baker that we have chosen.

**Table 4.2 – Angular Resolution & Astrometry Budget**

| Major Component | Contribution | Resolution ($''$, 80% Diam) | Astrometry ($''$, rms) |
|---|---|---|---|
| TELESCOPE | Design Residual | 8.0 | 0.0 |
| | Ground Fab/Align Tol. | 5.0 | 1.0 |
| | On-Orbit Alignment Tol. | 2.7 | 1.0 |
| | OPTICS SUM | 9.8 | 1.4 |
| DETECTOR | Preamp/TDC noise/walk | 6.1 | 1.0 |
| | electron cloud variance | 6.1 | 0.0 |
| | channel spacing | 3.0 | 0.0 |
| | photocathode spread | 0.0 | 0.0 |
| | DETECTOR SUM | 10.5 | 1.0 |
| ASPECT | drift reconstruction | 5.0 | 1.0 |
| | detector nonlinearity | 5.0 | 2.3 |
| | ASPECT SUM | 7.1 | 2.5 |
| TOTAL (rss) | | 16.0 | 3.0 |

The telescope, illustrated in **Figure 4.1**, was selected by zeroing the Seidel aberrations, and then minimizing the residual blur using an average spot size figure of merit over a large set of designs. Baffling of direct primary-detector rays will be accomplished with a set of conical baffles placed in the primary-secondary optical path as shown in **Figure 4.1**. They will produce vignetting of 7% on-axis and 14% 2.4° off-axis.

*Imaging Requirements.* The optical fabrication requirements are based on the system angular resolution error budget given below in Table 4.2, in which we have allocated $10''$ (80% encircled energy diameter) to the optics. This figure includes geometric aberrations, diffraction and scattering, filter chromatic aberrations, low-, mid-, and high- frequency surface errors, assembly tolerance and mounting strain, and thermally induced focus errors.

*Telescope Fabrication & Testing.* HDOS has audited the JUNO optical design. To achieve 80% encircled energy in the FUV within a $16''$ image diameter 2.4° off-axis we set a system wavefront error of $0.15\lambda$. Spot diagrams are provided in **Figure A.24**. The wavefront error budget (**Figure A.25**), provides flowdown requirements on mirror figure, ground assembly tolerances, and on-orbit structural performance. The on-orbit secondary mirror despace requirement of $1.2\mu$m is a system driver. We traded off active focus control versus an Invar structure and active thermal control and decided on the latter because of lower risk and cost.

HDOS shall procure three sets of the three (primary secondary, tertiary) zerodur mirror blanks from Schott. Schott will generate each blank to a best fit sphere, and cut the center holes and mounting interfaces into the blanks. On arrival at HDOS, the blanks will be generated to hyperboloids on the CNC (computerized numeric control) generator. HDOS will then proceed with a conventional grind and polish to the final surface figure quality of $\lambda/40$ rms. Metrology tests of the surface figure will be performed with reference spheres (Hindle and Silvertooth configurations). A complementary check on mirror figure, good to $\simeq \lambda/25$ rms, will be performed with a conventional knife edge test.

- *In order to verify telescope imaging performance, we will undertake two end-to-end far UV imaging tests with a JUNO detector by HDOS and CAL at HDOS (prior to buyoff) and at CAL.*

The JUNO utilizes two telescope assemblies which are identical except for the inclusion of six $CaF_2$ prisms in the object space of one of the telescopes. Each telescope assembly, shown in **Figure 4.1**, consists of a three-mirror telescope, detector assembly, interface structure, outer enclosure, aperture door, and thermal control components. The telescope's all-Invar structure is a truss of six struts which span the interface between the bulkhead and spider assembly forming a simple, robust mounting for the mirrors and detector assembly. The spider assembly, consisting of six spiders tangent to a central hub, supports the secondary mirror and its baffles as well as the detector assembly. The primary mirror is flexure mounted to the interface bulkhead with the tertiary mirror mounted, in turn, to the primary. The interface bulkhead also includes provisions for mounting the telescope assembly to the spacecraft and for supporting the telescope

enclosure. The bulkhead attaches to the spacecraft through a kinematic mount. The aluminum instrument enclosure, hermetic for contamination control, attaches to the interface bulkhead and surrounds the telescope, extending 700mm forward. The Al prism plate assembly and/or aperture door mount in the forward end of the enclosure. The former consists of a machined plate to which the six $CaF_2$ prisms are mounted, each pre-installed in its own bezel. A redundant stepper motor drive opens/closes the aperture doors. A solenoid operated latch determines whether the prisms open with the door or remain in place. Preliminary analysis of the telescope's thermal/mechanical design verifies its suitability for the flight environment in the four key areas of strength, first mode frequency, mass, and thermal alignment stability (§A.5).

Thermal control of the telescope assembly is achieved through the use of active and passive techniques including: MLI on inner and outer surfaces of the telescope enclosure, low emmisivity coating on the spiders and baffles (Maxorb tape), heaters (HST design) on the telescope struts, heaters behind the primary and secondary mirrors, and low conductance attachments for the baffles and spacecraft interface.

The polished and $Al/MgF_2$-coated mirrors will be assembled into the structure at HDOS. HDOS and CAL will jointly test the telescopes in the far UV for imaging and throughput, prior to buyoff (cf. §A.6) All post-coating operations will be performed under Class 1000 clean room conditions. For contamination control, the telescope enclosure is hermetic.

### 4.2 Filters and Objective Prism

Alkaline earth fluoride crystals make excellent far UV high pass filters. Their short wavelength cutoffs make them suitable for filtering the airglow lines of HI (Ly $\alpha$ 1216) and OI $\lambda$1304/1356. The transmission longward of the cutoff is generally high, >60%. They can be produced with sufficiently large areas and with thicknesses( >1.5 mm) that make them rugged for space flight. The prisms will be thin (3-6 mm) with a 2°wedge. Six 12 cm diameter prisms will be mounted in a single panel that can be rotated 100°out of the beam. Their wedge angles must be matched to $< 2''$, which is not a severe requirement for planar surfaces. Calcium fluoride is a good optical working material. Since the prisms are thin, the alignment tolerance is comfortable: a 0.2°angle mismatch between the prisms would produce a $0.8''$ difference in the diffraction angle. When not in the beam , the prisms are baffled and sufficiently recessed to prevent grazing reflections. Fluorescence, dn/dT, and ghosts in these materials are shown in §E.3 and §F.2 to be tolerable.

- *We have fabricated and tested two $CaF_2$ prisms and mounting design. The prism matching can easily be achieved within specifications (§A.3). To test the ruggedness of the prism and holder, we performed a successful shake test to SMEX qualification levels (14 g's rms) (§A.3).*

### 4.3 Detector

The JUNO detector requirements are derived from the three principal mission requirements: (1) all-sky survey to 18-19.5$^m$ in one year, (2) positions to $<3''$, (3) reliable, proven technology. This leads directly to these key detector requirements:

- 2000 × 2000 pixels, 30 $\mu$m/pixel.
- No red leak.
- Throughput $\sim 10^5$ cps (global).
- Far UV QE $\sim$ 10-20%.
- No cold surfaces and contamination.
- Capable of withstanding Pegasus or STS launch.

The JUNO detectors will incorporate microchannel-plates with opaque, efficient, and solar-blind CsI and KBr photocathodes. The MCP will be read out using a Helical Delay-Line (HDL) anode, which we have demonstrated will provide the necessary resolution, throughput, and mechanical robustness.

#### 4.3.1 Microchannel Plates.

Microchannel plate detectors today constitute one of the most widely used detection schemes in optical, ultraviolet, and soft x-ray astronomy. They offer a number of advantages over other methods, including photon detection, high imaging resolution, and high intrinsic gain. For the proposed application, they offer many advantages over CCD's. They are readily obtainable in large formats essential for a survey

mission. They do not need to be cooled, and exhibit absolutely no red leak. A CCD combined with a Woods filter gives low QE in the far UV ($\sim$ 3%), and is subject to severe condensable contamination as WFPC I has painfully demonstrated. MCP detectors provide timing information, and permit *ex post facto* drift compensation and high background elimination. Most importantly, MCP detectors have a long and successful history in space astronomy instruments, including EINSTEIN, ROSAT, and EUVE.

Microchannel plates have several relevant limitations, which must be taken into account in the instrument and mission design:

(1) *Count-rate Dynamic Range*: While MCP count rates are limited by the channel wall current, it has been shown that for small areas the count rate limit can be quite high (F91;ZF91;ST91), $\sim 1000-3000$ ct/s with limited saturation. The brightest stars will saturate, which we use to our advantage to reduce front-end electronics deadtime. This is discussed in §3.4 and §A.4.

(2) *Microchannel Plate Fatigue.* Charge extraction from microchannel walls produces a gradual but irreversible drop in the secondary emission coefficient, and consequently, in the gain. For conventional plates, a gain degradation is typically observed after a charge extraction of Q=1 $\mu$C/channel. This represents a concern for JUNO, since the image is well focused and bright UV stars could generate "dead" pixels. Our approach is threefold: (i) drift scan during the all-sky survey pointings to "spread the photons" from bright stars more uniformly; (ii) use a spacer in the MCP stack to spread the events over many channels in the third MCP; (iii) scrub the MCP stack to stabilize the gain. Based on our UV model analysis, presented in §A.4, we conclude that total charge lifetime of conventional MCPs is more than adequate for this mission.

(3) *Microchannel plate internal background.* Laboratory internal background in MCP detectors, dominated by radioactive trace elements, are routinely <0.5 $cm^{-2}$ $s^{-1}$, and rarely exceed twice that in orbit, if precautions are taken to prevent particle influx. A total background rate of 1 $cm^{-2}$ $s^{-1}$ can be compared with that produced by the far UV diffuse background, always >100 $cm^{-2}$ $s^{-1}$.

*Baseline Design.* The far UV survey detector will have an active area of 65 mm, and MCPs with a physical diameter of 70 mm. A Z-stack of three MCPs with 10 $\mu$m channels on 12 $\mu$m centers, and with L/D=80:1 will be operated at a gain of 2-3$\times 10^7$. The detectors will be overcoated with opaque CsI and/or KBr. Each detector will be baked and "scrubbed" to stabilize the gain prior to photocathode overcoating. To maintain the detector free of hot-spots and to stabilize the somewhat hygroscopic CsI, the detectors will be kept evacuated at all times prior to launch. A schematic of the detector is given in **Figure A.26.**

### 4.3.2 Helical Delay-Line Readout System

- *We have fabricated and extensively tested a prototype detector readout system that meets the resolution, linearity, stability, and count rate throughput requirements of the JUNO mission. Our tests included a successful vibration test of the helical delay-line anode to Pegasus qualification levels.*

To recover the position of the incident photon, the centroid of the electron cloud exiting the MCP stack must be determined by the anode and downstream electronics with an accuracy of $\sim 30\mu m$(FWHM). We have developed a helical delay-line detector with high spatial resolution and excellent count rate throughput. Delay-line position readouts for microchannel plate detectors (L87; SW87) are rapidly developing as a high-performance, robust, and low-cost alternative to discrete pixel readouts. The helical wound anode (SW87), incorporates two parallel coils wound for each dimension on an insulating frame. The parallel wires form a bifilar transmission line that is connected at each end to a broad-band differential preamplifier (cf. **Figure B.1**. MCP electron pulses fall on the anode and propagate at an effective velocity $v_e << c$ to both ends of the delay-line. The arrival time difference is related to the event position by $x = \frac{1}{2}v_e(t_2 - t_1)$. The pulse arrivals are timed with constant fraction discriminators (CFDs), which are used to start and stop time-to-amplitude converters (TACs). Flight detector electronics are discussed in §D.

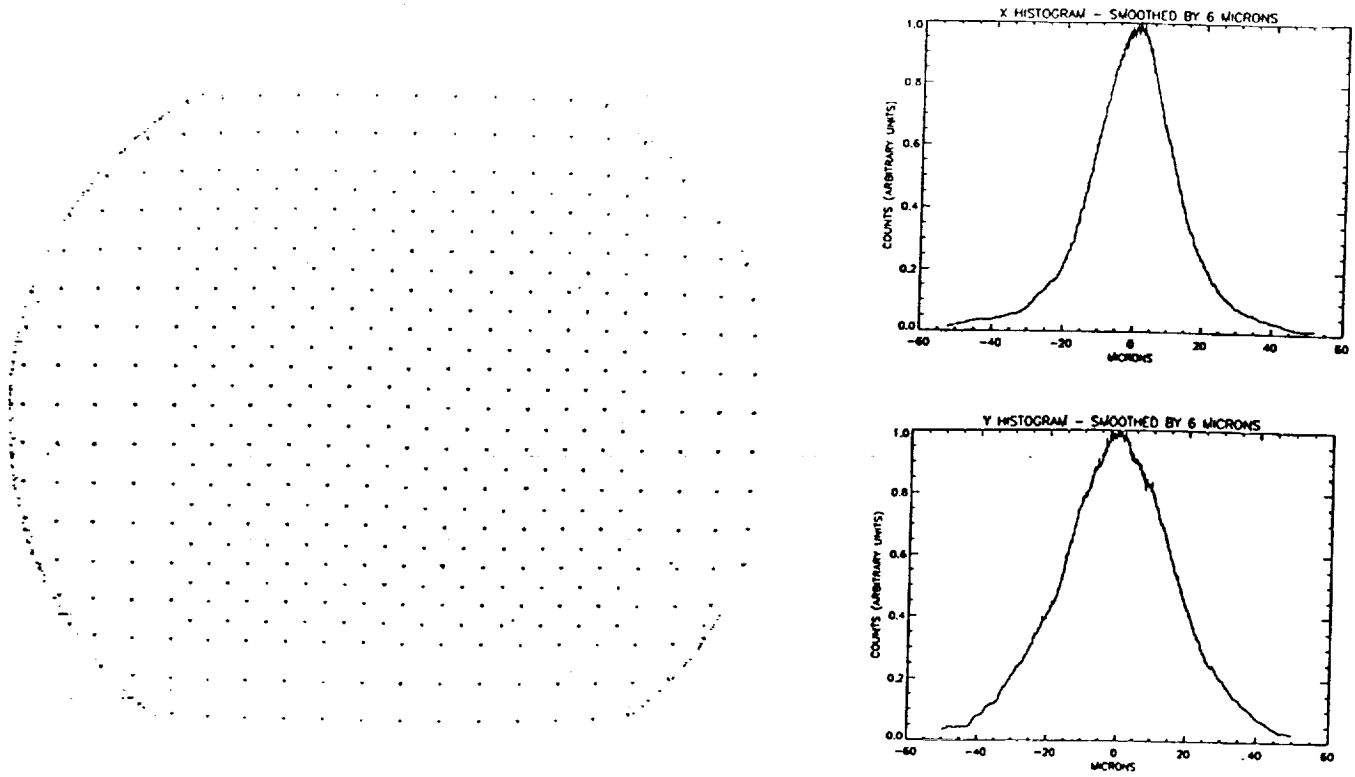


**Figure 4.2**: Image obtained with prototype helical delay-line detector showing a grid of 10 $\mu$m spots over the entire 40 mm active area, obtained with our precision UV spot positioning system. Also shown is a magnified histogram of 41 coadded spots. X- and y-resolution is$\sim$23 and 33$\mu$m (FWHM).

We have developed a prototype HDL detector (FMR90;F92;F93a) that satisfies JUNO requirements, described in detail in §A.2. Images obtained with the detector are shown in **Figure 4.2**. The flight JUNO detector will be somewhat smaller, 100 mm square, with a higher effective velocity, 1 mm/nsec. Although this increases the required timing accuracy, it also decreases the pulse rise time and increases its amplitude due to the decreased skin-effect attenuation. The net result is comparable resolution performance and higher throughput due to the smaller delay-time. Three critical detector readout performance characteristics are:

(1) *Resolution.* We have obtained routinely resolutions of 30$\mu$m(FWHM) in both dimensions. This is illustrated in **Figure 4.2**. This gives > 2000 × 2000 pixels across the active area, meeting the JUNO requirement. The anode contributes 15-20 $\mu$m with an MCP gain of $3 \times 10^7$, including 15$\mu$m from amplifier noise and 10$\mu$m from timing "walk". The channel spacing is 12 $\mu$m. Errors introduced by electronics nonlinearity and thermal shifts will add <5 $\mu$m blur. MCP electron cloud variance contributes < 20$\mu$m.

(2) *Linearity and Stability.* HDL linearity is ±30$\mu$m, or ±1 detector pixel, over 90% of the active area, degrading to ±50-100$\mu$m near the MCP support ring due to electron focussing. Most distortion is either 1D (anode related) or radial (E-field gradients) and can be calibrated and corrected to 3$\mu$m. Magnetic shielding and improved electrode design will reduce nonlinearity to <1 pixel (8″) everywhere, and corrections will be stable to <0.25 pixel (2″), in order to allow astrometry to ±3″. TIming electronics will be temperature compensated and continuously calibrated by a stim pulser.

(3) *Count rate Throughput.* Telescope/Detector throughput is limited by several factors: MCP saturation, delay-line readout-time and baseline disturbances, ADC and DPU speed. The theoretical limit of our delay line is $10^6$ cps for 10% coincidence loss. Front-end electronics (ADCs) will give $10^5$ cps with 10% dead-time. We tested the prototype HDL throughput up to 30,000 cps, with no evidence of performance change.

*Mechanical Tests.* The mechanical prototype HDL was wound onto a MACOR frame with machined

grooves to maintain wire positioning (Figure A.2). The wire-deviations were <5 $\mu$mpre-shake. The anode was vibrated at SMEX qualification levels. No measurable change in wire position or electrical properties occurred (cf. Table A.2).

### 4.4 Calibration

Preflight calibration of the instrument will be performed at the CAL VUV calibration facility. *Columbia University, in order to demonstrate its commitment to the success of the JUNO mission, will provide $200K in capital funding to renovate space to accommodate the JUNO integration and calibration efforts.* The facility is currently equipped with a 1 m diameter by 1.5 m long vacuum chamber cryogenically pumped to prevent optics contamination, connected to a 1 m far UV monochrometer with various sources. A 35 cm Cassegrain collimator will be added. Detector resolution, linearity, and field flatness will be extensively calibrated using our precision detector evaluation system. Telescope calibration will determine the reflectivity, point spread function, telescope throughput (including baffling) and scattering levels as a function of wavelength and field angle. Witness samples will be used to spot check the efficiency during S/C and Pegasus integration. The telescope-detector combination will be calibrated to determine system efficiency, linearity, and resolution as a function of wavelength and field angle, using the collimator, dual-axis gimbal platform, and NIST calibrated photodiode. We will achieve an absolute accuracy of $\pm 10\%$ for the efficiency calibration, and $\pm 1$ arcseconds for the distortion map. In-flight cross calibration with stars observed by other missions, particularly IUE, will enable regular updates of the instrument efficiency to the desired $\pm 10\%$ accuracy level. The continuous drift scans will allow checks of system distortions and field-flatness.

### 4.5 Technical Feasibility and Maturity

In 1988, our proposal for a SMEX all-sky UV survey received excellent scientific reviews, and very good technical reviews. Five principal technical criticisms were leveled. In the last four years we have devoted considerable effort in order to respond to these issues. In this section, we summarize the results. In Appendix A, we give a more detailed report.

1. *The detector is a single point failure.* We have incorporated two telescopes into the revised design. This provides redundant detectors, front-end analog electronics, high voltage supplies, and door mechanisms. The telescopes are identical save filters and prisms. One telescope has two narrow-band filters– $\lambda$1400 (**14**) and $\lambda$1800 (**18**). The other has one wide-band filter $\lambda 1400-2000$ (**16W**) and a rotatable objective prism array. This also yields a deep band useful for extragalactic surveys (**16W**), and coverage of the CIV$\lambda$1549 line with a synthesized narrow band [**16N=16W-(14+18)**].
2. *The detector readout was unproved.* We have developed and extensively tested a 2D helical delay-line (HDL) readout that satisfies the JUNO detector requirements (FMR90;F92;F93a). It yields <30$\mu$m FWHM resolution, 2000×2000 pixels, good linearity (<1 pixel), stability, and throughput. The detector is mechanically robust: we have vibration-tested it to SMEX qualification levels successfully. A sounding-rocket flight test of three HDL detectors will take place during the definition phase, in early 1994.
3. *Large $CaF_2$ prisms and faceplates.* We have fabricated a flight prototype of one $CaF_2$ prism, and vibration-tested it in a prototype mount. The prism integrity and alignment was maintained.
4. *The effects of photometric accuracy on source classification efficiency were not adequately addressed. Spectrum simulations were insufficient.* We have developed a detailed, statistically realistic model of the UV sky and the JUNO telescope, detector, electronics, and software data-compression systems, including the effects of S/C pointing drift. We have simulated UV images using digitized optical plates as positional templates, and standard source finding package (FOCAS) for source detection and evaluation. With the UV model, we have been able to determine:

- Source detection completeness vs. magnitude;
- Source classification efficiency and catalog purity;
- Source crowding and confusion of optical identification, and its effects on catalog purity;
- Photometric accuracy vs. magnitude;
- Quality of prism spectra and derived parameters such as redshift vs. magnitude;
- Count rate statistics in detectors, local and global;
- Most effective data compression algorithms;
- QSO z-distribution in detected sources;
- Effectiveness of extinction determinations.
- Hardware, software, and personnel requirements for JUNO data reduction tasks.

Using this, we have verified that the mission meets our science goals for optical ID and source classification efficiency. All magnitude limits and performance numbers quoted in the proposal are based on our UV model. *This work demonstrated unequivocally that system design, particularly system angular resolution (16"), is critical for making unambiguous optical IDs for the majority of the UV sources.*

5. *Payload integration was not adequately addressed.* We have developed a detailed test, calibration, and integration plan discussed in §4.6, §B, and in Volume II, §5.3.
6. *Additional Results.* We have also performed studies of the optical design, imaging error budget including structural design and thermal modeling, detector/telescope interface, data compression, memory design, contamination control, and of the optical identification approach.

In summary, the detector is proven, HDOS has fabricated a very similar telescope to this before (VUE; cf. Vol. II), and the Alenia spacecraft design is well established (cf. §4.6 and Appendix B). Because of our substantial progress in the JUNO mission design, we are confident that we can meet a three year development schedule (**Figure II.3**).

### 4.6 Instrument Integration

The JUNO spacecraft, funded by the Italian Space Agency (ASI) and built by Alenia-Spazio, is described in detail in §B. **Tab. 4.3** gives a brief summary of its main characteristics. Schematics of the instrument integration into the spacecraft and the spacecraft into the Pegasus are given in **Fig. 4.3**.

## 5. FLIGHT OPERATIONS AND DATA ANALYSIS

### 5.1 Flight Operations

In **Table 5.1**, we summarize the mission phases, pointing and viewing requirements. We estimate for the 18 month mission that 20% of the observing time will be used for overhead (SAA passages, uplink/downlink overlap, and instrument/spacecraft/mission operations problems). All mission operations activities will take place at the Italian ground station at Milinde and at CRA in Rome. Payload operations will take place at CAL. The following functions must be performed:

- Monitoring of spacecraft and telescope engineering health;
- Production of an attitude ephemeris following each orbit;
- Gyro drift compensation;
- Sky exposure monitoring and attitude program planning;
- Periodic in-orbit calibration;
- Production of quick look data for science planning functions;
- Mode changing and contingency commanding.

The flight operations system, illustrated in Figure 5.1, consists of three main components. At the ground station, a Rapid Analysis Station (RAS) will store telemetered data on a write-once read many (WORM) optical disk, perform a preliminary analysis in order to obtain the attitude ephemeris and compressed quick-

Table 4.3 – JUNO Spacecraft Summary

| Item | Value | Ref | Supplier/Heritage |
|---|---|---|---|
| Mass (Total/SM/PL) | 290/178/112 kg | Table B.11 | |
| Volume | 1.08×1.45×0.72 m | §B.4, Fig. B.4.3 | |
| P/L Sensitivity to Contamination | Sensitive to optical & EMI | §4, 6 | |
| Power (Eclipse/Day) | 227W/176W | Table B.8 | |
| Power (Acquisition/STDBY) | 121W | Table B.8 | |
| Solar panels | GaAs 3.7 $m^2$ Fixed/Deployed | Fig. B.4.3,§B.8, Tab. B.12 | FIAR, Fokker |
| Batteries | 32×22Wh NiCd cells | §B.8 | FIAR |
| ADCS | 3-axis Gyros+RW+STR | §B.7 | MATRA, TELDIX, Galileo |
| Accuracy/Stability | $10'/<5''/s$ | §B.7, §A.5 | |
| T/M P/L | 2.5 Mb/s–200Kb/s(OA) | §3.4, B.7 | Alenia |
| I/F–PL/SC | Mil 1553B/ESA Std. OBDH | | |
| Data Volume | 1.25 Gb/orbit–12 Tb total | §3.4, A.4 | |
| On-board DH System | ESA standard | §B.8 | Laben |
| Thermal S/C Elect (battery) | passive: -10/+40C(0/25C) | §B.6 | |
| Thermal Telescope OP | active: 25±1C | §4.1 | HDOS/HST |
| Thermal Standby/Survival | passive: 25±25C | §B.6 | |

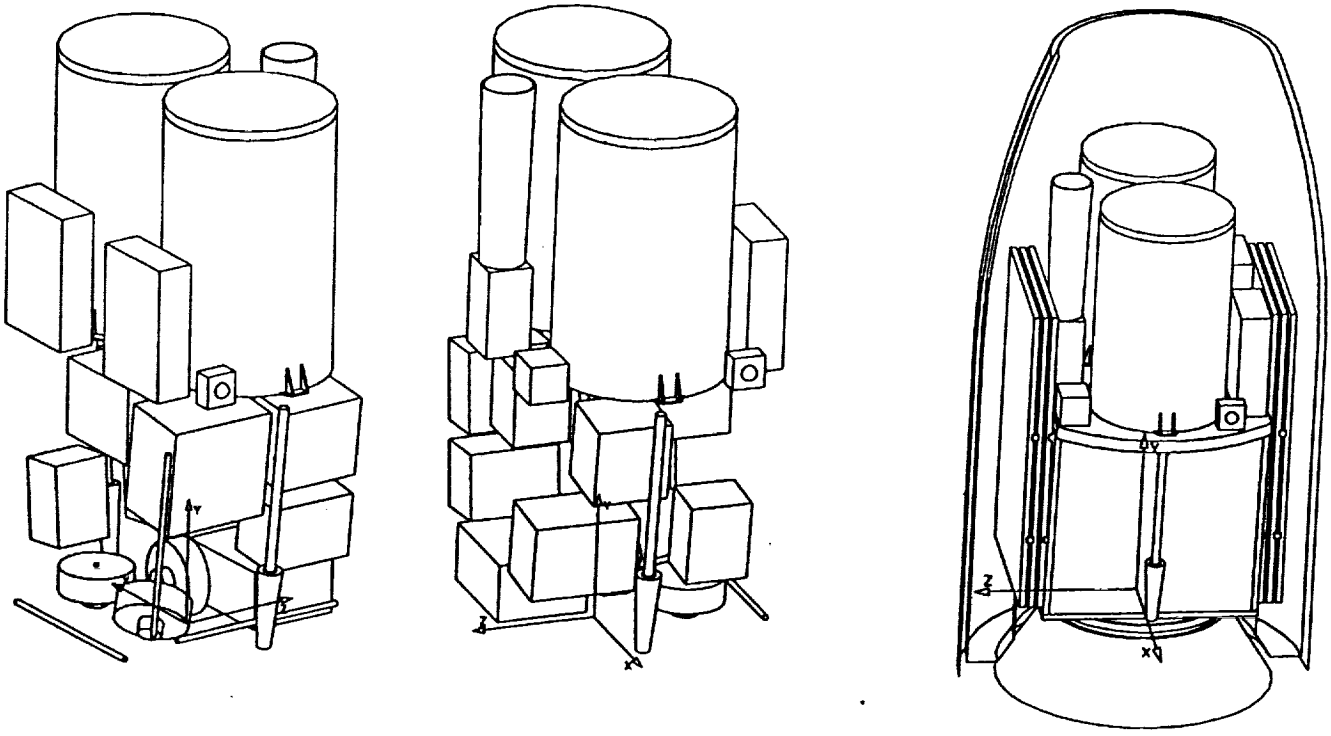

**Figure 4.3** Left: JUNO instrument integrated into ALS spacecraft. Right: JUNO spacecraft integrated into Pegasus launcher.

look data for near real time transmission to the SPOC. The Telescope Operations Station (TOS) will receive quick-look science and engineering data from the RAS over a dedicated 9600 baud communications link.

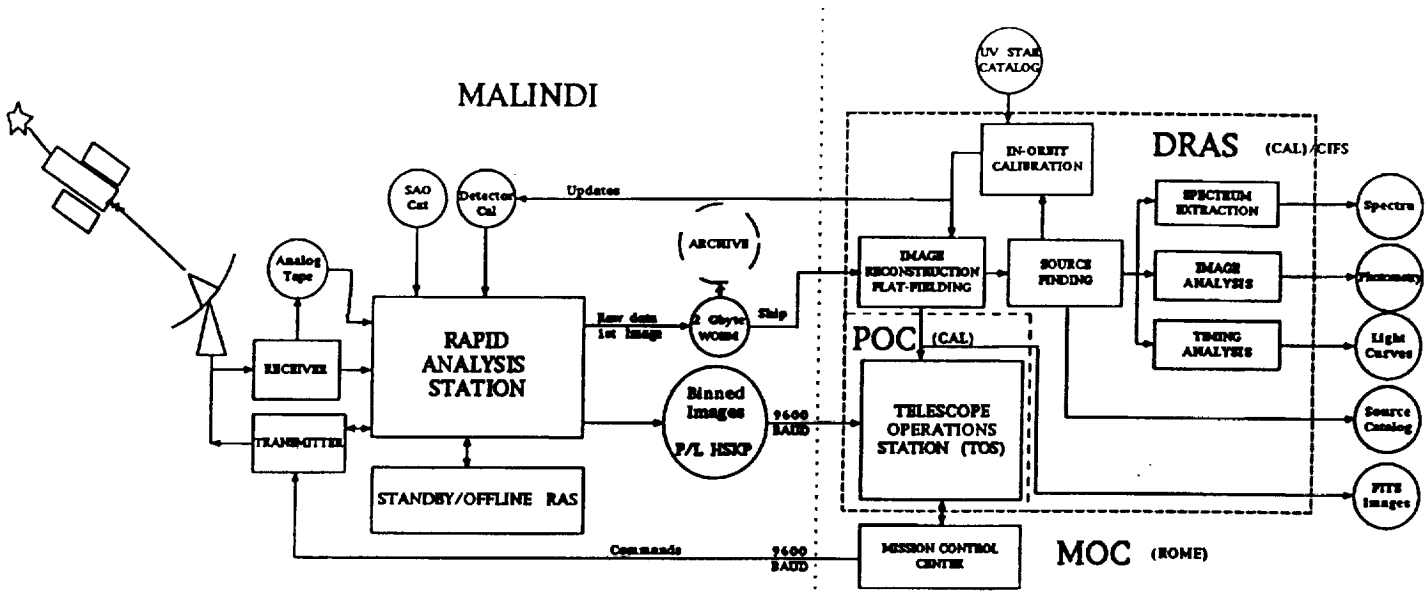


**Figure 5.1** JUNO Flight/Science Operations and Data Analysis System.

**Table 5.1 – Mission Breakdown (18 Month Mission)**

| Mission Phase | % | Days | Orbits | Exposure Typ. (sec) | Sky Coverage | Method | Pointing Absolute | Viewing Requirements | Mag. Limit ($5\sigma$) |
|---|---|---|---|---|---|---|---|---|---|
| All-Sky | 50% | 270 | 4500 | 1500 | 100% | $10''$/s slew | $\pm 10'$ | Sun-Horizon $< -15°$ | 17.5-19.5 |
| Deep | 6% | 33 | 533 | 40,000 | 1% | $10''$/s slew | $\pm 10'$ | Zenith Angle $< 70°$ | 21-22.5 |
| Spectroscopic | 24% | 130 | 2100 | 50,000 | 3% | $10''$/s slew | $\pm 10'$ | Tel/Sun Angle $> 100°$(OBS) | 17.5-19.5 |
| Overhead | 20% | 110 | 1700 | - | - | - | | Tel/Sun Angle $>30°$(STB) | |
| TOTAL | 100% | 550 | 8400 | - | - | - | | | |

This facility will support all science planning and command generation. All telescope commands will be forwarded to the Mission Operations Center (MOC), at CRA in Rome, where all satellite operations are controlled.

*Rapid Analysis Station (RAS).* During each ground station pass, the RAS will receive the telescope data from the station TM decoder, and write the raw 2.5 Mbps stream onto an optical disk. A single 2 GByte disk will hold 15 orbits worth of data. A copy of each disk will be made off-line using the backup RAS, and shipped by overnight delivery to the SPOC. The RAS acts fundamentally as a front end data compression system. It provides the TOS and MOC sufficient quick-look data for mission operations functions. The RAS derives a preliminary aspect ephemeris, constructs an image, a bright source list, and transmits them to the TOS/POC over a dedicated 9600Baud line. Many of the RAS functions have already been tested on our Sparc 3 workstation using the UV model. Our existing hardware can perform the required functions in near-real-time.

*Payload Operations Center (POC)* At CAL, the POC will receive near-real-time quick-look data from the RAS, and archived complete data. POC functions include:

- Telescope health monitoring and functional verification;
- Telescope command generation;
- Exposure map history to support pointing programming and replanning support;
- Interface to telescope prototype for on-board software revision verification;

- Analysis of science quick-look data for verification and optimization of telescope performance;
- Communications to the RAS and to the Mission Operations Control Center.

The TOS will display Instrument health data for continuous monitoring. Telescope commands will be sent to initiate in-orbit operation (opening the dust cover, the detector vent valve, first high voltage turn on), change detector processing modes (thresholds, count rate limits, bright star limits), and change filter or prism positions. In the event of a serious DPU problem, new S/W can be uplinked as well. Command packages will be generated at the TOS, run through local verification procedures, and forwarded to the MOC. The RAS and POC H/W will evolve directly out of the telescope ground support equipment (TGSE), since the three systems have many common functions.

Telemetered engineering and science data will be used to monitor regularly the end-to-end integrity of the JUNO telescope. The following program of regular checks will be performed:

- Verification of detector pulse height, count rates, and correct operation current;
- Verification of the linearity and gain of detector and timing electronics using stimulation pulser calibration;
- Verification of the valid operation of the data compression software;
- Monitoring of telescope calibration using standard stars;
- Monitoring of telescope thermal history;
- Monitoring of orbital backgrounds;
- Verification of correct processor and mass memory operation using on-board self checks;
- Verification of execution of timed and day/night commands.

### 5.2 Data Reduction and Analysis

Data reduction and analysis will be split between the CIFS SOC and CAL Science Data Reduction and Analysis System (SDRAS). Production processing begins with the daily 2 GByte optical disk received from Malinde by overnight mail. Image reconstruction, which includes telescope distortion corrections, derivation of a final aspect solution, and flat-fielding, yields a calibrated image of the sky. *We have verified using our UV model that image reconstruction of $5\times10^7$ events (maximum single orbit data volume), including drift correction from stars in the UV data can be performed in 30 minutes on a Sun Sparc (cf. §A.4)* This will form the input for FOCAS, which we will use for source finding and characterization for the AS and DS. For spectroscopy data, unique software will be required for source finding. The end result will be a source catalog, including positions, fluxes, colors, spatial moments, and preliminary source classifications.

- *Our UV model has already provided us with first version of the SDRAS, which allows us to size the hardware and personnel required for the task with confidence.*

The point source catalog forms the basis for all subsequent processing, which can be broadly classified as timing, image, and spectrum analysis. Timing analysis can be performed in batch mode once the catalog is generated for each field, to produce a variability catalog, including light curves, lag plots and FFTs. For extended sources, the numerous image analysis tools available in the IRAF package will be used. We will employ a combination of IRAF routines and mission unique software for spectrum extraction and analysis. Extraction routines will generate fluxed source, sky and flat-field spectra, and a wavelength scale. For time variable sources, spectra will be accumulated in time or phase bins.

We anticipate that the basic survey data derived from the JUNO mission will remain an essential resource for the world wide astrophysics community for decades to come. We therefore propose the following mechanism for making the JUNO results available in a timely manner. The mission's basic data products, outlined above include: raw data, calibrated sky images, source catalog, timing catalog, spectral catalog, sub-catalogs of selected source classes. A copy of the raw data, on optical disks, and the primary source catalog along with the timing and spectral catalogs will be delivered to the NSSDC and the NASA UV science archive (UVSARC) within 12-18 months of the end of the mission's flight phase (cf. Vol II, Figure 6). Calibration information (e.g., flat-fields, wavelength scales, etc.) will also be made available. Specialized sub-catalogs will be deposited as they become available.

*Optical Identification of JUNO sources.* Although much of the science which will emerge from the JUNO missions derives from the ultraviolet data alone, it is clear that optical magnitudes and colors as well as arc-second optical images and proper motions for each of the several million JUNO UV sources would enhance enormously the scientific value of the data base. We clearly require a fully "machine readable" version of the optical sky for comparison with the JUNO catalogs. Fortunately, such facilities exist at the StScI and will be partially distributed to the community before the JUNO launch.

In the process of creating the HST Guide Star Catalog, the StScI Guide Star Selection System (GSSS) has scanned the entire sky using the [1955] R-band Palomar survey in the north (to $> m_R \sim 21$) and the UK Schmidt Survey plates in the South (to $m_J \geq 22$). This digital database now exists at StScI on 350 optical disks. Photometric calibration will be completed in the next year, the magnitudes of all objects above these limiting magnitudes will be calculable to $\pm 0.1$; positions will be accurate in the global Hipparchos/Guide Star reference frame to $\leq 0.''3$. These accuracies are more than sufficient for our purposes. Furthermore, the GSSS is currently in the process of scanning a second set of plates in a second color, that will be complete to $m_J \sim 22$ (North) and $m_R \sim 22.5$ (South), taken at a second epoch.

The first epoch plates (available on CDROMS before JUNO launch) will be used in conjunction with the JUNO source positions to generate a catalog of identifications with an optical magnitude and position accurate to $0.''3$. This can be performed with inexpensive hardware (Sparc 2 running IRAF + CD-ROM jukebox, ~$15K) much faster than the real-time UV detection. Greater than 99% of the objects detected in the JUNO all-sky survey will have counterparts in this optical database. This catalog will then be used with the second epoch scans at StScI to generate a second catalog of sources with colors (accurate to $0.14^m$) and proper motions (accurate to $< 1-2$ m$''$/yr.). This can also be done much faster than the real-time UV detection. The combination of colors and proper motions will produce catalogs of WD's and QSOs with high purity (cf. §3.1 and §A.4).

Also available at CAL and CIFS will be a complete set of star, cluster and galaxy catalogs along with IRAS sky plates and catalogs, radio catalogs, HEAO-1, Einstein and ROSAT source lists, IUE standard spectra and other data products which will be used in constructing the JUNO catalogs.

## 6. PRELIMINARY PERFORMANCE ASSURANCE IMPLEMENTATION PLAN (PPAIP)

CAL has implemented and maintained a Quality Assurance and Reliability (QA&R) Program since 1971, with the beginning of its Orbiting Solar Observatory (OSO-8) Mission on which three CAL X-Ray experiments were flown successfully for three and one-half years. A Solar Flare X-Ray Polarimeter experiment was flown successfully on the Space Shuttle STS-3 Mission using a modified CAL QA&R program. During the definition phase of the SMEX Mission, CAL under the direct responsibility of the USPI, will develop a SMEX Program PA Implementation Plan (PAIP) using its existing Configuration Management Control System and meeting the requirements detailed in the SMEX Product Assurance Requirements (PAR) document, GSFC S-740-89-993, Rev B, dated July 20, 1992. CAL will simplify and extract existing key QA&R program elements, balancing program cost and complexity with performance assurance. Each of CAL's collaborators developing the JUNO experiment payload; HDOS for the mirror and telescope systems and SNL for the digital electronics design and flight electronics fabrication have extensive experience in developing and fabricating flight hardware for small scientific satellite missions. They will adapt their in-house PA Standards and Practices Manuals in a cost effective manner to meet the SMEX PAR. Their extensive knowledge and in-house capabilities will enable the rapid delivery time required to produce a successful JUNO SMEX Mission.

CAL, and its collaborators as required, will support all GSFC Design Reviews as formal design activities throughout the SMEX program as specified in §2 of the SMEX PAR. Informal design reviews will be implemented at whatever component, sub-system, or system level is most efficient in meeting the SMEX project schedule. Design reviews with all major sub-contractors will be conducted by CAL to insure

all the requirements, including system safety, of the SMEX PAIP are satisfied.

CAL will conduct a rigorous Verification Program including a Verification Plan Specification to insure that the JUNO instrument flight hardware meets the specified mission performance requirements. A Verification Plan/Specification matrix will be prepared in accordance with Tables 3-1 through 3-3 as specified in §3 of the SMEX PAR. The plan will include all the required functional and operational testing, physical and mass property measurements and analyses and complete environmental and EMC testing. Complete testing and environmental facilities are available at both of our collaborators' facilities to insure a rapid and economical turn around of testing at any desired sub-system or system level through all phases of the SMEX Program. Verification test reports will be completed for each verification activity and made available to GSFC review at CAL.

CAL will implement a JUNO instrument Safety Control Program in accordance with the SMEX System Safety Implementation Report (SSIP) as outlined in §4 of the SMEX PAR. CAL will maintain and document a system safety checklist, hazard analyses, hazard reports and a JUNO Safety Data Package. Typical hazards to be considered include the following; materials-contamination, structure-launch related, pyrotechnics-injury/explosion, pressure systems-explosion, and electronic-shock. CAL experience with the STS-3 Safety Hazards Requirements will greatly reduce cost, time and effort.

CAL, SNL and HDOS have extensive experience in the selection and use of space-qualified materials and process controls and EEE components. CAL is completely familiar with the standard EEE components listed in the GSFC Preferred Parts List (PPL) and the NASA Standard EEE Parts List MIL-STD-975. It is our intention to use only Category A, standard EEE parts throughout the JUNO instrument. CAL maintains a system of reviewing and assessing NASA Alerts as applicable to the requirements of the SMEX PAIP. CAL will conduct an EEE Parts Control Program and a Materials and Process Control Program in accordance with §5 and §6 of the SMEX PAR and will generate, update, and submit to GSFC for approval the EEE Parts Identification List (PIL) and the Materials and Process Lists in accordance with Appendix C of the SMEX PAIP.

CAL will ensure that design and reliability assurance provisions are integrated in all phases of design, development, fabrication and testing in accordance with §7 of the SMEX PAIP. Design specifications, drawings and test procedures, where applicable, will be generated for the JUNO instrument and for all components procured by sub-contract or tested separately. They will be reviewed by all groups to insure that they are complete and meet all functional and physical interface design specifications. CAL and its collaborators will perform the FMECA, Stress and Trend analyses in accordance with Appendix C of the SMEX PAR. No limited life items will be used on the JUNO instrument. CAL, HDOS and SNL will adapt their in-house well established QA manuals and provisions to meet all the QA requirements contained in §8 of the SMEX PAR. The Fabrication and Assembly Flow Plan, GSFC Malfunction Reports, PWB coupons and the End Item Acceptance Data Package (EIADP) will be submitted in accordance with Schedule C of the SMEX PAR. CAL experience in preparing the STS-3 EIADP will greatly reduce cost, time and effort.

CAL will conduct and implement a rigorous Contamination Control Plan in accordance with the requirements of §9 of the SMEX PAR. CAL will place stringent contamination controls on those materials and handling to insure that contamination by hydrocarbons and particulates are maintained below levels that would degrade telescope throughput. This is crucial because of the high absorption of hydrocarbons and other contaminates in the far UV. During operation all optional components and surrounding material will be maintained at $\approx 25°C$ to minimize condensation of volatiles on the optics. HDOS has already prepared a preliminary contamination control plan as applicable to the telescopes.

CAL will implement a Software Assurance Program and a Software Test Plan in accordance with §10 and Appendix C of the SMEX PAIP. Flight and Ground Support Software will be tested prior to use on the flight instrument. Emulators will help verify the test software.

# APPENDIX A

## Preliminary Definition Study

# APPENDIX A: PRELIMINARY DEFINITION STUDY

In 1988, our proposal for a SMEX all-sky UV survey received excellent scientific reviews, and very good technical reviews. Five principal technical criticisms were leveled:

1. The detector is a single point failure.
2. The detector readout was not proven.
3. Large and fragile $CaF_2$ prisms may not be flight-worthy.
4. The effects of photometric accuracy on science return, particularly classification efficiency, were not addressed. Insufficient spectrum simulations were provided.
5. Payload integration was not adequately addressed.

In the last four years we have devoted considerable effort in order to respond to these issues. Our goal was to maximize our technical readiness, and reach sufficient design maturity that a PDR could be held near the end of the SMEX Definition Phase. In this section, we summarize the principle results pertaining to points 1-4, and summarize in §A.5 additional design work that we accomplished. Payload integration is discussed in §4.6, §B, and in Volume II, §5.3.

## A.1 DETECTOR REDUNDANCY

We considered four options for removing the detector as a single-point mission failure:

1. *Single telescope & rotatable flat.* This scheme incorporates a rotatable flat which can be interposed between the tertiary and the detector to redirect the converging beam onto a detector mounted at the side of the telescope. This requires an additional mechanism, an additional reflecting surface (for the backup detector) which introduces polarization sensitivity, produces considerable vignetting, and strongly drives the telescope design.
2. *Movable detector.* We considered the possibility of sliding or rotating a spare detector into the focal plane in the event of detector failure. This requires an additional mechanism, and again strongly drives the optical and mechanical design of the telescope. A rotatable mechanism was clearly superior, but still the positional accuracy requirements for the mechanism would be severe.
3. *Split detector.* A third possibility is splitting the detector in the focal plane into two independent units. The simplest way to do this is to split the MCP stack and high voltage biasing, with both stacks sharing the same anode. The anode can also be split, with some loss of efficiency and/or redundancy in the center. This option adds complexity to the detector (thus introducing new failure modes), and certain elements of the two detectors must be shared (e.g. mechanical structure). A large central region must be given up, reducing the field of view and mission sensitivity. It is difficult to maintain a planar, undistorted MCP/anode field region with a split detector. Some failures in one detector introduce failures in the other.
4. *Dual telescopes.* The increased mass-to-orbit capability of the Pegasus launcher enabled us to consider a fourth option, a completely redundant second telescope and detector. There are many advantages to this choice. Two telescopes makes detectors, front covers, optics, and front-end analog electronics completely redundant. Detector, optics, and mechanical design simplicity are retained. By making one filter broadband (**16**), putting the prisms on the broad-band telescope, and retaining the original split focal-plane (**14** and **18**) in the other telescope, we accumulate three significant scientific benefits as well:(a) a deeper, wideband survey in the **16** band; (b) a convenient broad-band for detecting the entire objective prism spectra without a filter mechanism; and (c) a synthetic narrow band (**16N = 16W - [14 + 18]**) useful for isolating CIV$\lambda$1549 emission from nebulae, supernova remnants, and the hot interstellar medium. There are also some penalties: increased mass and cost, increased T/M requirement (due

to the wide-band telescope, and increased complexity of testing and integration. The programmatic impacts are mitigated by the fact that the telescopes are essentially identical, and will be fabricated, tested, and integrated identically. We estimate that the addition of a second telescope increases the program cost by at most 20%, while adding significant reliability and science enhancement. We have therefore chosen the dual telescope option.

## A.2 DETECTOR DEVELOPMENT

We have developed two imaging, 2-dimensional delay-line readouts for MCP detectors that combine high performance, robustness, and cost-effectiveness. We compare the performance of the helical delay-line detector (HDL) and the 2-D serpentine delay-line detector (SDL) to other detector schemes in **Table A.1.** Both systems meet the requirements for the JUNO mission. Our baseline plan is to use the helical delay line anode.

**Table A.1 – Potential JUNO MCP Detector Readouts: Demonstrated**

| Readout | Reference | Pixels | Resolution | Linearity | Throughput Theory/Demonstrated | Power Req. | Advantages | Disadvantages |
|---|---|---|---|---|---|---|---|---|
| Helical Delay Line | F93a | 2000×2000 | 30$\mu$m | 30$\mu$m | $10^6$/>30,000 c/s | 13.2 W | High resolution, large format<br>Electrical & mechanical simplicity & low cost<br>Proven robust by shake test | Suspended wires |
| 2D Serpentine Delay Line | F93b | 2000×2000 | 30$\mu$m | 30$\mu$m | $10^6$ | 13.2 W | High resolution, large format<br>Electrical & mechanical simplicity & low cast & mechanically rigid | |
| MIC | F89/F90 R92 | 2000×2000 | 27$\mu$m | <20$\mu$m | | 10W? | | CCD radiation sensitive.<br>Demanding centroid analysis transputer.<br>Throughput at resolution limit low<br>Flat-fielding difficulties (Moire patterns)<br>Multi-stage detector less reliable |
| MAMA | T91 | 1000×1000 | 25$\mu$m | 10$\mu$m | $10^6$ c/s | 20W | | 2000×2000 not developed<br>550 preamplifiers required<br>Special MCP required.<br>Flatness, PHD, and charge spreading critical |
| JUNO Requirement | | 2000×2000 | 35$\mu$m | ~30$\mu$m | $10^5$ | <15W per telescope | Simplicity, low cost, mass | |

*Operating Principle*

The two-dimensional helical delay-line readout technique employs a crossed pair of flattened-helical bifilar transmission lines (**Figure A.1**). Each delay line independently gives the position in one spatial dimension. Each delay line consists of a pair of bare CuZr wires, one of which is biased to collect electrons. The electron cloud from a MCP event falls over several turns of each transmission line. From that region pulses propagate to timing electronics at both ends of each transmission line. Differential-mode signal amplification minimizes noise pickup and $x-y$ crosstalk. The pulse arrival times at the ends of each delay line give the event position. The delay-line readout achieves its results by requiring pulses to travel ~200-300 times as far as they would in a straight path across the anode at an effective velocity $v_e \simeq pc/2l$, where $p$ is the anode pitch, and $l$ is the turn length. This reduces the effective propagation velocity of the pulse, thereby reducing by the same factor the spatial uncertainty derived from a timing measurement.

The spatial resolution of delay-line position readout systems are limited mainly by two factors. Preamplifier thermal noise $\sigma_V$ contributes a timing error $\sigma_{tp} \simeq \sigma_V \tau_r / V_{max}$, where $\tau_r$ is the output pulse rise time, and $V_{max}$ is the peak output voltage. For a MCP gain of $\sim 3 \times 10^7$, $\sigma_{tp} \simeq$10-50 psec. Timing errors

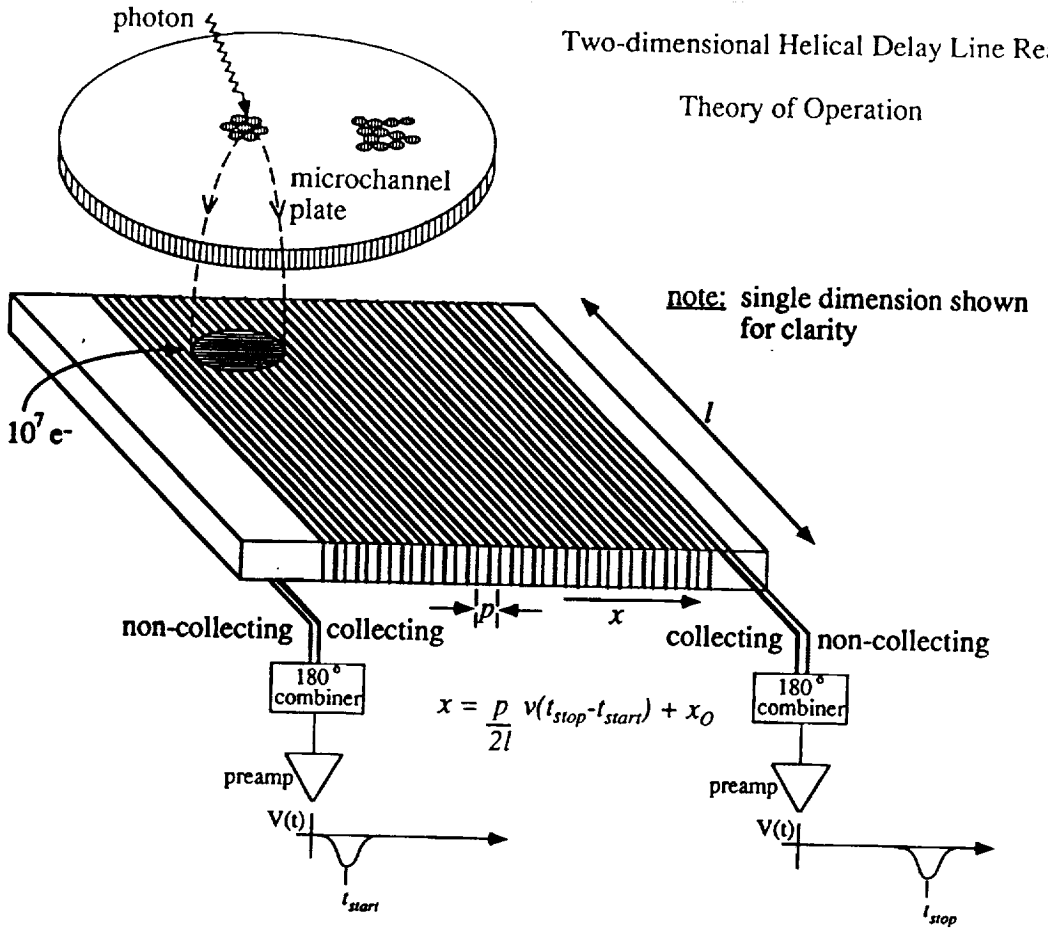


**Figure A.1** Helical delay-line anode operation principle.

due to "walk" in the pulse discriminator can contribute a fixed error $\sigma_{tc}$. This is typically <10 psec. The position resolution is then $\Delta x \sim \sqrt{\sigma_{tp}^2 + \sigma_{tc}^2}/v_e$. The maximum count rate is $CR_{max} \sim 1/T_d$, where $T_d$ is the total delay time across the anode.

*Prototype Designs*

*HDL1*. All image testing to-date has been performed on a 150 × 150 mm HDL anode with 0.5 mm wire-spacing and a total delay-time of 200 nsec. Annealed OFHC Cu wires were wound onto the MACOR frame using a lathe, and glued in place. This method was not considered flight worthy, and also leads to signal degradation due to microreflections at the glue-line. The anode rise-time is 6 ns, end-to-end attenuation 6 dB, and the effective propagation speed of 0.7 mm/ns.

*HDL2*. A prototype flight worthy HDL anode was designed to maintain wire positions using machined grooves in the MACOR frame. **Figure A.1** shows the anode, wire detail, and detail of wire end-staking. Both mechanical and electrical properties of HDL2 are superior to HDL1. Each axis of HDL2 is 80×100 mm, with an effective propagation speed of 1.1 mm/ns, anode rise-time 2.5 ns, and attenuation of 3 dB. Although the faster $v_e$ increases the required timing accuracy, it also decreases the pulse rise time and increases its amplitude due to the decreased skin-effect attenuation. The net result is comparable resolution performance and higher throughput due to the smaller delay-time.

*Mechanical Robustness and Flight Testing*

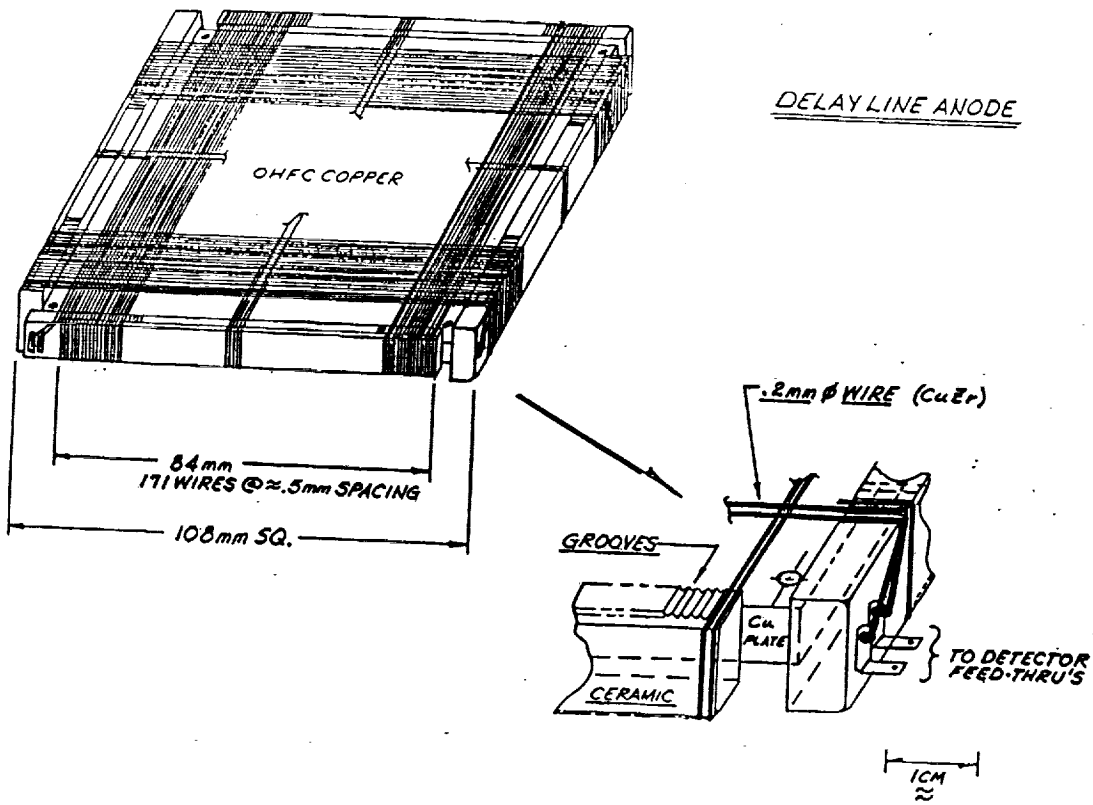


**Figure A.2** HDL2 prototype helical-delay line anode, showing a detail of wire positioning grooves and wire end attachment

HDL2 anode was shaken at Shuttle qualification levels (spec# A.O. No. OSSA 2-92 p. A-16, 14g's rms) for 4 minutes in the z-axis at HDOS. Before and after the shake test, wire tension was measured using a loudspeaker resonance frequency test, wire positions were measured with an optical comparator, and electrical properties including resistance, capacitance, and pulse shape were measured. **Table A.2** summarizes the pre- and post-shake test results. Digitized pulses transmitted by the anode obtained before and after the shake showed differences $<2\pm1.3\%$. We found no measurable change in any parameter except the wire tension, which exhibited a 5% drop. Given the lack of any measurable electrical change, and the high g-load of this qualification-level shake, this slight reduction in tension is considered inconsequential.

We will perform a final test of the space worthiness of the delay-line readout by flying three detectors on the NUVIEWS rocket, which is funded separately by a NASA Sounding Rocket Grant (NAG 5-642). The flight will be timed to occur early-on within the SMEX definition period. The NUVIEWS experiment consists of three wide-field (40°) far UV survey telescopes, one broad-band and two narrow band. As such, this experiment will provide an important test of the detector dynamic range, since many bright stars will appear in the NUVIEWS fields of view.

*Spatial Resolution and Linearity*

The pinhole-array image in **Figure A.3** gives an indication of the detector's performance. We have also measured the spatial resolution and linearity by precisely positioning a single nominal 10-$\mu$m UV spot on the front MCP. The gain of the $Z$-stack MCP is $\sim$1-10$\times10^7$. The FWHM resolution is 30 $\mu$m in both dimensions, as shown in **Figure A.4**, including the contribution of the UV spot. The figure also shows that the resolution is not a function of event pulse height, and maintained to event gains as low as $1\times10^7$. With this readout, even a poor pulse height resolution produces excellent spatial resolution.

*Linearity*

Table A.2
HDL2 Vibration Test

| Test | Pre-Shake | Post-Shake |
|---|---|---|
| Wire Positions | | |
| RMS changes in Wire Spacings | 5.3±2.5$\mu$m | |
| RMS changes in Wire Positions | 2.8±2.0$\mu$m | |
| Wire Tension (N) (Post-Pre) | $\Delta T/T$ = (-5.0±0.8)% | |
| Rise Time (thick) (ns) | 2.74±0.04 ns | 2.74±0.04 ns |
| Rise Time (thin) (ns) | 2.90±0.04 ns | 2.89±0.04 ns |
| Pulse Transmission | 1.00 | 0.99±0.01 |
| Capacitance | | |
| Outer Plane-Outer Wire to Inner Wire | 0.596±0.002 nF | 0.599±0.002 nF |
| Inner Plane-Outer Wire to Inner Wire | 0.558±0.002 nF | 0.562±0.002 nF |
| Outer Plane to Inner Plane | 0.104±0.002 nF | 0.106±0.002 nF |
| Resistance | | Ω |
| Inner Plane | | |
| Outer Wire-Inner Wire | 16.25±0.03Ω | 16.25±0.03Ω |
| Outer Wire-Inner Wire | (0 nS) | (0 nS) |
| Inner Wire-Inner Wire | 16.07±0.03Ω | 16.02±0.03Ω |
| Outer Plane | | |
| Outer Wire-Inner Wire | 17.03±0.03Ω | 17.04±0.03Ω |
| Outer Wire-Inner Wire | (0 nS) | (0 nS) |
| Inner Wire-Inner Wire | 17.09±0.03Ω | 17.09±0.03Ω |

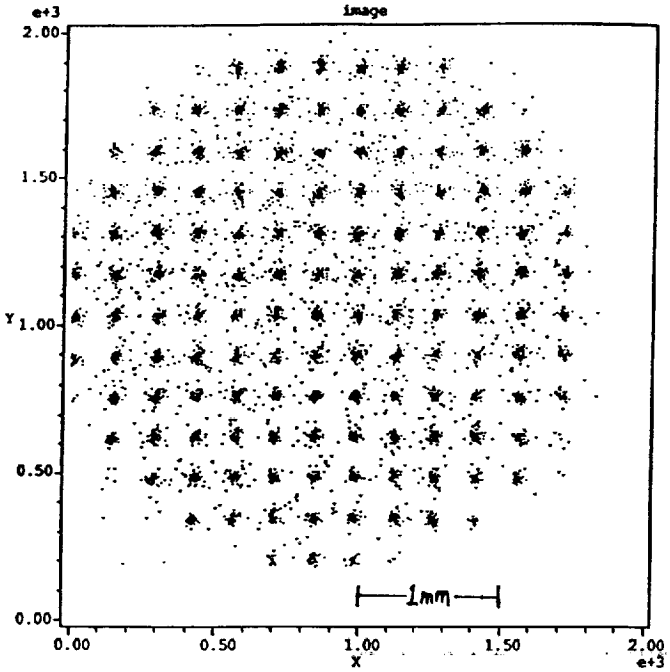


**Figure A.3** Image of resolution test mask produced by helical delay-line detector. Holes are on a 280 $\mu$m square, and 12 $\mu$m in diameter.

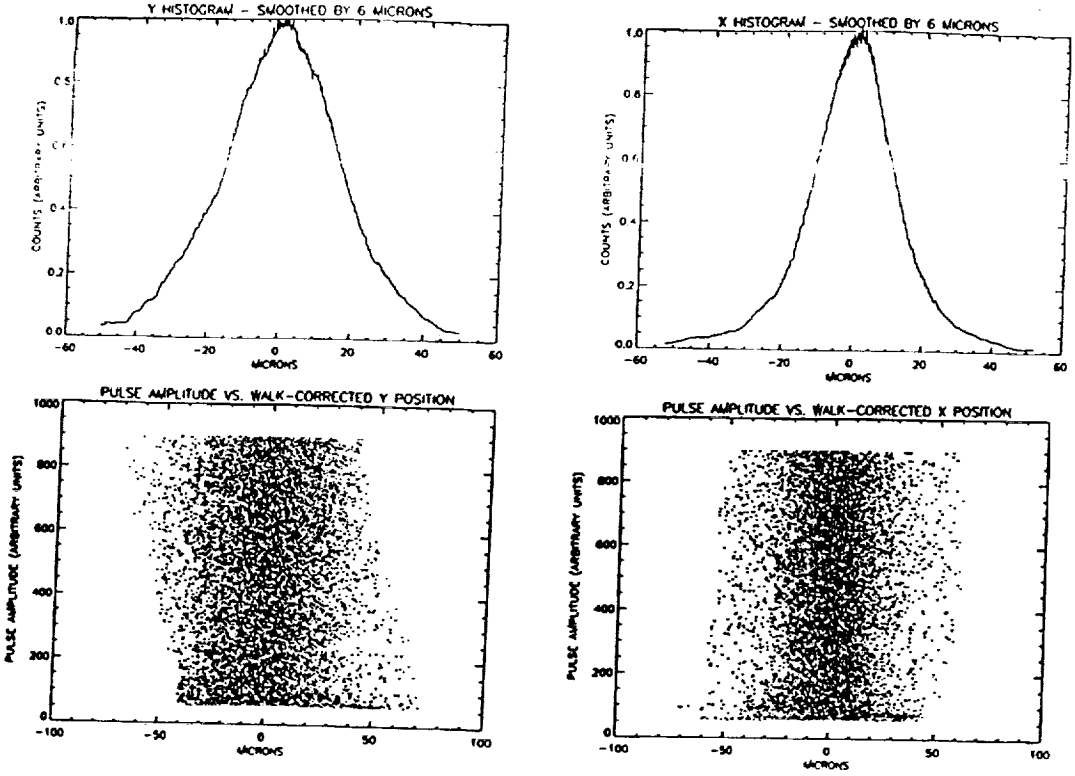


**Figure A.4** Image data for a coadded series of 41 separate spots with a total of 13,500 events, obtained from scan across the detector with the UV optical system and a 10$\mu$m pinhole. X- and y-histograms are shown, displaying 23 and 33$\mu$m FWHM resolution, respectively. A scatter diagram showing walk-corrected $x$ and $y$ vs. pulse amplitude is also shown. A software walk correction eliminates slight variations in the position with pulse-amplitude that are not completely eliminated by the CFD. Note the lack of dependence of the resolution on the pulse amplitude.

We performed various tests of the linearity of an MCP with and HDL readout. Several factors contribute to nonlinearity in HDL anodes, although the overall linearity performance is quite good. These are: (1) Anode gap E-field gradients; (2) B-field gradients in the anode gap; (3) HDL signal baseline disturbances; (4) HDL wire spacing errors; (5) TAC and ADC nonlinearity, and (6) local (non uniform) MCP fatigue. *Figure A.5* shows the global linearity of the 40 mm detector, with a grid of UV spots. Small-scale spatial linearity residuals are 3–9 $\mu$m rms over 2–4 mm. Large-scale HDL linearity is $\pm$30$\mu$m, or $\pm$1 detector pixel, over 90% of the active area, and $\pm$50$\mu$mover the remainder (MCP rim). Most nonlinearity is either 1D (anode related) or radial (E-field gradients) and can be calibrated and corrected to 3$\mu$m. Magnetic shielding and improved electrode design will reduce nonlinearity to <1 pixel (8″) everywhere, and corrections will be stable to <0.25 pixel (2″), in order to allow astrometry to $\pm$3 ″.

*Dynamic Range*

Based on the UV model, the JUNO mission requires a detector which can accommodate global count rates as high as $10^5$ cps, without degrading the other performance characteristics. The theoretical limit of our delay line is $10^6$ cps for 10% coincidence loss. We have tested HDL1 to 30,000 cps (global), which was the saturation limit of the low current MCPs that we were using. We simultaneously focused a UV spot 50$\mu$m in diameter (like the JUNO PSF). No degradation in spatial resolution of the spot or positional shift was measured.

*Modeling & Optimization*

We have developed a transmission-line model for helical and serpentine delay-lines that successfully predicts the pulse propagation velocity, rise time, and attenuation over a wide range of design parameters (Martin and Friedman 1993). We have used our model, along with a resolution figure of merit, to determine

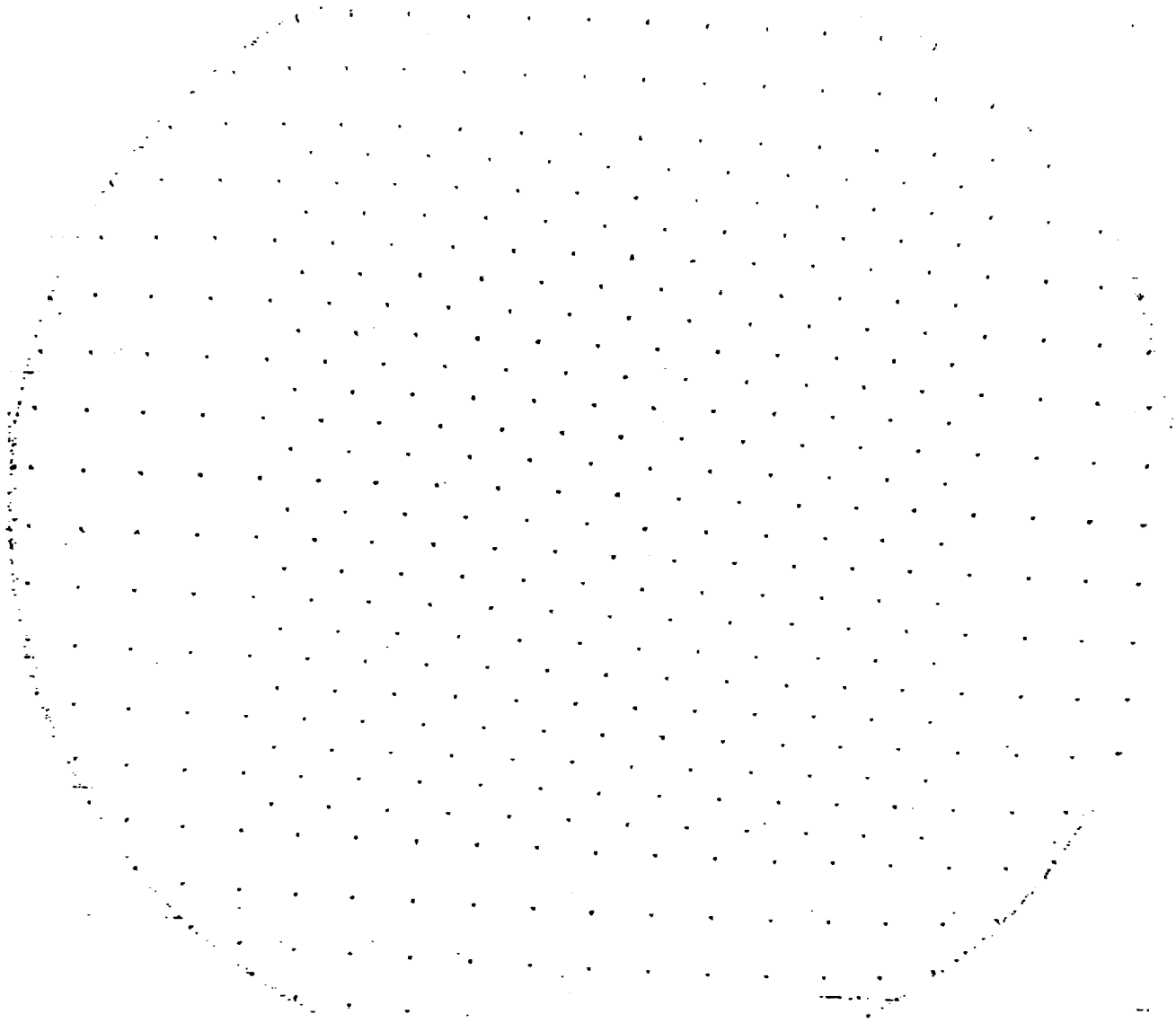

**Figure A.5** Global linearity of HDL detector. Region is 20 mm on a side, and UV spots are equally spaced on a 2 mm grid.

optimal delay-line design for the JUNO detector.

*A.2.2 Serpentine Delay-Line Detector*

In parallel with our helical delay-line development effort, we have recently fabricated and tested a multilayer serpentine delay-line detector (SDL) (Friedman *et al.* 1993). The SDL performance is comparable to the HDL that we tested.

Lampton *et al.* (1987) first showed that a single serpentine microstrip delay-line could give high spatial resolution over a large, one-dimensional detector format ideal for spectroscopic detectors. Serpentine delay-lines are constructed by conventional etching on copper cladded epoxy-fiber-glass or RT/Duroid PTFE-alumina composite printed-circuit boards. The other dimension was read out using wedge-wedge charge division electrodes interleaved with the serpentine delay-line. The spectroscopic serpentine delay-line (SDL) developed at the University of California, Berkeley has achieved very high resolution ($< 30\ \mu$m; ) over large-formats (90 mm) in one-dimension (Siegmund *et al.* 1992). Resolution in the perpendicular direction can be almost as good ($\sim 30\ \mu$m) but the number of pixels and height are limited. A multilayered serpentine delay-lines has been proposed (Siegmund *et al.* 1990) to extend the high number of pixels into two dimensions, but have not yet been demonstrated.

We have demonstrated by our vibration test that the HDL is mechanically robust. Simultaneously, we have explored the SDL as an alternative mechanical realization of a two-dimensional delay-line anode. While the rigid multilayer architecture offers obvious mechanical advantages, the choice between HDL and SDL boils down to maximizing reliability and minimizing program cost. Because the HDL and SDL require the same readout electronics, and have the same demonstrated performance, the choice is purely a mechanical one.

A schematic of the multilayer SDL is shown in **Figure A.6.** The serpentine delay line is constructed from individual microstrip serpentine layers fabricated by a conventional photoetching process. The delay lines are etched in 1 oz. Cu on Teflon composite substrates. The bottom delay-line is a conventional microstrip, with a continuous ground sheet. The top delay-line has a ground sheet that is interrupted in the gaps between the top delay-line strips, in order to permit passage of electrons to the bottom delay-line. The two microstrip boards are bonded with a center Teflon composite dielectric onto a brass substrate. The dielectric between the top layer strips, in the top and center layers, is removed allowing electrons to fall onto the bottom delay-line. The resulting anode is extremely robust. The transmission-line properties of the individual microstrips are slightly modified, but are not degraded by the bonding process and dielectric removal.

*Resolution and Linearity Performance.*

We have routinely obtained $30\mu$m (FWHM) resolution (**Figure A.7**) in both dimensions over the 40 mm active area that we tested in the prototype SDL anode. Small-scale linearity was measured to be $< \pm 7\mu$m. Global linearity is $\pm$ 34$\mu$m over the central 90% of the detector (**Figure A.8**). Thus the SDL is equivalent to the HDL in performance.

*Modeling & Optimization*

The transmission-line modeling discussed above was also applied to the SDL anode. We found that the prototype design that we fabricated and tested was not optimal, and the resolution figure of merit can be improved by as much as a factor of two. This is particularly important for the performance at the edge of the anode, where attenuation of the signal traveling the long way begins to limit the signal-to-noise and resolution at the boundaries.

## A.3 PRISM DEVELOPMENT

In our original prism design, we incorporated two large rectangular prisms (6×12 cm) in separate

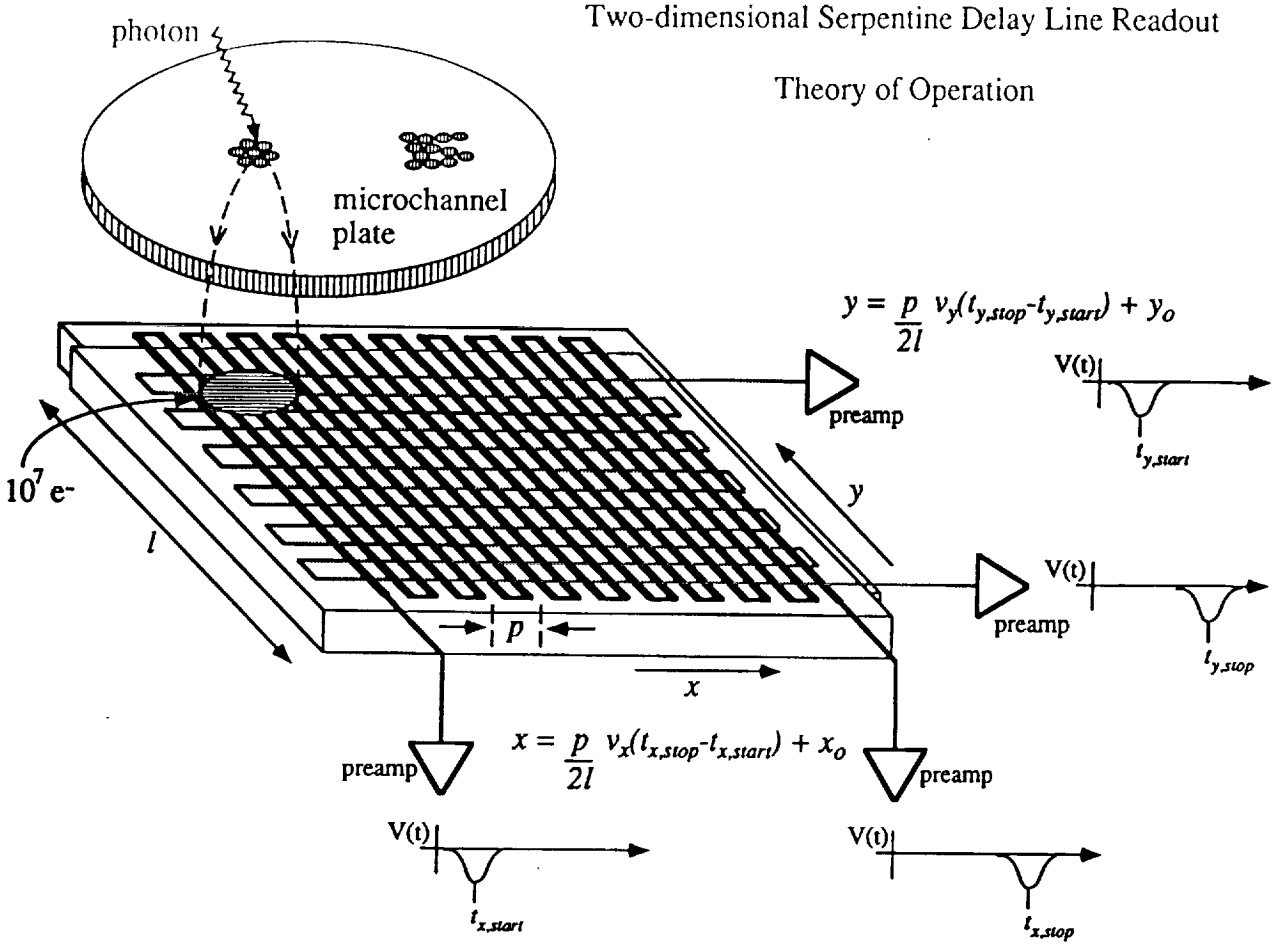


**Figure A.6** Schematic of serpentine delay-line anode.

rotating panels. At the suggestion of Richard Rockwell at HDOS, we made a substantial improvement in the prism mounting and deployment scheme. There are now six individual 12 cm diameter prisms, mounted together in one rotatable panel (shown in **Figure A.9**). This vastly simplifies prism fabrication, mounting, alignment, and the design of the prism plate and deployment mechanism. In order to comply with the telescope imaging/wavefront budget, the prisms must be aligned to 30 arcmin (perpendicular to the telescope axis) and 1.8 arcmin (azimuthally around the axis).

Two prototype prisms, 120 mm in diameter and 3-8 mm thick were fabricated by Englehart to the JUNO specifications. This requires a wedge-angle matching of <10″, which can be accomplished on wedges without significant difficulty. The prisms have a transmission of >70% at 1350Å. The prisms were fabricated from considerable larger crystals than the ultimate 120 mm diameter, and we are therefore confident that we can obtain $Ca_2$ in the required dimensions without difficulty.

A prototype version of the new prism mounting scheme was designed and fabricated at CAL. Each of six prisms is mounted in an Aluminum bezel with PTFE shims and staked with Scotch-Weld 2216 B/A Gray epoxy, used successfully on HST. Each bezel is mounted kinematically to a supporting frame.

In order to verify the robustness of the $CaF_2$ prisms and mounts, and to ensure that the required alignment could be maintained, we performed a vibration test of a prototype prism. The in-plane alignment specification is very generous. Prism rotation was measured before and after shake with scribed lines. One

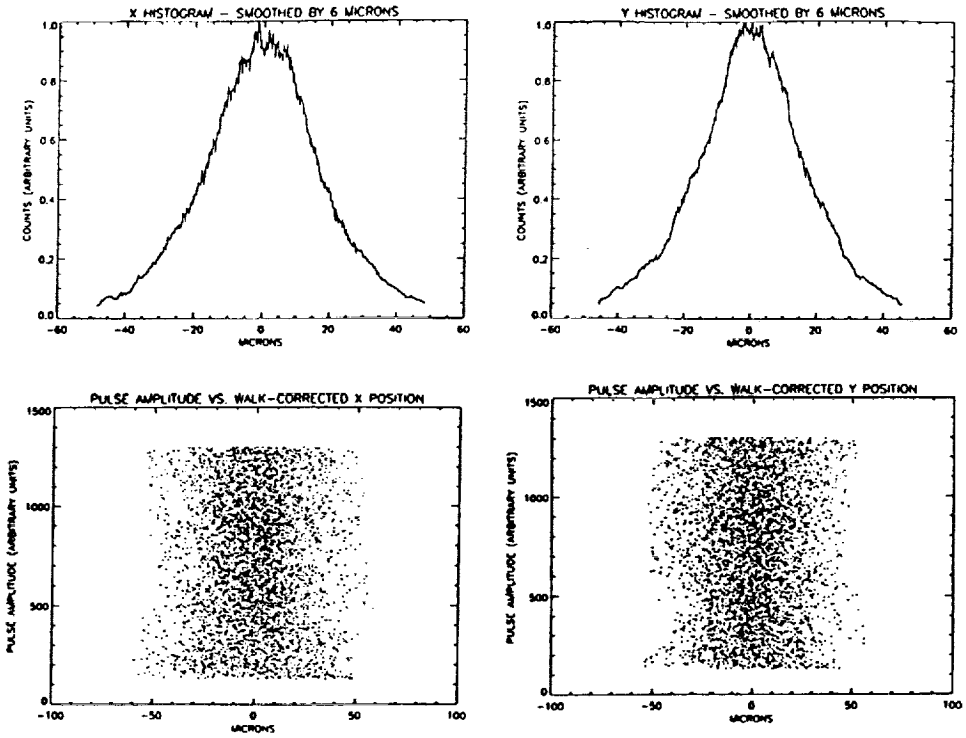


**Figure A.7** Image data for a coadded series of 16 separate spots with a total of 5140 events, obtained from scans across the detector with the UV optical system and a 10$\mu$m pinhole. X- and y-histograms are shown, displaying 31$\mu$m FWHM resolution. A scatter diagram showing walk-corrected position vs. pulse amplitude is also shown. Note the lack of dependence of the resolution on the pulse amplitude.

glass and one $CaF_2$ was subjected to a 4 minute z-axis qualification-level shake (spec# A.O. No. OSSA 2-92 p. A-16, 14 g's rms). The prism integrity and alignment were maintained in both cases.

## A.4 UV MODEL

We have developed a detailed, end-to-end model which incorporates a simulation of the UV sky, the JUNO telescopes and detectors, the data compression algorithm, the *ex post facto* drift reconstruction, and the data analysis routines. We have used it to address a number of issues related to the JUNO mission and science goals, including:

- Source detection completeness vs. magnitude;
- Source classification efficiency and catalog purity;
- Source crowding and confusion of optical identification, and its effects on catalog purity;
- Photometric accuracy vs. magnitude;
- Quality of prism spectra and derived parameters such as redshift vs. magnitude;
- Count rate statistics in detectors, local and global;
- Most effective data compression algorithms;
- QSO z-distribution in detected sources;
- Effectiveness of extinction determinations.
- Hardware, software, and personnel requirements for JUNO data reduction tasks.

Using this model, we have verified that the mission meets our science goals for optical ID and source classification efficiency. All magnitude limits and other performance numbers quoted in the proposal are based on results derived from the UV model. *This work demonstrated unequivocally that system design, particularly system angular resolution (16"), is critical for making unambiguous optical IDs for the majority*

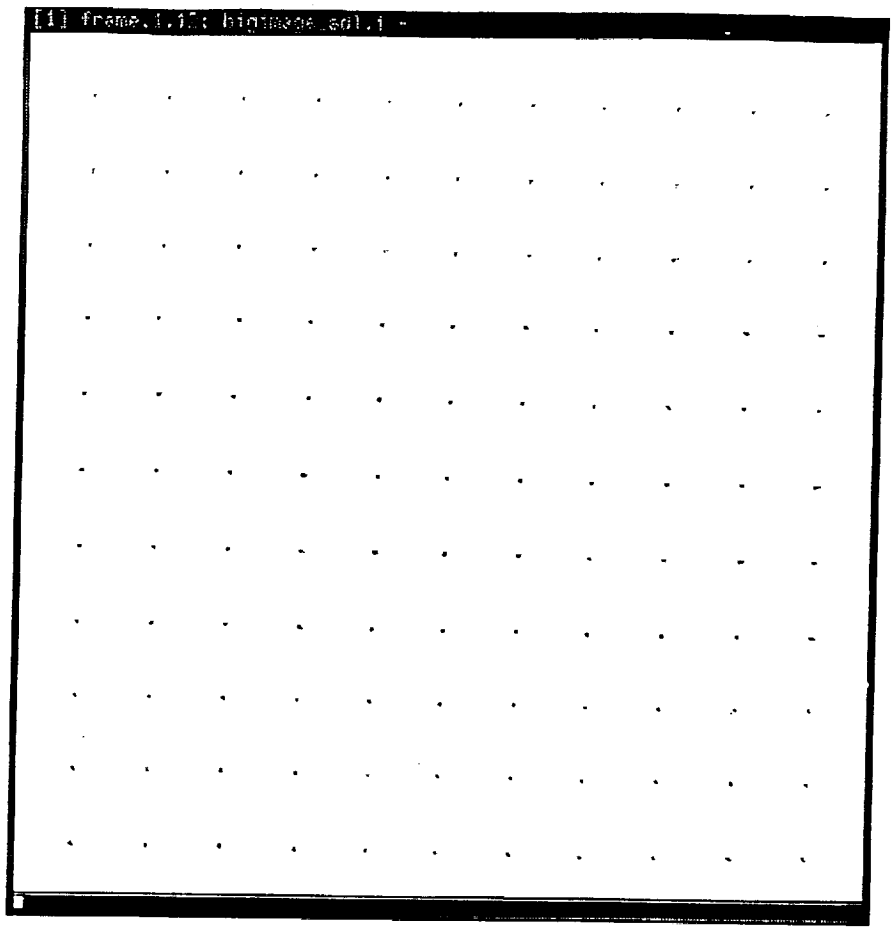

**Figure A.8** Global Linearity of SDL detector. Region is 20 mm on a side, and UV spots are equally spaced on a 2 mm grid.

*of the UV sources.*

*A.4.1 UV Model Description*

The UV model is a realistic simulation of the end-to-end process of the JUNO mission. It consists of several parts:

(1) **src:** UV sky model that incorporates up-to-date luminosity functions and spectral energy distributions for important far UV sources, including main-sequence stars, white dwarfs, subdwarfs, cataclysmic variables, QSOs, early- and late-type galaxies, and the far UV background. Actual SAO stars are used for the brightest stars. Resolved galaxies with random inclination angles and orientations are included. **src** also incorporates realistic statistical models for galactic dust extinction, constructing individual "clouds" chosen using a "luminosity function" for cloud extinction, assuming a constant density for each cloud type, and calculating the implied cloud diameter and keeping track of the patchy extinction that results. For extragalactic sources, we include a statistical model for Lyman $\alpha$ clouds and Lyman limit (LL) absorbers. Individual spectra are calculated for each source including the cumulative effects of numerous Ly$\alpha$ clouds and LL systems chosen randomly from the distribution $dn/dN_H(z)$ measured by Tytler (1986) and others. The model produces a source list (positions, magnitudes, type, etc.) and spectrum catalog that can be "observed" by the telescope model **tel**. In order to test the efficiency for optical identification, actual optical catalogs can be used to generate the source positions. Spatial

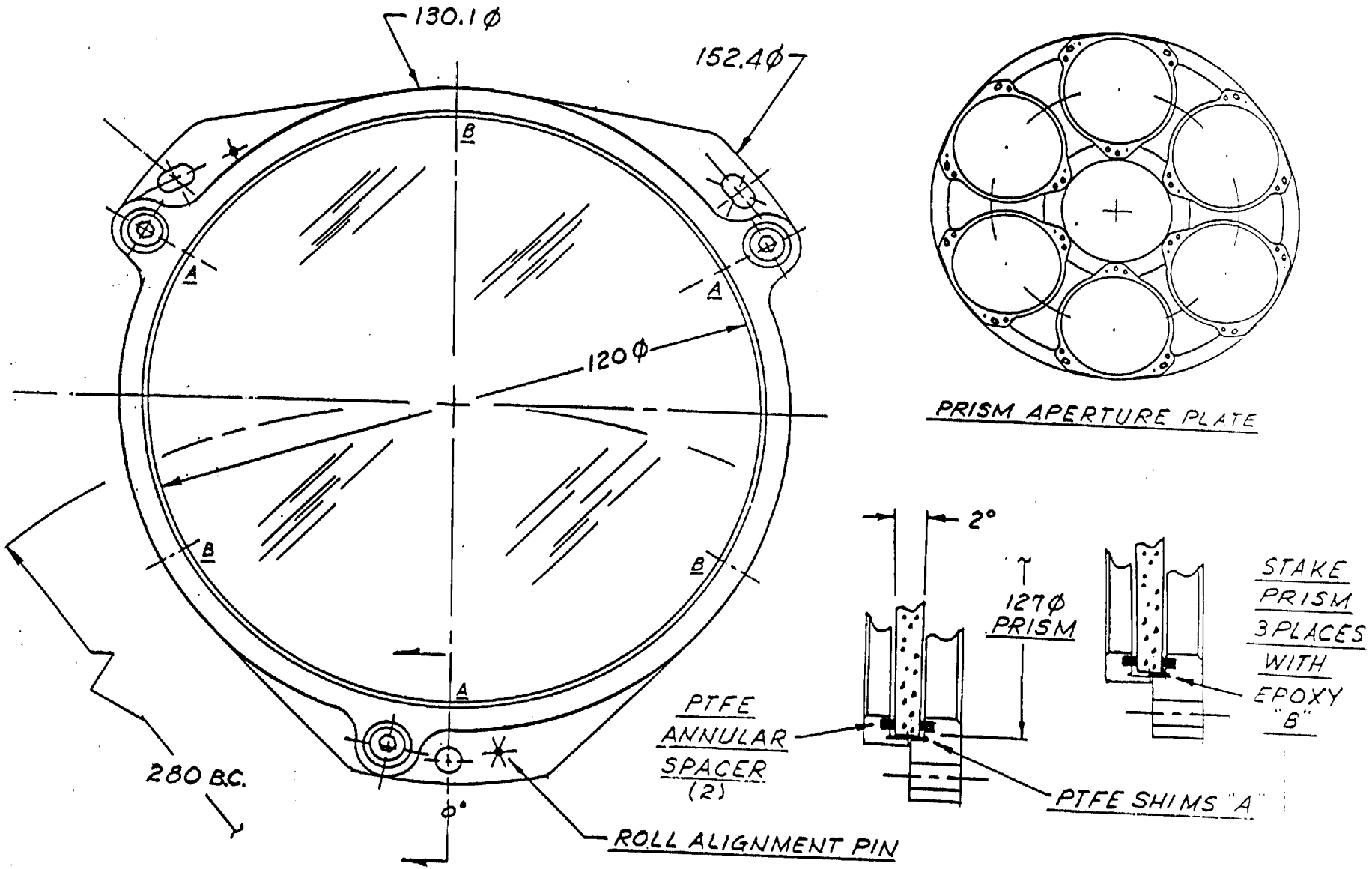


**Figure A.9** Prism mount and assembly mechanical design.

information about galaxies (size, inclination, position angle) is also stored. A summary of the objects included in the model, and the origin of source data is included in **Table A.3**.

(2) **tel:** Model of the JUNO telescopes that incorporates pointing drift, geometric aberrations due to the telescope and chromatic aberrations in the filters, prism dispersion, telescope vignetting, detector blur, MCP saturation, high count rates pulse overlap/position error due to anode reflections, and on-board data compression. The output is the T/M stream.

(3) **image:** Bins raw photon list (T/M stream) into image, correcting for known drift and detecting UV stars and using them to correct for unknown drift. Also reconstructs compressed star images.

(4) **phot:** Detects and get photometric data on UV sources in image. Currently uses *FOCAS* operating in an *IRAF* environment. *FOCAS* generates positions, spatial moments, various magnitudes, and other pertinent source classification information.

(5) **match:** Matches optical and UV catalogs for source classification purposes.

(6) **class:** Preliminary classification of sources based on **14, 16, 18 , 14-18, 16-V** magnitudes and colors.

(7) **spect:** Spectrum extraction routine. Calculates local background, accounts for spectrum overlap, registers zero-order to recover wavelength scale.

The UV model will continue to evolve as new source data and refined understanding of instrument behavior become available.

**Table A.3**
**UV Model: source data**

| Object | SED Source | LF Source |
|---|---|---|
| MS Stars (O3-F5) | IUE Spectral Catalog | Allen 1977 |
| White Dwarfs (>10K) | Wesemael 81 | Liebert *et al.* 1987 |
| Sub-Dwarfs | Wesemael 81 | Liebert *et al.* 1987 |
| CVs | | Patterson 1984 |
| Normal Galaxies | Bruzual 1980 | Guiderdoni & Rocca-Volmerange 1990 |
| "Blue" Galaxies | Kinney *et al.* 1992 | Wasilewski 1982 |
| QSOs | Cristiani & Vio 1990 | Schmidt & Green 1983; Crampton, Cowley, and Hartwick 1987 |
| Diffuse Clouds | | Spitzer |
| Molecular Clouds | | Spitzer 1978 |
| Lyman alpha clouds | | Tytler 1987 |
| Lyman Limit Systems | | Tytler 1987 |

*A.4.2 All-Sky Survey*

*Detector Count Rate Statistics & MCP Saturation.* A wide field UV survey includes many bright stars, and their statistics determine the requirements for detector local and global count rate throughput, data compression algorithms, and T/M requirements. Our simulation incorporates a model for MCP count rate saturation (ZF91;FPLP91;ST91), consistent with MCP behavior measured in our detector laboratory. This model explains the variation in MCP saturation with local current density and illumination area. We

have examined the distribution of stellar count rates predicted for several galactic latitudes, and several choices of detector saturation parameters. We can draw several conclusions: (1) The count rates tend to be dominated by the brightest stars that do not saturate, rather than a large number of lower count rate stars. This makes the star compression algorithm straightforward and efficient. (2) Because of (1), the count rate statistics are strongly influenced by the detector saturation behavior. For this reason, we will specify MCPs conservatively, with slightly more than optimal saturation. With MCP saturation total stellar count rates range from ~10,000(-7000,+20,000) c/s in the galactic plane to ~1000(-500,+2000) c/s at the poles.

*Total Charge Extraction.* Using the UV model, we have studied the statistics of charge extraction from the flight detectors during the all-sky survey. We find that drift scanning a full detector diameter (5°in 1500 s = 10″/s) for each nighttime integration distributes the charge fatigue due to bright stars quite uniformly over the detector. To be conservative, we took galactic plane observations and assumed no MCP saturation (i.e., full charge extraction from bright stars was assumed). The resulting distribution of extracted charge after 2500 orbits is shown in **Figure A.10**. Since the detectors will be pre-scrubbed to 1 C/cm$^2$, the cumulative effect of bright stars can be seen to be negligible.

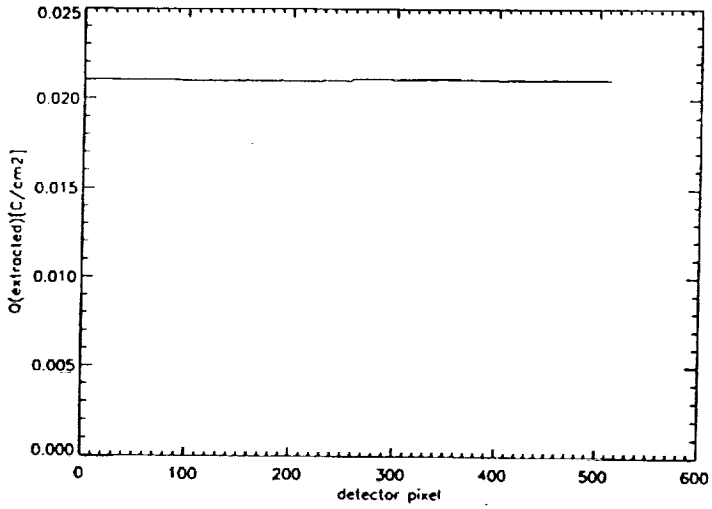


**Figure A.10** Cumulative charge extracted from a JUNO detector, vs. position (in this figure, 1 pixel=0.1 mm), after 2500 orbits observing the galactic plane and assuming no MCP count rate saturation due to bright stars.

*High Count Rate Effects.* High local and global count rates lower the MCP gain until a large fraction of events no longer trigger the hardware threshold. These events do not disappear entirely, and we have incorporated in our detector model their perturbing effects on detected events. This is produced by baseline disturbances created by the interaction of the coils and the center plate for the first 200 ns, followed by a series low amplitude reflections decaying with a 1$\mu$s time-constant. These disturbances are proportional to the event amplitude. Based on our HDL1 measurements, we have included the two main effects: rare coincidence of an event leading edge (used for timing) with the 200 ns ringing of a previous, low amplitude event, and more frequent overlap of the 1$\mu$s decay of a previous event with a new one. Event coincidence perturbs the position calculation, creating a diffuse halo as well as spikes aligned with the anode. The overall impact is very slight, and the PSF of all star images are effected equally. We have found that it does not degrade the photometric or astrometric precision of the survey. Even so, the flight anode will be designed to minimize these long-term disturbances further.

*T/M Rate & Data Compression.* In order to avoid in-orbit image accumulation (cf. §3.3) we compress

bright star data, and telemeter all other time-tagged photons individually. We have developed a simple algorithm for bright star compression, and tested it using the UV model. The algorithm and detector count rates derived from the UV model formed the basis for the DPU design. The algorithm works by accumulating a course image map from drift-, walk-, and distortion-corrected (using look-up tables) photon positions, and testing the pixels in the course map for count rates above an adjustable threshold. Bright pixels, rather than stars, are monitored for simplicity and speed. Photons falling in the bright pixels are not telemetered, rather used to update pixel count rates every second. Bright pixel count rates are telemetered periodically. With a 2.5Mb/s T/M rate, 500 seconds/orbit for downlink, a total of 1.25Gbits can be accumulated per target. With 32 bits/photon (x: 12-bits, y: 12-bits, pulse-height: 4 bits, and time-vernier: 4-bits), 40 Mphotons can be accumulated in the two detectors, 10 Mphotons from the **14+18** telescope, and 30 Mphotons from the **16** telescope. With star compression active, the T/M rate is dominated by the diffuse background. The maximum integration time per orbit when observing at low latitudes will be less than 1500 s (as low as 600 s). The effect of this inefficiency is not great at low latitudes, for two reasons: (1) the **16** band is background limited; and (2) because of extinction, the effective survey volume is not a strong function of the limiting magnitude.

*Image Reconstruction.* We have used the UV model to verify that primary data from UV stars can be used for *ex post facto* drift reconstruction. The **tel** routine includes a random drift component in the telescope pointing direction. To be conservative, we have assumed a drift rate of 10″/s in a 60″ dead-band box. When the axis reaches one side of the box, a reflection occurs with a random angle added. When the drift is left uncorrected, the image in **Figure A.11(a)** from a high-$b$ pointing model results. The **image** routine finds bright stars events in the T/M stream, corrects their coordinates for walk and optics/detector distortion, calculates running centroids using a software FIFO, and corrects the event coordinates accordingly. The resulting image is shown in **Figure A.11(b)**. Note that the ultimate stellar PSF's have 13″ FWHM, and the drift contribution has been reduced to <5″. This was carried out independently on both the **14+18** data and the **16** data. Source data derived from images created with drift and correction were equivalent in astrometric precision with those produced without drift and correction.

*Source Detection & Matching.* We have used the Faint Object Classification and Analysis System (FOCAS; Jarvis and Tyson 1981) running in an IRAF environment to detect and evaluate the sources generated in our simulated UV images. This is not ideal, since FOCAS is not designed to accommodate very low sky backgrounds or variable PSF's. The photometry of the faintest sources is thereby compromised. However, we have found it to be suitable for demonstrating that the JUNO mission meets the basic scientific requirements that we have set forth. FOCAS proceeds in several steps: detection (sky evaluation and source detection), evaluate (source photometry and moment calculation), autopsf (evaluation of the source PSF), and classify (source classification based on spatial moments). Typically, we have set the detection threshold at 2.5$\sigma$, and experimented with the effect of that threshold on the survey completeness and source purity. The result of the FOCAS pass is a catalog of source positions and instrumental magnitudes. These magnitudes will ultimately be adjusted using an exposure map. Sources from the **14,18**, and **16** catalogs are matched with each other and with optical sources. The latter is done either with the actual optical catalog (if this was used to generate the positions) or using a statistical model of optical source densities. The principle goal here is to determine the number of false optical IDs. Matching is based on a maximum likelihood method to ensure that the process is unbiased and the results described quantitatively. For this we write a likelihood function

$$L_i = -logP(m_{16}, m_{16} - V_i, r_i)$$

where P is the *a priori* probability for finding a random source of magnitude $V_i$ at a distance $r_i$ from the detected UV source with magnitude $m_{16}$. The identification which maximizes $L$ is chosen.

*Completeness and Catalog Purity.* We can evaluate the completeness (number of sources detected over possible detections) of the model survey by matching the detected with the source catalog. Some results are

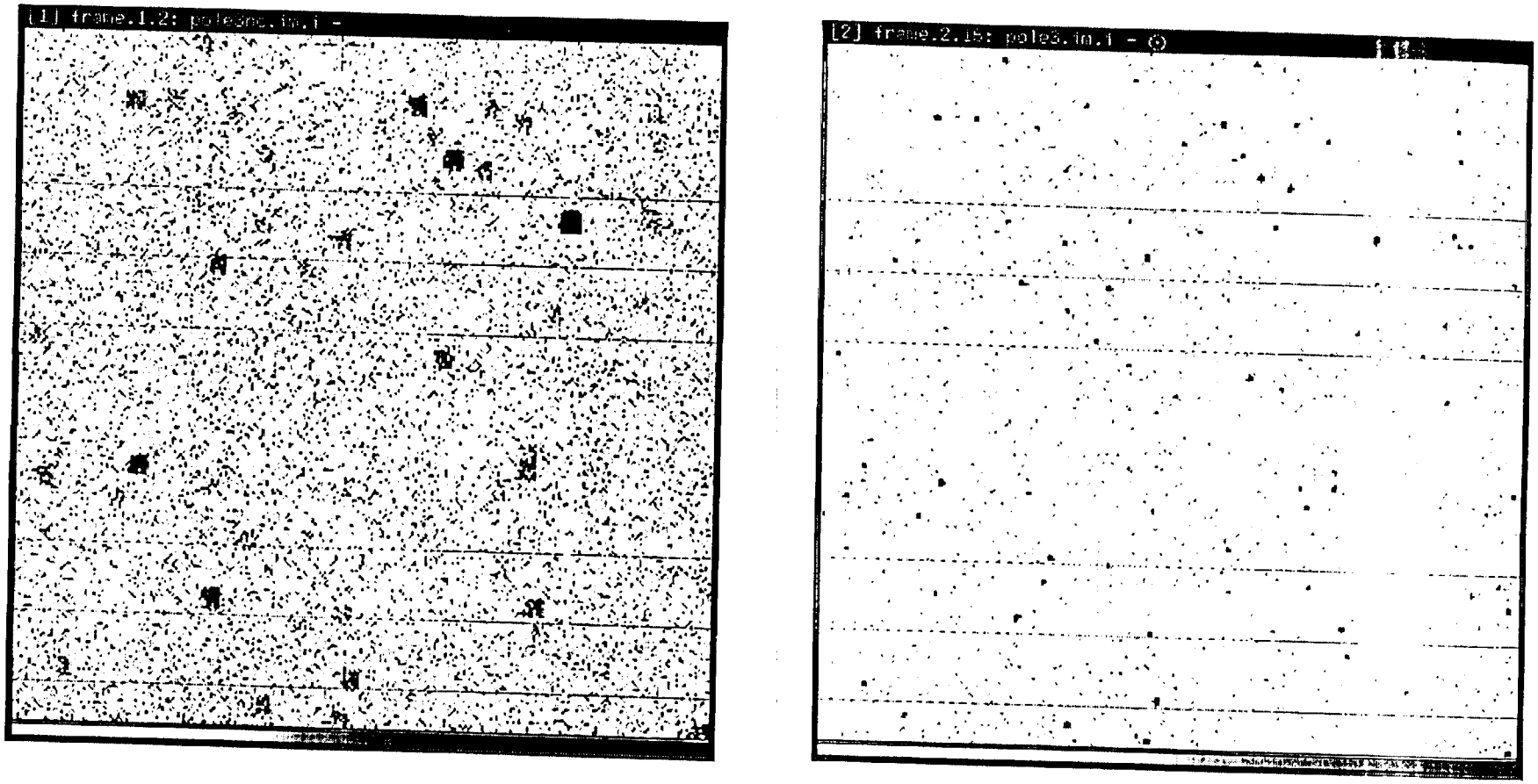

**Figure A.11** (a) JUNO image without drift correction. (b) JUNO image with *ex post facto* drift reconstruction.

shown in **Figure A.12**. As the magnitude limit of the sample is increased, the fraction of spurious sources increases to 5% at the catalog limit. Spurious sources are virtually eliminated (<5%) if we demand either an optical ID be found, or a match between two of **14**, **18**, and **16**.

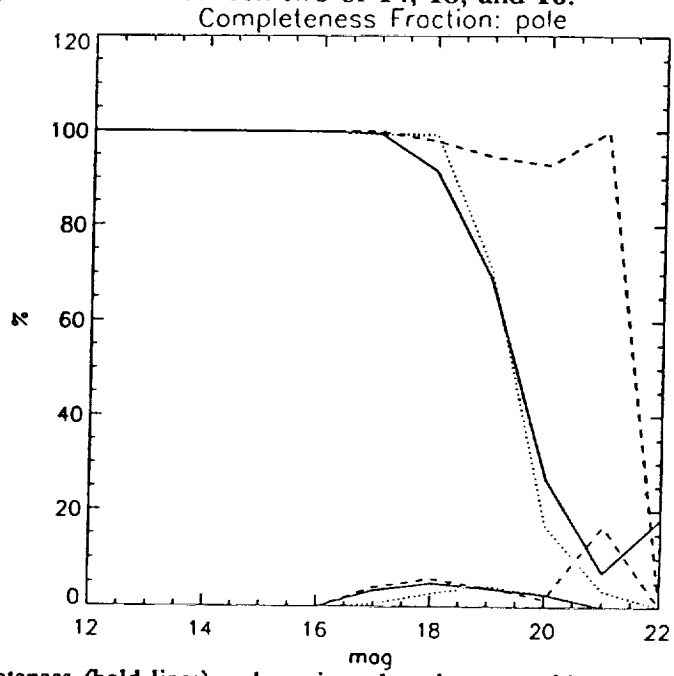


**Figure A.12** Completeness (bold lines) and spurious detection rate with optical IDs (unbold lines) vs. input source magnitude, all-sky survey. Solid line: **14**, Dotted line **18** and dashed line **16**.

*Photometric Accuracy.* The rms photometric error vs. magnitude is given in **Figure A.14**. Systematic error has not been included, but will be minimized by the presence of numerous calibration sources (from IUE and HST) and the averaging effects of drift scanning.

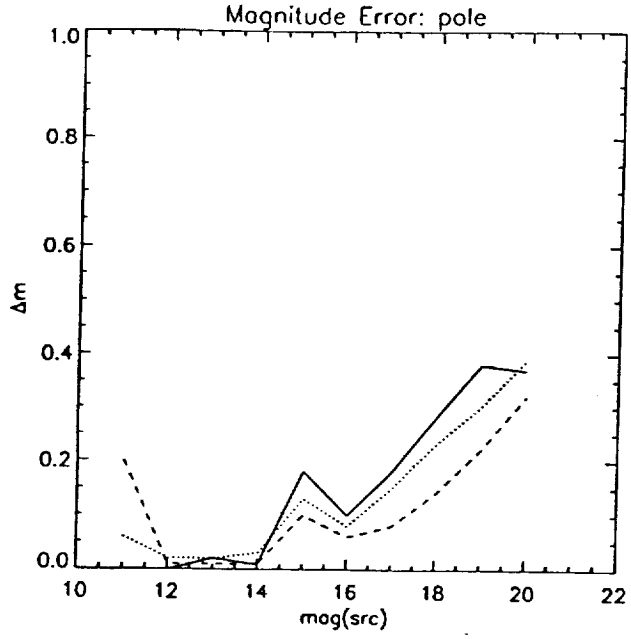


**Figure A.14** Rms photometric error vs. detected magnitude. Solid line: **14**, Dotted line **18** and dashed line **16**.

*Optical ID Efficiency.* The core of the JUNO classification strategy is unambiguous optical identifications and derivation of UV-Visible flux ratios. The optical ID efficiency is extremely sensitive to the astrometric precision. With geometric and chromatic aberrations, high count rate effects, and pointing drift and reconstruction, the rms error between source and detected positions is $\sigma_p \simeq 1.5\text{-}2''$. We consider the two limiting cases, poles and plane, separately.

(1) *High galactic latitude:* At the poles, we found using optical catalog positions that only 0.05% of the UV sources were misidentified. All of these are galaxies that are misidentified with other galaxies due to their clustering and large variance in surface density. One possible source of contamination of the QSO catalog is galaxies (very numerous at faint magnitudes) that are mistakenly identified with optical stars. No sources that were galaxies were mistaken for stars in our test field.

(2) *Low galactic latitudes:* In the plane ($b = 2.5°$), we found from a statistical simulation of optical star densities that erroneous optical IDs occur <1% of the time.

*Classification Efficiency.* We used detected magnitudes, **14-18**, and **16-V**, colors to produce preliminary classifications of the UV model detections. These were then compared with the original source class. In **Figure A.18**, we show color-magnitude diagrams for a galactic plane simulation. Symbols give source classes. Using a simple classification schemes, we derive the total number of sources in class $i$ ($N_s$), the number of sources detected and correctly classified ($N_d$), and the number of sources detected and incorrectly classified ($N_e$). We can then determine both the detection efficiency $\epsilon_d(i, m_{16}) = N_d/N_s$, describing the probability that a source of class $i$ will be successfully detected and classified, and the catalog purity $\epsilon_c(i, m_{16}) = N_d/(N_d + N_e)$, the fraction of sources in the catalog which are actually of class $i$. **Table 3.1** and **A.4** give $N_s$, $N_d$, $\epsilon_d$ and $\epsilon_c$ for various major source classes. We discuss several examples:

*High Galactic Latitude Survey*

1. *QSOs and their redshifts.* As **Table 3.1** shows, QSOs are detected and classified with high efficiency using **16** and **16-V**. QSOs with redshifts $z > 1$ are attenuated in the far UV by Lyman alpha and Lyman limit absorption. This leads to a reddening in **16-V** with $z$, illustrated in **Figure A.15**. Because of the relatively tight distribution in low-$z$ QSO **16-V** color (Bechtold *et al.* 1986), and the clean separation of QSOs from galactic stars (**Figure 3.4**, **16-V** can be used to separate low- and moderate-$z$ QSOs. Thus it will be possible from color-number counts alone to (1) constrain low-$z$ Lyman limit system evolution and (2) determine angular correlation functions for low- and moderate-$z$ QSOs.
2. *White dwarfs.* White dwarfs with T>15,000K will be cleanly separated from QSOs and normal galaxies. They may however be confused with blue galaxies that appear stellar on the POSSII digitized survey. We have estimated that blue galaxies with $z > 0.2$ will appear stellar, and that all emission line galaxies (as defined by Wasilewski, 1986) have the seds as measured by Kinney *et al.* 1992. This still leaves a substantial number of galaxies which could be confused with white dwarfs. We will use proper motions derived from the two epochs of digitized POSSI and II surveys that will be available to us. With an accuracy of <1 m″/yr, 50% of white dwarfs with velocities of 30 km/s can be detected to 6 kpc, and 90% to 1 kpc. **16-V** and **14-18** give WD temperature, and **16** gives distance for DA and DB stars (the vast majority). Thus a byproduct of this work will be a distance-velocity survey of white dwarfs, a powerful probe of galactic star formation history.
3. *Subdwarfs.* These will generally appear at brighter magnitudes. The small number of subdwarfs in the halo will be separated from nearby white dwarfs by proper motion.
4. *Galaxies.* Galaxies will be separated from stars on the digitized optical surveys using a combination of the peak density, second and higher moments, and integrated density. The POSSII plates in particular are very sensitive to low surface brightness nebulosity, and will be able to discriminate galaxies with $z < 0.2$.

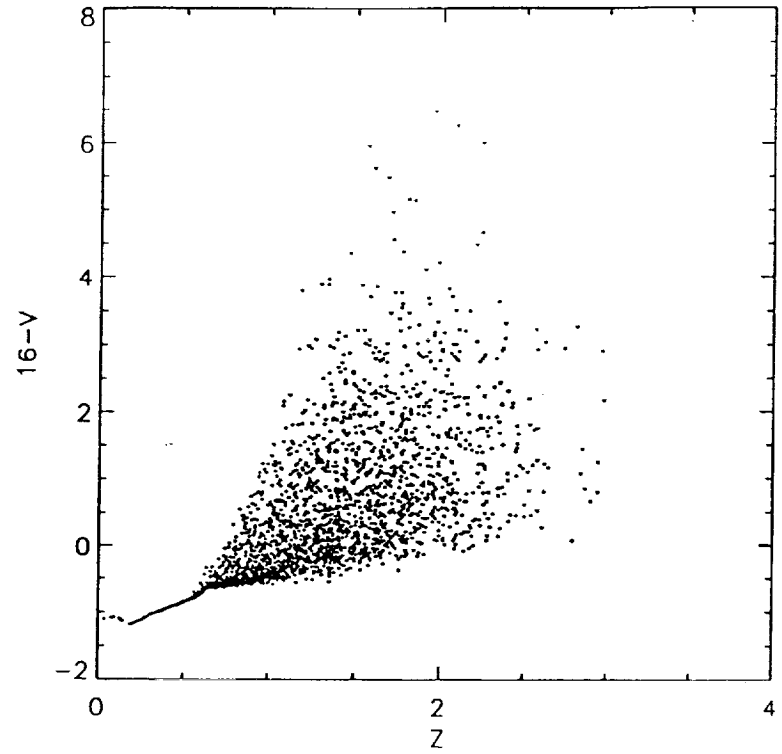


**Figure A.15** QSO Ly$\alpha$ forest "extinction" in **16-V** vs. redshift.

5. *Extinction Determinations.* The photometric survey will produce a complete map of the reflection from high latitude dust. We will be sensitive to features of 200 $(\Omega/1\ sq.\ arcmin)^{-1}$ ph $cm^{-2}s^{-1}\AA^{-1}$on angular scales of $\Omega$. Because the scattering is optically thin at the poles, and the albedo and scattering function are unlikely to vary, the reflection map is essentially equivalent to an extinction map. We will use the UV galaxy number count survey to verify this on intermediate scales, providing an independent measurement of extinction variations.

*Galactic Plane Survey*

In the Galactic plane, extinction adds additional uncertainty to the classification and evaluation of sources. During the low and intermediate latitude parts of the all-sky survey, we will use A0 stars to map out the galactic dust distribution with unprecedented scope and detail: E(B-V) will be determined with an accuracy of $\pm 0.02$ mag, with a three dimensional resolution of $< 50$pc, and to a distance of $>5$ kpc. We have tested our ability to reconstruct three-dimensional extinctions from A0 stars in the field of view, using the UV model. We isolate A0 stars using **14-18** color (which is very insensitive to extinction), and then combine **16** and **16-V** to derive distance and $A_{16}$. In **Figure A.16**, we show the results of this analysis for one field, graphing derived vs. input distance and $A_V$. **Figure A.17** gives **16-V** vs. **16** for the plane survey, and **Figure A.18** gives **14-18** vs. **16-V** colors.

This leads to a straightforward classification procedure, outlined here. For each detected source, we can then derive a relationship $A_{16}$(D) from the A0 star extinction map. For any given source type $i$, the apparent magnitude is

$$m_{16} = A_{16}(D) + 5logD - 5 + M^i_{16}$$

and is a function of $D$ only. The UV-visible flux ratio is

$$m16 - V = (A_{16} - A_V)(D) + (16 - V)^i{}_0$$

also is a function of $D$ and $i$ only. The observed $m_{16}$ and $m_{16}$-V can then be used to derive $D$ vs. a function $M_{16}$(**16**-V)$_0$. As $D$ is varied as a free parameter, a curve in $M_{16}$ vs. $16 - V$ space is traced out. This is illustrated in **Figure A.19**. Object classification can be made if the curve intersects an object type locus in this plane. The object types are given with large, bold symbols. For each observed source, a

series of points are plotted at successive distances separated by 50 pc. For example, considering the figure, all the main sequence stars (plusses) are cleanly separated from post-main sequence. Two white dwarfs (diamonds) are identified as a 50K WD at 250 pc, and a 16K WD at 100 pc. The latter could also be a quiescent DQ Her star. The two observed CV's are a DQ Her (275 pc) and a DN in the high state (350 pc). The latter is confused with subdwarfs at a greater distance, SdB (450-500 pc). With proper motion, we should be able to separate the cooler WD/CV-Sd degeneracy. The number counts of cool WD's will be low, so the classification efficiency for CVs and subdwarfs will be ~25% (cf. Table A.4).

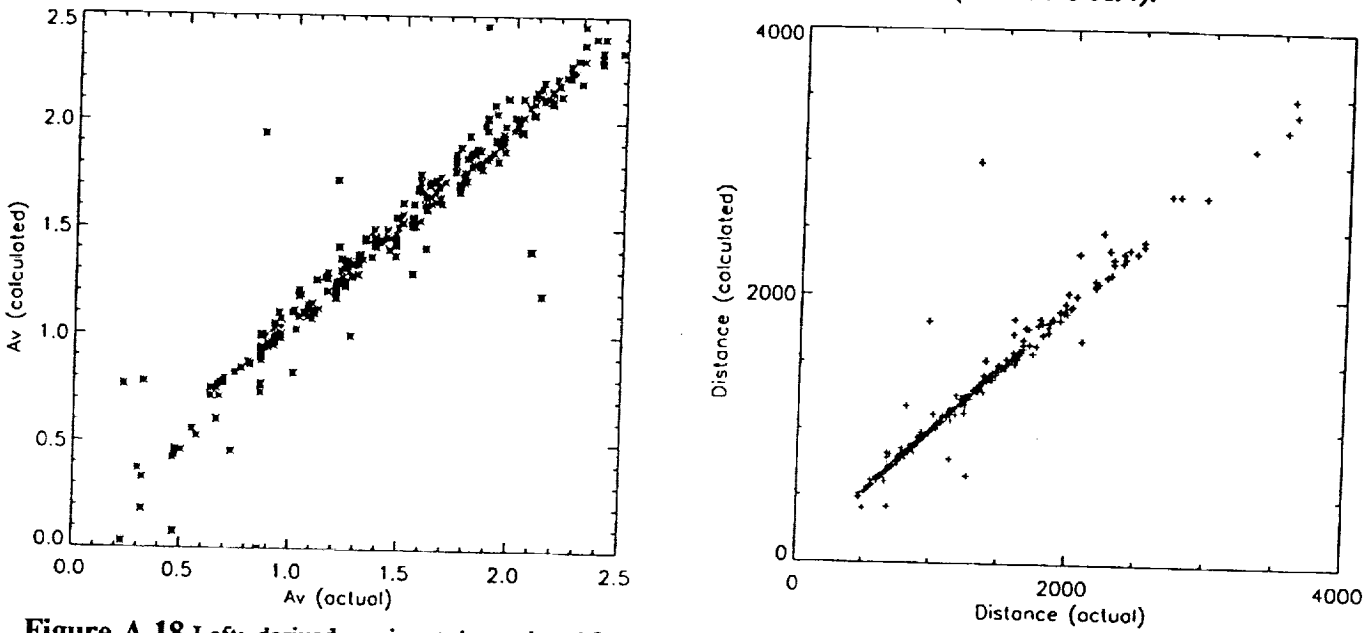


**Figure A.18** Left: derived vs. input $A_V$ using A0 stars. Right: same for distance.

**Table A.2 – Detection & Classification Efficiency: Low $b$ Surveys**

| Input Sources ($m_{16} < 19$) | #/20 sq. deg | Detected & Classified Sources MS Stars | CVs | WD's | Unclassed | $\epsilon$(DET)(%) |
|---|---|---|---|---|---|---|
| MS Stars | 3910 | 698 | 3 | 0 | 3209 | 18% |
| WD's | 154 | 0 | 11 | 66 | 77 | 43% |
| CVs | 12 | 0 | 6 | 0 | 6 | 50% |
| Unsourced/Other | 837 | 16 | 6 | 2 | 813 | |
| $\epsilon$(CAT) | | 98% | 23% | 97% | | |

*Data Reduction Hardware Requirements.* The UV model has permitted us to estimate the hardware, software, and personnel required to reduce the JUNO data set in near real-time. We show in **Table A.5** the approximate running time for various reduction routines on a Sun Sparc 2 with 2.6Gbyte of hard disk and 16MB RAM, at peak data rates (in the galactic plane, for example) Using a Sun Sparc 10 with 64MB

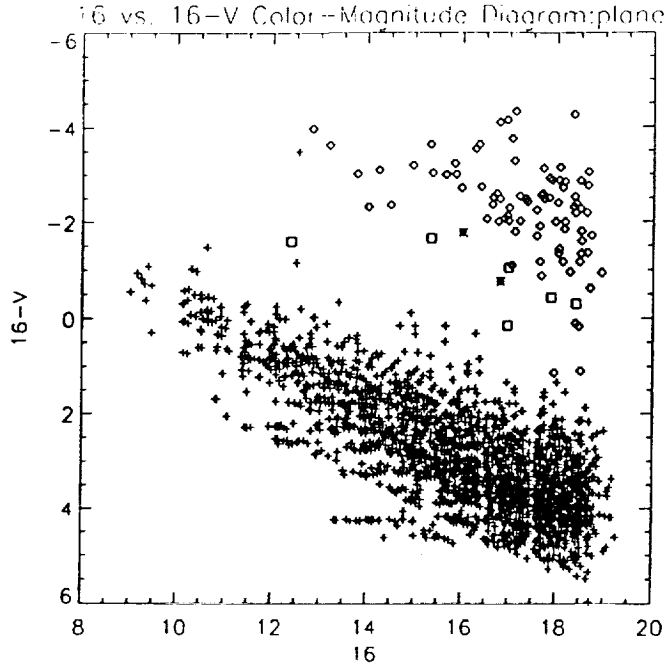


**Figure A.17** Galactic plane simulation, **16** vs. **16-V**, one JUNO pointing (20 square degrees). Symbols give source type: +MS star, , ◇WD, LICV, △subdwarf.

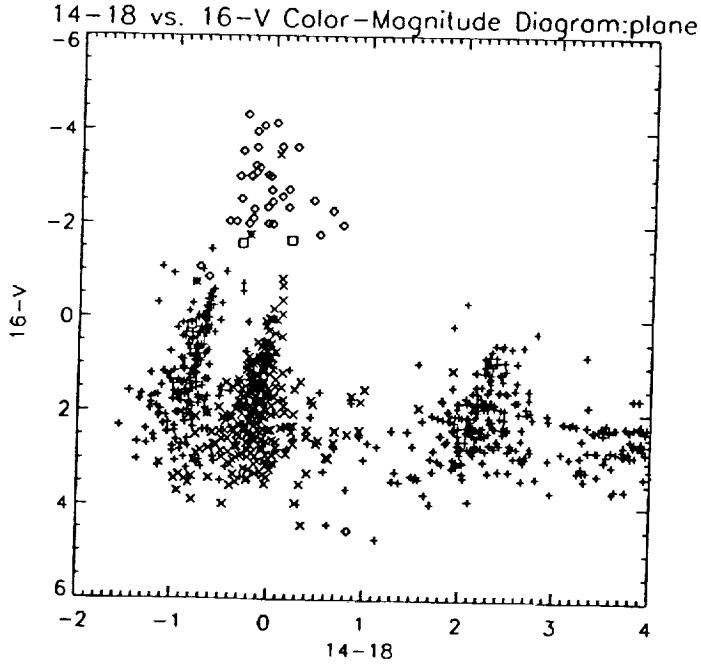


**Figure A.18** Galactic plane simulation, **14-18** vs. **16-V**, one JUNO pointing (20 square degrees). Symbols give source type: +MS star, , ◇WD, LICV, △subdwarf.

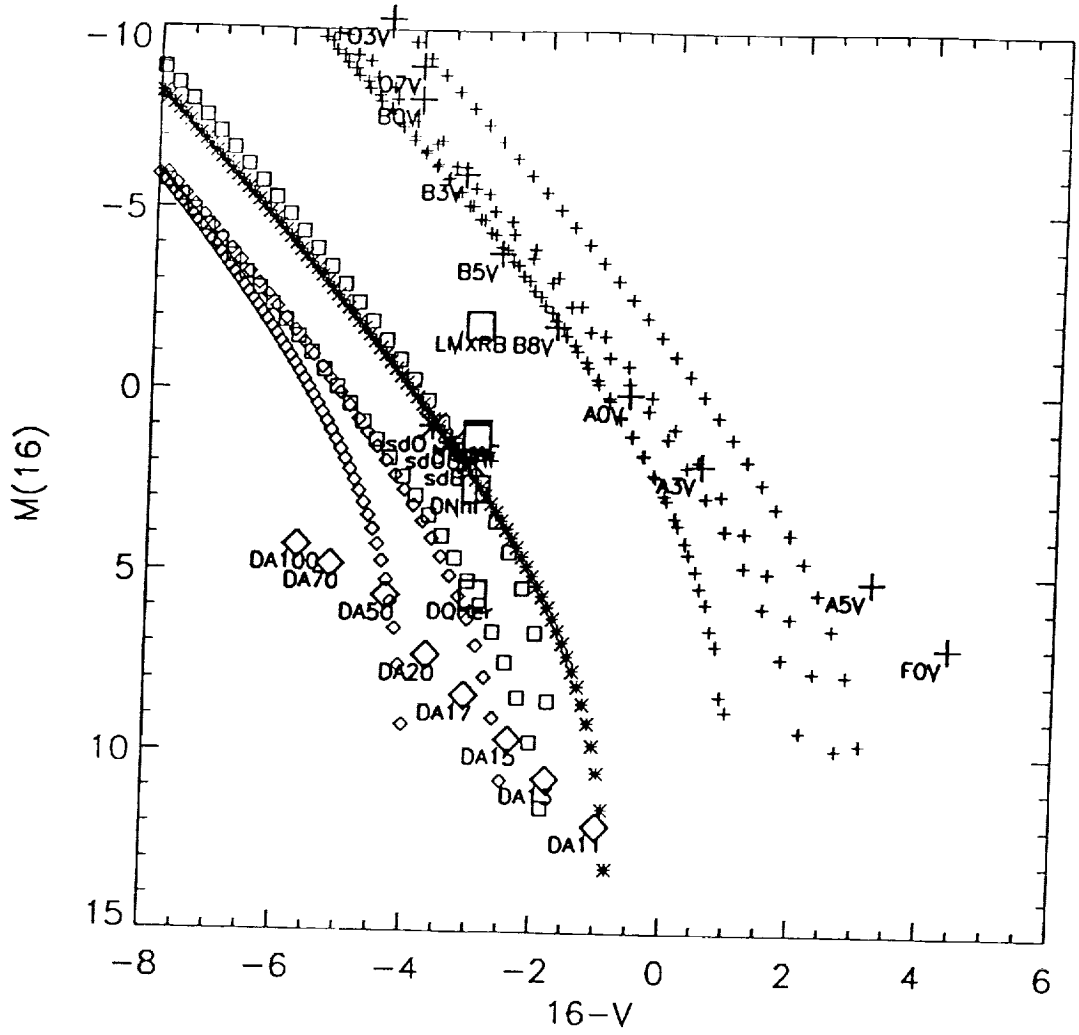


**Figure A.19** Galactic plane simulation: absolute magnitude (at 1600Å) and 16-V color (dereddened) for various object types. White dwarfs (DA*TT*) are given by diamonds with *TT*=T/1000K, main sequence stars by pluses, subdwarfs by asterisks, and CVs by squares. Bold, large symbols give input source positions. Small symbols in a line give inferred position on the diagram for a single detected source, for various distances (50, 100, 150, 200, ... pc). Intersection of this locus with source type gives tentative identification.

RAM and a 10 Gbyte hard disk will further speed up the production. One Sparc 10 at the US SPOC will be used for continuous production, while a second will act as an off-line analysis station. A third will be available for backup and for UV/optical/auxiliary catalog management. All will be linked via a LAN.

*A.4.3 Deep Surveys*

We used the UV model to repeat the process described above for a 1°×1°central region of a deep survey pointing at the galactic pole. We used 40,000 s integration times. In **Figure A.20**, we give completeness and spurious detection rate (with optical IDs) vs. magnitude for the three bands. **Figure A.21** shows the photometric error vs. magnitude for the deep survey pointings.

*A.4.4 Spectroscopic Survey*

The introduction of objective prisms into the wide-band telescope has several important effects:

1. Spectra occupy ~50 times more area than the undispersed images.
2. High count rate stars are spread out, saturating less and challenging the star compression system more.

Table A.5 – JUNO Data Reduction Running Times (Based on UV Model)

| Analysis Step | Mphotons $day^{-1}$ | Ksources $day^{-1}$ | Images $day^{-1}$ | Sparc 2 Run Time (meas.) | Sparc 10 Run Time (est). |
|---|---|---|---|---|---|
| Image Reconstruction | 600 | 50 | | 7.5 hr | 3 hr |
| Source Detection & Evaluation | - | | 150 | 5 hr | 2 hr |
| Source Matching & Optical IDs | - | | 150 | 15 hr | 6 hr |
| TOTAL | | | | 27.5 hr/day | 11 hr/day |

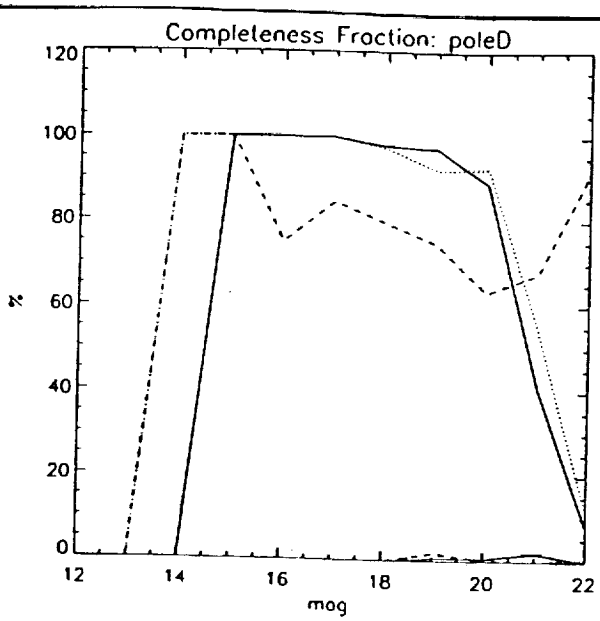


**Figure A.20** Completeness (bold lines) and spurious detection rate with optical IDs (unbold lines) vs. input source magnitude, deep survey. Solid line: **14**, Dotted line **18** and dashed line **16**.

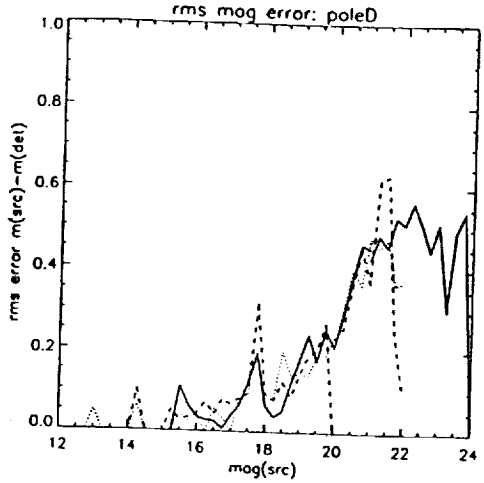


**Figure A.21** Deep survey photometric error vs. magnitude. Solid line: **14**, Dotted line **18** and dashed line **16**.

3. Zero order images are produced located half a degree away from their associated spectra.

4. Drift reconstruction is more difficult.
5. The telescope efficiency is reduced by 30-40%.

Our design accommodates this behavior, as we have verified with the UV model. A model image showing objective spectra obtained at high latitude is shown in **Figure A.22.** A selection of extracted spectra are also shown.

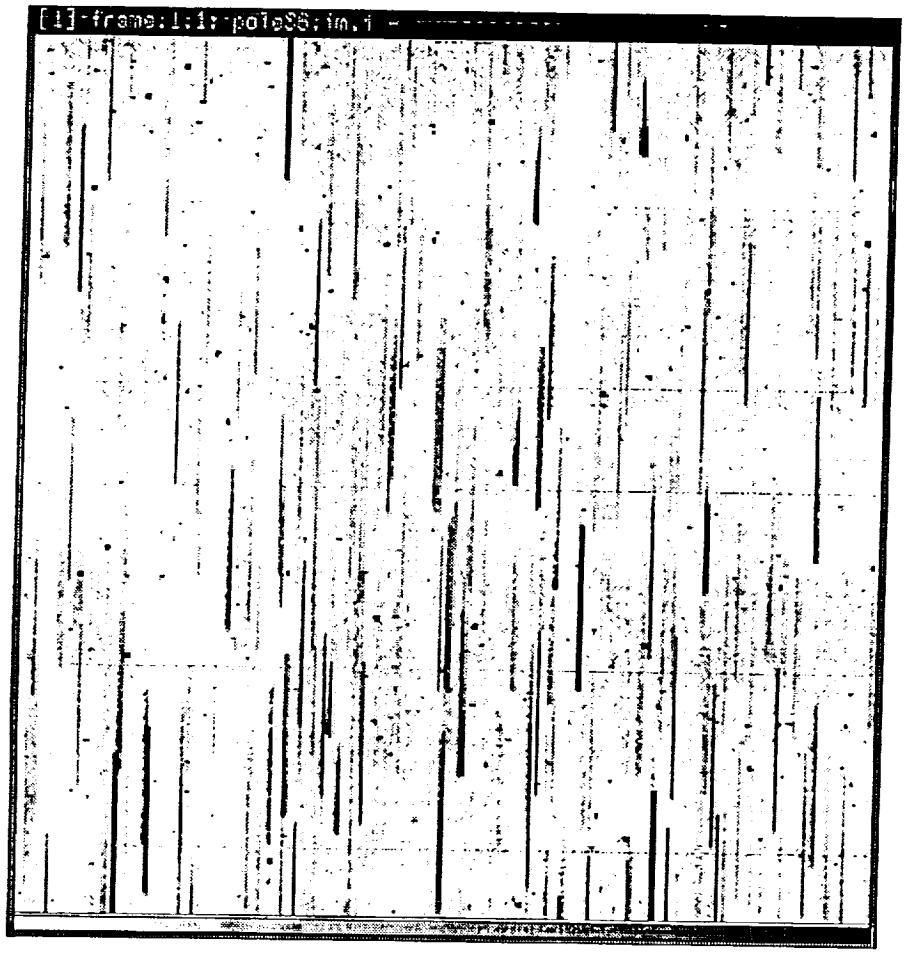

**Figure A.22** Objective spectra image.

*Detector Count Rate Statistics & Data Compression.* Bright stars are more spread out, and therefore less subject to saturation. The result is a higher mean gain for bright-star events, and correspondingly greater dead-time. We include front-end dead-time in the UV model, which is determined by the ADC speed. The data compression algorithm has been tested under these very different conditions, and found to work well, with an efficiency of 99.5%. The trick is to bin the star-finding image more coarsely in the dispersion direction.

*Image Reconstruction, Spectrum Extraction, and Spectrum Quality.* The image reconstruction routine will use the zero order images to track uncorrected drift. Spectra are extracted using information from the AS to determine the approximate positions of all sources. Prior to extraction, the positions of all source spectra are determined in order to track overlap and regions of clear background. Bright sources are removed first, followed by successively fainter ones. Surrounding uncontaminated regions are used for background evaluation and subtraction. The position of the "zero-order" image, the measured dispersion

curve, (and ultimately the prism temperature) are combined to reconstruct the wavelength scale for each extracted spectrum. **Figure A.23** show spectra for a selection of magnitudes and a variety of source types. For 50,000 s integrations, S/N=10 spectra are produced for $m_{16}$ =16. We tested the velocity measurement accuracy for the QSO redshift survey, and found $\sigma_v \simeq$ 2000 km/s for a median magnitude of $m_{16}$=16.5. This is mostly due to systematics, and can be improved.

## A.5 Additional Study Topics

### A.5.1 Telescope Optical Design Study

We performed an extensive optical design study to determine the optimal telescope design. We varied f/#, focal length, primary f/#, and construction parameters. We used an average resolution figure of merit, and considered the mechanical requirements of each design (size, mass, and so on). This study resulted in a modification of the telescope design from that presented in our original proposal (Martin *et al.* 1988). The design residual for the telescope was reduced from 11″ to 8″, which permitted some relaxation of manufacturing and thermal control requirements. The major mechanical change was the introduction of an axial space between the primary and the tertiary. The resulting spot diagrams for the design, which was audited by HDOS, are given in **Figure A.24**.

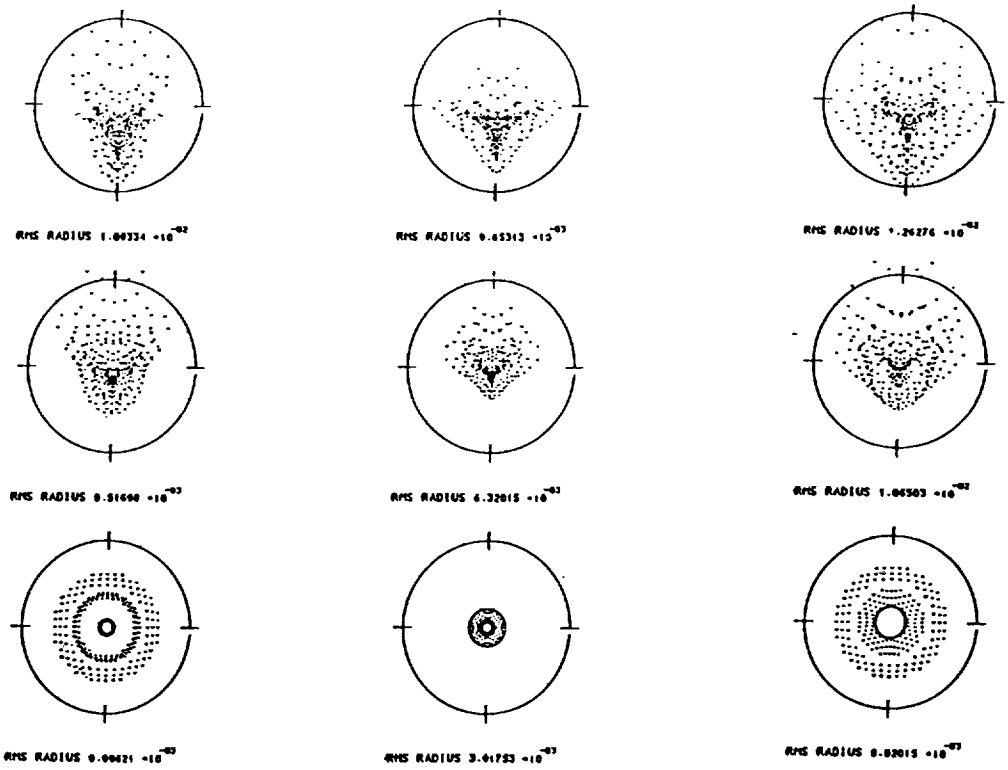

**Figure A.24** Spot diagrams for JUNO telescope, at various field positions, wide-band filter.

### A.5.2 Telescope Wave Front Error Budget

HDOS prepared a detailed telescope error budget, using the top level budget given in Table 4.2. The budget, illustrated in **Figure A.25**, includes fabrication tolerance, ground alignment tolerance, ground-to-orbit alignment tolerance, and in-orbit thermal alignment tolerance.

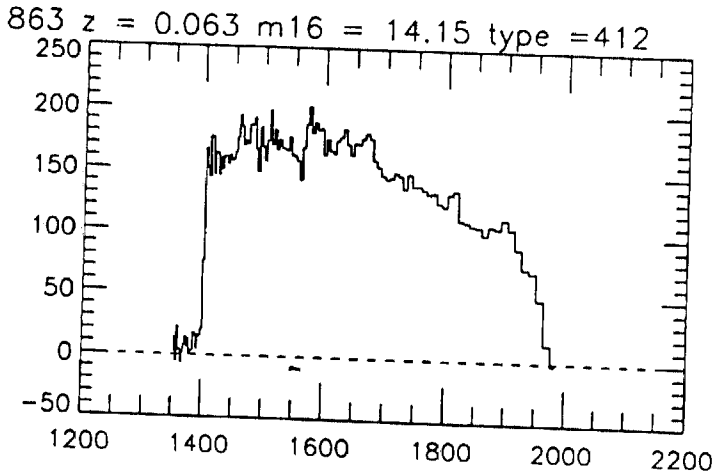


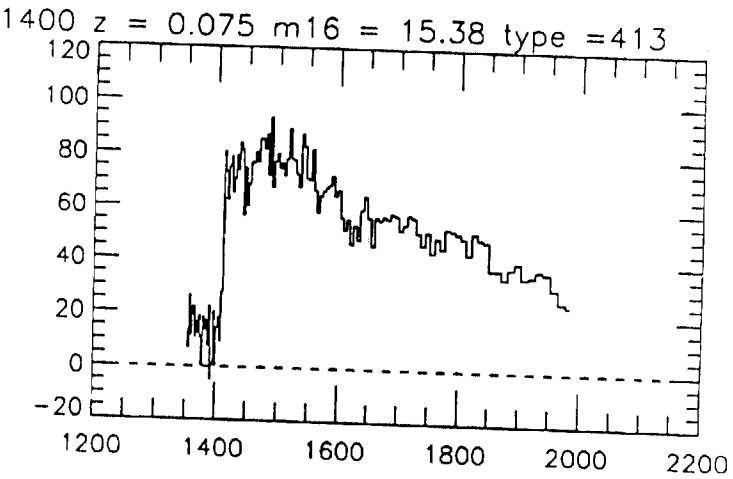


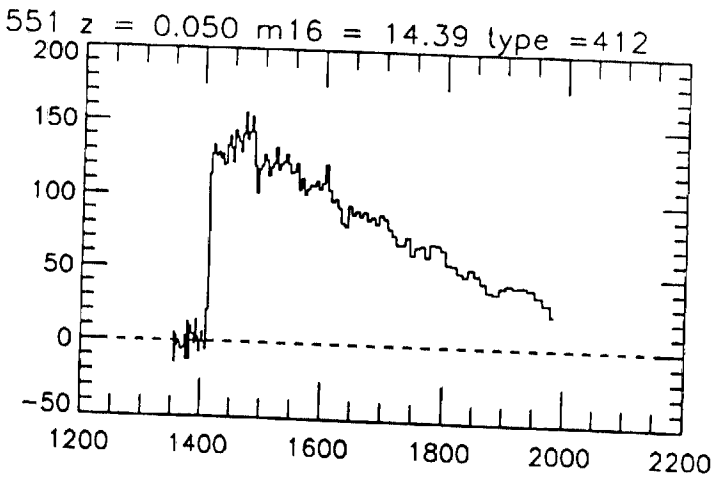


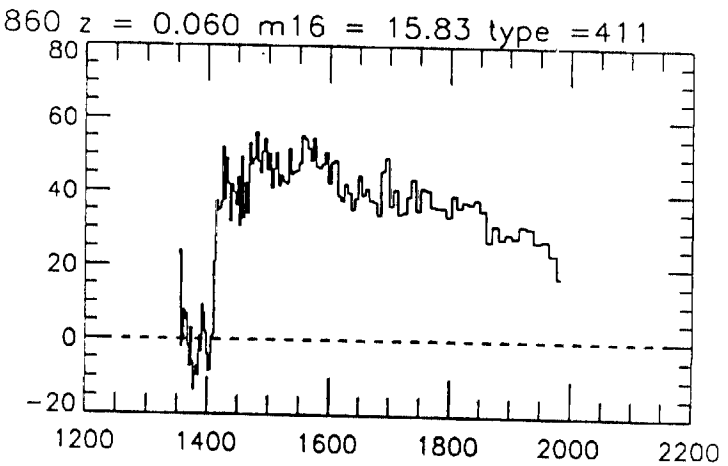


**Figure A.23** Spectrum quality vs. source magnitude. Moderately redshifted UV bright galaxies are shown.

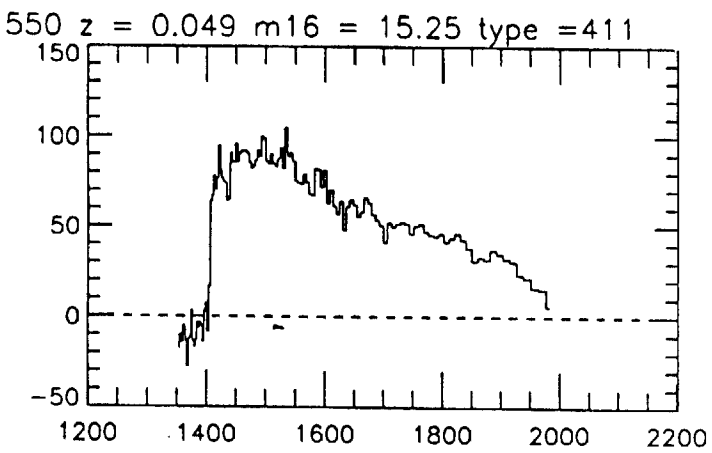


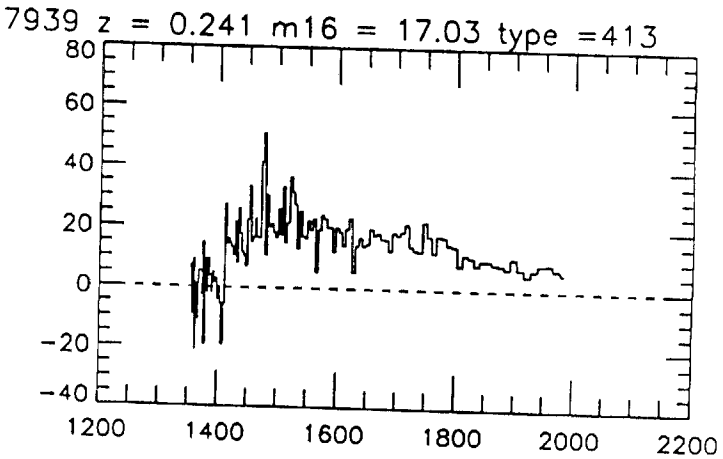


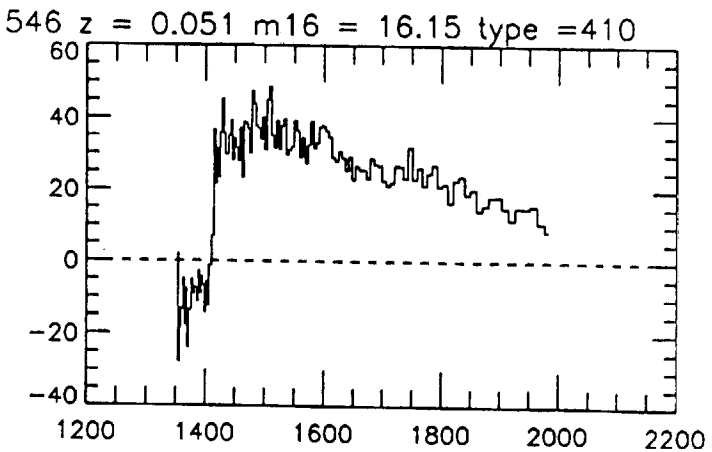


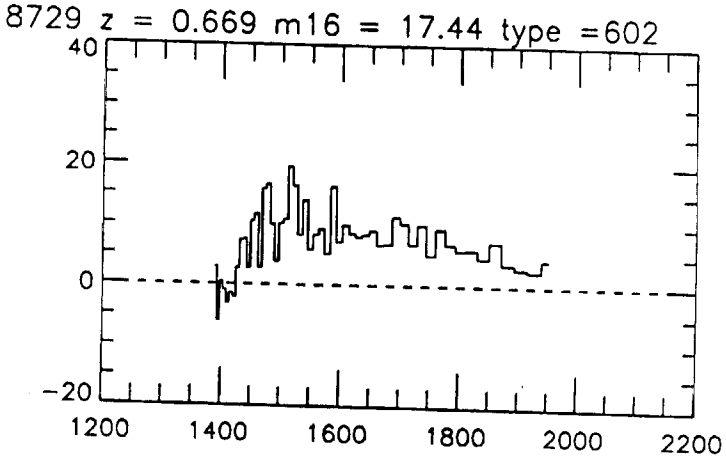


**Figure A.23** Spectrum quality vs. source magnitude.

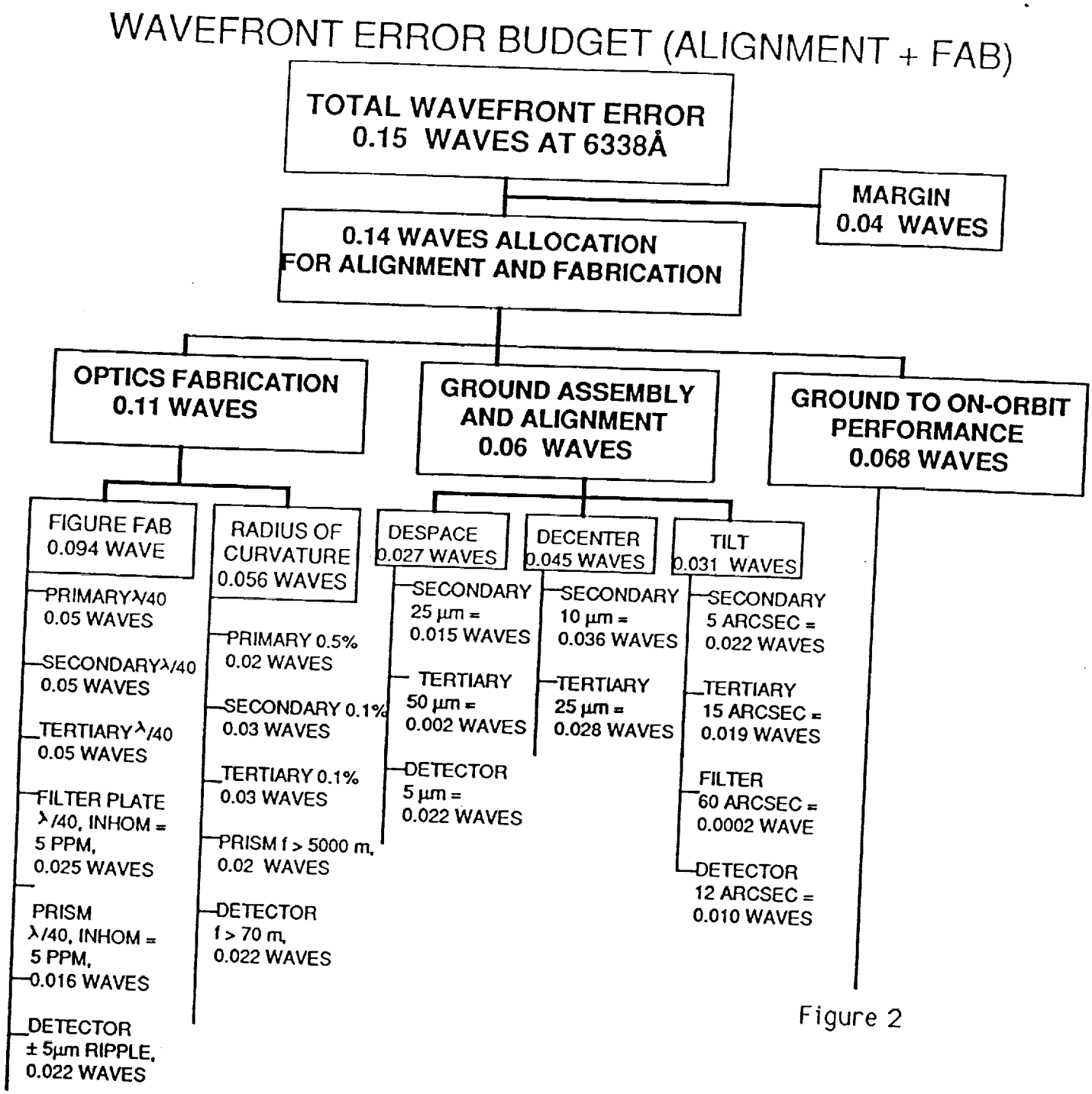


Figure 2

**Figure A.25** JUNO telescope fabrication, alignment, launch, gravity release, and thermal alignment tolerances.

### A.5.3 Detector/Telescope Interface

The most complex and mechanically critical interface in the JUNO instrument is between the telescope and detector. Interface requirements include:

1. Telescope/detector axial despace $<5\mu$m.
2. Telescope/detector axial tilt $<30''$.
3. Detector baffling mounted with secondary.
4. Detector mounting has minimal effect on secondary figure.
5. Detector cabling is mounted on secondary spider.
6. Telescope/detector thermal interface consistent with thermal requirements.

Because of the importance of this interface, we have performed a preliminary design, which is illustrated in **Figure A.26**. We show the detector assembly, detector housing, and entrance window, the secondary and secondary mount, and various secondary and detector baffles. This interface will be taken to the PDR stage prior to completion of Phase I. The detectors are integrated into the telescopes early in the development schedule, during mid-year two of Phase III.

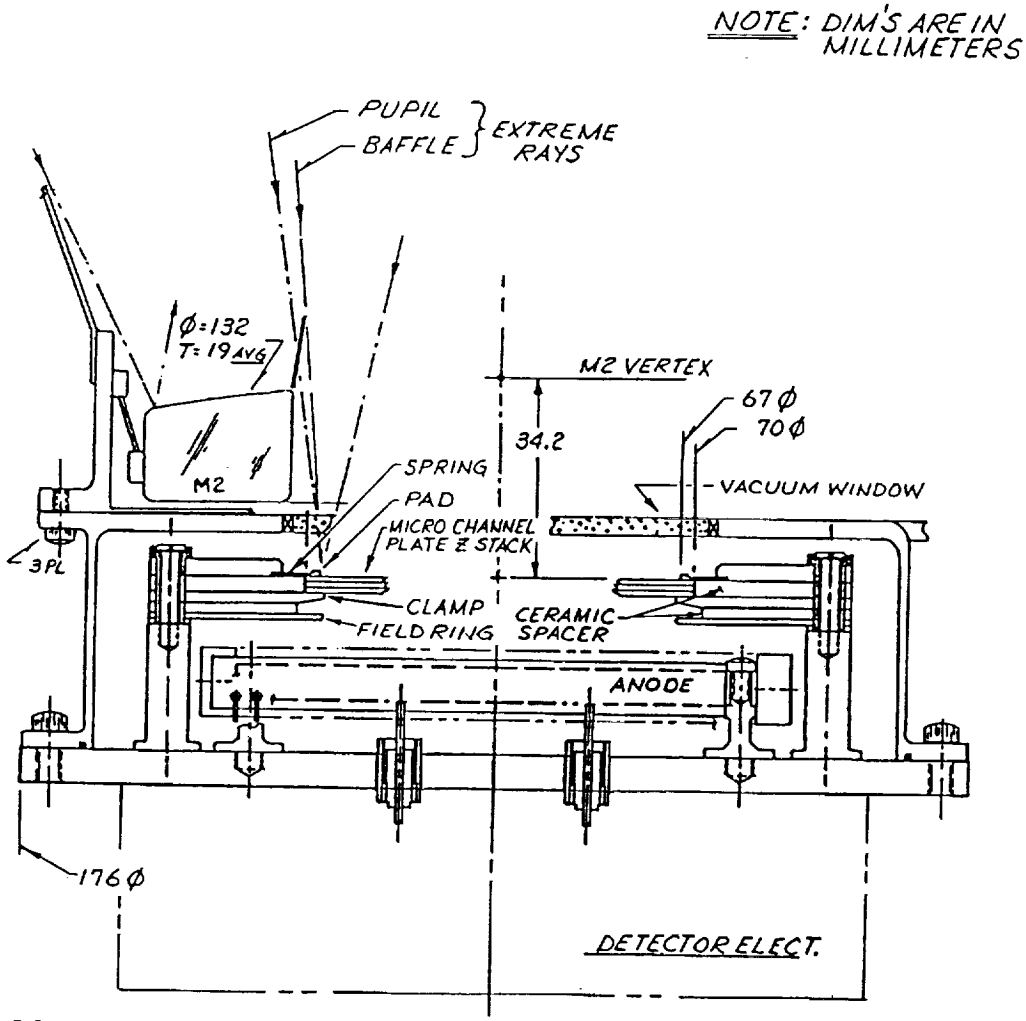


**Figure A.26** Preliminary layout of Telescope/detector interface.

# APPENDIX B

## Spacecraft Description

# APPENDIX B – SPACECRAFT DESCRIPTION

## B.1. Introduction

The efforts in the JUNO design have been mainly devoted to define a light and compact spacecraft which allows scientific requirement compliance still assuring a satisfactory level of reliability and operational flexibility.

The preliminary satellite configuration design is based upon the following mission assumptions:

- the nominal orbit is perfectly circular, equatorial and has an initial altitude of 600 Km.
- the satellite lifetime is $\geq$ 2 years
- the PEGASUS launcher has been chosen for JUNO launch.
- a spacecraft total weight must be $\leq$ 290 Kg (PEGASUS limit for the chosen orbit).

For the selected orbit a single equatorial ground station (San Marco) can provide a good ground coverage (about 10 minutes of ground link every orbit).

The required satellite lifetime (> 2 years, including margin) can be achieved if all subsystems work with renewable sources and the orbital decay for the chosen altitude and operative period is not too great.

## B.2. Orbital Analysis

A preliminary analysis has been performed to optimize the orbital parameter choices, based on the following driving factors:

- orbital decay due to aerodynamic drag which impacts on satellite lifetime
- mass constraints
- ground-link communication requirements

As a data-rich mission, JUNO requires an equatorial orbit to take advantage of a downlink once per orbit. This permits us to telemeter 5-10× as much data as with a non-equatorial orbit.

A nominal orbit has been identified and its principal characteristics are shown in the table B.2.1.

The satellite orbital decay rate depends on the launch date because of the atmospheric density dependence on the solar flux activity, which has a period of about 11 years.

The satellite orbital decay has been calculated using the 1977 MSIS model for the atmospheric drag. The MSIS model is based on the numerical integration of the diffusion equation for each major atmospheric constituent and uses spherical harmonics to represent the variations of temperature associated with each constituent.

Table B.2.1 - Nominal orbit characteristics

| | |
|---|---|
| Altitude (Km) | 600 |
| Eccentricity | 0 |
| Inclination (deg) | 0 |
| Orbital Period (min) | 96.4 |
| Max. shadow time (min) | 35 |
| Ground link with the San Marco station (min) | 10.6 |

To perform the orbital decay simulation the following additional parameters have been estimated from the S/C design:

- the spacecraft drag coefficient is assumed to be = 2.0
- the cross sectional area, averaged on the whole orbit, is = 3.1 $m^2$
- an apogee/perigee difference of 50 Km has been assumed as a consequence of the launcher injection error.

The simulation results have shown that for a mission beginning in 1997 (the SMEX launch date in the A.O.) the orbital altitude remains almost constant for the whole lifetime. However, to be conservative we have assumed JUNO flies during solar maximum (2000-2001). Simulations show that an initial apogee altitude of 600 km will fulfill the two year lifetime requirement also for a launch date during solar maximum. Figure B.2.1 shows the satellite orbital decay profile for a 2000 launch date.

## B.3. Mission Operations

*Initial Phase Operations*

The launcher releases the satellite once the operative orbit has been reached. An automatic sequence must perform including at least the antennas deployment and the telecommunication system switch-on.

The following operations must be performed during the initial phase:

1) Separation from the launcher final stage
2) Satellite rate reduction and acquisition of a sun-pointing safe attitude. The satellite residual small tumbling after separation from the launcher last stage can be controlled with the reaction wheels. The simple and reliable Coarse Sun Sensors (CSSs) are used to perform a first attitude determination and also sun position tracking.
3) Solar panels deployment (up to now power has been provided by the battery). The solar arrays must be obviously deployed as soon as possible but launch window must be chosen in such a way the panels deployment occurs at the beginning of orbital day.
4) 3-axis attitude acquisition.
5) Spacecraft healthy status verification. To verify the spacecraft healthy status checks and tests of the equipments and on-board software must be performed.

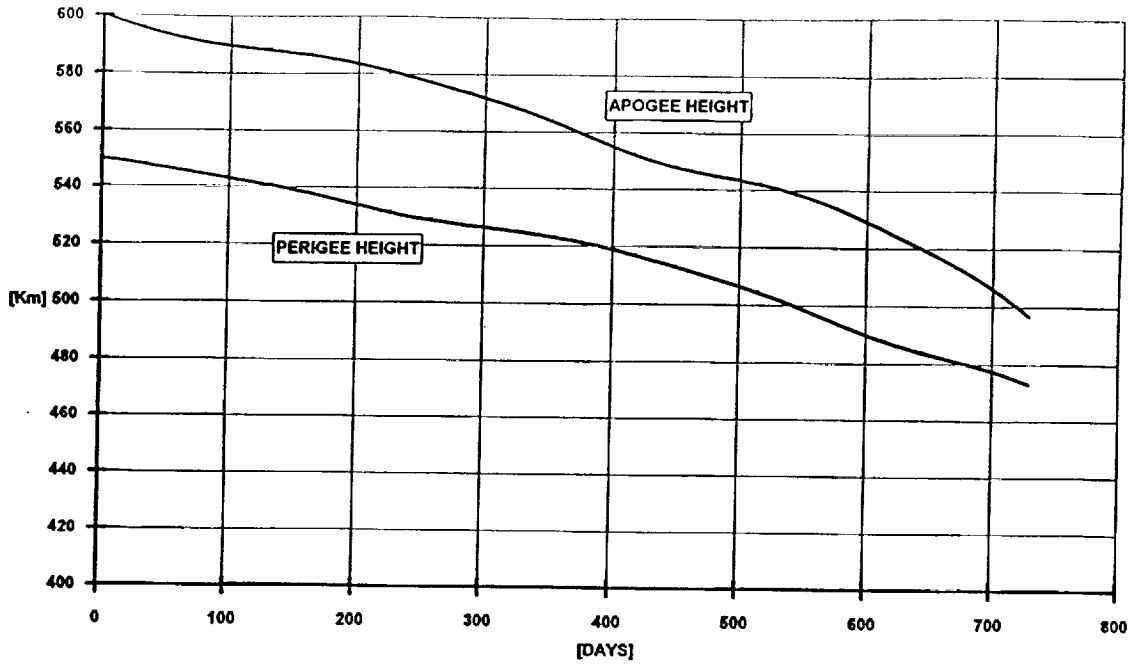


Figure B.2.1 - Orbital decay profile

6) Payload instruments switch-on and healthy status verification.
7) Scientific commissioning activity and instrument calibrations. In general the commissioning activity will require at least 2 – 3 weeks. The calibration of the instruments and star tracker can be performed by pointing the telescope at well-known targets.

*Operative Phase Operations*

The JUNO mission is composed of three different observing phases:

1) the all-sky survey (AS).
2) the deep survey (DS).
3) the spectroscopic survey (SS).

In the AS the two telescopes drift very slowly (drift scan velocity = 10″/sec) during the nighttime observation which lasts about 25 minutes. The attitude remains fixed through the daylight phase until the next observation begins. Assuming 33% overlap and 80% nighttime observing efficiency, the whole sky can be covered with 3800 pointings which can be performed in 253 days.

During the all-sky survey a sequence of pointings to tile the sky can be automatically performed by the on-board subsystems (under the ground operator control and support). The ground operator could intervene on the next pass to modify the observation sequence

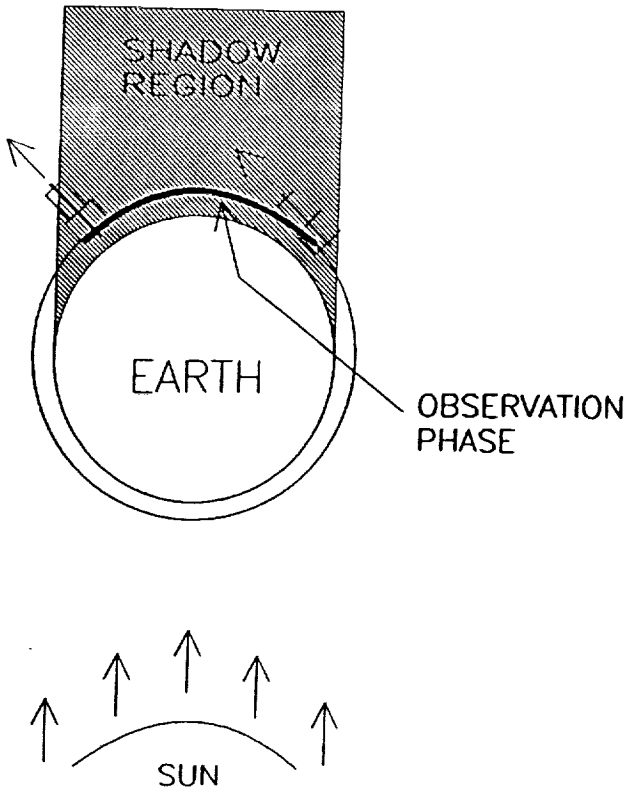


Figure B.3.1 - Spacecraft required attitude for observation in the equatorial plane.

if, for example, a portion of scientific data were lost and an observation needed to be repeated.

The deep survey and spectroscopic survey phases are very similar from an operational point of view. Oservations of up to several days are performed at this time. The observations can be performed only during nighttime and must be interrupted and restarted at the beginning and end of orbital day. The target pointing attitude must be held during orbital day in order to avoid target reacquisition.

Between about twenty and fifty targets are observed during the DS and the SS. Each of these surveys lasts six months. The ground operator, on the basis of weekly science schedule and the previous scientific results, will plan and uplink the next observation sequence and relative attitude maneuvres.

The observational requirements of JUNO impact on the satellite configuration design and, in particular, on the solar panel size. To observe targets in the celestial equatorial zone a particular attitude must be held (and maintained during orbital day) to avoid earth horizon occultation (see figure B.3.1). This imposes an oversizing of the solar arrays by a factor of $1/\cos(45°)$ to provide the required power in sun-light phase.

An alternative to the solar arrays oversizing could be to reorient the satellite at entrance and exit of the orbital day, but this technique is complex and hazardous (many maneuvers implies more failures hazards).

*Safe Mode*

An operational safe mode must be available for the satellite to allow survival in a contingency situation. When a critical equipment/software failure occurs the satellite is switched to an automatic sequence of operations aimed at controlling the satellite in a safe attitude (solar radiation could damage the telescopes, star tracker, and detectors). During the safe operational mode all the complex operations should be as far as possible avoided; the satellite must achieve and maintain an attitude (safe attitude) with the solar panels perpendicular pointing to the sun. This attitude allows maximum solar panel power and prevents solar radiation from entering in telescopes.

The safe attitude determination and control should be easy to perform and it could be based upon simple and reliable hardware (e.g the coarse sun sensors, the magnetic torquers and possibly one or two reaction wheels).

## B.4. Spacecraft Configuration

The JUNO satellite configuration will be driven by the guidelines of simplicity and design-to-cost to accomplish the severe cost and schedule requirements.

It will be compatible with the PEGASUS payload total weight and C.G. location requirements as well as with the fairing dimensional constraints for the 23-inch Attach Fitting (see figure B.4.1). The assumed reference system is shown in the figures and it has the origin at the spacecraft/launcher separation plane.

The JUNO satellite is mainly composed of:

- two telescopes with their electronic boxes
- a box containing the subsystems (service module), with two deployable S-band antennas and two symmetrical deployable solar panels attached to the box itself (see figure B.4.2).

The service module and the telescope dimensions are shown in figure 4.3. The $+X$ and $-X$ panels are slightly inclined to allow a better launch longitudinal loads distribution. The service module box houses almost all the spacecraft equipments and mates with the Pegasus Payload Attach Fitting.

The deployable solar arrays are composed of six panels (three for each side) of $0.6 \times 1.025$ m. As explained above in the Mission Operations section the solar panels must be oversized of a $1/\cos(45°)$ factor in order to fulfill both scientific observations requirements and power provision requirements.

The payload instruments and the relative electronics are accommodated outside the service module and are interfaced only to the upper side of the payload platform (that is the service module box top cover).

The payload and subsystem box accommodation is shown in figures B.4.4 and B.4.5. The envisaged boxes dimensions are those of existing units.

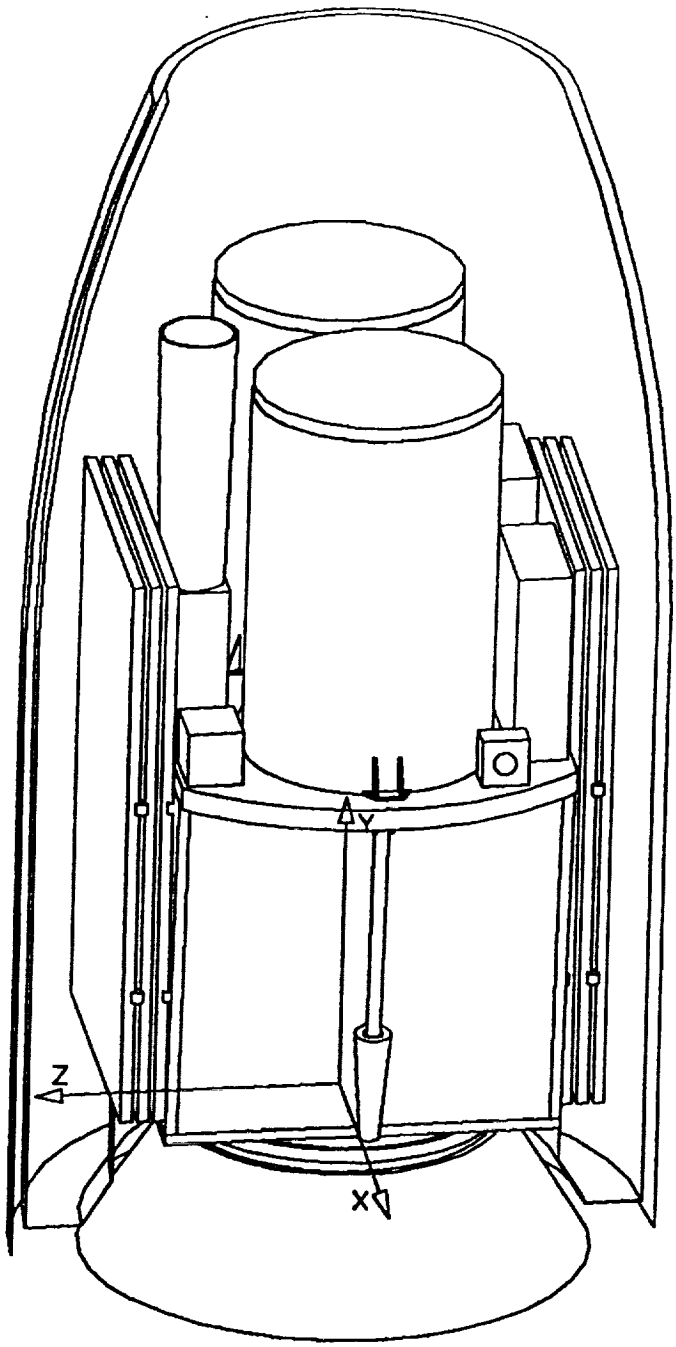


Figure B.4.1 - Spacecraft launch configuration

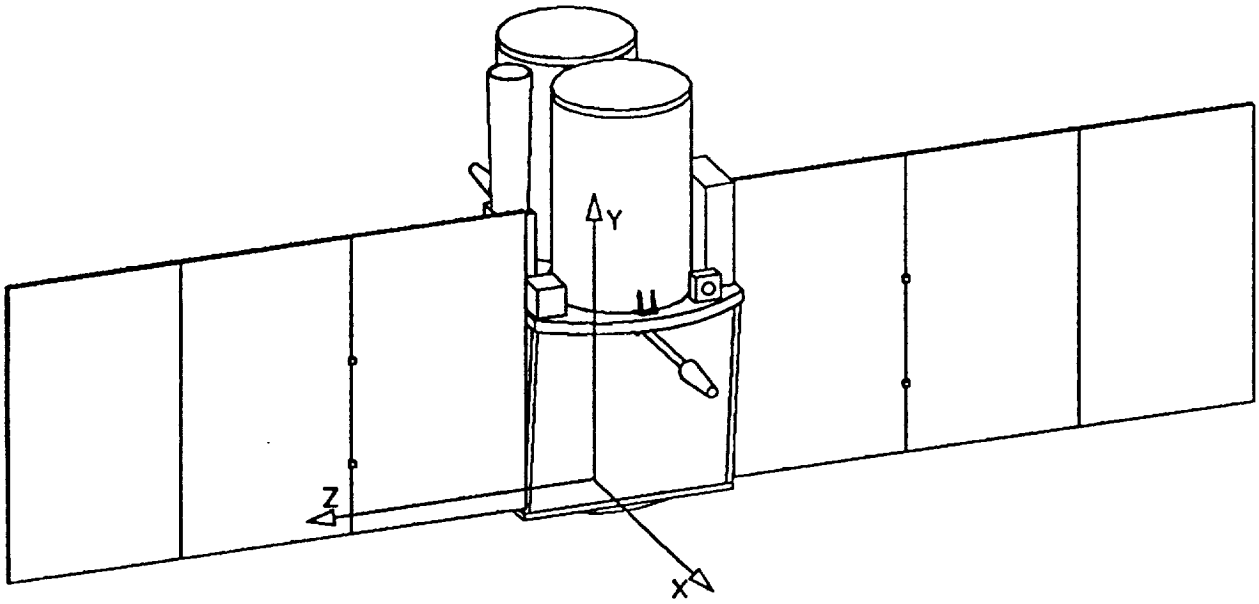


Figure B.4.2 - JUNO flight configuration

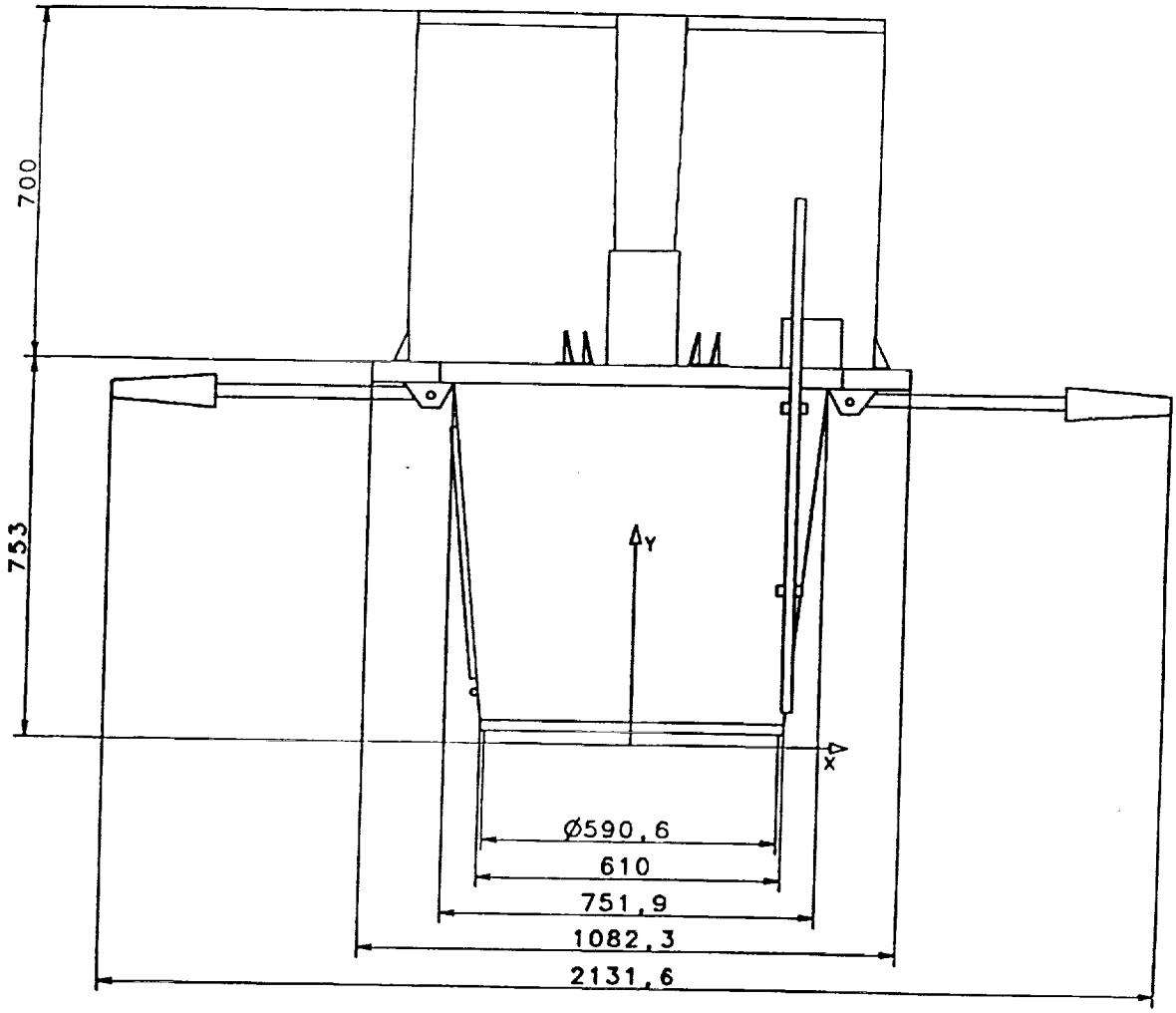


(a)

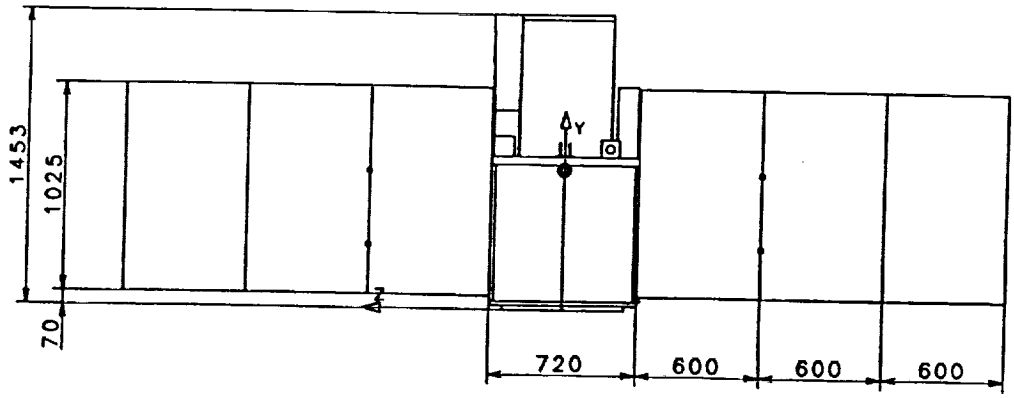


(b)

Figure B.4.3 - Spacecraft dimensions (mm)

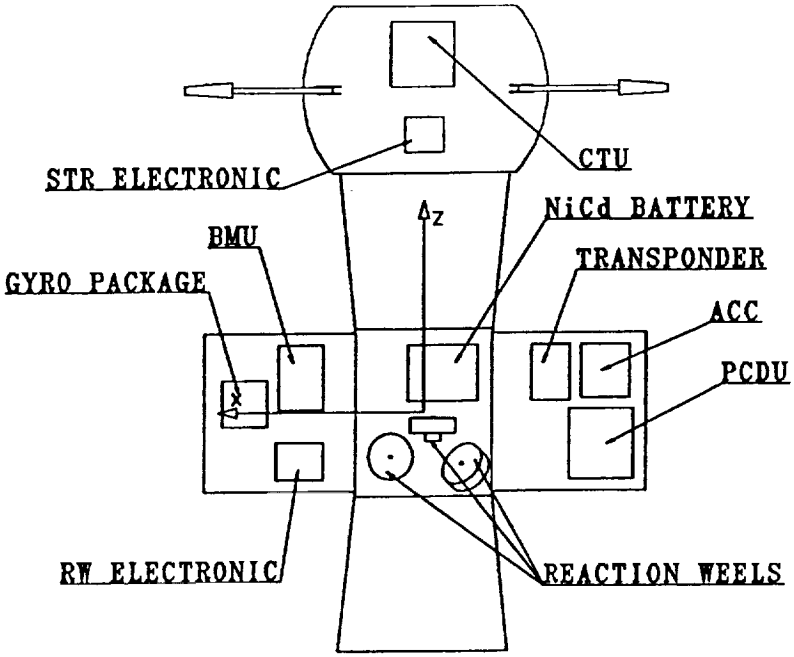


Figure B.4.4 - Unfolded view of the internal boxes accommodation

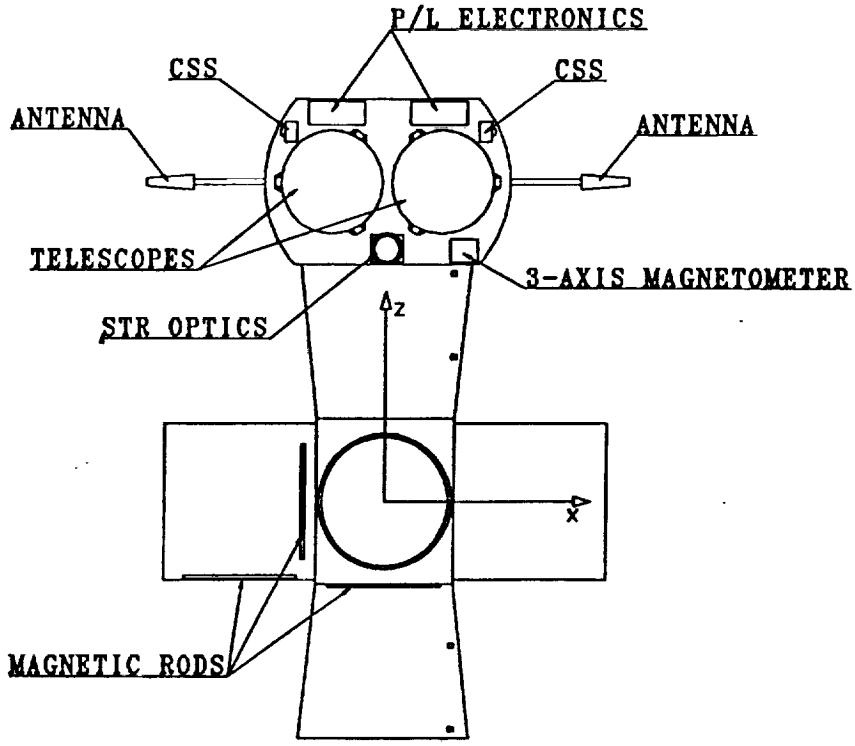


Figure B.4.5 - Unfolded view of the external boxes accommodation

Table B.4.1 - Spacecraft center of mass coordinates and moment of inertia

| | Launch Configuration | On-orbit Configuration |
|---|---|---|
| $X_{cm}$ | −16 mm | 14 mm |
| $Y_{cm}$ | 593.7 mm | 591 mm |
| $Z_{cm}$ | 15 mm | 15 mm |
| $I_{xx}$ | 31.2 kg*m$^2$ | 51 kg*m$^2$ |
| $I_{yy}$ | 44.9 kg*m$^2$ | 75.3 kg*m$^2$ |
| $I_{zz}$ | 50.1 kg*m$^2$ | 89.6 kg*m$^2$ |

A 3-D internal box layout is shown in figure B.4.6. Spacecraft balancing criteria have been taken into account in the design of the box accommodation layout.

The spacecraft center of mass coordinates and the moment of inertia values with respect to the center of mass are shown in table B.4.1.

The 594 mm CM distance from the separation plane ($Y_{cm}$) is well below the maximum distance limit imposed by the Pegasus launcher for a 290 kg spacecraft (850 mm).

## B.5. Structure Sybsystem

The main structural elements, as showed in fig. B.5.1, are:

1. – an adapter ring (PAF) made of aluminum alloy, which is the interface between the launcher and the spacecraft. The ring has a diameter of 59 cm to mate with the standard 23″ Pegasus payload attach fitting.
2. – a bottom plate on which are attached the adapter ring and part of the subsystems. As the loads of the whole structure are distributed, through the lateral panels to the bottom plate, higher material strength will be required in parts of the panels. During the definition phase we will select aluminum honeycomb of higher density in the more stressed areas, namely the panels connections points, to ensure:
   – an optimum load path from the lateral panels, through the bottom plate, to the adapter ring .
   – a good shear strength of the plate.
3. – four lateral panels connected among them with cleats or corner bars.
   a) the ± x panels support part of the Servic Module (S/M) electronics and equipment
   b) the ± z panels have no electronics mounted on them, and they are removable to allow accessibility for the internal equipments integration.
4. – a top platform stiff enough to minimize misalignment among the instruments mounted on it. Some strength requirements could be given by the relative high telescopes mass,

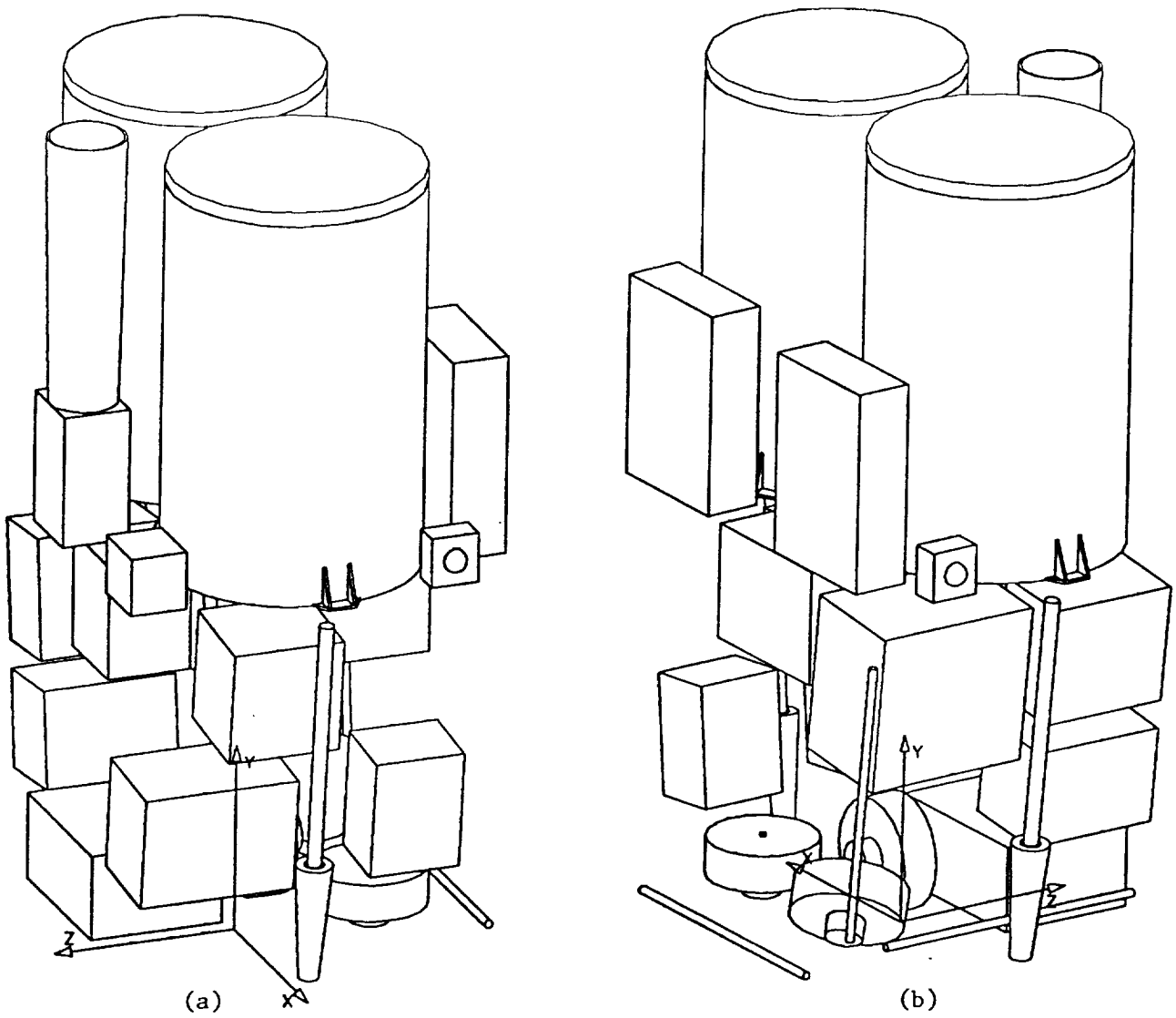


Figure B.4.6 - Internal boxes 3-D lay-out

under the effects of shock and random vibrations, so that it may be desirable to reinforce the honeycomb core in the proximity of the spacecraft interface points.

All the panels are sandwich structures with both core and skins made of aluminium alloy. We have chosen the aluminium, which is very easy to manufacture, low cost, and low-outgassing, for all the main structural elements (skins and cores) instead of some other advanced and lighter composite materials, such as Carbon Fibre. For our small structure, the possible weight saving would be negligible compared to their manufacturing complexity and cost.

The main structural elements have been dimensioned to withstand the Pegasus Launch requirements defined in the SMEX AO (appendix A).
Launch dynamic requirement:

- Lateral frequency $f > 20$ Hz

Launch maximum static loads requirements:

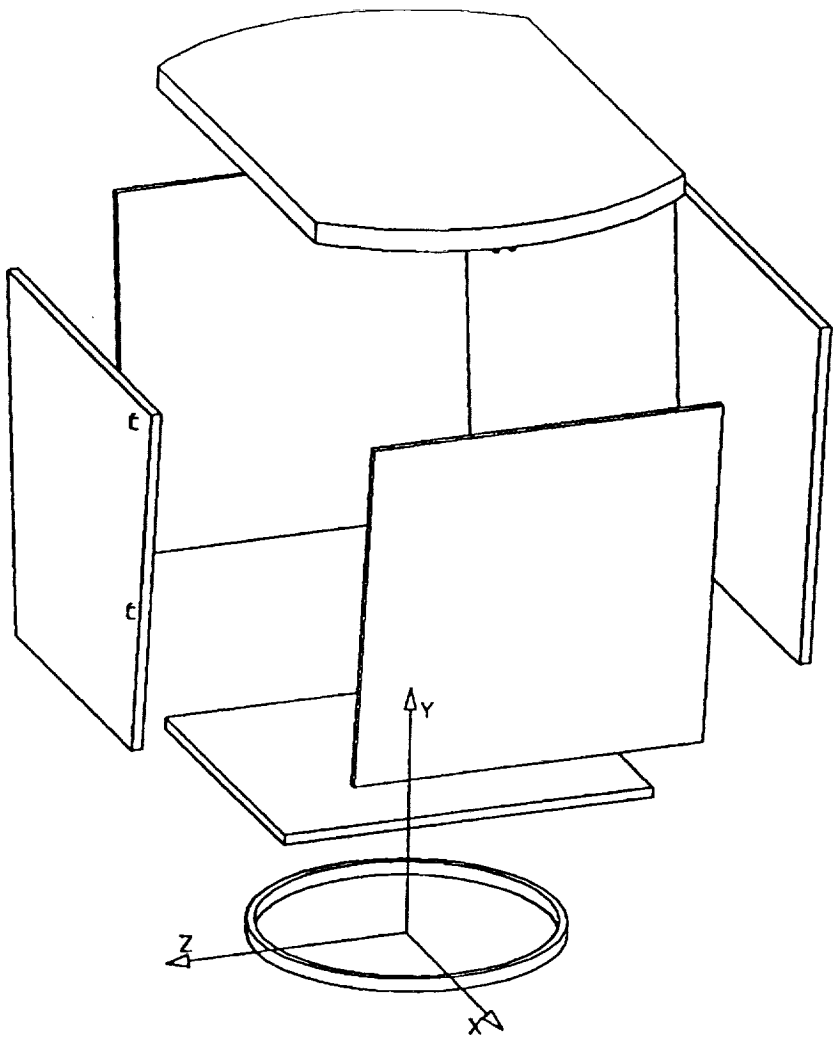


Fig. B.5.1 - Satellite primary structure

- axial = 10 g
- vertical = ± 6 g
- horizontal = ± 1.5 g

The Pegasus dynamic lateral frequency requirement has been multiplied by a 15%, a usual safety factor used in space applications, requiring a lateral payload frequency of 23 Hz.

Comparing the above Pegasus requirements, we made the hypothesis supported by simulations reported below, that the high lateral frequency of 23 Hz had the major impact on the structure design and, as a consequence, the stiffness of the structure was considered as the driving requirement.

Table B.5.1 - Structural elements characteristics

| Str. Elements | Skins [m] | Core [m] | Weight [kg] |
|---|---|---|---|
| P A F | – | – | 4.0 |
| Bottom Plate | 0.001 | 0.050 | 3.2 |
| ± Z Panels | 0.001 | 0.050 | 2.0 |
| ± X Panels | 0.001 | 0.040 | 2.5 |
| Top Platform | 0.001 | 0.060 | 4.2 |

In addition each panel supporting the electronic equipments has been dimensioned for a first mode lateral frequency above 50 Hz, as usual in many aerospace applications.

The static loads requirements represent the worst conditions, in the axial vertical and horizontal directions, that the Pegasus payload will experience during the different events foreseen for Pegasus launch: captive flight, drop transient, aerodynamic pull-up, stage burnout and abort landing.

A NASTRAN dynamic analysis has been performed to verify that with the identified panel thickness (see table B.5.1), the dynamic requirements are fulfilled. Also a NASTRAN static analysis has been performed to verify the capability of the identified primary structure to withstand the static launch loads.

The following analysis conclusions can be highlighted:

- the 23 Hz lateral frequency requirement imposed by Pegasus is accomplished so that there is no dynamic coupling between the satellite and the launcher
- the structural panels have large static safety margins, confirming that the stiffness requirements are dimensioning for the structure, as hypothesized above.

The identified structural weight of table B.5.1 has been increased by a 30% factor, in the JUNO mass budget, to take into account of:

- all probable local density and thickness increments of the honeycomb core, as mentioned in the previous paragraphs
- the uncertainties of the finite element model.

## B.6. Thermal Control Subsystem

Thermal control is important to instrument and electronic box performance; the temperature must to be maintained within a certain range and stability level in order to assure the correct behaviour of the equipment.

The acceptable subsystem units working temperature ranges are:

- electronics $-10°C \Leftrightarrow 40°C$
- batteries $0°C \Leftrightarrow 25°C$
- structure $-30°C \Leftrightarrow 60°C$

As design margins has been assumed:

- 5°C at lower limit of temperature requirement
- 10°C at upper limit of temperature requirement

Considering the reference orbit and the satellite characteristics a purely passive thermal subsystem should comply with the temperature requirements.

*Service Module Thermal Design*

The Service Module (S/M) external panels are wrapped by Multi Layer Insulation (MLI kapton space side: $\alpha = 0.35$ Beginning-of-Life (BOL), $\alpha = 0.4$ End-of-Life (EOL), $\epsilon = 0.65$) except some radiative areas, that are necessary to dissipate the internal electronics heat.

The radiative surfaces have the following area and locations:

- 0.12 $m^2$ on -X panel
- 0.2 $m^2$ on bottom platform panel.

In order to maximize their efficiency all these areas are covered by Optical Solar Reflector (OSR UVS3 $\alpha = 0.06$ BOL, $\alpha = 0.11$ EOL, $\epsilon = 0.80$ m=0.5 $Kg/m^2$). Internally the Service Module should be black painted (PU1 $\epsilon = 0.9$ m=0.08 $kg/m^2$) in order to make uniform the internal environment temperature.

All the internal electronics are mounted on the SVM panels; the electronics/panels conductivity is increased by inserting thermal filler at mounting interfaces. The NiCd battery has been decoupled from the environment by wrapping it by an aluminized ($\epsilon = 0.05$) MLI and its thermal control has been achieved by a radiative areas of 0.0875 $m^2$ (included in the 0.2 $m^2$ radiative surface on the bottom platform.

No heaters are foreseen in the present preliminary SVM thermal model but a power of 6 watts has been allocated in the JUNO power budget for possible SVM internal heaters.

*Payload Electronics Thermal Control*

The lower thermal limit of the Payload electronics boxes mounted externally on the top platform should be guaranteed by wrapping them with Multi-Layer Insulation (MLI) (Kapton on space side $\alpha = 0.35$ BOL $\alpha = 0.40$ EOL, $\epsilon = 0.65$ m=0.6 $Kg/m^2$) and using heaters.

The rejection to space of their dissipation heat in hot conditions has been obtained coupling them conductively with a dedicated radiator (Area=0.09 $m^2$) on the $-Z$ side.

The temperature of the SVM top platform is strongly dependant on the electronic boxes working temperature, so, in order to reduce the telescope thermal gradients and shifts,, the electrical and mechanical interfaces between the telescopes and the top platform must be designed to minimize heat leak toward the telescopes: for example inserting at mounting interface fibrous insulations or Mylar polyester films.

*Analyzed Cases and Results*

The reference orbit has been analyzed with three different attitudes in order to identify the worst cases for both hot and cold thermal loads. The thermal transient analysis has been performed with the ESATAN software. The following thermal conditions have been analysed:

- Sun in the XY plane at +45° w.r.t. +X axis: hot case for the SVM top Platform (winter solstice, thermo-optical properties EOL)
- Sun along +X direction: hot case for the Telescopes (winter solstice, thermo-optical properties EOL)
- Sun in the XY plane at −45° w.r.t. +X axis: cold case for the telescopes and the top platform (summer solstice, thermooptical properties BOL).

The first and third cases are representative respectively of the maximum hot and cold conditions.

The maximum and minimum level of the temperatures in one orbit for the different principal electronics and for the SVM external panels are shown in the tables B.6.1, B.6.2 and B.6.3.

The analysis results show that the acceptable temperature range requirements are fulfilled with the identified thermal control design.

## B.7. Attitude Determination and Control Subsystem

The Attitude Determination and Control Subsystem (ADCS) must measure and control the spacecraft attitude during both the initial phase and the operative phases; in particular, it must guarantee the required level of telescope pointing accuracy and of on-ground attitude reconstruction accuracy.

*Pointing Accuracy*

The main attitude requirements, the ADCS must accomplish about the direction perpendicular to the telescopes line of sight (pitch and yaw direction), are:

- absolute pointing error $\leq$ 10 arcmin
- attitude reconstruction error $\leq$ 3 arcsec (1 $\sigma$ of probability level) with an error drift

Cold Case for Service Module Top Platform
Electronics inside the Service Module

| | Batteries | PCDU | CTU | Reaction Wheels Electronic | Gyro Electronic | Transponder |
|---|---|---|---|---|---|---|
| t MAX [°C] | 10.5 | 10.3 | 5.5 | 14.5 | 14.4 | 10.0 |
| t MIN [°C] | 7.0 | 8.6 | 4.6 | 13.8 | 13.8 | 8.2 |

Hot Case for Service Module Top Platform
Electronics inside the Service Module

| | Batteries | PCDU | CTU | Reaction Wheels Electronic | Gyro Electronic | Transponder |
|---|---|---|---|---|---|---|
| t MAX [°C] | 12.3 | 16.2 | 12.0 | 19.4 | 19.4 | 14.8 |
| t MIN [°C] | 9.4 | 15.1 | 11.1 | 18.4 | 18.5 | 12.9 |

Table B.6.1 - Internal boxes temperature range in one orbit for the hot and cold thermal cases

Cold Case for Service Module Top Platform and Telescopes

| | Top Platform | Bottom Platform | Lateral Platform +X | Lateral Platform -Z | Lateral Platform -X | Lateral Platform +Z |
|---|---|---|---|---|---|---|
| t MAX [°C] | 5.7 | 13.0 | 11.1 | 10.2 | 8.7 | 14.5 |
| t MIN [°C] | 4.4 | 11.8 | 10.0 | 8.5 | 8.0 | 13.7 |

Hot Case for Service Module Top Platform

| | Top Platform | Bottom Platform | Lateral Platform +X | Lateral Platform -Z | Lateral Platform -X | Lateral Platform +Z |
|---|---|---|---|---|---|---|
| t MAX [°C] | 12.5 | 16.3 | 16.3 | 15.0 | 13.7 | 19.3 |
| t MIN [°C] | 11.6 | 15.4 | 15.1 | 13.2 | 12.8 | 18.4 |

Table B.6.2 - External panels temperature range in one orbit for the hot and cold thermal cases

Cold Case for SVM Top Platform
Electronics on Top Platform

| | PLM Electronics |
|---|---|
| t MAX [°C] | -1.5 |
| t MIN [°C] | -2.2 |

Hot Case for SVM Top Platform
Electronics on Top Platform

| | PLM Electronics |
|---|---|
| t MAX [°C] | 21.1 |
| t MIN [°C] | 20.3 |

Table B.6.3 - External boxes temperature range in one orbit for the hot and cold thermal cases

rate $< 5$ arcsec/sec

The telescope absolute pointing error is the total angular error with respect to the desired telescope pointing; it is due to the following error sources acting at different frequencies:

- attitude measurement and control systematic errors (sensors and actuator bias)
- sensors and actuators noise and structural high frequency vibration (short term errors)
- thermo-elastic and aging deformations of the attitude sensors/telescope structural chain (respectively medium and long term errors)

Most of these errors sources effects can be removed by suitable attitude sensors/telescope calibrations to be performed periodically.

The 10 arcmin absolute pointing error requirement is quite loose considering the following: are accounted for:

- the satellite has a compact and stiff configuration from a structural point of view
- the STR is close to the instrument and they are both mounted on the same platform (this reduces the relative deformations).
- the thermal conditions during the observations (always in eclipse) are relatively stable but not entering eclipse
- the identified STR is very accurate.

The attitude measurement accuracy depends on the sensor systematic errors (i.e. random biases), on the relative telescope/sensor pointing drift (mainly thermo-elastic) between two periodic calibrations and on the calibration errors themselves.

The attitude measurement data must be used in real-time by the image compression algorithm; these data come from the on-board attitude estimator which, starting from the raw sensor data, performs the angular and angular rate best estimate. Thus, the attitude state estimator removes from the attitude measurement most of the sensors noise effects.

*Attitude measurements*

The attitude measurement hardware consists of:

- a Gyro Package Unit (GPU)
- a 3-axis magnetometer (MGM)
- 2 Coarse Sun Sensor (CSS)
- 1 Star Tracker (STR)

The Star Tracker is our fine angular measurement sensor; both attitude reconsruction error and absolute pointing error are deeply affected by its performance. We note however that in the event of a tracker failure, stars in the prime data set can be used for ex post facto drift correction (§A.4).

The identified sensor characteristics are shown in the table B.7.1.

Table B.7.1 - Attitude Sensors Characteristics

| | |
|---|---|
| Two-axis Star Tracker (STR) sensor: | |
| • FOV | $3 \times 4$ deg. |
| • Sensitivity | up to magnitude 8 |
| • number of stars trackable at the same time | up to 5 |
| • Bias | 1.1 arcsec ($1\sigma$) |
| • Noise | 1.65 arcsec ($1\sigma$) |
| Gyro Package Unit (GPU) | |
| • gyro random drift | 0.03 deg/hr/hr ($1\sigma$) |
| • gyro rate noise | 2.2 arcsec/sec ($1\sigma$) |
| Course Sun Sensor (CSS) | |
| • FOV | $160 \times 160$ deg |
| • accuracy | $\approx 1$ deg |
| Magnetometer (MGM) | |
| • range | $\pm$ 400 $\mu$ Tesla |
| • accuracy | 0.6 deg |

The STR must perform the angular measurements about pitch and yaw directions and also about roll direction. To perform roll angular measurement at least two stars must be detectable in the STR Field-of-View (FOV).

The roll measurement accuracy is proportional to the angular separation between the two stars which is anyway limited by the STR Field-of-View (FOV). With the identified STR, an angular separation between the stars of 2 deg allows to achieve a roll measurement accuracy of about 1 arcmin.

Because of the spacecraft cost limit a second spare STR is not foreseen in the present design. The STR has an intrinsic high reliability (97.5%), and the telescope science data provides a backup!

The GPU consists of four gyros (one for each axis and the fourth for redundancy). In the baseline attitude determination mode both the STR, for angular measurements, and the GPU, for angular rate measurements are continuously used; the two sensors data are filtered through an attitude state estimator. The estimated attitude data is then provided to the attitude control loop. The GPU must be frequently updated with the STR data. During the STR occultation by the earth, the attitude determination relies completely on

the GPU measures.

The MGM and the CSSs have low accuracy but thanks to their intrinsic simplicity are used for many different purposes (see the mission operations section):

- initial attitude acquisition
- magnetic field measurement (for magnetic rods working)
- sun tracking also in nominal mode.
- attitude anomaly detection
- attitude determination in the safe mode

*Attitude Control*

The ADCS command unit and actuators are:

- 1 Attitude Control Computer (ACC)
- 3 Reaction Wheels (RW)
- 3 Magneto-torquers (MGT).

The ACC is the ADCS control computer with real-time data handling capabilities. It communicates with the sensors and actuators through a dedicated ADCS bus and it hosts the attitude determination and control software.

The identified RWs can exert a maximum torque of 0.2 Nm and can store angular momentum up to 2.2 Nms. Three RWs are required for a complete 3-axis control. The MGTs provide a magnetic moment of 30 $Am^2$. Each MGT is internally redundant.

The JUNO attitude control scheme is based on a traditional approach. The identified control loop block diagram is shown in figure B.7.1.

*Control strategy*

For the three RWs provide an accurate attitude control, they have to perform the following tasks:

- to guarantee the slow scan rate (about $X$ and $Y$ axes) required during the observations
- to counteract the external perturbing torques
- to exert the required torques to perform the attitude manoeuvres to acquire new targets.

The RW lay-out is shown in the figure B.7.2. The first wheel is aligned along the $Y$-axes, the second wheel is aligned along the $Z$-axes and the third one is at an angle of 45° with respect to the $X$ asix with equal $Y$ and $Z$ components.

The orientation of the RWs facilitate torque exertion and accumulation of angular momentum about any direction. The magnetic torquers would be used, in normal working mode, only to unload the accumulated wheel momentum. The RWs unloading could be conveniently performed during the orbital day when observations are never performed and the solar panels can provide the required extra power.

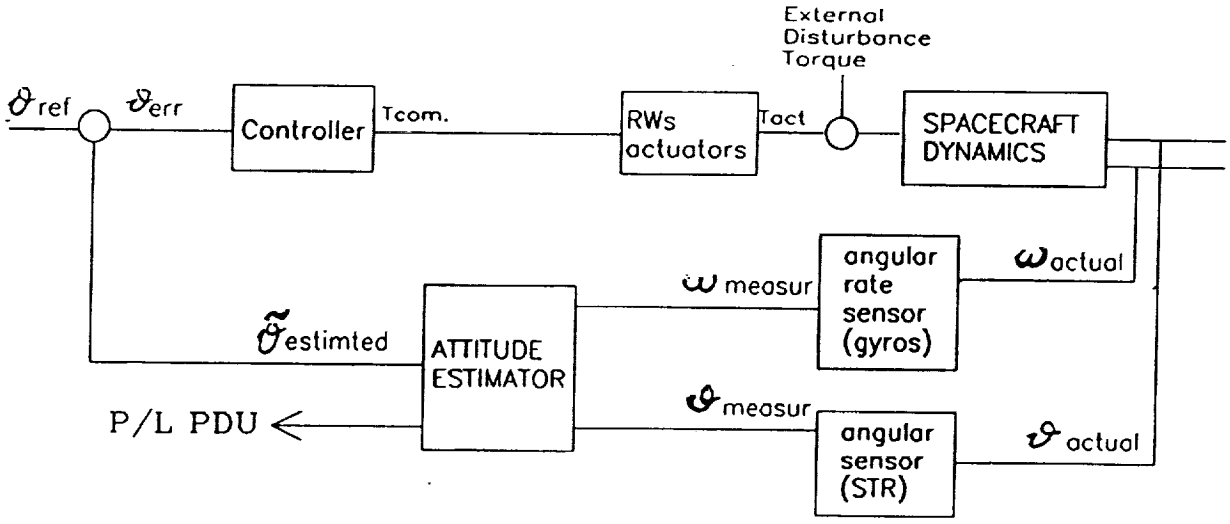


Figure B.7.1 - Attitude control loop block diagram

The satellite may still be controlled after the loss of one RW. In this case the magnetic torquers could be used also as direct actuators (together with the two surviving wheels). With the MGTs (generating torques in a plane perpendicular to the magnetic field direction) and 1 or 2 RWs generating torques about their spin axes, it is still possible to provide torques about any direction. It must be pointed out that torques about the magnetic field direction ($\vec{B}$) cannot be provided if the RWs torques are just perpendicular to the magnetic field direction itself. This condition must be avoided. For this reason the RWs orientation has been chosen in such a way for any possible wheel failure the mentioned critical condition never occurs as explained below.

The unloading of RW momentum using the MGTs requires a particular strategy because the MGTs cannot provide torques about any direction but only in a plane having a normal that is perpendicular to $B$. During an orbit, $B$ changes continuously describing a cone of 21 deg (half cone angle) in the spacecraft reference system. Considering the MGTs control limits described above and the equatorial orbit chosen for JUNO it could be particularly difficult to unload the component $H^{\perp}$, of the accumulated angular momentum, along the orbital plane perpendicular direction (that is the magnetic field average direction). The $H^{\perp}$ component can be completely unloaded by activating the MGTs to induce angular momentum accumulation about a direction perpendicular to $H^{\perp}$; this second angular momentum component can be stored by the wheels and unloaded when B has reached a favourable direction (see figure B.7.3).

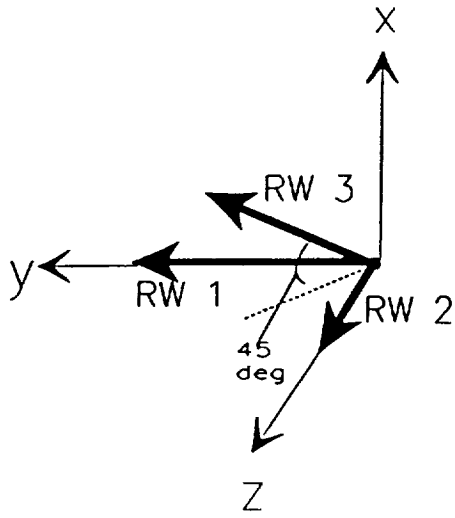


Figure B.7.2 - Reaction Wheels configuration

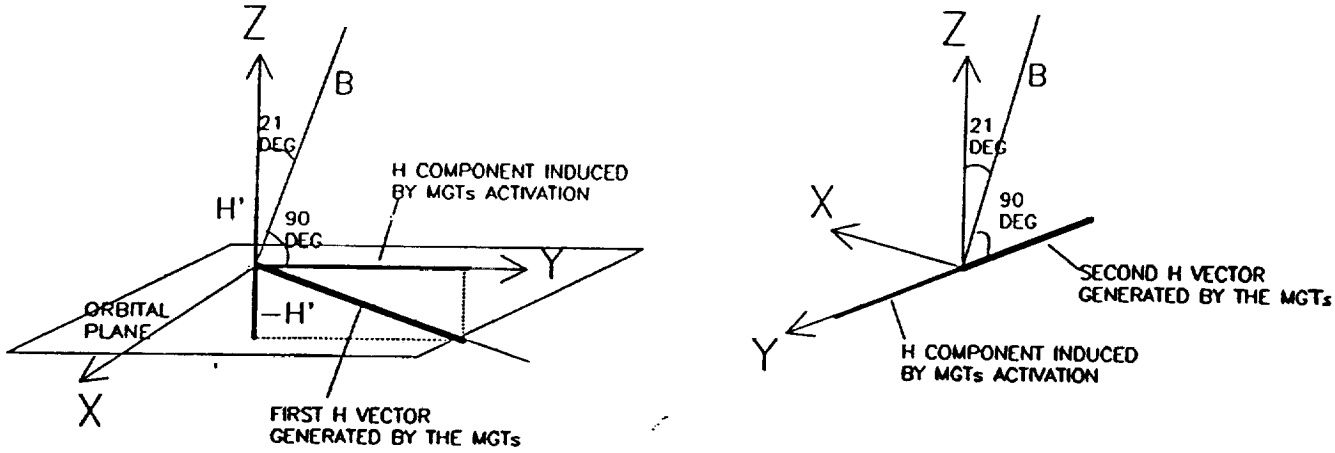


Figure B.7.3 - $H^{\perp}$ component unloading strategy.

*Actuator Dimensioning*

The RW dimensions must be chosen taking into account both the angular momentum accumulated for the external perturbing torques and the angular momentum induced by

the $H^{\perp}$ component unloading.

The MGT dimension have been chosen taking into account the maximum angular momentum to be unloaded and also of a reasonable unloading maneuver duration.

Simulations have been performed to evaluate the level of perturbing torques experienced by the spacecraft during an orbit. To compute the total external perturbing torques the following effects have been taken into account:

- air drag
- gravity gradient
- solar pressure
- magnetic interaction of the spacecraft residual magnetic moment (0.7 $Am^2$ along Y-axes and 0.2 $Am^2$ for X and Z axis have been assumed) with the Earth field.

In tables B.7.2 and B.7.3 the simulation analysis results are shown. The values of the total perturbing torques and of the total accumulated angular momentum are the maximum ones among the values derived for different analyzed attitudes. The maximum solar activity condition has been considered as the worst case for atmospheric drag.

To assess the total torques and angular momentum, also the acceleration/deceleration torques and angular momentum excursion required by the slew maneuvers should be considered, but fast slews are not required and therefore these manoeuvres have a marginal influence in the RWs dimensioning.

Even if very long slew manoeuvres had to be performed to acquire new targets (deep survey and spectroscopic phases), they could be performed in the long orbital stand-by period (61 minutes) and therefore the actual angular momentum excursion would be rather low. If, for example, we assume a 180 deg slew about $X$ axes in 55 minutes (6 minutes are allocated for the settling time) an angular momentum excursion of only 0.085 Nms needs to be temporarily stored by the reaction wheels.

The maximum perturbing torques and accumulated angular momentum is well below the performance of the identified RWs and there would be still a large margin, if required, fast slew maneuvers.

Due to the JUNO compact and well balanced configuration (low differences between the axial moments of inertia and the center of pressure very close to the center of mass), the external perturbing torque and accumulated angular momentum are very low. Moreover the angular momentum component is not affected by the gravity gradient effect; in fact, for a circular orbit, the accumulated angular momentum component along the out-of-orbital-plane direction is zero.

Considering the wheels skewed configuration the maximum torques and angular momentum the wheels can exert and store are, in the spacecraft reference frame:

- $T_x = 0.14$ Nm, $H_x = 1.55$ Nms

Table B.7.2 - Maximum orbital perturbing torques

| | $T_x$ (Nm) | $T_y$ (Nm) | $T_z$ (Nm) |
|---|---|---|---|
| Total Torque | 2.8 e-5 | 7.3e-5 | 9.5e-5 |

**Table B.7.3 - Total accumulated angular momentum over one orbit**

| | $H_x$ (Nms) | $H_y$ (Nms) | $H_z$ (Nms) |
|---|---|---|---|
| H' (*) | 0.07 | 0.06 | 0.1 |
| H'' (**) | 0.13 | 0.13 | 0.14 |
| Total H | 0.2 | 0.19 | 0.24 |

(*) maximum angular momentum due to the environmental disturbance torques.
(**) angular momentum induced during the angular component unloading.

- $T_y$ = 0.2 Nm, $H_y$ = 2.2 Nms
- $T_z$ = 0.2 Nm, $H_z$ = 2.2 Nms

Even though the wheels could accumulate angular momentum for several orbits (up to about 7) the RWs unloading manoeuvre must be often performed (typically once per orbit in orbital day); this unloading approach has the advantage of preventing high wheel speed and allowing performances of the attitude control and wheel unloading operation in a smoother way with small MGTs.

Considering the low level of angular momentum accumulated over one orbit, MGTs having a low magnetic moment (10 $Am^2$) would be sufficient to perform a wheel desaturation in about 24 minutes (about any axis); nevertheless in order to have a margin on the storable angular momentum and to shorten the unloading manoeuvre duration 30 $Am^2$ MGTs have been used in the baseline configuration.

### B.8. Power Subsystem

The power subsystem is charged to provide and distribute power to the other subsystems and to the payload both in daylight and in night-time phase. The power subsystem will be designed in accordance to the ESA standard on electromagnetic compatibility requirements for space systems.

The power subsystem consists of:

- two deployable solar panels
- one NiCd battery
- a Power Control and Distribution Unit (PCDU)
- a Battery Monitoring Unit (BMU) including a Battery Discharge Regulator (BDR),
- a Battery Charge Regulator (BCR) and a Battery Control Electronics (BCE).

The PCDU power control provides to the solar panels (through the shunt), power distribution to the loads, power line switching and protection against short circuits.

The power system electrical architecture is shown in figure B.8.1

A dedicated solar panel section is used for battery charging at higher voltage (50 VDC) than the main section Voltage (30.5 VDC); this approach allow the use of a step down mode for the BDR. This mode has good efficiency (about 0.88).

The main power bus is regulated to a voltage of 28 Volt +/- 2%. The solar arrays panels and the battery sizes are based on the spacecraft power requirements in sunlight and in eclipse condition.

The solar array must provide power for the spacecraft working in sun-light phase and for battery charging. In order not to oversize the solar panels the peak power is provided by the battery.

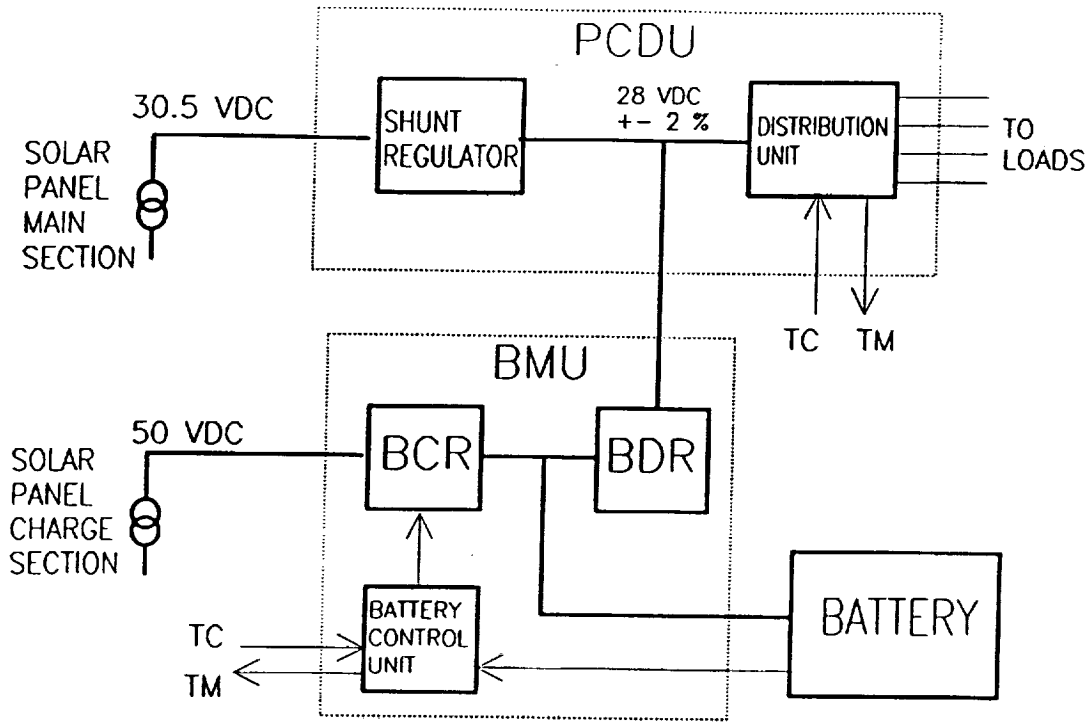


Figure B.8.1 - JUNO ELECTRICAL ARCHITECTURE

On the basis of the chosen hardware power consumption (see budget table 11.2) an estimation of the total spacecraft requested power in the different operating modes has been done:

- initial acquisition phase = 121.2 W
- sun-light phase ( 61.4 min.) = 176.4 W
- eclipse phase (35 min.) = 233.6 W
- average = 197.3 W.

All these values include a contingency of 20%.

The transmitter peak power (20 W for about 10 minutes) is included in the eclipse phase power budget as well as the sunlit phase because some fraction of the downlinks will occur during eclipse phase.

The battery and solar panels sizes are based upon realistic parameters. The battery, BDR and solar arrays principal characteristics are:

- BDR efficiency = 0.88

- Battery Depth Of Discharge (DOD) = 20%
- GaAs cells efficiency = 19%
- Solar panels filling factor = 0.88
- GaAs cells temperature degradation factor = 0.85
- GaAS cells aging degradation factor (for 2 years) = 0.95
- Other GaAs cells degradation factor (cabling losses, cells mismatch, etc ) = 0.95
- Cosine loss = $\cos 45° = .71$
- Solar constant (minimum) = 1326 W/m$^2$

A DOD of 20% is a realistic and conservative assumption for a NiCd battery flying in LEO for 2 years (about 11000 cycles).

The required energy to the battery is 155 Wh. To guarantee this level of energy in eclipse 29 cells with a capacity of 22 Ah each are required (battery capacity = 774 Wh). For redundancy reasons one or more cells are added to the cells strictly necessary for power provision; a 32 cell battery should then weigh about 24 kg.

Taking into account all the degradation factors and the GaAS cell efficiency the achievable GaAS solar panel performance is 120 W/m$^2$. The power required by the solar panels is of 431 Watt. A solar panels area of 3.6 m$^2$ can then provide the required power

We point out that thanks to the high battery capacity, the power provision during the spacecraft initial phase (when the solar panels are not working yet) is not a critical constraint.

## B.9. TELEMETRY TRACKING AND COMMAND

In agreement with the JUNO payload preliminary telemetry requirements, the TTC subsystem design is based on the following assumptions and requirements:

Data transmission in S-band; 2025-2125 Mhz for Telecommand and 2200-2290 Mhz for telemetry and tracking

- the ground station choosen for the elaboration of the link budget is the Malindi station. (longitude E 40 19″ – 3 0″). In an equatorial orbit one ground contact for each orbit is available.
- The communications with the ground station are based on the ESA (European Space Agency) Packet Telecommand and Telemetry Standard.
- the radio frequency interconnections coupling and switching between the antenna system and the transponders have been evaluated in agreement with the ESA requirements.
- the antenna has been assumed a cardioid type with a gain of −4 dB. This value includes the interference due to the metallic spacecraft structure with the antenna radiation pattern.
- the uplink telecommand data rate has been supposed of 2 kbps.
- the down-link house-keeping telemetry data rate has been supposed of 2 kbps.

The required payload telemetry data rate is about 3 Mbps for a 600 Km orbit the ground link time, above the assumed elevation lower limit of 5 deg, is of order 10.6 minutes.

Taking into account of the other telecommunications activities (carrier tracking telemetry synchronisation, etc.) 9 minutes are assumed available for telemetry.

The estimated observations data are 1.5 Gbits per orbit; these data must then be downlinked in 9 minutes. Considering a 5% of data margin to take into account of data formatting for telemetry and including the spacecraft and house-keeping data rates, the total telemetry data rate is 2.92 Mbps.

The ground visibility time slightly decreases as the orbital altitude decreases during the satellite lifetime; therefore, for a worst case launch date (year 2000, maximum solar activity), the telemetry available time, at the end of lifetime, is not sufficient to downlink all the 1.5 Gbits data per orbit. This slight reduction in effective telemetry rate can be accepted in the last two observation phases (deep survey and spectroscopic).

The minimum ground link time at end of life is, for a launch in the year 2000, 9 minutes (perigee altitude = 475 km); this correspond to a downlink capability of 1.33 G bits data per orbit. (For all evaluations of scientific performance, we have assumed 1.26 Gbits/orbit.)

The identified Telemetry & Telecommand Control (TTC) fixed antennas must guarantee a omni-directional coverage. Two cardioid antennas seem suitable for our purposes. An almost full spherical coverage is allowed with the identified antennas accommodation (see the configuration chapter).

To guarantee the required high data rate for telemetry a high performance transponder has been considered in the baseline TTC configuration. The identified transponder has the capability to handle up to 3 Mbps of data rate. If required this transponder could also transmit data through the TDRS (in Ku-band).

The transponder can operate either in noncoherent mode by using a local oscillator, or in coherent mode with a turnaround frequency of 240/221. In coherent mode it is possible to measure the ranging and the range rate.

*Radio frequency budget*

A preliminary link budget has been evaluated with 2.5 W radio frequency output power. The main assumptions and results are shown below:

| | |
|---|---|
| altitude: | 600 Km |
| elev. angle: | 5° |
| telecommand rate | 2 kbps |
| telemetry rate | 2920 kbps |
| coding: | no |
| telem. mod index | 1.13 radpk |
| ranging | 0.60 radpk |

| | | Nominal (NOM) | Worst-Case (ADV) | Best-Case (FAV) |
|---|---|---|---|---|
| Malindi Station: | | | | |
| Tx/Rx ant. gain | dBi | 44.0 | 44.0 | 44.0 |
| EIRP | dBW | 68.9 | 68.9 | 68.9 |
| Tx ant axial ratio | dB | 1.0 | 1.4 | 0.6 |
| Rx ant axial ratio | dB | 0.3 | 0.9 | 0.0 |
| System noise | dBK | 21.3 | 21.3 | 21.3 |
| Spacecraft: | | | | |
| Tx/Rx ant. gain | dBi | −3.0 | −4.0 | −2.5 |
| Tx ant axial ratio | dB | 3.0 | 7.0 | 2.0 |
| Rx ant axial ratio | dB | 3.0 | 7.0 | 2.0 |
| ant noise temp | K | 240.0 | 280.0 | 200.0 |
| cable phys. temp | K | 330.0 | 383.0 | 280.0 |
| circuits temp. | K | 290.0 | 330.0 | 240.0 |
| VSWR losses | dB | 1.3 | 1.6 | 1.2 |
| RFDU losses | dB | 0.2 | 0.2 | 0.2 |
| Diplexer losses | dB | 0.5 | 0.7 | 0.3 |
| Cable attenuat. | dB | 1.0 | 1.5 | 0.75 |
| S/C EIRP | dBW | −1.34 | −3.34 | −0.24 |
| Uplink margin | | | | |
| Rx S/No | dBHz | 99.76 | 96.15 | 101.83 |
| carrier rec. marg. | dB | 53.44 | 47.99 | 56.96 |
| telecom. rec. marg | dB | 45.31 | 40.03 | 48.41 |
| Downlink margin | | | | |
| PFD telem. margin | dB | 22.13 | 20.16 | 25.33 |
| carrier rec. marg. | dB | 17.03 | 10.11 | 21.75 |
| telem. rec. marg. | dB | 5.65 | 1.24 | 8.08 |



C-2

## B.10. On-Board Data Handling

The On Board Data Handling (OBDH) shall have to provide the following general functions:

- to provide the capability of controlling and operating the satellite with real-time and delayed commands
- to store on-board the spacecraft houskeeping data and to transmit them during the ground contact period
- to perform the on-board data processing function to support all the subsystems and payload working both in nominal and in contingency conditions.

The JUNO data handling architecture is based upon a European standard approach.

The On Board Data Handling is composed of the following equipments:

- a Central Terminal Unit (CTU)
- an ESA (European Space Agency) standard OBDH bus
- ESA standard interfaces (RBI and RTU)

The CTU is the central on-board computer, it acts as the central communication node of the satellite to the ground station and as on-board supervisor of the entire OBDH. It hosts software to perform all the control function required for satellite survival and maintenance (failure detection and recovery) and to plan all the required mission operations. The CTU reliability is high because of a number of internal redundancies

An ESA standard OBDH bus can be composed of by three buses:

- an Interrogation Bus (serial)
- a Response Bus (serial)
- a Block Transfer Bus (16 bit parallel)

The RTU unit interfaces with the not intelligent equipments which are provided only with I/O signals. The RTU main functions are the following:

- distribute commands and data;
- data acquisition;
- distribute clock signals.

A single RTU can provide the following capabilities:

- to distribute from 7 to 28 Memory Load Commands;
- to select one of 128 input lines to acquire analogue or digital;
- to select one of 128 output lines to ON/OFF commands;

For JUNO it may be possible to adopt the simpler and lower cost mini-RTU rather than the RTU. The mini-RTU executes a subset of the operational modes of the RTU; in particular there are only 32 I/O lines with respect to the 128 of the RTU. The RBI interface is

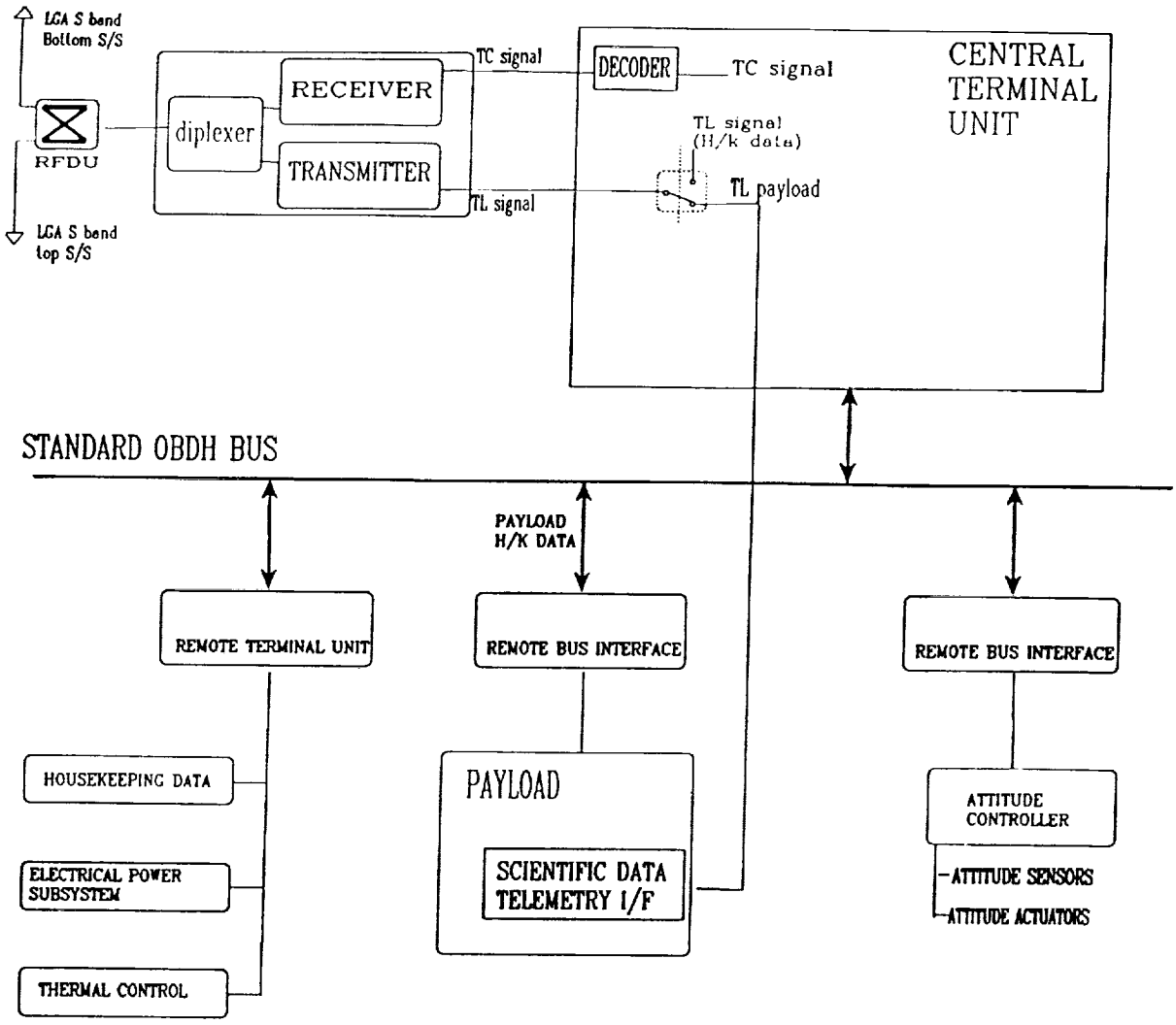


Figure B.10.1 - OBDH electrical Scheme

used with the intelligent equipment. The RBI shall provide a more complex interface with respect to the RTU. The RBI has the following capabilities:

- 16 bits parallel address bus;
- 16 bits bi-directional, parallel data bus;
- it controls and/or handshake signals;
- it provides clocks and flags to the equipments;
- provides the equipments status monitoring

The JUNO OBDH electrical architecture scheme is shown in figure B.10.1

One RTU interfaces the thermal control and power control units to the OBDH bus (to gather housekeeping data and transmit on/off commands).

One RBI connects the ACC to the bus while a second RBI interfaces the payload equipments to transmit/receive houskeeping data and commands.

The very high scientific data rate cannot pass through the standard bus; a dedicated direct

link between the payload mass memory and the transmitter is proposed to allow the high scientific data rate telemetry (up to 3 Mbps) (cf. Appendix D).

The scientific data should be already stored in the payload mass memory in a transmission compatible format so no formating is required by the encoder.

The attitude measurement data required by the payload for image compression, can be provided in real time, to the payload units through the CTU and ESA Standard Bus.

## B.11. Budgets

**Table B.11.1. JUNO MASS BUDGET**

| | Nr | Unitary Mass (kg.) | Total Mass (kg.) | Dimension (CM) | Possible Supplier * |
|---|---|---|---|---|---|
| ADCS SUBSYSTEM: | | | | | |
| ACC | 1 | 7 | 7 | 13 × 23 × 21 | ALENIA / ITALY |
| STR OPTICS | 1 | 3 | 3 | 14 × 23 × 12 | GALILEO / ITALY |
| STR ELECTRONICS | 1 | 3.2 | 3.2 | 20 × 17 × 15 | GALILEO / ITALY |
| CSS | 2 | 0.2 | 0.4 | 9 × 9 × 5 | GALILEO / ITALY |
| 3-AXIS MAGNETOMET. | 1 | 0.8 | 0.8 | 10 × 10 × 12 | SCHONSTEDT |
| GYRO-PACKAGE | 1 | 4.1 | 4.1 | 20 × 20 × 18 | MATRA / FRANCE |
| MAGNETIC RODS | 3 | 1 | 3 | ○ 2 × 50 | FOKKER / NETHERLANDS |
| REACTION WHEELS | 3 | 2.7 | 8.1 | ○ 20 × 7 | TELDIX / GERMANY |
| RW ELECTRONICS | 1 | 3 | 3 | 21 × 16 × 13 | TELDIX / GERMANY |
| **TOTAL** | | | 32.6 | | |
| POWER SUBSYSTEM: | | | | | |
| NiCd BATTERY | 1 | 24 | 24 | 16 × 24 × 31 | FIAR / ITALY |
| GaAs SOLAR ARRAYS | 2 | 9.5 | 19 | 150 × 110 | FIAR, FOKKER |
| PCDU | 1 | 8.1 | 8.1 | 30 × 28 × 20 | FIAR |
| BMU | 1 | 5.9 | 5.9 | 17 × 28 × 20 | FIAR |
| **TOTAL** | | | 57 | | |
| OBDH SUBSYSTEM: | | | | | |
| CTU | 1 | 12 | 12 | 20 × 28 × 28 | LABEN / ITALY |
| RTU | 1 | 2 | 2 | 10 × 10 × 10 | LABEN / ITALY |
| RBI | 2 | 0.3 | 0.6 | Negligible | LABEN / ITALY |
| **TOTAL** | | | 14.6 | | |
| TT&C SUBSYSTEM: | | | | | |
| TRANSPONDER | 1 | 7 | 7 | 19 × 25 × 15 | ALENIA |
| RFDU | 1 | 0.2 | 0.2 | 6.7 × 5.6 × 3.5 | ALENIA |
| ANTENNA | 2 | 0.3 | 0.6 | 6.5 × 6.5 × 26.5 | ERICSON / SWEDEN |
| **TOTAL** | | | 7.8 | | |
| SVM STRUCTURE: | | | | | ALENIA |
| SVM LATERAL PANELS | | | 21.3 | | |
| MECHANIC I/Fs | | | 3 | | |
| BALANCING MASS | | | 2 | | |
| ADAPTER RING | | | 4 | | |
| **TOTAL** | | | 30.3 | | |
| SVM THERMAL CONTR.: | | | 4 | | ALENIA |
| HARNESS MASS: | | | 8 | | |
| PAYLOAD: | | | | | |
| TELESCOPE 1 | 1 | 31 | 35.19 | ○ 45 × 70 | |
| TELESCOPE 2 | 1 | 33 | 40.23 | ○ 45 × 70 | |
| ELECTRONICS BOX | 2 | | 21.3 | 10 × 25 × 35 | |
| **TOTAL** | | | 96.72 | | |
| S/C TOTAL MASS | | | 251.02 | | |
| + MASS CONTING. (%) | | | 15 | | |
| = | | | 288.673 | | |
| MARGIN WRT 290 KG | | | 1.327 | | |

*It must be pointed out that most of the identified equipments has already flown on a number of European satellites. Other equipments as the STR (selected also in some future European porgrams) and the transponder is going to be qualified on the Italian X-ray astronomy satellite SAX, which will be launched at the end of 1995.

**Table B.11.2 – JUNO POWER BUDGET**

| | Acquisition Phase | Eclipse Phase | Sun-Light Phase | |
|---|---|---|---|---|
| ADCS: | | | | |
| ACC | 7 | 7 | 7 | |
| CSS | negligible | | negligible | |
| STR | | 16 | 16 | |
| 3-AXIS MAGNETOMET. | 2 | | 2 | |
| GYRO-PACKAGE | 23 | 23 | 23 | |
| MAGNETIC RODS | 6 | | 6 | |
| RWs + ELECTRONICS | 11 | 11 | 11 | |
| **AOCS TOTAL POWER** | 49 | 57 | 65 | |
| POWER: | | | | |
| PCDU | 10 | 10 | 10 | |
| BMU | 8 | 8 | 8 | |
| **POWER TOTAL POWER** | 18 | 18 | 18 | |
| OBDH: | | | | |
| CTU | 15 | 15 | 15 | |
| RTU | 2.4 | 2.4 | 2.4 | |
| RBI | 0.6 | 0.6 | 0.6 | |
| **OBDH TOTAL MASS** | 18 | 18 | 18 | |
| TT&C: | | | | |
| RECEIVER | 6 | 6 | 6 | |
| TRANSMITTER | | | | 20 (*) |
| **TT&C TOTAL POWER** | 6 | 6 | 6 | 20 (*) |
| SVM THERMAL CONTROL | 6 | 6 | 6 | |
| HARNESS LOSS | 4 | 4 | 4 | |
| **PAYLOAD TOTAL POWER** | | 80 | 30 | |
| **TOTAL POWER CONSUMPTION** | 101 | 189 | 147 | 20 (*) |
| + 20 % OF MARGIN = | 121.2 | 226.8 | 176.4 | 24 (*) |

# APPENDIX C

## Additional Science Objectives

## APPENDIX C. ADDITIONAL SCIENCE OBJECTIVES

In this appendix we highlight additional science investigations that will be undertaken with the JUNO UV surveys. In Table C.1, we summarize the predicted number counts for various object classes in the JUNO surveys.

**Table C.1**
**Estimated Source Counts**

| Type | All-Sky | Spectroscopic | Type | All-Sky | Spectroscopic |
|---|---|---|---|---|---|
| **White Dwarfs** | 300,000 | 6,000 | **Binary Systems** | 7000 | 150 |
| DA | 240,000 | 4800 | Dwarf Novae | 3300 | 70 |
| DB | 33,000 | 700 | AM Her stars | 400 | 8 |
| DO | 10,000 | 200 | Classical Novae | 3200 | 70 |
| DC | 14,000 | 280 | Low Mass X-ray Binaries | 12 | - |
| Eclipsing WD Binaries | 6000 | 120 | Eclipsing CVs | 400 | 10 |
| PNNs | 6000 | 120 | **Active Galaxies** | 130,000 | 2500 |
| PG1159-035 | | | Seyferts/AGN | 25,000 | 500 |
| ZZ Ceti stars | 10,000 | 200 | BL Lacs | 3,000 | 60 |
| | | | QSO | 100,000 | 2,000 |
| **Pre-White Dwarf Stars** | 100,000 | 2000 | **Galaxies** | 2,500,000 | 50,000 |
| Horizontal Branch Stars | 66,000 | 1300 | Spirals | 2,000,000 | 40,000 |
| sdB | 35,000 | 500 | Ellipticals (UV bright) | 30,000 | 600 |
| sdO | 7000 | 140 | Ellipticals/S0s (UV faint) | 2000 | 50 |
| dMe | - | 500 | HII/Blue Compact Galaxies | 50,000 | 1000 |

In many cases, JUNO data will make possible critical HST and FUSE observations at high spatial and spectral resolution in the far UV and visible. A selection of areas where JUNO will compliment HST and FUSE is given here:

- UV "Palomar Sky Survey Catalog".

  Science program design, target selection, and exposure planning for UV observations with HST and FUSE would be vastly improved with an all-sky catalog.

- The ionization of the intergalactic medium.

  The HeII Gunn-Peterson test using QSOs discovered in the all-sky survey that are visible to rest wavelengths <304.

- QSO accretion disk spectrum in the extreme UV.

  Using QSOs discovered in all-sky survey visible to rest wavelengths 100-300Å, determine from HST and FUSE UV spectroscopy whether spectrum is consistent with thermal accretion disk model, determine black hole mass from turnover.

- The ionization of the universe.

  QSOs visible to high redshift delineate "holes" in IGM in which deep searches for ionization sources can be performed by HST ARC UV imaging. The source of ionization in the IGM is still unknown.

- Star forming galaxies at z=0.2-0.8.

  These may be the source of high optical galaxy counts, UV background and x-ray background. Thou-

sands should be found in the deep survey portion of a UV survey explorer. Imaging by HST and AXAF, and possibly HST spectroscopy by STIS, will be necessary to determine whether these are dwarfs undergoing starbursts, mergers, or something else.

- QSOs near galaxies for halo absorption studies.

  An all-sky survey is the best method for discovering QSO/galaxy coincidences with small impact parameters and sufficiently bright QSOs for high-resolution spectroscopy by HST and FUSE.

- High resolution dust and extinction map.

  An all-sky UV survey with 15 arcsecond resolution will provide the most detailed map yet of dust at high galactic latitudes, important for assessment of the extinction in HST and FUSE extragalactic targets.

## C.1 Cosmology

### C.1.1 Large Scale Structure

One of the key issues confronting astronomers in the 1990's is the large scale organization and distribution of matter. The structure of luminous matter may be closely related to the mean mass density, the presence and properties of dark matter, and the spectrum of initial matter fluctuations. It may have been affected by primordial explosions of young galaxies or cosmic strings (Ostriker and Cowie 1981). It is generally accepted that large scale structure is fundamentally related to galaxy formation. The presence of structure on scales 0.1-50 $h^{-1}$ Mpc has been demonstrated by galaxy-galaxy two point correlation statistics, photometric surveys of elliptical galaxies (Dressler *et al.* 1987), and most dramatically by galaxy redshift surveys (de Lapparent, Geller and Huchra 1986; Tully and Fisher 1987; Giovanelli et al. 1982). Large scale clustering is now seen on much larger scales than thought just a few years ago and the size of the largest structures is still unknown. Surpisingly large regions devoid of any galaxies appear to be quite common, although no survey has gone deep enough to allow reasonable statistics of this phenomenon. A surprisingly strong correlation between galaxy clusters violates the canonical theories of hierarchical clustering. Filamentary structures of galaxies are real (Bhavsar and Ling 1988) and hint at collapse on extraordinarily large scales. At this juncture, the following questions are critical: What is the largest structure in the universe? What is the relationship between luminous and dark matter: is biasing important? Are voids a common feature of the luminous matter distribution? What is the large scale distribution of voids? Are there fundamental differences in galaxies depending on where they are formed? Is there matter left over in the voids? Can structure on large scales (as determined by COBE) and smaller scales be reconciled with pure Cold Dark Matter models?

The JUNO mission will make three contributions to the study of large scale structure, which will complement those that are currently underway with ground-based telescopes. We will perform a galaxy redshift survey in the range 18,000-50,000 km/s. A slice of the universe out to z=0.6 will be mapped by a QSO Lyman $\alpha$ survey, and the QSO two-point correlation function will be determined over a large fraction of the sky. Finally, QSO Lyman limit systems will be mapped in the redshift interval $0.5<z<1.1$. The latter two topics were discussed in the body of the proposal.

*Galaxy Redshift Survey.* One fifth of the JUNO mission will be devoted to a spectroscopic survey of a slice of the universe 30 degrees in arc and 12 degrees across. The survey will span the north galactic pole, extending across a large area of very low extinction. Galaxies with $z>0.04$ will be smaller than the instrument point spread function, and integrated spectra will be obtained with S/N>5-13 for $m$ <17. Using spectral templates and the cross correlation technique, we will measure 1000-3000 galaxy redshifts. The limiting velocity will be $z \simeq 0.14$, or $v = 40,000$ km/s for an $L_*$ galaxy.

Optical redshift surveys to deeper magnitudes in limited fields are underway, and are likely to reach similar levels by the time of the JUNO mission. The UV information will provide a unique perspective on

the relationship between structure and galaxy morphology. As we discuss in section C.2, the far UV band is extremely sensitive to the morphological type, age, metallicity and star formation rate in galaxies. The JUNO galaxy survey will permit a statistically sound study of the relationship of each of these characteristics to the location of the galaxy in voids, ridges, clusters and superclusters. The suggestion of an enhancement of more active galaxies in the Bootes void (Kirshner et al.1987) must be tested systematically in many vacant regions.

### C.1.2 Primordial Abundances

In the nucleosynthesis phase of a homogeneous big bang, the abundances of light elements are determined by two parameters: the baryon/photon density ratio and the number of lepton families (neutrino types) (Wagoner, Fowler and Hoyle 1967; Alpher, Gamow and Herman 1967) . In principle, a measurement of the primordial abundances of D, $He^3$, $He^4$, $Li^6$ and $Li^7$ can constrain the baryon density and the number of lepton families. The consistency of all the abundances with primordial nucleosynthesis theory will test the assumption of initial homogeneity, which has been challenged (Applegate et al. 1987). Stellar processing can modify the abundances from their primordial values: $He^3$ and $He^4$ are increased at the expense of D. Current abundance measurements have been limited to stars and the galactic ISM, and represent at best either upper or lower limits on the primordial abundances. Targets must be observed in the halo of this galaxy and the disks and halos of other galaxies in order to calibrate the effects of stellar processing and their dependence on other metallicity indicators. Ultimately, a measurement of the abundances in a truly primordial gas cloud (if such an object exists) is the only way to guarantee the validity of such a determination.

The JUNO mission will make several critical contributions in this area. It will naturally find Lyman limit systems in the proper column density regime for a deuterium measurement. It will locate QSO's behind galaxy halos, extragalactic HI regions, and other potential locations of pristine gas, that can then be observed by the high resolution spectrographs of HST and FUSE/Lyman. It will also find the brightest high redshift QSO's that have not been significantly absorbed by intervening Lyman limit systems, so that a search for the He line forest can be made and the primordial He/H ratio determined.

*Intergalactic Deuterium and Helium* The Lyman limit survey may detect $\sim 30-100$ systems in the ideal column density range for a survey of deuterium abundance in intergalactic clouds. At $[(D/H)/(10^{-4})]N(HI)/1$ 1, the D L$\alpha$ line is just starting to saturate, and the HI L$\alpha$ line has not yet become damped. A measurement of D/H in ten systems yielding ten consistent results would be convincing evidence that a truly primordial abundance had been determined.

Since the resonance lines of helium lie beyond the Lyman limit, the only way to measure the He/H abundance by *absorption* in a truly primordial gas may be the detection of the $He^+$ L$\alpha$ forest and $He^+$ ionization breaks in high redshift QSOs. This effort is complicated by the HI Lyman limit systems that attenuate and often completely block the $\lambda_{rest} < 912$Å continuum of high redshift QSOs. The JUNO survey naturally selects for high redshift QSOs with the strongest far UV continuum–i.e., those least affected by intervening Lyman limit systems.

*Primordial Abundance Background Source.* A number of extragalactic objects may contain primordial abundances, assuming that they were not polluted by a Population III of massive stars. A fair number of extragalactic HI regions have been detected. The HI envelopes of Blue Compact Dwarf galaxies (BCDs) have morphological and dynamical properties that suggest they may be still collapsing. If this is so, the envelopes could be primordial. The metallicity (and in most cases the existence) of normal galaxy halos is not known, but many may have primordial abundances (cf 1.2). QSO Lyman alpha clouds (although probably not the Lyman limit systems) may carry pristine gas.

Absorption line measurements are generally the only method available to investigate the abundances of the light elements in these gas clouds. Therefore background objects with suitably bright, preferably

featureless continua must be found. The JUNO all-sky survey will detect all QSOs with $m$ <19.5, including all those that fall behind objects currently known or to be discovered. This will provide ~30 QSOs per square degree, many observable by the HST High Resolution Spectrograph and STIS. FUSE will make high resolution observations of QSOs with $m < 15$. Only an all-sky survey in the far UV band will locate all of the brightest sources behind targets of interest.

## C.2 Formation and Evolution of Galaxies and the IGM

The study of the formation and evolution of galaxies is central to current astrophysics. In spiral and late-type irregular galaxies, the far UV band is extremely sensitive to the integrated contribution of young stars, and therefore to the ongoing rate of star formation. Early type galaxies exhibit either a strong or a weak but detectable far UV continuum. In neither case is the source well understood. In Blue Compact Dwarfs (BCD's) and other active star forming galaxies, the far UV luminosity is particularly strong, and the extinction comparatively low.

### C.2.1 Normal Galaxies: Stellar Populations and Star Formation

JUNO photometric and spectroscopic surveys of galaxies will be used to study the stellar populations in spirals and ellipticals, the local and global processes governing star formation, and the nature of the hot stars in population II systems. The spectroscopic survey will permit detailed spectral synthesis analysis and extinction modelling. Incorporating the results of the spectroscopic work, the photometric survey will provide large samples for refined statistical studies of star formation in galaxy samples subdivided by inclination, morphology, luminosity and gas content.

*Far UV spectral energy distributions: spirals.* It is suprising that after a decade of UV observations with the IUE, little is known about the integrated spectra of galaxies in the UV. This is simply because the IUE was not designed to obtain spectra of extended objects with low surface brightness. This is unfortunate for several reasons. The far UV band is redshifted into the B band starting at z=1, and thereafter influences galaxy colors, number counts and the spectral appearance of highly redshifted galaxies in the optical and near infrared to redshifts of z<8. The formation of the Lyman $\alpha$ line is crucial for finding and studying high redshift galaxies, yet has only been studied in a few compact galaxies (Hartmann et al. 1988; Deharveng et al. 1986).

Spiral galaxies span a wide range in colors and spectral classification. The later type galaxies, Sc and Sd, have a larger range than the early type Sa and Sb (Humason, Mayall, and Sandage 1956). Sc's are distributed uniformly in spectra from type F0 to G3 and many have recently undergone intense star formation periods. It is unclear however if the wide range in specral index found today arises principly from the sporadic nature of star formation rates in these galaxies or from differences in the rates of a smoothly time- varying star formation rate. If it is the latter it would be quite intriguing to try to uncover what causes this basic difference between systems that are otherwise quite similar. A UV survey of a large sample of galaxies is needed to determine the present character of star formation activity in spiral galaxies.

Comparisons between the UV and IR fluxes of IRAS or SIRTF promise to be highly informative. Both are measures of the star formation and one may suppose that they will on the whole correlate well. Preliminary correlations of IRAS 60 and 100 $\mu$m and OAO-2 luminosities indicate that this is indeed the case (Martin and Bowyer 1989; Gallagher 1987). Verification of this average behavior will be an important prerequisite for exploiting the sensitivity of the UV luminosity to the star formation rate.

The best data to date on the far UV distribution in galaxies is for UV bright galaxies in the compilation by Kinney et al. 1992. IUE generally observed the high surface brightness central regions of these galaxies. Kinney *et al.* found that extinction in these galaxies does not appear as a 2200Å feature. They conclude that dust absorption that does occur is optically thick, and that remaining starlight escapes with little extinction. This "picket fence" behavior simplifies the interpretation of galaxy spectra and photometry in the far UV,

since the spectral energy distribution is not affected, only the overall normalization. If $f$ is the mean covering factor of the dust, and the star formation rate is $\dot{M}$, then $F_{16} \sim \dot{M} * (1 - f)$ and $F_{60\mu} \sim \dot{M} * f$.

If the J flux is also absorbed by optically thick clouds, the **16-J** flux gives the star formation rate (per unit J flux). The implication is that by combining the far UV spectrum with the visible and far IR fluxes, we can infer the stellar population mix from the UV continuum and line spectrum, the star formation rate from the UV/V flux ratio, and the dust covering factor from the FIR/Far UV flux ratios. With a large spectral data set, it will be possible to learn the variation of these parameters with morphological type, inclination, presence of a companion, luminosity, and atomic and molecular gas HI properties.

A few of the IRAS bright galaxies that have large IR to visible flux ratios are found to be highly deficient in atomic hydrogen flux (Mirabel and Sanders 1989). This at first seems a paradox, how can there be star formation and energy redistribution into the infrared without gas? A possible explanation is that under some conditions the atomic hydrogen in a galaxy is formed by dissociation of the molecular gas (Shaya and Federman 1987). Galaxies with large IR/visual flux ratios probably contain their star formation sites deeper in dark clouds, extinguishing all ultraviolet radiations. It may therefore be that galaxies with high IR/visible flux ratios are lacking in ultraviolet flux as well as 21 cm line radiation. By combining information from the infrared and optical with the UV survey, information will be gained as to the fraction of star formation embedded deep in clouds and on the edge of clouds. Star formation theories make predictions of where the stars are generated; for instance, if star formation is induced by cloud collisions then stars should preferentially be formed in the center of the cloud complex formed by the collision (Sanders et al. 1988).

The possibility of having nearly all star formation embedded deeply in some galaxies indicates the need to be careful in translating UV flux into star formation rates, but it is an important and worthwhile goal. Extinction determination is a complicated matter and can only be partially described here. Several procedures will be followed for extinction determination. A safe procedure to begin with is to examine only those galaxies for which the UV spectra are obtained. From the absorption line measures and the continuum band ratios the general early stellar constituents can be determined. A fitting procedure can be applied to the data which uses a library of early type stars, white dwarfs, and Wolf-Rayet stars, plus some standard extinction from dust grains. We will derive both the total unextinguished UV flux and the mean ages of the major stellar components contributing to the UV flux.

It will be extremely interesting to learn whether the picket fence model applies to the average spiral galaxy. A correlation plot between UV surface brightness and inclination for galaxies within a given Hubble morphological class will reveal how much of the ambient flux is being absorbed by dust clouds. For galaxies with similar intrinsic surface brightness $I_0$ and similar optical depths along the normal to the plane $\tau_o$, we have

$$I_1 = I_o e^{-\tau_o \csc(i_1)}$$

$$I_2 = I_o e^{-\tau_o \csc(i_2)}$$

which implies:

$$\tau_o = \left( \frac{1}{\csc(i_2) - \csc(i_1)} \right) ln \frac{I_1}{I_2}$$

A measure of the optical depth of the general interstellar medium provides a conversion from the observed uv flux to the ambient uv flux at different heights within the galaxy.

The integrated spectrum will supply information about the mix of O,B, and A stars in the galaxy, the history of star formation, the slope and high mass limit of the initial mass function, the galaxy metallicity, and the fraction of UV light intercepted by dust. In Figure C.2, we illustrate the sensitivity of the UV spectrum to metallicity, by showing JUNO simulated spectra of a metal rich irregular and the metal poor

galaxy I Zw 18. While O and early B-type stars have similar continuum slopes in the far UV band, the absorption lines can be used to deconvolve them. O-type stars show lines of SiIII ($\lambda$1300, 1333), OV ($\lambda$1371), SiIV ($\lambda$1394,1403), CIII ($\lambda$1428[B1],1453[O4]), CIV ($\lambda$ 1548) and NIV ($\lambda$ 1718). B-type stars exhibit SiII ($\lambda$1265,1300), CII ($\lambda$ 1336, 1400) and CIII ($\lambda$465). A-stars have strong features at $\lambda$1850 and 1933, and a continuum slope that is a strong function of type. The SiIV and CIV lines in O and early B-stars displays a strong positive dependence on luminosity, and can be used to constrain the upper mass limit and time since the last star burst.

The spectroscopy survey will collect 5,000 galaxy spectra with S/N>10-20. For each galaxy, it should be possible to derive the star formation rate, age, metallicity, and extinction for the population I stars. Some information about the star formation history may also be derived, such as whether the star formation occurred in widely separated bursts or in a continuous fashion. From this spectral study, we will be able to interpret the galaxy colors obtained from the all-sky and deep photometric surveys. Also, we will examine the relationship between star formation activity, metallicity, and large scale structure, as part of the galaxy redshift survey.

*Far UV spectral energy distributions: ellipticals.* While HUT and UIT have provided tantalizing observations of early-type galaxies (Ferguson et al. 1992; O'Connel et al. 1992), the origin of the far UV rising flux in early-type stellar systems has no been firmly established. Low resolution photometry from OAO and ANS for a dozen or so galaxies has shown that a residual continuum is alway present in the far UV. In most cases, it is 3-4 magnitudes below that in the V band. This residual cannot be due to main sequence stars in the dominant low mass population. Possible sources include blue stragglers, hot white dwarfs, subdwarf OB stars, planetary nebula nuclei, horizontal branch (HB) stars, post-AGB stars, and young main sequence stars. All but the last are expected in an evolved population, but the required populations of most are likely to be too high. Horizontal branch stars are considered the most likely candidate, if only because they are the least understood. The evolution of HB stars is very sensitive to metallicity, mass loss during and after the red giant stage, and an unknown "second parameter" which has complicated the analysis of all population II systems. There is some indication that lower mass stars become bluer HB stars (Ciardullo and Demarque 1979). In this case, the far UV band would be sensitive to the age of the population. There is also evidence that the UV flux is correlated with metallicity, which is suprising given that the bluest HB stars are the most metal poor. Young stars may form out of gas produced by red giant mass loss.

Approximately 20% of ellipticals observed by OAO and ANS exhibit enhanced far UV continua, which is probably associated with nuclear activity. The spectroscopy survey will produce more than 100 spectra of normal elliptical galaxies. It is critical to collect a large sample in order to deconvolve the effects of galaxy luminosity, metallicity, age, and the unknown second parameter. From the survey of stars in population II systems in the Milky Way (halo, bulge, and globular clusters), we will have at our disposal a complete set of stellar spectra forming the basis of a population synthesis analysis. Using continuum shapes and absorption lines, and without significant extinction, it should be possible to determine the mix of objects producing the flux. It is likely that with this information, the UV band can provide important diagnostics of population II systems. As with the spirals, we will use the spectral information as a basis for the interpretation of elliptical galaxy far UV colors.

*Spiral Galaxy photometric survey* Nearby galaxies will be candidates for imaging photometry. Color information obtained from the spectroscopic survey will be used to map populations in spirals and ellipticals. Far UV imaging photometry of spirals can be correlated with optical, near and far infrared photometry, HI and CO maps, non-thermal radio surveys, and x-ray studies. We will resolve OB associations in a large number of galaxies, and can derive a luminosity function and IMF "spectrum" for these basic units of star formation. This should relate directly to the mass spectrum of molecular clouds and theories of massive star formation.

With the large sample of galaxies produced in the all-sky and deep photometric surveys, more than $10^6$,

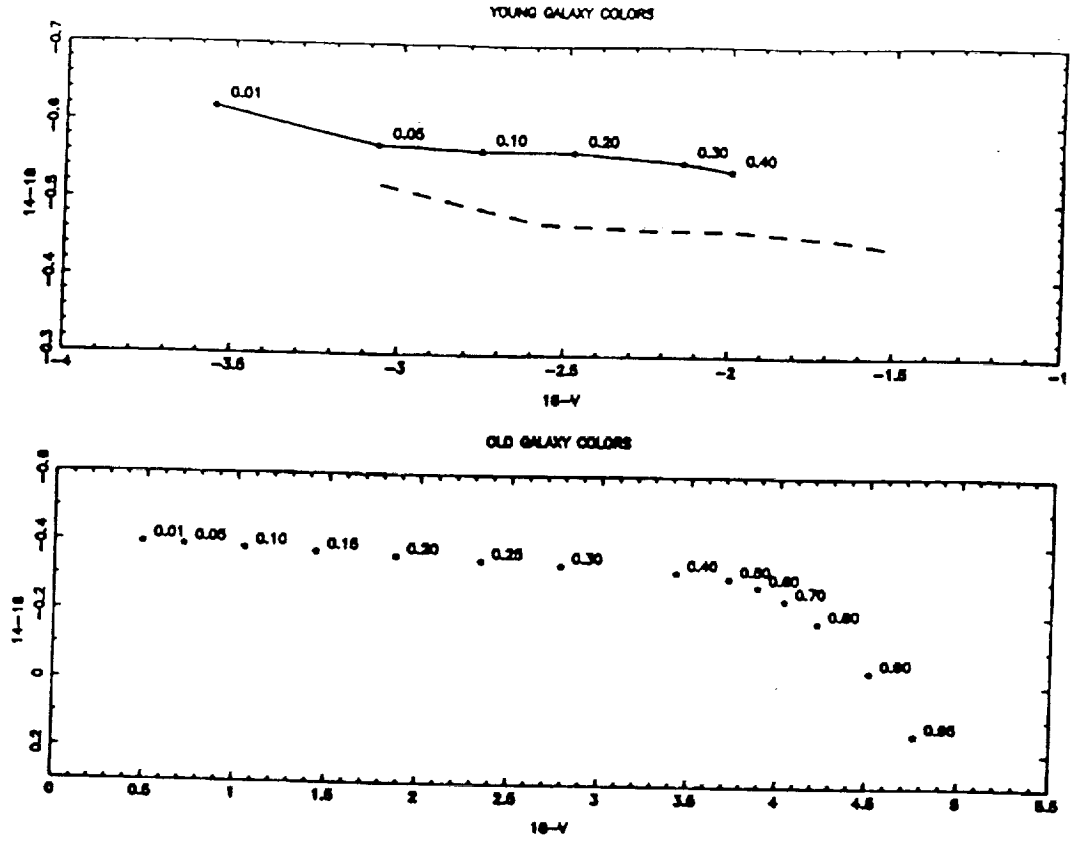


Figure A.1 Unreddened galaxy colors from models of Bruzual (1980). Top panel shows young galaxies labelled by their age in Gyr. Bottom panel shows coeval galaxies, age 15 Gyr, with differing exponential star formation histories. Labels are $\mu$-parameter, which is the fraction of gas used up in the first Gyr.

it will be possible to make extremely refined statistical studies of the star formation activity in spirals. The large sample will allow us to partition the galaxies into *homogeneous* subsets and analyze each separately. For example, we will be able to consider a set of Sb galaxies with -21< $M_V$ <-20 and with inclination less than 70 degrees. For each subset, we can examine the dependence of star formation activity on HI mass, HI surface and volume density, $H_2$ content, $H_2$ surface and volume density, total mass, presence, number, and definition of spiral or flocculent morphology, and presence of bars.

This information will be critical to understanding the global mechanisms driving star formation in galaxies. In the earliest models, the star formation rate was determined by a density law ($SFR \sim \rho^n$, with $n \sim 2$, or $SFR \sim M(t)$), and disks were assumed to be closed systems with a steadily decreasing gas supply (Tinsley 1972a,b; Searle, Sargent and Bagnuolo 1973). Other theories incorporate slow infall from the galactic halo or accretion from the intergalactic medium (Oort 1974; Larson 1972; Larson and Tinsley 1978). Recently, several self-regulating feedback mechanisms have been invoked, such as gas dispersion by stellar winds and photoionization, and by supernovae (Franco and Shore 1984; Franco and Cox 1983; Cox 1983). Global models must incorporate spiral density waves or stochastic self-propagating star formation to account for spiral and flocullent morphology. The strength and frequency of spiral waves may be affected by differential rotation, dark matter in the disk and halo, and the galaxy angular momentum.

The UV luminosity function for local spirals is necessary to interpret faint galaxy number counts in the far UV, optical, and near infrared, understand the contribution of galaxies to the cosmic far UV background, derive the ionization of the intergalactic medium, and assess the degree of evolution in distant clusters and field galaxies.

*Elliptical Galaxy Photometric Survey.* In more than one hundred nearby elliptical galaxies, we will map the UV component and compare the light profile with optical and infrared images. This will test the young star hypothesis, since we expect that star formation will produce patchy distributions. Comparison with the metallicity gradient should indicate the importance of HB and post-AGB stars. The photometric survey of elliptical galaxies will include more than 2000 objects. As with the spirals, such a large sample will provide the material for detailed statistical analyses which bear on the nature of the UV component.

*Stellar Populations in the Magellanic Clouds.* The Magellanic Clouds, which will be targets for the deep photometric surveys, will provide a prime opportunity for a detailed study of the population in an irregular galaxy. Since we will obtain **14-18** colors along with absolute magnitudes, it will be possible to construct an HR diagram for all resolved stars with absolute magnitude $M_{16}$ <2.5. This is important since source confusion will complicate the derivation of **16**-V colors. The HR diagram will include blue supergiants, main sequence stars earlier than A5, blue horizontal branch stars, planetary nebula nuclei, Sds and pulsating pre-WD objects, and many cataclysmic variables, most of which have never been detected before.

### C.2.2 Galaxy Evolution

In four investigations related to galaxy evolution, the JUNO mission will determine far UV number counts for $13 < m_{16} < 23$, search for the Butcher-Oemler effect in cluster and field galaxies, relate star formation activity to local galaxy density and large scale structure, and search for damped L$\alpha$ lines in QSO spectra.

*Faint Blue Galaxies and Far UV Number Counts.* One of the most intriguing discoveries in cosmology over the last few years is the population of faint, blue galaxies which appears to have a non-evolving redshift distribtion, while at the same time exhibiting number densities a factor of 2-3 above the local galaxy density (Broadhurst et al.; Colless et al.). A working hypothesis has emerged that these are low luminosity dwarf galaxies undergoing bursts of star formation activity at redshifts $0.2< z <1$. If this is true, then number counts in the far UV should exhibit a dramatic excess over and above the non-evolving predictions. However, if these galaxies are predominantly at higher redshifts, no such excess will be observed, because at high redshifts the Lyman limit almost certainly makes these galaxies dark in the far UV. The number count distributions in the **14**, **16**, and **18** bands are a critical test of models with strong evolution in the $0< z < 1$ range and comparison of the distributions to each other and to those in the J and U will definitively constrain the redshift distribution. While the galaxies counts at the faintest magnitudes will probably be measured by WFPCII on HST, it has insufficient field of view to determine the distribution for $m_{16} < 23$ (with typical WFPC counts of a few per field in deep pointings). The angular correlation function of these galaxies, which may be more weakly clustered than z=0 spirals (Efstatiou et al. 1991) can also be measured with high statistical significance, since these galaxies will be easily distinguished from normal spirals by their UV bright **16**-J colors.

*Morphology-Density Relationship.* With a measurement of the two-point galaxy-galaxy angular correlation function in the photometric survey, and the spatial correlation function in the spectroscopic survey, it will be possible to make a systematic and sensitive study of the relationship between morphological type and galaxy density that has been observed optically (Dressler 1980). This is possible because of the sensitivity of the far UV band to present star formation rate, which increases rapidly toward later Hubble types. In fact, we will measure directly the star formation rate-density relationship, rather than relying on morphological typing. The effects of patchy galactic extinction, which can bias correlation measurements,

will be eliminated using a combination of far UV reflection, far IR emission, and HI observations (cf. section 1.4). This correlation study will permit us to survey a large number of galaxies over a wide range of density. With this information, we can assess the effects of the environment on galaxy evolution, such as the role of ram pressure stripping by intergalactic media, galaxy-galaxy collisions, and tidal disruptions by passing and satellite galaxies. Processes affecting formation time, age, and current gas supply (such as biasing) can also be manifested as a dependence of star formation rate on local density.

*The Butcher-Oemler Effect in Cluster and Field Galaxies.* In a related measurement, we will determine whether evolution in the star formation rate occurs to redshifts of 0.7, in either cluster or field galaxies. Again, we exploit the sensitivity of the far UV band to star formation rate. For the field, we will use number-magnitude relationships obtained in the all-sky and deep surveys, to magnitude $m < 21.5$. We will determine whether the mean star formation rate has increased, decreased or remained constant over the last $\sim$50% of the age of the universe.

Because of environmental influences, and possibly because of intrinsic differences in their properties at formation, galaxies in clusters may exhibit radically different evolution than in the field (Dressler 1984). The evidence for a rapid increase in blue galaxies in clusters with redshift, originally presented by Butcher and Oemler (1978b, 1980), is still disputed (Dressler 1984; Dressler and Gunn 1982, 1983) . We will observe clusters at low, intermediate, and high ($z = 0.5$) redshifts in the all-sky and deep surveys. We will choose clusters that show both smooth and clumpy x-ray morphology, which may be indicative of the differences in the dynamical age and extent of gas stripping.

*Damped Lyman $\alpha$ Systems.* Damped L$\alpha$ lines, which are believed to be formed by galaxy disks (Wolfe 1988), will be detectable in systems with $N(HI) > 10^{20}$ cm$^{-2}$ (corresponding to $EW > 7$Å). Reasonably accurate column densities ($\sigma(N_H)/N_H < 0.25$) will be obtained in most cases. Damped L$\beta$ lines will also be detectable when $N(HI) > 7 \times 10^{20}$ cm$^{-2}$. It will be very important to compare the redshift and column density distributions of these lower redshift systems with those of the higher $z$ lines found optically. This will provide an unbiased probe of the evolution of galaxy disks over the last 50% of the age of the universe.

### C.2.3 Galaxy Formation

A variety of galaxies show active star formation that may exhibit processes similar to those that accompanied galaxy formation. A subset of these, Blue Compact Dwarfs, may be truly late forming galaxies. The JUNO survey will study active star formation in nearby galaxies, and search for low metallicity galaxies that may have recently formed.

*Starburst Galaxies.* Several classes of galaxies appear to be associated with strong star formation processes, including irregular galaxies, blue compact galaxies, dwarf ellipticals, interacting galaxies, and emission line galaxies. Hundreds of good S/N spectra of these galaxies should be obtained in the spectroscopic survey. These will allow us to study how star formation is triggered and sustained under a wide range of conditions. We will use the methods discussed above for normal spirals to understand the stellar populations, metallicity, starburst history, and the relationship between young stars and molecular clouds traced by dust. The UV extinction in galaxies with starburst nuclei is much greater than that in BCD's, which may be indicative of a different triggering mechanism. This might be confirmed by a statistical comparison of the IMFs and starburst histories derived from the JUNO survey. In the case of narrow line active galaxies, there are some indications that the stellar contribution in the UV is not sufficient to explain the infrared emission (Boisson and Durret 1986), and that a 20,000K disk may be present. The L$\alpha$ line can be studied in the highest redshift starburst galaxies, and we can test whether the L$\alpha$/H$\beta$ ratio is inversely correlated with metallicity (Deharveng et al. 1986), which would be expected if the L$\alpha$ is destroyed by dust which correlates with metallicity. Using starburst galaxies obtained in the redshift survey, we will search for relationships between activity and the local galaxy density, and the location relative to other galaxies, clusters, voids and ridges. Starburst galaxies will be photometrically identified by their colors, and with a

large sample we can search for subtle differences in the two-point correlation functions of galaxy-galaxy pairs and galaxy-starburst galaxy pairs.

*Young Galaxy Search.* Our understanding of galaxy formation and evolution could be dramatically modified by the discovery of a relatively nearby galaxy in the process of formation (Silk 1988). At the same time, such an object would provide one of the best opportunities to determine the primordial abundances of the light elements. A UV photometric survey stands out as the most sensitive method for searching for such galaxies, since low metallicity galaxies are likely to have the least extinction and the bright UV continuum of young massive stars will dominate the luminosity.

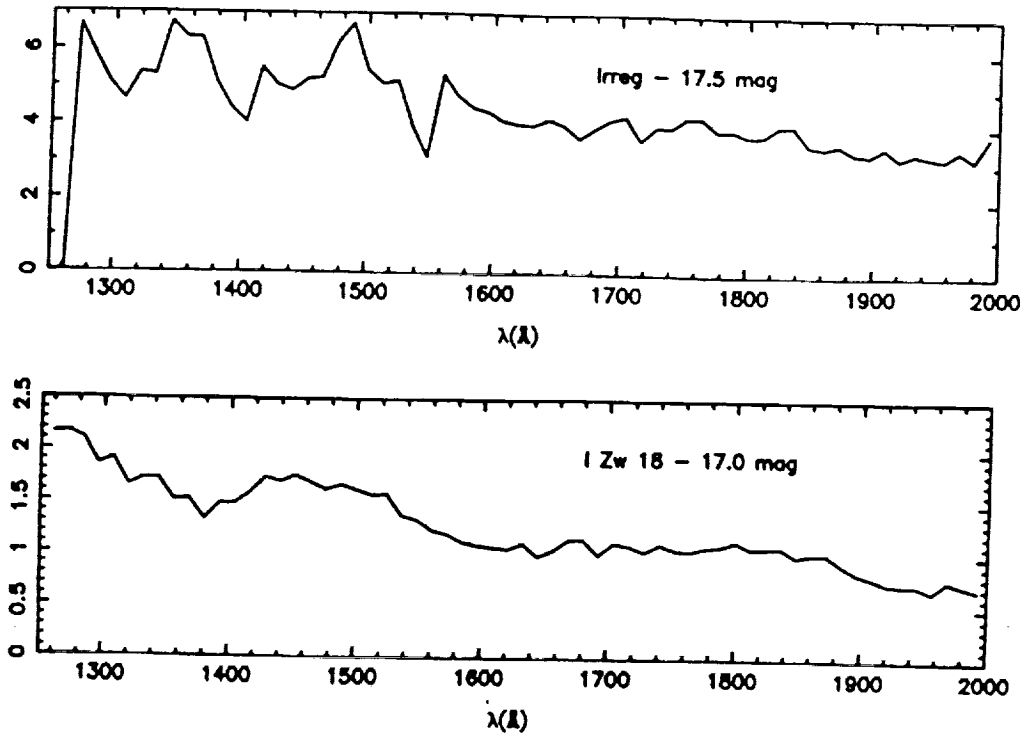


Figure A.2 Simulated spectra produced by (a) top: a metal rich Magellanic irregular type galaxy at $17.5^{m}$ and (b) bottom: a metal poor galaxy similar to I Zw 18 at magnitude 17.

Optical photometry is biased against the detection of extremely low surface brightness galaxies (Davies et al. 1988). These may be more sensitively detected against the comparatively faint far UV background, which is typically 1% of the visible night sky, if they are late type galaxies. If galaxies of this type could be observed it would be possible to look for the causes of their late formation and the role of the intergalactic medium, and to study the correlation of these young galaxies with large scale structure.

*Galactic Halos in Absorption.* The existence and role of galactic halos in galaxy evolution remains a mystery. Many theories of galaxy evolution (e.g. Larson 1976) posit a halo which may provide primordial matter for ongoing star formation to match observed metallicity profiles and prevent prompt gas consumption, or accommodate hot gas from the disk in a static corona or dynamic fountain which can influence metallicity gradients. The enrichment history of halos may be effected by the formation of the

spheroid and globular clusters, tidal disruption by and of companions, galactic winds and fountains produced by supernovae in the disk, high $z$ star mass loss and supernovae, and the accretion of intergalactic gas. The ionization and composition of galactic halos can only be studied using absorption line measurements, if suitable continuum objects can be found. Both HST and FUSE/Lyman can make the absorption line measurements of a large number of important lines. Unfortunately, the current catalog of galaxy/QSO coincidences includes no impact parameter closer than 12 kpc.

The JUNO survey is ideally suited for discovering galaxy-QSO coincidences which can be exploited for absorption line measurements by HST and FUSE/Lyman. The JUNO photometric survey will locate approximately 650(r/10 kpc)$^4$ random galaxy-QSO coincidences with impact parameter$r_{imp} < r$ , including *only* cases where JUNO can resolve the two objects. More than five cases are expected with impact parameters as small as 3 kpc. The deep survey observation of M31 should find 160 QSOs within a 10 kpc radius. Along with absorption line measurements of halo, we will search for extended disks in face on galaxies, and measure the abundance and ionization state of this gas which may be present without star formation.

### C.2.4 The Intercluster and Intergalactic Medium

*Galaxy Cluster Cooling Flows* The hot x-ray gas in many galaxy clusters is sufficiently dense to cool radiatively on time scales much shorter than a Hubble time. Many clusters exhibit centrally condensed x-ray emission with lower central temperatures (Canizares et al. 1979; Fabian et al. 1981; Mushotsky et al. 1981; Jones and Forman 1984) implying cooling rates of 100-400 $M_\odot\ yr^{-1}$. Recent BBXRT observations have solidified this conclusion (Mushotsky 1992). Many of these clusters also show prominent emission line regions, with both centrally condensed and filimentary morphologies (Kent and Sargent 1979; Heckman 1981; Cowie et al. 1983; van Bruegel et al. 1984). These observations indicate that thermal instabilities in the hot gas form cooling flows which may dictate the gas behavior in cluster centers (Cowie and Binney 1977; Fabian and Nulsen 1977), leading to gas accretion onto and growth of the central galaxy.

The emission spectrum of radiative cooling gas should be similar to that of radiative shocks. The emission measure of gas at temperature $T_6 = T/10^6K$ is $EM(cm^{-2}pc) = 2\dot{M}(< r)T_6^{1.5}r_{kpc}^{-2}$, where $\dot{M}(< r)$ is the mass flux in the cooling flow inside a radius $r$. Observed optical emission from cluster cooling flows suggest spectra that combine recombination, radiative cooling, and shock excitation. Far ultraviolet observations (Norgaard-Nielsen et al. 1984) have detected HI L$\alpha$ only. In the case of A1795 (one of the more luminous cooling flows), the observed L$\alpha$/H$\alpha$ ratio is $\sim$10, consistent with radiative shock predictions of 10-30 (Shull and McKee 1979). In general, the flux in the L$\alpha$ line should be $F(L\alpha) \sim 10^{-16}L_{40}z^{-2}$, where $L_{40} = L(H\alpha)/10^{40}\ erg/s$. The JUNO spectroscopy survey can detect L$\alpha$ emission from cluster cooling flows to a redshift limit of $z < 0.2{L_{40}}^{1/2}$. Most clusters condensed x-ray cores have $1 < L_{40} < 100$. We estimate that >50-100 clusters will be detectable in L$\alpha$, and > 10 may exhibit observable higher ionization lines, particularly CIII $\lambda$ 1908 and CIV $\lambda$1548.

A critical question for understanding cooling flows is the most obvious: what is the fate of the accreted gas? Most likely it is used up in star formation in the central galaxy. However, no direct evidence of this has observed (e.g., recent UIT null result by Smith et al. 1992). With both the spectroscopic and photometric surveys, we will make a senstive search for continuum emission from massive young stars that could be formed in the cooling flow. Assuming a galactic IMF (Miller and Scalo 1979), the luminosity at $\lambda$1900 produced by a continuous star formation of $\dot{M}_{sfr}$ ($M_\odot/yr$) is $5 \times 10^{39}\ erg/s/$Å. The limiting redshift for detection of star formation is $z < 0.13\dot{M}_sfr$ in the spectroscopic and all-sky photometric surveys, and $z < 0.7\dot{M}_{sfr}$ for the deep survey. Cooling flow mass fluxes 10 <$\dot{M}$< $100M_\odot/yr$ are typical. In the spectroscopic survey, star formation will be distinguishable from non-thermal continua that may be produced by a central radio source by the spectral shape and by the presence of absorption lines. Photometric colors will distinguish stellar continua from power law emission with indexes $\alpha > 0.5$. Unless the IMF is so

different in cooling flows as to be completely devoid of high mass stars, it should be possible to detect them in many clusters.

*Star Formation History in the Milky Way.* The all-sky and deep photometric surveys will determine the bright end of the white dwarf luminosity function to galactic scale heights as far as 4 kpc, and therefore in the old disk and the halo (spheroid). The luminosity function is determined by the WD formation rate and cooling function. The formation rate is a measure of the stellar birthrate in the mass range near the turnoff mass, for a coeval population. For a continuously forming population, the rate is an average over the star formation history weighted by the initial mass function. Since the scale height and stellar age are coupled kinematically, the $z$ dependence of the luminosity function will constrain the history of star formation over the age of the galaxy.

*Emission from HI 1216 and HeII 304 in Lyman Limit Systems.* The surface brightness of a LLS produced by recombination into L$\alpha$ is $I(L\alpha)$=$\Pi(s^{-1})N(HI)(1+z)^{-3}$ ph cm$^{-2}$s$^{-1}$Å$^{-1}$. Here, $\Pi$ is the ionization rate at redshift $z$. For a saturated, local cloud ($N(HI) >> 3 \times 10^{17}$cm$^{-2}$, z=0.07, $\Pi \simeq 10^{-13}s^{-1}$, we expect a surface brightness of $I(L\alpha) \sim 10^4$ph cm$^{-2}$s$^{-1}$Å$^{-1}$. This is detectable in the JUNO spectroscopic survey if the cloud subtends >0.5 square arcminutes. At z=0.07, such a object would need to be 45 h$^{-1}$ kpc in diameter. Deharveng and Buat (1987) have also found that in 1 in 1000 directions, high redshift Lyman alpha clouds may exhibit He II 304 emission as well.

*IGM Ionization and Evolution: HeI and HeII Gunn-Peterson Test.* Gunn and Peterson (1965) first pointed out that a homogenous intergalactic medium with a cosmologically significant HI density would produce an absorption trough shortward of redshifted L$\alpha$ in QSO spectra, the cumulative result of L$\alpha$ absorption along the line of sight. No such trough is observed, implying that if a uniform IGM exists, it must be highly ionized. The L$\alpha$ forest is produced by discrete clouds along the line of sight, with neglible cumulative mass density. It is likely that these clouds are pressure confined by a hot matrix, but the characteristics of this medium are still only loosely constrained by the x-ray background and GP limit. Important constraints on the temperature, ionization, and physical conditions in both the clouds and the hotter substrate will be obtained by searching for a HeI and HeII line forests, continuum breaks produced by the cumulative effects of these lines, and Gunn-Peterson continuum jumps. The HeI test can be performed towards QSOs with $z > 0.6$, and has already been performed by IUE for a few cases, and by HST for HS1700+638 (XXX REF). However, in most models the HeI density is expected to be low. With a large sample of QSOs, we will be able to search for rare cases of HeI continuum absorption in systems with $2.8 > z > 1.6$, which would be found while comparing a continuum break with the redshift of damped L$\alpha$ lines observed by HST or optically. To perform the HeII test, QSO redshifts of $z > 2$ are required for measurements by FUSE/Lyman, and $z > 3.1$ for HST. Measurements by both will be required to study the evolution of the IGM over time. Lyman limit systems act to reduce the continuum flux at the wavelengths required to perform the HeII GP test, in many cases completely blocking it. Based on IUE observations of two dozen QSOs, at $z = 2$, 30% of QSOs remain, while at $z = 3$ only 10% will avoid strong Lyman continuum systems (Bechtold et al. 1984; Tytler 1982). Clearly, the optimal method for discovering QSOs suitable for HeII observations is with the JUNO photometric survey. We predict that > 200 QSOs will be discovered in the all-sky survey, and ~100 in the deep survey with significant far UV continuum in the $2.5 < z < 3.5$ range. As we show in §3.1 and §A.4, it will be possible to identify the majority of these based solely on their colors.

At the same time, since we will obtain a detailed understanding of the continuum spectra of QSOs, the statistics of absorbers, and the dependence of each on redshift, we will derive a much more thorough understanding of the intergalactic ionizing radiation field and its variation with redshift.

### C.3 The Physics of Compact, Energetic Systems

The JUNO mission will make several important contributions to the study of energetic astrophysical

sources. Systems with accretion disks will often radiate a large fraction their observable luminosity in the far UV band. Flux limited samples will be representative of the evolution of the accretion disk, which may prove fundamental. The time resolution of JUNO will prove important in both the discovery and the study of accreting binary systems, particularly those that are short period and/or eclipsing. In many systems, reprocessed x-ray emission and accretion disk coronae will produce far UV line emission. Time resolved spectrophotometry of CVs, LMXRBs, AGNs and QSOs will provide kinematic, ionization, and abundance diagnostics.

### C.3.1 Binary star systems: CVs and LMXRBs.

Cataclysmic variables radiate the bulk of their luminosity in the far and extreme ultraviolet, and the JUNO survey will discover a large number of new dwarf novae, quiescent novae and magnetic variables. Selection of magnetic stars and some dwarf novae will be based on variability, which will be investigated on timescales of $10^3$, $10^5$ and $10^7$ seconds. Many dwarf and classical novae and will be identified by their typical $\nu^{1/3}$ disk spectrum, at low latitudes where their number counts will dominate those of 20,000K white dwarfs that occupy the overlapping color range.

*Cataclysmic Variables: Luminosity Function.* The UV-optical ratio, combined with UV colors, is potentially the most sensitive measure of the mass accretion rate in a CV (Tylenda 1981). There are still considerable difficulties in practice however, due to the lack of physically realistic models, and because of uncertainty in the white dwarf mass (Cordova and Howarth 1987; Patterson 1984). With the aid of more accurate modelling, a flux-limited measurement of the CV luminosity function would bring an approximate but powerful global constraint on the average mass accretion rate of WD binary systems. This in turn would constrain scenarios for the formation and evolution of these systems, the formation of neutron stars by accretion, and the evolution to type I supernovae. We will determine the luminosity function in the disk, the halo, the galactic bulge, and the Magellanic Clouds, and ask whether the progenitor population is related to average CV properties. Deep surveys of the LMC and galactic bulge will be dominated by CV's at the faint magnitudes, variability will be observed in many cases, distances will be secure and follow-on identification mostly unnecessary. We expect to net several thousand CV's in each.

*Cataclysmic Variables: Variability Survey.* Variability on timescales from $10^{-4}$-$10^5$ seconds will be explored during the deep and spectroscopic surveys. Orbital variability in systems with P< 1 day will be measured for all systems. It will be possible to derive a distribution function for DQ Her star rotation periods which, when combined with magnetic field strengths, will constrain evolutionary models of magnetic CV's. We will locate more than 400 eclipsing systems.

*Cataclysmic Variables: Time Resolved Spectroscopy.* Time-resolved far UV spectroscopy will provide information about the structure and radiative transfer in the accretion disk. In eclipsing systems it may be possible to separate the contributions from the inner and outer disk, and map the temperature structure with even greater precision. This will be important for determining the correct radiation law acting in disks, which must be found to derive the accretion rates, the observable effects of inhomogeneities in the flow, and disk instabilities. Disk winds transport angular momentum out of the system and are therefore directly responsible for maintaining Roche lobe overflow and accretion flow. They are best studied using UV resonance line profiles. Mapping the profiles over orbital periods (with $\Delta v \simeq 1000$ km/s) will determine the geometry and mass loss rate of the wind. In DQ Her systems, temporally resolved spectroscopy will help separate the many emission components which are present in these systems, including thermal and nonthermal radiation from the accretion cap, reprocessed radiation from the secondary and accretion flow, and the white dwarf itself.

*Cataclysmic Variables: Evolution and Precursors.* The small number of known CV's has made the derivation of evolutionary models extremely uncertain at best (Patterson 1984). The JUNO mission will provide five new elements that will improve this predicament: (1) a large increase in the number of known

CV's, with approximate accretion rates; (2) many new eclipsing systems, for which system parameters are most unambiguously derived; (3) flux-limited luminosity functions and scale heights, with population dependancies; (4) an extensive catalog of white dwarfs in detached binary systems (cf. §2.2); and finally, (5) sensitivity to rare evolutionary stages that may have been missed in the present sample.

*Low Mass X-ray Binaries* These objects may be among the hottest to be detected. The accretion disk has a theoretical power law index of 1/3 (in frequency) but the strong X-ray heating/reprocessing may increase the index to nearly 2. In fact, the range of power law indexes observed with IUE is 0-2 (Cordova and Howarth 1987). In the photometric mode all non-obscured LMXRB in our galaxy and in the Magellanic Clouds should be detected, along with many in M31. Time variability over the observation period should be observable for all objects. Many LMXRB seen edge-on and therefore not detected in X-rays should also be found in the UV. Follow-up observations of these objects with ground based telescopes should reveal their eclipsing character. Supercritical accretion in High-Mass X-ray Binaries could also show up as strong ultraviolet sources with Eddington luminosity and could be detected for the first time.

### C.4 The Interstellar Medium

*Dust and Extinction.* Interstellar dust is widely believed to form in the cool extended atmospheres and winds of red giant stars. Dust is removed by star formation, and may be modified or destroyed in supernova shocks. The behavior of dust in the UV has usually been studied using early-type stars, yielding relative extinction measurements (Bless and Savage 1972; Witt et al. 1981, 1984) and scattering properties (Witt et al. 1982; Bohlin et al. 1982) in dusty OB associations. Less is known about the UV characteristics of dust in low density, high galactic latitude areas. Since far UV extinction is produced by a distinct population of smaller grains that scatter and absorb less efficiently in the visible, the measurement of UV extinction provides an independent probe of dust properties.

Considerable effort has been expended to determine the absolute visual extinction at the galactic poles. This quantity must be known in order to interpret accurately standard candles for extragalactic distance determination, faint galaxy count surveys, and in general all photometric extragalactic observations, including those of this mission. At the same time, this information is important for understanding the relationship between dust and gas in various phases of the interstellar medium, and the potential importance of processes which create, disperse, and destroy dust in the ISM. Most recent determinations of the visual extinction at the poles have found $A_V < 0.05^m$, corresponding to $A(1600\text{Å}) < 0.13$ with the extinction law of Bohlin *et al.* (1978). There is also evidence for widespread regions of gas with *no* associated dust, manifested as an offset in the N(HI)-E(B-V) relationship (and the galaxy count-N(HI) correlation)(Heiles, Stark and Kulkarni 1981; Burstein and Heiles 1982). At the same time, IRAS observations at 100$\mu$m have brought to light patchy infrared "cirrus" in some directions at high galactic latitudes. The dust in the cirrus is at 25K, generally in equilibrium with the interstellar radiation field, although a hot component may be present as well. The cirrus shows structure on scales of a few arcminutes to degrees. There is generally an excellent correlation of far IR and 21 cm emission, with occasional exceptions (Low et al. 1984, Terebey and Fich 1986) . Observations of the far UV diffuse background have demonstrated that it is dominated by backscattered starlight from galactic dust (Paresce, McKee and Bowyer 1980; Hurwitz, Bowyer and Martin 1991).

The heating of dust in external galaxies by young stars is responsible for the infrared luminosity of many galaxies. A complete accounting of the galaxy's luminosity requires a measurement of both the far IR and the far UV flux, where an significant fraction of the stellar luminosity escapes.

The JUNO photometric survey will provide four measurements which bear on dust and extinction in this and other galaxies. The photometric survey will produce a complete map of the reflection from high latitude dust. We will be sensitive to features of 200 $(\Omega/1\ sq.\ arcmin)^{-1}$ ph $cm^{-2}s^{-1}Å^{-1}$on angular scales of $\Omega$. Because the scattering is optically thin at the poles, and the albedo and scattering function

are unlikely to vary, the reflection map is essentially equivalent to an extinction map. We will use the UV galaxy number count survey to verify this, providing an independent measurement of extinction variations. During the low and intermediate latitude parts of the all-sky survey, we will use A0 stars to map out the galactic dust distribution with unprecedented scope and detail: E(B-V) will be determined with an accuracy of $\pm 0.02$ mag, with a three dimensional resolution of $< 50$pc, and to a distance of $>5$ kpc (see section 2). Finally, our spectroscopic and photometric galaxy survey will combine UV stellar population synthesis and comparison with IRAS observations to study systematically the physical properties of dust in external galaxies and their relationship to metallicity, stellar population, morphological type, and other observables.

*Galactic Bubbles and Supperbubbles.* The galactic extinction map derived from A0 stars will provide a global survey of the three dimensional distribution of dust within a 5 kpc radius. We will search for voids in the distribution which may accompany low density "bubbles" and "superbubbles" which may have been carved out by the action of single or multiple supernovae and stellar winds. We will determine whether these low density regions, which form an important component of certain global ISM models (McKee and Ostriker 1977; Castor, McCray and Weaver 1977; Heiles 1987; MacLow and McCray 1988), are common in and out of spiral arms. Voids can be associated with HI 21 cm features (supershells, arcs, "worms") and with diffuse soft x-ray emission, to determine the energetics and influence on the ambient ISM.

*Late Radiative Supernova Remnants in the Disk of Our Galaxy* JUNO will perform a survey of Galactic disk for late-stage radiative supernova remnants, by detecting the CIV line in the synthetic **16N** band. It is commonly accepted that supernova explosions (and to a lesser extent stellar winds) create the hot ISM in galaxies. However, no global theory for the generation and maintainance of the hot phase has been successfully confronted with observations. In all hot ISM theories, the late evolution of supernova remnants plays a critical role in determining the temperature, pressure, and filling factor of the hot phase. For example, the supernova rate and the radiative diameter determines the filling factor ($f_H$) and the basic topology of the hot phase. If a typical SNR grows to overlap a neighboring SNR prior to becoming fully radiative, $f_H \sim 1$. Thus the presence of fully radiative SNR should be anticorrelated with that of a distributed hot ISM. Radiative SNR with shock velocities $v_s > 60$ km/s are copious emitters of far UV line emission. All SNR younger than 200,000 yrs expanding into a homogeneous ambient density of $n_0$=1 $cm^{-3}$ will have $v_s > 60$ km/s. A large number of SNR will be present in Sb/Sc galaxies with ages younger than this, ~4000 for a galaxy like the Milky Way. Although several hundred would be predicted to be within 2 kpc of the Sun, only a handful of very old SNR have been identified.

The JUNO survey of the Galactic disk should detect $\sim$ 1000 radiative SNR. A typical remnant would be 60-120 arcminutes in diameter. The SNRs would be bright enough to be mapped with 4′ resolution (S/N=5). (Note that if $n_0$=0.1 $cm^{-3}$, rather than 1 $cm^{-3}$, there will be more SNR with lower surface brightness.) With large number of predicted old remnants, it should be possible to test scenarios for the late stages of SNR evolution. From the far UV measurements alone, we will obtain diameter and flux, along with the statistical distribution and correlation function in the galaxy. From these, we can estimate the distribution of ages and ambient density, and the overall supernova rate. the morphology of the remnants will tell us much about the final stages of SNR, and about the connection between SNR and the distributed hot ISM. We will thus be able to probe the importance of ISM inhomogeneity, magnetic fields, correlated SNe, remnant overlap and the formation of connected, hot tunnels on the demographics and evolution of late stage SNR.

### C.5 Stellar Formation, Evolution, and Activity

#### C.5.1 Young Stars and Stellar Activity

*Early-type stars, Winds and the IMF Upper Mass Limit.* As hot stars emit the bulk of their energy in the UV, they can be very useful in mapping more deeply the spiral arms of galaxies. As demonstrated by earlier experiments, the UV is also a useful probe of stellar atmospheres, since there are many spectral

lines in the proposed wavelength range that are sensitive to the star temperature and luminosity. Reliable spectral classification of early type stars can be performed with low resolution spectra. Also, mass loss and wind ionization can be studied. The luminosity sensitive SiIV and CIV lines can be used to study the upper mass limit of the initial mass function in a large number of normal and active galaxies, to determine whether the cutoff depends on metallicity, gas density, or other parameters.

*Stellar Activity.* Stellar activity is a generic term referring to phenomena that occur when mechanical heating and/or locally strong magnetic fields modify the momentum and energy balance in the outer layers of a stellar atmosphere. In spite of the enormous progress achieved through the observations with the IUE and SMM, many issues remain. For example, the nature of stellar activity, its dependence on the strength of the dynamo that amplifies magnetic fields and, consequently, on stellar rotation and on the convective turn-over time continue to be unclear. A UV diagnosis of stellar activity can be made through the detection of emission lines of He II, C IV, Si IV, S I, C I and Fe II in the range 1300-2000 Å. The identification of a large sample of different classes of active objects can help us to understand the causes for the great variation in the characteristic parameters as one goes across some specific regions in the HR diagram (the Linsky-Haisch dividing line). The sharpness of the transition and its implications in terms of stellar evolution and mass loss could be statistically investigated. More UV data, in particular for objects in this region of the HR diagram can help us to investigate the causes of transition between "solar" and "non-solar" types of atmospheres, and the existence of "hybrid" stars that show both types of behaviour. Yellow and red giants and supergiants would be the best targets for such a study. The time resolution capability of the instrument would also be useful to discriminate different kinds of objects: flare stars, for example, with brightness variations on a timescale of a few minutes can be used to classify the sources. During the whole survey a very large number of flares should be detected, allowing us to study in detail the UV luminosity and frequency functions for this phenomenom. For the brightest sources, spectroscopic information from lines such as Si IV 1400 Å can be used to test the origin of the flares, since these lines seem to be formed in a cooling plasma during the decay phase of the event. For the coolest members of the active dwarfs, like de dMe6 objects, only a few ($\sim$100) would be spectroscopically observable out to 35 pc; for dMe5 this number grows to 1,500 out to a distance of 80 pc, and reaches a large number for earlier dMe types.

*Activity in Very Young Stars* A deep spectroscopic survey on selected fields could yield information on T Tauri stars, such as their spatial densities in massive OB associations, the presence of T Tauri out of clouds, and the presence of a large number of post-T Tauri objects in the Galaxy. It would be also interesting to use spectroscopic information from the broadened lines of C IV and Si IV that are present in Herbig Ae objects and in particular, to see if this kind of population is always spatially related to cloud regions. The Herbig Haro objects, which are structures associated to star formation regions, can also be detected in any survey of T Tauri stars.

### C.5.2 Post Main-Sequence Evolution: Massive Stars

*Wolf-Rayet Stars* It is believed that the remnants of evolved massive stars, after they have lost their outer H-rich envelope by a strong wind, are Wolf-Rayet (WR) stars (Maeder 1987). This scenario, as well as which stars are the progenitors of WR stars, can be tested through the comparison of the spatial density ratio between suspected progenitors and WR's with the ratio between the relevant life-time in each evolutionary phase. Also, the comparison of the star formation history in our own galaxy with that which occurred in other nearby systems, such as the Magellanic Clouds, is very important for studying the effects of the different environmental conditions (e.g., metallicity effects). The census of the WR stars in the Magellanic Clouds is restricted at the moment to the bright-side of the luminosity distribution. The proposed experiment should detect all of the WR stars in the MCs, as well as M31 and M33. Besides that, spectroscopic observations in the far UV and in the optical will provide enough information for a reliable classification in subtypes (WNs and WCs). The WN/WC density ratio can be used to compare the star

formation history in our galaxy, the Magellanic Clouds, M31 and M33

### C.5.3 Post Main-Sequence Evolution: Low Mass Stars

*Blue Horizontal Branch Stars.* The all-sky survey will produce a complete sample of blue horizontal branch stars in the halo. The sample size will be so large that many stars will be found in rare stages of stellar evolution. This is particularly true in fields toward the nuclear bulge. The stars responsible for the mysterious far-UV rising flux in late galaxy populations may be identified in the bulge of our own galaxy. JUNO will discover rare phases of post-asymptotic giant branch evolution in the outer portions of the Magellanic clouds and possibly in some galactic globular clusters.

*Planetary Nebula Nuclei (PNN).* The nuclei of planetary nebulae (PNN) are thought to have evolved away from the Asymptotic Giant Banch (AGB). This evolutionary scenario can be tested in if the PNN are placed in the HR diagram. However, for many high-excitation nebulae, the PNN were not detected at optical wavelengths, since they are quite faint. On the other hand, the temperature of those PNN, based on the energy loss from the nebula through the collisionally excited lines (the Stoy-Temperature) are expected to be quite high. Values around 150,000 K or even higher are estimated from the Stoy-method. The sensitivity of the experiment at $\sim$1600 Å will certainly allow the detection of many of those unseen PNN. Moreover, spectral data in the 1250-1900 Å range will give additional information about the continuum emission from the PNN, as well as about the presence (or not) of a stellar wind in those hot objects.

*Subdwarfs.* The evolutionary status of subdwarf stars is unclear. Currently, four classes of Sd stars have been recognized, on the basis of their temperature: SdB, SdOB, SdO and "hot Sd". One possibility is that these classes form the bluest end of an extended horizontal branch (EHB) formed by stars that suffered the greatest mass loss as red giants. (Greenstein and Sargent 1974). Alternatively, they could represent an evolutionary sequence following on the asymptotic giant branch (AGB) phase (double shell burning) and planetary nebula formation, or directly from the HB stage (when there is insufficient envelope mass to support shell burning). The observed range of He/H ratios in Sd's are not comfortably accommodated by either scheme. Observationally, the basic difficulty is the small number of known Sd's and PNN's, which renders statistical conclusions about the lifetime of each state and the relationship between classes extremely uncertain. The JUNO mission will discover a large number of new objects, and provide spectral typing information for many. The deep surveys of the Magellanic Clouds and the galactic bulge will detect all PNN and Sd stars, and UV-V colors will allow us to construct complete HR diagrams in population I and II systems. The spectroscopic survey will detect most of the PNN and Sd stars in the MC's and bulge. In the disk and halo, a large number of Sd's will be found in the all-sky and spectroscopic surveys, including many in galactic and globular clusters. The disk Sd's at moderate to high galactic latitudes will be much brighter than WD's in the same color interval. Halo Sd's (which can be detected beyond 10 kpc), will be distinguished by their redder 14-18 colors. In the spectroscopy survey, helium rich subdwarfs will exhibit strong HeII $\lambda$1640 line, which can used along with the continuum to derive the temperature and gravity.

# APPENDIX D

## JUNO

# APPENDIX D. JUNO

## JUNO EXPERIMENT ELECTRONICS

A detailed description of the MCP detector is given in Section 4.3, and A.2 of the proposal. A complete discussion of the resolution, area, pixel size, linearity and count rate limitations of the MCP detector and delay line readout is also presented in Section 4.3, and A.2 of the proposal. This section deals with the front end electronics and the digital processing units.

### D.1. Front End Electronics

Each telescope microchannel plate (MCP) detector has an identical dedicated front end electronics section as shown in Figure D.1. The signals from each end of the delay line are differentially connected to wide bandwidth (100 MHz), low noise ($20\mu$V rms), $\sim 40$ db gain, differential input preamplifiers through an impedance matching broadband transformer. The totally differential input minimizes noise pickup and crosstalk between the x,y delay lines (high common mode rejection) and reduces the time dispersion of the signal. There are now readily available current feedback opamps utilizing thin/thick film resistor and bipolar junction transistor (BJT) technology that offer a nearly constant 3 db bandwidth over a wide range of gain in contrast to the normal voltage feedback types with nearly consant gain-bandwidth product. This tremendously eases the selection process. Completed measurements in the lab with these current feedback types have demonstated very satisfactory results.

As discussed in the Technical Section of this proposal, the position measurement is performed by differencing the time of arrival of the pulses eminating from both ends of the delay line with constant fraction discriminators (CFD's) and converting the time difference into a proportional amplitude analog signal using a time to amplitude converter (TAC). The CFD's are used to generate start and stop timing pulses which in turn, controls the height of a ramp voltage generated in the TAC. The analog signal is then digitized into a digital signal using a fast analog to digital converter (ADC).

The pulse signals exiting the delay lines have rise/fall times in the order of $5 \pm 2$ nsec with a full width half maximum (FWHM) time-width of $9 \pm 3$ nsec and an amplitude variation of 4:1. The total delay of the delay lines is in the order of 100 nsec which requires a time resolution in the order of 30 psec (FWHM) to produce the necessary position resolution of 30 $\mu$m (FWHM).

To realize this resolution, the timing discriminator must be independent of amplitude and independent of irregularities in the pulse shape over a wide temperature range. The constant fraction discriminator provides these type of characteristics because the crossover time is determined only at a fraction of the pulse height, that is, the crossover time is normalized to the pulse amplitude and not the shape of the pulse. The exact fraction required depends on the pulse shape and has been experimentally determined to be in the order of 0.5. A preliminary design of the constant fraction discriminator has been completed using the Plessey SP9687 ultra fast dual comparator. The comparator is manufactured by a high performance bipolar process with a differential input and complimentary emitter

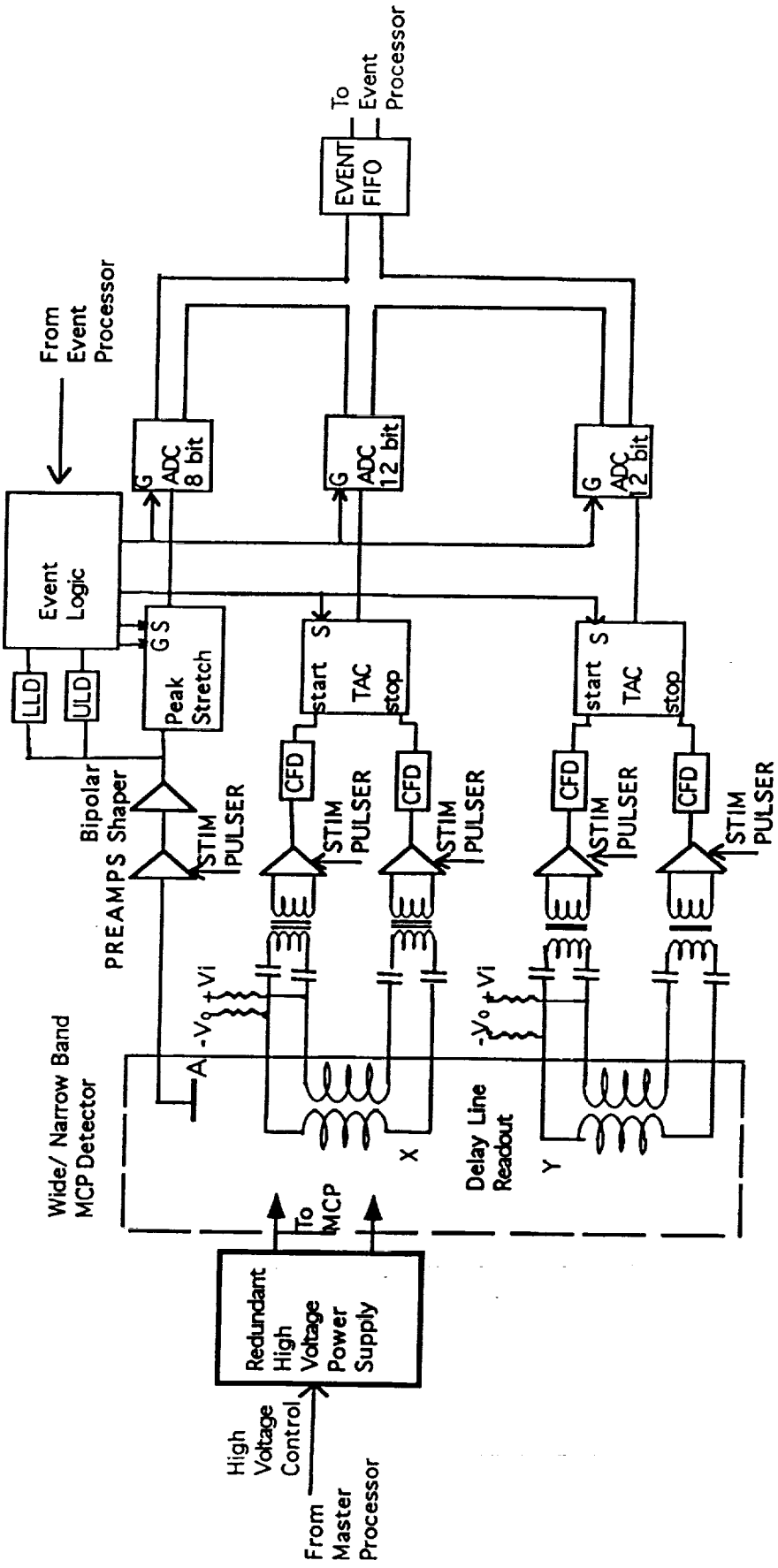


**Fig. D.1. 1/2 UV SMEX Front End Electronics Block Diagram**

coupled logic (ECL) outputs designed for 50 ohm terminations. ECL digital circuits are then used to provide the required start and stop signals. The timing walk and jitter are approximately 7 psec (FWHM) each, over the temperature range.

In addition to the ramp generator, the TAC contains timing management logic to prevent erroneous conditions between the start and stop pulses from locking up the system or causing pile-up situations.. Examples of such conditions include cases where the start pulse is not followed by a stop pulse within a specified time interval, the stop pulse arrives before the start pulse and to inhibit successive pulses until the conversion is completed. In addition to time walk and jitter compensation circuitry, it is anticipated that temperature compensation will also be required to provide a differential non-linearity of 1.0% and an integral non-linearity of 0.1% over the operating temperature range. The time walk and jitter will be maintained to 12 psec (FWHM). The design goal is that the CFD and TAC operate successfully with a 1 MHz pulse rate with a pulse-pair resolving time of 1$\mu$sec without any degradation of the stability requirements. The output of the TAC's will be digitized with 12 bit ADC's.

A pulse amplitude is picked off from the bottom anode and is used to control event timing. The anode pulse is bipolar shaped with a fast semi-gaussian waveshape for triggering the event control logic, for generating the event time signal and for coincidence avoidance. The amplitude is peak stretched and digitized with an 8-bit ADC.

The design requirements for the ADC is to handle a random 100 kHz event rate with 10% dead time. In order to keep the power dissipated per ADC less than or equal to 1 Watt (a good rule of thumb), and to meet the overall conversion time of 1$\mu$sec, we will use dedicated ADC's for each conversion. The ADI671, for example, a high speed 12 bit ADC, uses a subranging flash conversion technique, with a digital error correction for the first part of the conversion cycle, to provide a 500 nsec conversion time and dissipating only 0.5 Watt.

The digitized data from the three ADC's is then transferred by hardware and event timing to the event FIFO for temporary storage to be formatted by the event processor.

## D.2. Digital Processing Units (DPU)

Since the two telescopes require separate front end electronics, it is natural to extend this concept as a feature through the digital processing electronics as well. Two identical DPU's will be built, one dedicated to each telescope. This both simplifies the interface to the detectors and insures that no single point failure will result in the complete loss of the experiment. At this point, we are considering cross-strapping the inputs and/or the outputs of the DPU's to provide additional reliability at very little cost, space and time.

The potentially high detector event rate of 100 kHz requires that the two DPU's be capable of high real time performance. We propose to achieve that performance with a series of relatively simple, yet powerful, processors arranged in pipeline configurations (see Figure D.2, Block Diagram of the DPU), so that individual processors are carefully matched with the various processing tasks required. This approach simplifies the design of the individual processor sections and also relaxes timing requirements on components and communication pathways.

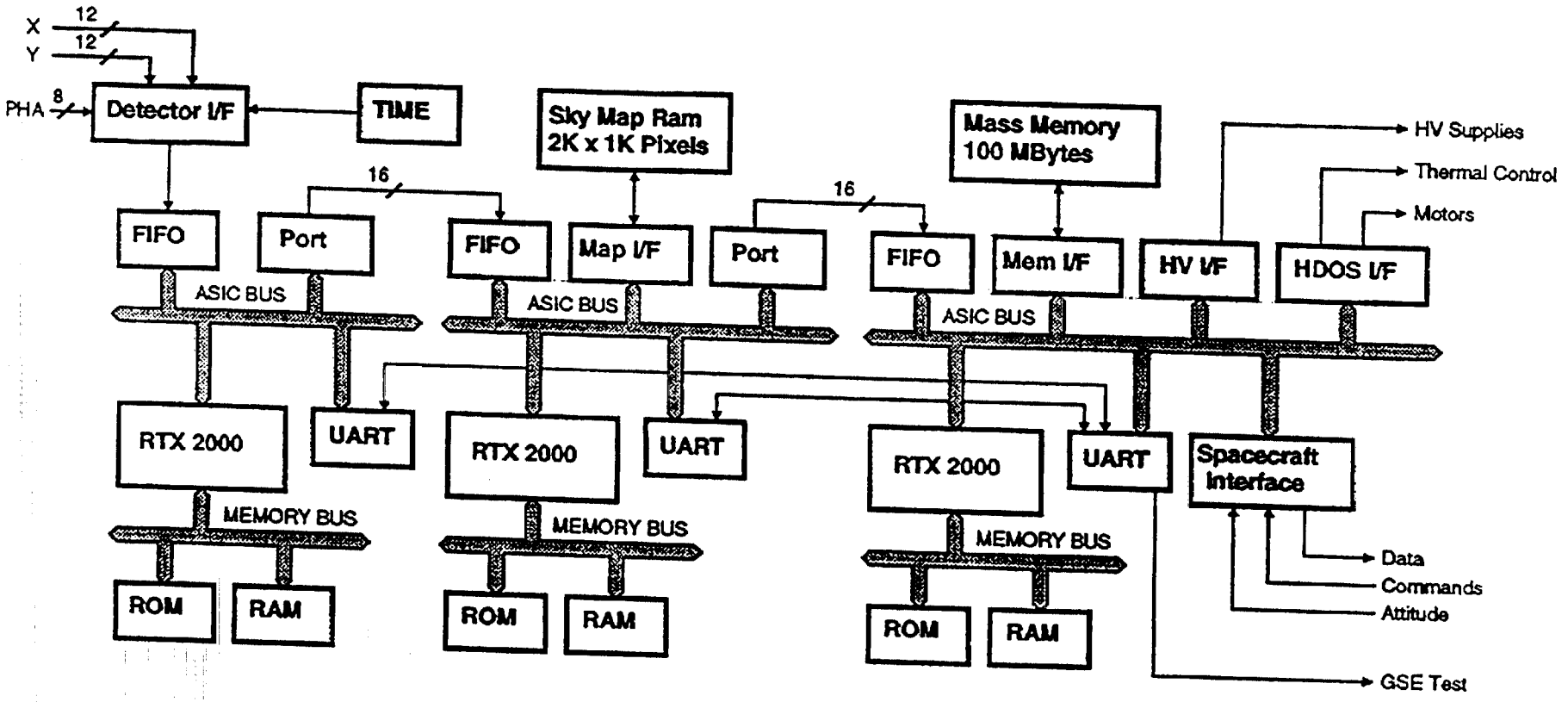


**ASIC Bus** - Application Specific IC Bus, Dedicated I/O Bus of the RTX 2000

**FIFO** - First-In First-Out Memory used as a temporary data buffer

**HDOS I/F** - Interface to the Hughes Danbury Optical Systems Electronics

**HV I/F** - Interface to the High-Voltage Power Supplies

**Map I/F** - Interface to the Sky Map RAM

**Mem I/F** - Interface to the Mass Memory

**RT X200** - Harris, High-Speed 16-bit Microcontroller

**UART** - Universal Asynchronous Receiver Transmitter, Serial Communication Port

**Fig. D.2. 1/2 UV SMEX DPU Block Diagram**

Each DPU contains three Harris RTX-2010 microcontrollers. The RTX-2000 is a fast (8-10 MIPS) 16-bit processor well suited to tasks requiring high real-time performance. It is a stack-based processor with two internal 256-word stacks. The programming language FORTH is used as its assembly language. It supports both a 16-bit wide memory bus and a separate 16-bit I/O bus, called the Application Specific IC bus (ASIC bus), allowing simultaneous data transfers on both.

The first processor inputs position, pulse-height, and time data from the detector via a FIFO memory. This processor is responsible for correcting position errors due to various detector non-linearities and spacecraft drift. When this task is completed, the results are output to a second FIFO memory which is at the input to the second processor.

The second processor forms and maintains a sky image in memory by incrementing pixel locations which correspond to input photon events. This sky image allows bright objects to be located. Events that are associated with bright objects are logged into a bright pixel list; events that are not associated with a bright object are sent to the third processor (again via FIFO memory) where they can be stored in raw form into a mass memory.

The third processor maintains the large mass memory ($\gtrsim$100 MBytes), interfaces with the spacecraft, and controls and monitors the various experiment subsystems such as the low-voltage power supplies. It also communicates with the other processors via a relatively slow-speed serial communication link that is switched by the third processor. The third processor, which is the master, uses this communication link to control the other processors and to receive low-priority state-of-health data. This communication link is also used by the third processor to communicate with Ground Support Equipment during instrument testing.

The two Data Processing Units are housed in separate boxes (see Fig. D.3, Design Layout). Each box contains a low-voltage power supply for the digital and analog electronics, a high-voltage power supply for the detector, a detector interface module, a spacecraft interface module, three processor modules, two memory modules for the sky image, fourteen memory modules for the mass memory, three miscellanneous interface and FIFO modules, and one spare module. The sky image memory contains hardware Error Detection and Correction circuitry (EDAC), but the mass memory relies only on software error detection. Watch-dog timer circuitry are included in each processor module to guard against radiation-induced upsets. Table D.1 shows the DPU box size and weight estimates.

## D.3. Data Compression and Storage

To accomodate the the large dynamic range of count rates from weak to bright stars, $10^4 - 10^5$ counts per second, the fast front end electronics (FFEE) and the DPU's with digital processing compression techniques, are used to prevent saturation of the mass memory and to efficiently transmit a huge amount of data to the ground station. The second digital processor will accumulate a temporary Coarse Imaging Memory Map (CIMM) and a Bright Pixel List (BPL). Each photon received from the event corrected processor will be temporarily stored and incremented in a bin location corresponding to its positional (x,y) coordinates in the CIMM. When the accumulated count in a bin exceeds a commandable event rate threshold, the position of this star is "flagged" and is placed in the BPL. The

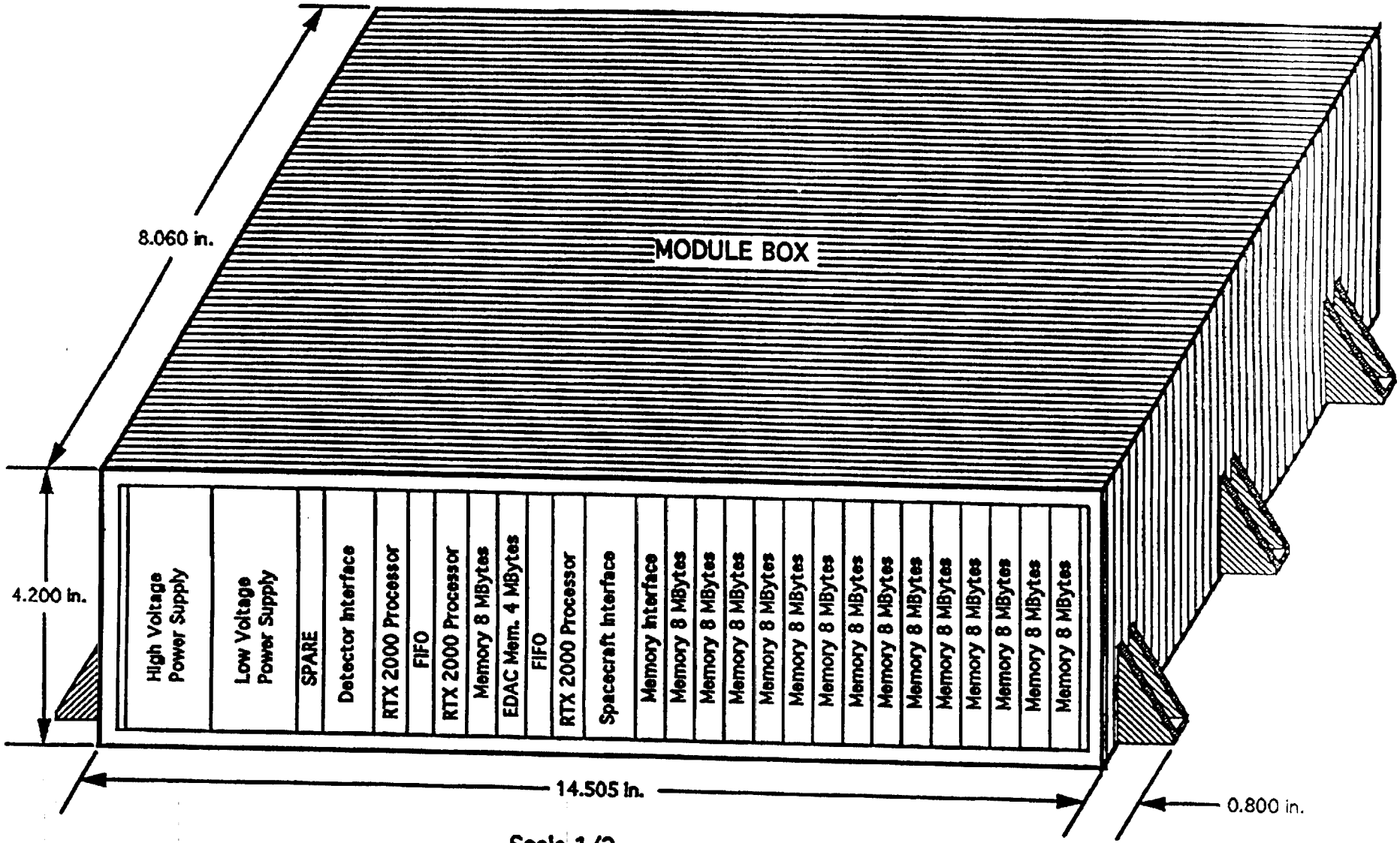


**Fig. D.3. UV SMEX Design Layout**

## Table D.1: DPU Box Size and Weight Estimates*

| Item | Quantity | Spacing | Cumulative Width | Weight | Cumulative Weight |
|---|---|---|---|---|---|
| | | | | | |
| Memory Module | 16 ea. | 0.425 in. | 6.800 in. | 0.57 lb. | 9.12 lb. |
| Processor Module | 3 ea. | 0.475 in. | 1.425 in. | 0.40 lb. | 1.20 lb. |
| FIFO Module | 2 ea. | 0.375 in. | 0.750 in. | 0.30 lb. | 0.60 lb. |
| Low Voltage Power Supply | 1 ea. | 1.250 in. | 1.250 in. | 1.10 lb. | 1.10 lb. |
| High Voltage Power Supply | 1 ea. | 1.250 in. | 1.250 in. | 1.10 lb. | 1.10 lb. |
| Detector Interface | 1 ea. | 0.750 in. | 0.750 in. | 0.45 lb. | 0.45 lb. |
| Spacecraft Interface | 1 ea. | 0.750 in. | 0.750 in. | 0.45 lb. | 0.45 lb. |
| Memory Interface | 1 ea. | 0.425 in. | 0.425 in. | 0.30 lb. | 0.30 lb. |
| Spare Module | 1 ea. | 0.375 in. | 0.375 in. | 0.30 lb. | 0.30 lb. |
| | | | | | |
| Box Clearance | 2 | 0.125 in. | 0.250 in. | | |
| | | | | | |
| Box Walls | 2 | 0.240 in. | 0.480 in. | | |
| | | | | | |
| Module Box & Cover | | | | | |
| Motherboard Frame, Module & Cover | | | | 2.50 lb. | 2.50 lb. |
| | | | | 1.50 lb. | 1.50 lb. |
| Total | | | 14.505 in. | | 18.62 lb. |

*Notes: This estimate is for one DPU Box.
Two DPU boxes comprise a complete system.
Because of the width of the box, we may need to add a stiffening rib in the middle.
This would add an additional 0.350 in. to the width and 0.3 lb. to the weight.
We may also need to add an additional mounting foot on the front of the box.

BPL will be sub-commutated with the prime science data. Each photon not contained in the BPL is shifted to the third processor where it is formatted and stored in the mass memory as a 32 bit word. The 32 bit event word consists of 12 bits of x,y position data, 4 bits of pulse height and 4 bits for time of arrival.

A single nighttime orbit ($\sim$ 25 minutes) requires a 200 MByte memory. The mass memory will be divided into two 100 Mbyte sections, each contained in one of the DPU's. The 200 Mbyte mass memory consists of 384 - 4 Mbit CMOS static ram ceramic flat packs processed to MIL-STD-883, Method 5004. We are presently evaluating monolithic and hybrid 4 Mbit ceramic packs. Sixteen of the 4-Mbit rams are located on one printed circuit board as shown in Figure D.4, to form an 8 MByte ram module. Twenty-four 8 MByte ram modules constitute the 200 MByte mass memory.

A typical 4 Mbit CMOS static ram is the Hitachi HM628512, 524,288 wordx8 bit monolithic integrated circuit (IC) CMOS static ram. The access time is available in 70/85/100 nsec versions. The stand-by power is 10 uW typical and the typical operating power is 275 mW. It is powered by a single 5V supply. There are two modes of operation. The IC memory under control of the CS, OE and WE control functions sets the IC memory for stand-by or read/write operations. The bulk of the mass memory is stand-by while one or two memories are in operation at any given time.

## D.4. Telemetry

The 200 MByte mass storage requires a 2.5 MBit/sec telemetry rate to dump the data in approximately 10 minutes, the typical time for a ground station pass. The 2.5 MBit/sec plus several hundred KHz for the satellite housekeeping (under 3 MHz) is limited by the telemtry rate of most current S-Band transceivers and ground station capabilities. The telemetry data will be formatted in a Manchester II (Biphase-L) Encoded Time Division Serial Code to take advantage of the bandwidth reduction, self-error detection and ease of synchronization over the usual NRZ code. The Manchester II encoding can be accomplished with a two chip set including a Harris CMOS Manchester Encoder-Decoder HD-15531 chip and a DDC BUS-63100 Series 1553 Transceiver or equivalent. The telemetry data will then modulate the Quadruple Phase Shift Keyer (QPSK) modulator of the transmitter as described in the Alenia Spacecraft section of the proposal.

A simplified scheme for time tagging events can be obtained by using the 4 bits as a vernier in conjunction with the spacecraft clock or synchronization frequencies (e.g. 1 Hz). Assume the telemetry is formatted in a 40 (Row) $\times$40 (Column) word matrix consisting of 32 bit words. A single row of data, referred to as the minor frame, will take .512 msec to be shted out to the QPSK modulator. A major frame consisting of 40 minor frames would take 2.048 msec to shift out. The mass memory, referred to as the block frame, would consist of 800 major frames. Frame synchronization identification codes, GMT time, frame counting words and parity checks are provided to maintain synchronization. The clock used for the time of arrival must be in synchronism with the spacecraft clock. The 4 bits of time information will function as a vernier scaled from the time interval similar to the minor frame, e.g. 0.512 msec will provide 32$\mu$sec time resolution.

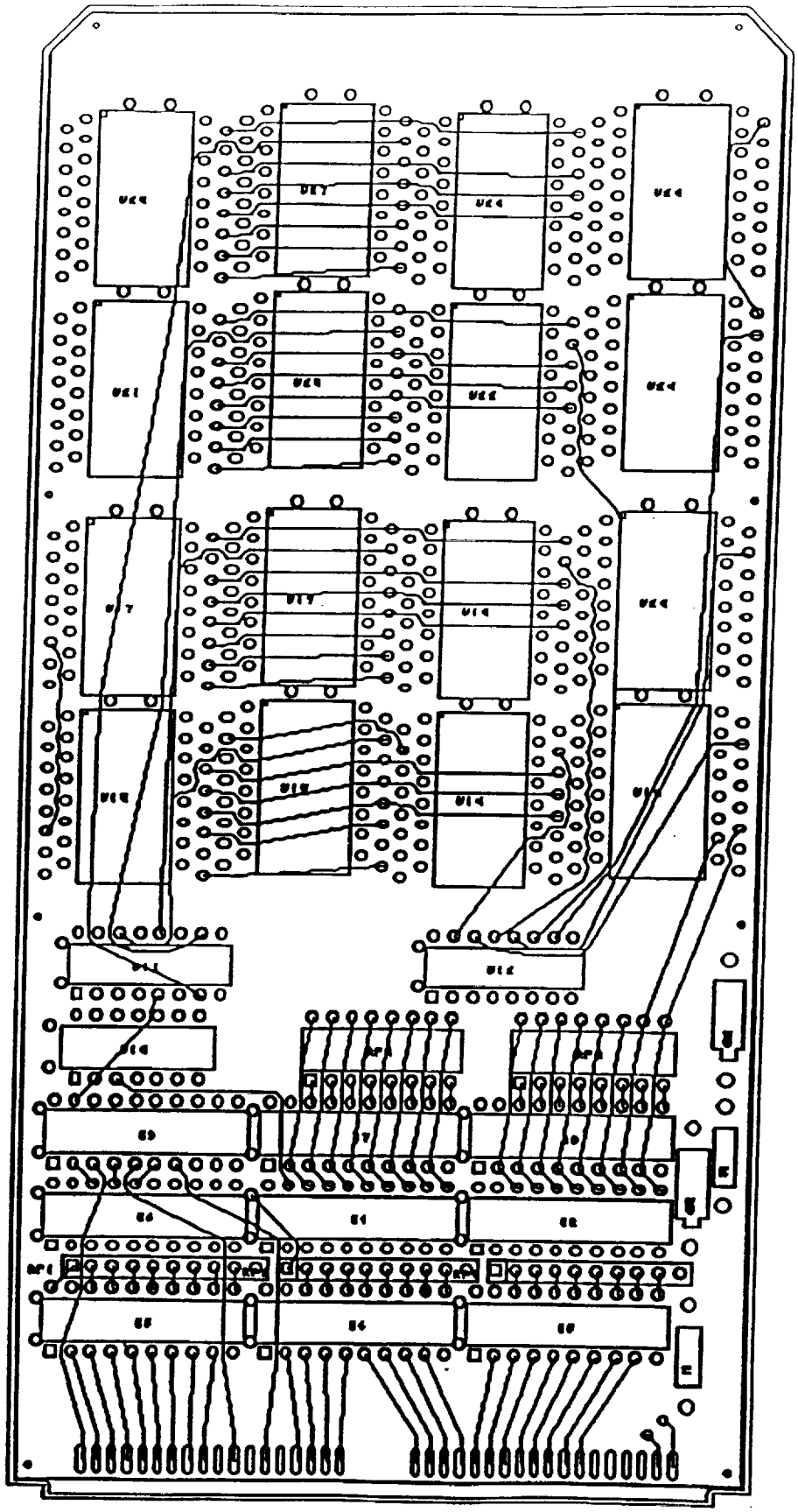

Fig. D.4. Printed Circuit Board Layout of 8 MByte Ram Module

### D.5. Secondary Science

The event processing logic will provide background and diagnostic science parameters such as lower and upper rates, valid event rates and system busy losses. These secondary science parameters will be stored and formatted by the event processor and sub-commutated at a very low rate with the prime science.

### D.6. High Count Rate Monitor

A commandable, high count rate threshold monitor will ramp the MCP detector high voltage power supply to a low value when the incoming event rate exceeds a commandable threshold. This will decrease the gain of the MCP detector to zero and enhance the lifetime of the detector. Ramping minimizes stessing the high voltage components. The monitor will be extremely useful in detecting when the JUNO experiment is approaching and leaving the South Atlantic Anomoly region. Sufficient hysteresis will be provided to to minimize stressing during shut-down and turn-on periods.

### D.7. High Voltage Power Supply

The MCP detector will be biased by a redundant pair of programmable bias high voltage power supplies (HVPS). The design of the HVPS utilizes a dc-dc converter with a non-saturating sinusoidal oscillator to minmize EMI and switching transients. A high operating frequency of 200 kHz minimizes filtering requirements and reduces the weight and size of the components. Magnetic shielding reduces the magnetic effects. A sense winding on the transformer tightly coupled to the output winding, supplies a feedback signal through an error difference amplifier to control the high output voltage. This technique of regulation and feedback achieves a high degree of regulation, temperature stability and efficiency. Reverse polarity/input protection and isolated grounds between the input and output are provideed.

Sandia National Laboratories has extensive experience (i.e. $>$ 15 years) in building HVPS for use in rockets, satellites, and deep space probes. Incoming inspection tests including x-ray analysis, vibration and shock testing, thermal vacuum cycling and life testing in vacuum will be utilized to secure a high level of reliability and quality assurance. CAL has satisfactorily flown these types of HVPS in more than 15 rocket flights, on the OSO-8 Mission, and on the Space Shuttle STS-3 Mission.

### D.8. Command System

The JUNO experiment will require discrete bilevel commands and a 16 bit serial digital command. The discrete bilevel commands will be used to control magnetic latching relays for on/off control of power and heater circuits. Bilevel commands may also be used for releasing the dust cover, on/off control of the detector valve, various drive mechanisms, and the CPU resets. The serial digital command will be used for programming the various rate thresholds, pulse height level window, MCP detector high voltage power supplies and thermistor settings. The uplink bandwidth will be in the 2-4 kHz range.

## D.9. Stimulation Pulser

A charge stimulation pulser will be incorporated into the design for the "on-board" flight calibration of the electronics system. A commandable, low power, low noise, CMOS analog multiplexer, will be used to gate the test pulse or pulse pair into any combination of preamps. The test pulser will be used to verify the gain stability and noise of the Delay Line Readout channel and test the operation of the event processing logic and the prime science telemetry output stream. A preprogrammed test will calibrate the electronic imaging resolution and linearity across the entire field of view.

## D.10. Power Requirements

A summary of the JUNO experiment power requirements is shown in Table D.2 below.

**Table D.2. JUNO SMEX Power Budget**

| | | Power/ Unit | #/Tel | Power Reg | Power Unreg |
|---|---|---|---|---|---|
| DETECTOR | HV Supplies | 1.20 | 1.0 | | 1.20 |
| | Preamps | 0.50 | 5.0 | 2.50 | |
| | CFD's | 1.00 | 4.0 | 4.00 | |
| | TAC's | 0.80 | 2.0 | 1.60 | |
| | ADC (12 bit) | 0.80 | 2.0 | 1.60 | |
| | ADC (8 bit) | 0.20 | 1.0 | 0.20 | |
| | Discriminator | 0.30 | 2.0 | 0.60 | |
| | Peak Stretch | 1.00 | 2.0 | 2.00 | |
| | Shaper | 0.50 | 1.0 | 0.50 | |
| | Telescope 1 | | | 12.00 | 1.2 |
| | Telescope 2 | | | 12.00 | 1.2 |
| DPU | Event Logic | 0.50 | 1.0 | 0.50 | |
| | Processors | 0.50 | 3.0 | 1.50 | |
| | Fifo | 0.20 | 3.0 | 0.60 | |
| | Program Map | 0.40 | 3.0 | 1.20 | |
| | Sky Map Memory | 0.30 | 1.0 | 0.30 | |
| | Mass Memory | 2.00 | 1.0 | 2.00 | |
| | TM/CMD I/F | 0.80 | 1.0 | 0.80 | |
| | Housekeeping | 0.50 | 1.0 | 0.50 | |
| | Contingency | 0.80 | 1.0 | 0.80 | |
| | DPU 1 | | | 8.20 | |
| | DPU 2 | | | 8.20 | |
| TOTAL REGULATED | | | | 40.40 | |
| TOTAL UNREGULATED | | | | | 2.40 |
| LOW VOLTAGE CONVERTER 70% | | | | | 17.31 |
| OBSERVING TOTAL (Peak) | | | | | 60.11 |
| THERMAL CONTROL | | | | | 20.00 |
| TOTAL ORBITAL AVERAGE | 0.43 x P (op) + P (th) | | | | 45.85 |
| CONTINGENCY 20% | | | | | 9.17 |
| TOTAL ORB. + CONTINGENCY | | | | | 55.02 |

# APPENDIX E

## Orbital Environmental Effects

# APPENDIX E. ORBITAL ENVIRONMENTAL EFFECTS

## E.1. Radiation Effects on Electronics Systems

### E.1.1. Radiation Environment

The ionizing radiation environment in a low altitude equatorial orbit is comparatively benign. The radiation encountered in the low equatorial orbit of the JUNO satellite includes a reduced charged particle flux (eg. protons, electrons, alpha particles, ions, etc...) from the South Atlantic Anomoly, Solar Flare Activity and energetic solar particles. The JUNO satellite orbit is shielded from the galactic cosmic ray flux by the earth's magnetosphere. Protons trapped in the earth's radiation belt and cosmic rays are the source for single event upsets to be encountered in orbit. The non-charged radiation environment in the low orbit consists mainly of gamma radiation. For the purposes of assessing radiation levels, we have assumed a critical orbit dispersion which achieves the maximum effective altitude (95% confidence level). This orbit has an 800 km apogee and 650 km perigee. We estimate conservatively from particle flux contours (Stanissopolis 1974) that with 3 $gm/cm^2$ shielding, the total mission dosage will be <0.5 kRads(Si).

### E.1.2. Radiation Effects

During the last two decades and especially the latter half of the 1980's with the advent of VLSI (Very Large Scale Integration) technology, the radiation environment in space has been observed to produce transient (temporary) and permanent damage to semiconductor integrated circuits flown in satellites. Radiation particles can be divided into three basic categories; photons (e.g. gamma rays, X-rays, etc...) charged particles (e.g. protons, electrons, cosmic rays, heavier ions, etc.) and neutrons. The interaction of these particles and energies with the different types of active semiconductor structures (e.g. nmos, pmos, cmos, bjt, etc...). in LSI or VLSI architectured devices can be broken down into two main malfunction mechanisms; displacement of atoms from their lattice structure (displacement damage) and generation of electron-hole pair carriers (ionization damage). Displacement damage caused by heavy charged particles and neutrons has not generally been observed in the space environment. Most malfunctions to microelectronic devices in spacecraft has resulted from ionization radiation. Ionization radiation, which accumulates in a device over a long period referred to as "total dose", produces an increase in charged carriers and trapped charges on the device surface layers. The charge trapping may cause threshold voltage shifts and increase leakage in MOS devices (eg. NMOS threshold decreases making it easier to turn-on and PMOS threshold increases making it harder to turn-on) eventually resulting in a device malfunction. CMOS devices are less sensitive to threshold shifts because of the highter threshold and use of complimentary pairs. Bipolar technologies are not strongly affected by total dose and have a threshold in the 100 kRad (Si) range. MOS and CMOS devices are unaffected by neutron bombardment up to fluences of $10^{15} n/cm^2$. Bipolar transistors are affected by neutrons because of the reduction in transister current gain caused by degraded carrier lifetime but also have a threshold in the order of $10^{14} n/cm^2$.

In recent years, microelectronics has turned to static CMOS technology to take advantage of the increased packing density and lower power requirements yielding cooler operating devices. Static CMOS microprocessors and memories do not require refresh write/read circuitry to retain storage data, further decreasing power drain. CMOS offers higher noise immunity providing a higher threshold voltage to ionizing radiation. One of the major disadvantages to CMOS technology was the "latch-up" effect. Early users of CMOS devices remember that static charges deposited simply by touching the device would sometimes cause the device to latch-up and malfunction.

The latch-up phenomenon has been thoroughly investigated and has been found to be caused by a four layer parasitic path (pnpn) existing in bulk CMOS devices shunting the CMOS device layout. The pnpn path is formed by parasitic npn and pnp bipolar transistors. During normal operations, one of these bipolar transistors forms a reversed-biased vertical path (junction) in the well material and the other a reversed-bias lateral path (junction) in the substrate. During irradiation, the gate and field silicon oxide materials ionize generating electron-hole carriers and trapped charges at the interface of the field oxide and the bulk silicon. When accumulated ionizing radiation ("total dose") produces sufficient current carriers, one or both of the parasitic transistors becomes forward-biased, pnpn regeneration takes place and a low impedance, high current path from $Vdd$ to ground ($Vss$) latches-up the device. Once attained, functionality is lost and device destruction may follow either through metallization or junction failure.

Bulk CMOS VLSI technology has resulted in smaller memory storage cells with smaller semiconductor structures yielding higher packaging densities. These trends initially seemed to have enhanced the latch-up problem and introduced some additional single event radiation effects. However, the requirements of VLSI technology in the last decade has resulted in new semiconductor technologies that have the capability of eliminating most malfunction radiation effects on microelectronic devices.

Smaller memory storage cells have resulted in smaller critical charges for changing the state of the data bit. Single event upsets (SEU) caused by heavy ion or cosmic ray particles results in a "soft error", when the charge deposited ("Threshold Linear Energy Transfer", LET) is greater than the critical charge required to change the state of the cell. No permanent damage results and the cell can be re-written.

Single event latch-up (SEL) can also occur when the heavy ion or cosmic ray particle has sufficient LET and the remaining ionizing track is long enough to punch through the well-substrate interface. This can induce the perviously discussed latch-up mechanism with the same results.

Radiation hardened (radhard) CMOS devices eliminate the latch-up problem completely by using Silicon-On-Insulation (SIO) technology including Silicon-On-Sapphire (SOS) and Silicon Isolated by Implanted Oxygen (SIMOX) to completely isolate the substrate, thereby eliminating the pnpn path that existed in bulk CMOS. These radhard devices feature a total dose capability of (30-100) kRad (Si), elimination of latch-up and SEL and reduced SEU events $\leq 1 \times 10^{-9}$ *upsets/bit-day.*

Another factor to consider is that many applications do not require this high level of radhardness and so new and cheaper technologies using bulk CMOS were developed. Polysilicon gate materials were developed in lieu of metallic gates eliminating alignment

tolerance problems and larger parasitic capacitances, and reducing interface state generation. Epitaxial-buried layer CMOS fabrication processes similar to bulk standard CMOS processes has completely eliminated the latch-up problem. The expitaxial layers reduce the lateral and vertical resistance paths in the substrate and well materials reducing voltage drops necessary to forward-bias the parasitic transistors and reduce the gain of the vertical parasitic transistor preventing regeneration. Control of the minority carrier life time by gold dopping or neutron irradiation has also eliminated latch-up but is more effective in larger geometries. The use of guard bands surrounding the n-channel devices prevents leakage current from the p-well flowing through parasitic paths (used in radhard devices). The use of some of these technologies in standard bulk CMOS devices has extended the total dose capabilities to 6–15 k Rad (Si), eliminated single event latch-up (SEL) and reduced single event upsets.

Table E.1 lists by Manufacturer some of the specific microelectronic devices proposed for flight use on this instrument and the results of performed radiation tests.

**Table E.1: Radiation Test Summary for Proposed Flight Microelectronics Devices**

| Device | Total Dose [kRad(Si)] | SEL $\frac{\text{Latchups}}{\text{mission}}$ | SEU $\frac{\text{upsets}}{\text{bit} - \text{day}}$ |
|---|---|---|---|
| Hitachi HM628512 RAM | to be tested at Sandia Natl. Labs. | | |
| Harris RTX 2010 Microcontroller | 100 | none | none |
| Analog Devices AD671 | 10 | not tested | not tested |
| Predicted Level | $< 0.5$ | | |

## E.2. Sources of Nighttime UV Background

A wide field imaging imaging experiment must contend with nighttime orbital background. The background rate affects the total counting rate of a photon-counting detector, and can degrade efficiency by increasing processing dead time. The faint magnitude limit will be determined by the background present in a resolution element. The background level is especially crictical for the objective spectroscopy phase. With a properly designed set of filters, the night sky in the far UV range can be as low as 1% of the visible night sky. To minimize airglow background, three observational constraints will be imposed on all observations: 1. the solar-zenith angle must be >130°(> 15 °below the depressed horizon); 2. the target-zenith angle must be <70°at all times, and 3. the sun-target angle must be > 160°. In this context, we consider here the important sources of nighttime background.

*Airglow.* By far the brightest emission line is from geocoronal HI Lyman $\alpha$ ($\lambda$1216), from solar Ly$\alpha$ multiply scattered into the shadow. Since I(1216)~1-3 kilorayleighs (1 Rayleigh = 1 R = $10^6/4\pi$ ph cm$^{-1}$ s$^{-1}$ Å$^{-1}$ sr$^{-1}$), it must be strongly attenuated by filters.

Nighttime recombination of ionospheric $O^+$ produces emission at $\lambda$1304 or $\lambda$1356. The former is a resonance line and can multiply scatter in the topside ionosphere. This process is enhanced at tropical latitudes, due to the Appleton anomaly and the tropical arc phenomenon (Hicks and Chubb 1970; Meier and Opal, 1973; Carruthers and Page 1976). During the day, an upward $E \times B$ ion drift produces enhanced densities in the tropical zones, peaking near ±15°magnetic dip latitude. Following sunset, there is increased recombination and its associated radiation. In the absence of magnetic storms, there is an emission trough at magnetic dip equator, ~15°wide. The average intensities observed for these lines , looking up from 600 km were measured by the P78-1 experiment (Bowyer et al. 1981; Chakrabarti 1984). They found typical intensities of 4 R in both lines outside the tropical arcs, and 20 R in the arcs, where in both cases the ratio I(1304)/I(1356)~3. The arc enhancement can be a strong function of local time, disappearing after local midnight. The equatorial minimum is observed to be washed out during strong geomagnetic storms, leading to intensities looking down from 600 km ~50-75% those in the arcs (Abreu et al. 1984). This implies that looking up, 10-15 R could be expected during geomagnetic storms. During the mid-1994 to late-1995 mission period, solar flare induced magnetic storms may be expected to occur at least monthly, with decay times of $\sim 1-2$ days. The oxygen lines can also be produced by collisional excitation by energetic particles. This process is important in the South Atlantic Anomaly, which our equatorial orbit grazes once per revolution. Existing data on SAA airglow is sparse, but indicates that oxygen collisional excitation is only modestly enhanced, and then only in the southeast region (Gledhill 1976). However, since the orbit altitude may range as high as 750 km, and the high energy particle background may also preclude observations in the SAA, we have assumed conservatively that SAA passages are unusable.

Emission from other atmospheric constituents, including chemiluminescent dissocation of NO and LBH $N_2$ bands, is expected to be negligible looking up at >450 km, because of the low N density at these altitudes. This has been confirmed by the UVX ultraviolet background experiments (Martin and Bowyer 1988; Tennyson et al. 1987). From the above discussion, we conclude that in order to ensure that a low background is achieved for the

photometric survey, the OI emission lines should be attenuated by filters.

*Ram Glow.* The first sensitive search for vehicle or ram glow in the far UV was performed by the UVX experiments referred to above, on board Space Shuttle at 280 km. No evidence of glow was found, with limits <50 ph $cm^{-1}$ $s^{-1}$ $Å^{-1}$ $sr^{-1}$. We therefore expect that at altitudes as high as 500 km, no significant UV emission will be present.

*Zodiacal Light.* The zodaical light, a major source of background in the visible, is neglible in the far ultraviolet, with a predicted intensity of 10 ph $cm^{-1}$ $s^{-1}$ $Å^{-1}$ $sr^{-1}$at $\lambda$1800, and <1 ph $cm^{-1}$ $s^{-1}$ $Å^{-1}$ $sr^{-1}$at $\lambda$ (Pitz 1978; Feldman 1977; Frey et al. 1977).

*Cosmic Far Ultraviolet Background.* With the proper choice of filters to eliminate OI emission, the cosmic UV background remains as the dominate source of diffuse emission in the 1350-2000Åband. Over the past 15 years, a combination of photometric data (Paresce et al. 1980, Jakobsen et al. 1984) and spectroscopic data (Maucherat et al. 1981, Hurwitz, Bowyer and Martin 1988) have demonstrated that the bulk of the diffuse continuum is due to scattering of galactic starlight by dust. From the recent UVX experiment (Martin and Bowyer 1984; Hurwitz et al.), we have confirmed that the diffuse background has a minimum in directions of low N(HI) of 200 ph $cm^{-1}$ $s^{-1}$ $Å^{-1}$ $sr^{-1}$, and rises to 1000 ph $cm^{-1}$ $s^{-1}$ $Å^{-1}$ $sr^{-1}$in the galactic plane. The source of the former flux is still unknown, while the latter value may include a significant unresolved stellar component. For the purpose of assessing its impact on the mission sensitivity, we model the background approximately with I(ph $cm^{-1}$ $s^{-1}$ $Å^{-1}$ $sr^{-1}$)=300+700cos($b$).

*Instrumental Background.* As is discussed in the next section, the detector dark background combined with filter fluorescence and phosphorescence should not exceed a few cts $cm^{-2}$ $s^{-1}$, which is equivalent to a continuum background of ~10 ph $cm^{-1}$ $s^{-1}$ $Å^{-1}$ $sr^{-1}$.

## E.3. Environmental Effects on Filters

When alkaline earth flouride crystals are used in a space environment, three negative characteristics must be addressed. These are (1) fluorescence and phosphorescence due to ionizing radiation, (2) transmission loss due to cumulative particle bombardment, and (3) temperature dependence of the index of refraction.

Both $CaF_2$ and $BaF_2$ exhibit fluorescence and phosphorescence from ionizing particles. Based on the fluorescence yields of Viehmann et al. (1975), the $BaF_2$ and $CaF_2$ emission spectrum, CsI photocathode quantum efficiency, and energy loss in 4 mm, 3 MeV electrons and 30 MeV protons should be detected with 100% efficiency. Outside the South Atlantic Anomoly (SAA), the detector background will increase by less than 1 ct $cm^2$ $sec^{-1}$, which is negligible compared to the diffuse UV background. This was confirmed during the flight of the Berkeley far UV spectrometer on Space Shuttle (Martin and Bowyer 1988), where background rates showed no detectable increase above the laboratory rate of 0.7 ct $cm^2$ $sec^{-1}$, with a 2 mm $BaF_2$ filter mounted at the detector. The equatorial orbit will graze the SAA for several minutes each orbit. The background rate at those times will be $10^2$-$100^3$ ct $cm^2$ $sec^{-1}$. At the high end of this range, observations will not be possible. Phosphorescence will occur after each SAA passage, with a time dependance: $R_{phos}(ctcm^2sec^{-1}) = 5exp(-t/2\ min) + 2exp(-t/45\ min) + 0.5exp(-t/580\ min)$, which represents an average increase of the background level of <4 ct $cm^2$ $sec^{-1}$.

We have assumed in the mission planning that no useful observations can take place while the spacecraft is grazing the SAA. The detector will be automatically shut down by a high countrate shutoff monitor.

The UV transmission of alkaline earth flourides degrades after bombardment by large fluences of high energy particles (Heath and Sacher 1965). Barium fluoride is extremely stable, showing no measurable change in the far UV after a $10^{14}$ $cm^{-2}$ fluence of 1 MeV electrons. Calcium fluoride shows a 10-20% absolute transmission loss, and magnesium fluoride a 10-30% loss. The total fluence of 1 MeV electrons will be $< 10^{10}$ $cm^{-2}$, (assuming no sheilding), and therefore we do not expect measurable degradation.

A third concern is the temperature sensitivity of the index of refraction. This has two effects: the short wavelength cutoff has a positive temperature slope, with $d\lambda_0/dT \sim 0.3$Å°C. As the temperature decreases, the transmission to the airglow emission lines of HI 1216Å($CaF_2$) and OI 1356Å($BaF_2$) increases. The Ly$\alpha$ transmission of the combined 2.5 mm and 1.5 mm filters will vary with temperature approximately as $T(1216) = 10^{-6}exp(-0.22T)$, where $T$ is in °C. We will maintain the of the detector filters $T > 10$°C, to ensure that $T(1216) < 10^{-7}$, which should be accomplished largely by the close thermal coupling with the detector and preamplifiers. In addition, a filter heater will be mounted nearby.

The index of refraction of the filters and prism changes with temperature. The resulting change in focus will be neglible, even over the 0-50°C range. However, the prism refraction angle will exhibit a shift in the range 0-1Åwith a 25°C excursion. Since we expect that temperature gradients across the prisms will be <5°C, this shift can be corrected to better than 0.1-0.2Å, with passive thermal monitoring, and without active temperature control.

# APPENDIX F

## Additional Concerns for Wide Field Astronomical Telescopes

# APPENDIX F. ADDITIONAL CONCERNS FOR WIDE FIELD ASTRONOMICAL TELESCOPES

## F.1 Spectrum Confusion.

Deep objective prism surveys are subject to source crowding. One advantage of performing surveys in the far UV is the dramatically reduced number of stars. However, at the faintest magnitudes, galaxies dominate the surface density distribution.

To evaluate the crowding problem, we have assumed that galaxies are as bright at 1400Åas in the V, based on the work of Code and Welch (1981). On average, a $20^m$ galaxy spectrum overlapping an $18^m$ spectrum would produce an error in the measurement equal in magnitude to a $1\sigma$ statistical error. This will happen for approximately 10% of the spectra at the limiting magnitude, if the spectra are obtained in a single roll angle about the telescope axis. Spectra will be obtained at more than one roll angle, so that the fraction of spectra with overlap will be <1%. The overlap can be detected using either the dispersed continuum, which can be detected to $20.5^m$ by binning over 400Å, and the "zero order" reference image, which should be detectable to $22^m$. Thus those cases with overlap can be easily detected and dealt with appropriately.

At the same time, the reference image will produce another overlap problem: the zero order image of a faint galaxy could masquerade as an emission line in a detected spectrum, while the spectrum that accompanies it remains undetected. This occurance, which may happen in one out of four spectra, can be easily detected and compensated for by observing each field in at least two roll orientations, separated by $\sim 1°$. The apparent angle on the sky of the spectrum relative to the reference image is determined by the roll angle of the telescope about its axis. Rolling will cause the spectrum to rotate about the reference image. When this is done, overlapping zero order images will be found to roll away from (or into) the spectrum, while true emission lines will move with the spectrum. Clearly, spectrum overlap will limit the utility of observing in crowded fields, such as near the galactic plane. Based on our stellar model, we estimate that the UV star density will be similar to the pole galaxy surface density at $b \sim 5$ degrees. Fortunately, most galactic sources can be effectively surveyed at $b > 10°$.

## F.2 Reflection Ghosts.

Telescopes employing transmission filters and prisms are subject to the effects of reflections at each filter/vacuum interface. The detector photocathode will also produce a reflection, a portion of which will be returned to the detector by filter/prism reflections. These reflections produce defocussed "ghosts" of each source in the field of view, which can increase the local and general background for other sources, and decrease the efficiency of detector saturation which we have used to minimize the impact of the brightest stars. Some prism ghosts are weak additional spectra with different dispersions than the main spectrum. In Table F.1 we summarize the 18 second order reflection ghosts which will be present in the JUNO telescope. The ghosts are labeled by the surfaces that produce the reflection: detector (D), window(W), filter (F) and prism (P), with $a$ and $b$ denoting the detector and sky surfaces respectively. Note that most of these are extremely weak. Stars brighter than the critical star magnitude will produce halos with a surface brightness in excess of the minimum cosmic UV background (At the galactic poles), for which $I_0$=200 ph $cm^{-2}s^{-1}Å^{-1}$. The worst ghost is $DW_b$, which has a critical magnitude of 4.2 and a diameter of 70 arcminutes. In the galactic plane, there will be an average of three of these per field of view, occupying 15% of the field with halos. However, the cosmic background and unresolved starlight will be at least a factor of five larger in the plane, minimizing the effects of these ghosts. Prism ghost include halos and ghost spectra. There are three of the latter, and in the table the critical magnitude in this case is the faintest level producing a detectable ghost ($m_ghost < 18$). There will be about 10 ghost spectra at high galactic latitudes produced mainly by the $P_bP_a$ ghost. They will be predictable *a priori* with the known distribution

of stars, and they will be recognizable as well by the incorrect ratio of the "zero order" flux to the spectrum intensity. The total percentage of light reflected into ghosts is 1.6% for the photometric mode, and 3.7% for the prism mode. In the sensitivity and dynamic range estimate presented in section 3, we assumed 5%.

**Table F.1**
**Reflection Ghosts**

| Ghost | Type | Reflectivity (%) | Diameter (arcmin) | Critical star magnitude | Angular shift (deg) |
|---|---|---|---|---|---|
| $DW_b$ | Halo | 0.60 | 72 | 3.2 | 0.0 |
| $DW_a$ | Halo | 0.15 | 100 | 1.0 | 0.0 |
| $W_aW_b$ | Halo | 0.25 | 170 | 0.3 | 0.0 |
| $DF_b$ | Halo | 0.15 | 225 | -0.8 | 0.0 |
| $DF_a$ | Halo | 0.06 | 250 | -2.0 | 0.0 |
| $F_aF_b$ | Halo | 0.42 | 40 | 4.0 | 0.0 |
| TOTAL (photometric) | - | 1.60 | | | |
| $DP_b$ | Spectrum | 0.06 | - | 10.0 | >2° |
| $DP_a$ | Spectrum | 0.02 | - | 8.5 | >2° |
| $P_aP_b$ | Spectrum | 0.25 | - | 11.5 | >2° |
| $F_aP_b$ | Halo | 1.00 | 180 | 1.7 | - |
| $F_bP_b$ | Halo | 0.25 | 190 | 0.1 | - |
| $W_aP_b$ | Halo | 0.42 | 90 | 2.3 | - |
| $W_bP_b$ | Halo | 0.11 | 90 | 0.8 | - |
| $F_aP_a$ | Halo | 0.25 | 180 | 0.2 | - |
| $F_bP_a$ | Halo | 0.06 | 190 | -1.3 | - |
| $W_aP_a$ | Halo | 0.10 | 90 | 0.9 | - |
| $W_bP_a$ | Halo | 0.03 | 90 | -1.7 | - |
| TOTAL (prism) | | 3.7 | | | |

## F.3 Diffraction Spikes

As much as 5% of the light will be sent into diffraction spikes. Those produced by the detector/secondary spider will be the largest. We have estimated their size and influence in the case of bright stars. This is a particular concern since: (1) we are using detector saturation to attenuate bright stars, and (2) diffraction spikes can degrade the detectability of faint sources and generate spurious ones.

The diffraction profile is compared in Figure F.1 to that of the geometric and chromatic telescope aberrations. It can be seen that in most cases, the total energy sent into spikes outside of the main point spread function is extremely small, less than 0.5% of the incident light. Thus the impact of diffraction spikes on either of the above points is negligible.

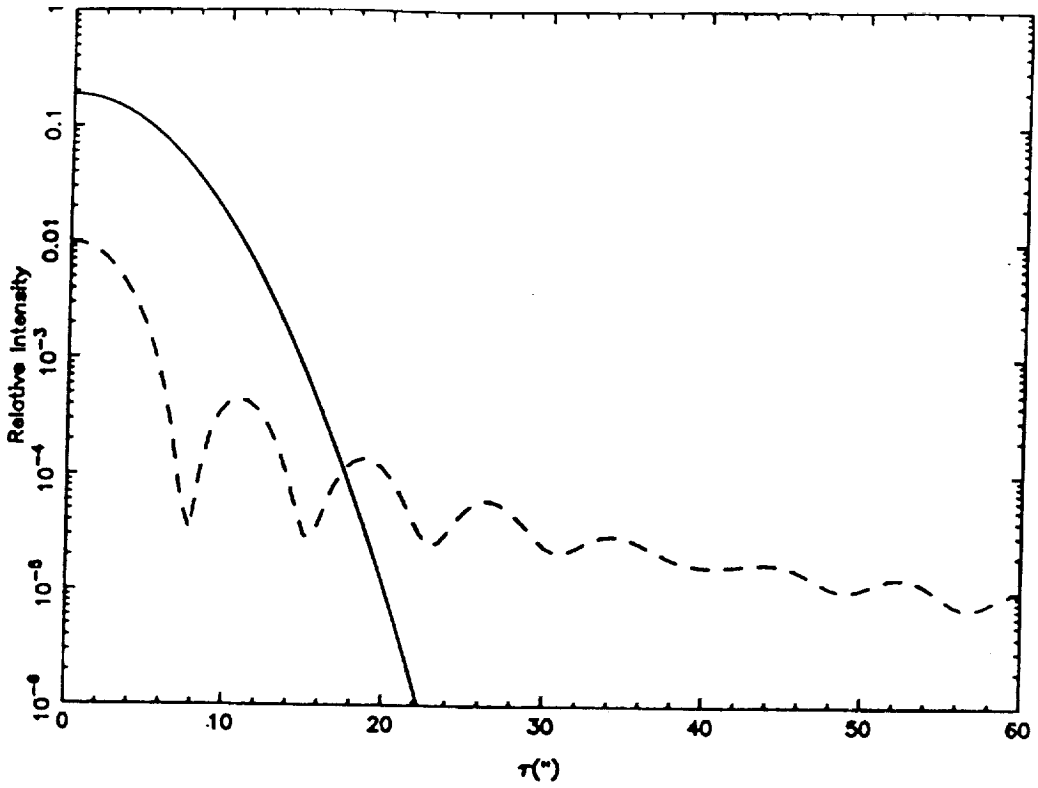


Figure F.1 Predicted point spread function due to aberrations (solid lines) and diffraction (dotted line).

# APPENDIX G

## References

## REFERENCES


Allen, C. W. 1976, *Astrophysical Quantities* (London: Athlone Press).

Alpher, R., Gamow, G., and Herman, R. 1967, *Proc. Natl. Acad. Sci. USA*, **58**, 2179.

Applegate, J. H., Hogan, C. J., and Scherrer 1987, *Phys. Rev. D.*, **35**, 1151.

Bahcall, J.N., et al. 1991, *Ap. J. (Letters)*, **377**, L5.

Bhavsar, S., and Ling, N. 1988, *Ap. J. (Letters)*, **331**, L63.

Begelman, M. 1985, in *Astrophysics of Active Galaxies and Quasi-Stellar Objects*, ed. J. S. Miller (Santa Cruz: University Science Books).

Bechtold, J. et al. 1984, *Ap. J.*, **281**, 76.

Bless, R. C., and Savage, B. D. 1972, *Ap. J.*, **171**, 293.

Bohlin, R. C., Savage, B. D., and Drake, J. F. 1978, *Ap. J.* , **224**, 132.

Boisson, C., and Durret, F. 1986, *Astr. Ap.*, **168**, 32.

Broadhurst, T.J., Ellis, R.S., & Shanks, T.1988, *M.N.R.A.S.*, **235**, 827.

Bruzual, G. 1980, Ph.D. Thesis, University of California, Berkeley.

Bohlin, R. C., Hill, J. K., Stecher, T. P., and Witt, A. N. 1982, *Ap. J.*, **255**, 87.

Braccesi, A., Formiggini, L., and Gandolfi, E. 1970, *Astr. Ap.*, **5**, 26.

Braccesi. A., Zitelli, V., Bonoli, F., and Formiggini, L. 1980, *Astr. Ap.*, **85**, 80.

Burstein, D., and Heiles, C. 1978, *Ap. J.*, **225**, 40.

Burstein, D. and Heiles, C. 1982, *Astr. J.*, **87**, 1165.

Butcher, H., and Oemler, A. 1978a, *Ap. J.*, **219**, 18.

Butcher, H., and Oemler, A. 1978b, *Ap. J.*, **226**, 559.

Canizares, *et al.* 1979, *Ap. J. (Letters)*, **234**, L33.

Castor, J., McCray, R., and Weaver, R. 1975, *Ap. J. (Letters)*, **279**, L43.

Chen, K., and Halpern, J. 1989, *Ap. J.*, **344**, 115.

Ciardullo, R.B., and Demarque, P., 1979, Dudley Obs. Rep. No.14, p. 317. .

Code, A. D., and Welch, G. A. 1982, *Ap. J.*, **256**, 1.

Colless, M., Ellis, R.S., Taylor, K.,and Hook, R.N. 1990, *M.N.R.A.S.*, **244**, 408.

Cordova, F.A. and Howarth, I.D., 1987, in "Exploring the Universe with the IUE Satellite" ed. Y. Kondo, p. 395. (Dordrecht: Riedel).

Cowie, L. L., and Binney, J. J. 1977, *Ap. J.*, **215**, 723.

Cowie, L. L., Hu, E. M., Jenkins, E. B., and York, D.G. 1983, *Ap. J.*, **272**, 29.

Cox, D. P. 1983, *Ap. J. (Letters)*, **265**, L61.

Davies, J. I., Phillips, S., and Disney, M. J. 1988, *M.N.R.A.S.*, **231**, 69P.

Deharveng, J. M., Joubert, M., and Kunth, D. 1986, in *Star-Forming Dwarf Galaxies and Related Objects*, ed. by D. Kunth, T.X. Thuan, and J. Tran Thanh Van, (Gif-sur-Yvette : Editions Frontieres), p. 431.

Deharveng, J. M., and Buat, V. 1987, in *High Redshift and Primeval Galaxies*, ed. by J. Bergeron *et al.* , (Proceedings of the Third IAP Workshop, Editions Frontiers), p. 441.

de Lapparent, V., Geller, M. J., and Huchra, J. P. 1986, *Ap. J.*, **302**, L1.

Dressler, A. 1980, *Ap. J.*, **236**, 351.

Dressler, A., and Gunn, J. 1982, *Ap. J.*, **263**, 533.

Dressler, A., and Gunn, J. 1983, *Ap. J.*, **270**, 7.

Dressler, A. 1984, *Ap. J.*, **281**, 512.

Dressler, A., Faber, S. M., Burstein, D., Davies, R.L., Lynden-Bell, D., Terlevich, R. J., and Wegner, G. 1987, *Ap. J.*, **313**, L37.

Fabian, A. C., Hu, E. M., Cowie, L. L., and Grindlay, J. 1981, *Ap. J.*, **248**, 47.

Fabian, A. C., and Nulsen, P. E. J. 1977, *M.N.R.A.S.*, **180**, 479.

Fleischman, J.R., Friedman, P.G., and Martin, C. 1992, *B.A.A.S.*, **24**, 1281.

Fleming, T. A., Liebert, J., and Green, R. F. 1986, *Ap. J.*, **308**, 176.

Foltz, C. B., Chaffee, F. H., Weymann, R. J., and Anderson, S. F., 1988, in *QSO Absorption Lines*, Space Telescope Science Institute Symposium Series, ed. J. C. Blades, D. Turnshek, and C. A. Norman, p. 53 (Cambridge; Cambridge University Press).

Fordham, J.L.A., Bone, D.A., Norton, T.J., and Read, P.D.1990, *SPIE Instrumentation in Astronomy VII*, **1235**, 636.

Fordham, J.L.A., Bone, D.A., Read, P.D. Norton, T.J., Charles, P.A., Carter, D., Cannon, R.D., and Pickles, A.J. 1989, *Mon. Not. R. Astr. Soc.*, **237**, 513.

Formiggini, L., Zitelli, V., Bonoli, F., and Braccesi, A. 1980, *Astr. Ap. Suppl.*, **39**, 129.

Francis, P.J., and Hewitt, P.C. 1992, submitted to Astr. J..

Franco, J., and Shore, S. N. 1984, *Ap. J.*, **285**, 813.

Franco, J., and Cox, D. P. 1983, *Ap. J.*, **273**, 243.

Fraser, G. W., Pain, M.T., Lees, J.E. and Pearson, J. F. 1991, *Nuc. Inst. Meth.*, **306**, 247.

Friedman, P.G., Cuza, R.A., Fleischman, J.R., Martin, C., and Schiminovich, D. 1993a,b to be submitted to *Rev. Sci. Instr.*.

Friedman, P.G., Fleischman, J.R., and Martin, C. 1992,.

*Proc. of the 10th Int'l Coll. on UV and X-Ray Spectr. of Astrophys. and Lab. Plasmas, Berkeley, CA*

Friedman, P.G., Martin, C., and Rasmussen, A. 1990, *SPIE EUV, X-Ray, and Gamma-Ray Instrumentation for Astronomy*, **1344**, 183.

Fukugita, M., Watamura, S., and Yoshimura, M. 1982, *Phys. Rev. D*, **26**, 1840.

Gallagher, J. S. 1987, *Mitt. Astr. Ges.*, **70**, 126.

Gallagher, J.S., and Hunter, D. A., 1987, in *Star Formation in Galaxies*, ed. C. Persson, p. 167.

Giovanelli, R., Haynes, M.P., and Chincarini, G. L. 1982, *Ap. J.*, **262**, 442.

Greenstein, J. L., and Sargent, A. 1974, *Ap. J. Suppl.*, **28**, 157.

Gunn J. E. and Peterson, B. A. 1965, *Ap. J.*, **142**, 1633.

Hartmann, L. W., Huchra, J. P., Geller, M. J., O'Brien, P., and Wilson, R. 1988, *Ap. J.*, **326**, 101.

Hartwick, F. D. A. and Schade, D., 1990, *A. R. A. A.*, **28**, 437.

Heckman, T. M. 1981, *Ap. J. (Letters)*, **250**, L59.

Heiles, C., Stark, A. A., and Kulkarni, S. 1981, *Ap. J. (Letters)*, **247**, L73.

Heiles, C. 1987, *Ap. J.*, **315**, 555.

Heitt, P.C., Foltz, C.B., and Chaffee, F.H. 1992, submitted to Ap.J. Letters.

Humason, M., Mayall, N., and Sandage, A., *A. J.*, **61**, 97.

Hurwitz, M., Martin, C., and Bowyer 1988, I.A.U Symposium.

Hurwitz, M., Bowyer, S. and Martin, C. 1991, *Ap. J.*, **372**, 167.

Iben, I., amd Tutukov, A. V. 1984, *Ap. J. Suppl.*, **54**, 335.

Ikeuchi, S. and Turner, E. L. 1991, *Ap. J. (Letters)*, **381**, L1.

Jarvis, J. F. and Tyson, J. A. 1981, *Ap. J.*, **86**, 476.

Jones, C., and Forman, W. 1984, *Ap. J.*, **276**, 38.

Kahn, S. M., Wesemael, F., Liebert, J., Raymond, J. C., Steiner, J. E., and Shipman, H. L. 1984, *Ap. J.*, **278**, 255.

Kent, S. M., and Sargent, W. L. M. 1979, *Ap. J.*, **230**, 667..

Kirshner, R. P., Oemler Jr., A., Schechter, P. L. and Shectman, S. A. 1987, *Ap. J.*, **314**, 493.

Lamb, D. Q., and Van Horn, H. M. 1975, *Ap. J.*, **200**, 306.

Lampton, M., Siegmund, O. H. W., and Raffanti, R. 1987, *Rev. Sci. Instrum.*, **58**, 2298.

Larson, R. B. 1972, *Nature*, **236**, 21.

Larson, R. B. 1976, *M.N.R.A.S.*, **176**, 31.

Larson, R. B. , and Tinsley, B. M. 1978, *Ap. J.*, **219**, 46.

Lockman, F. 1984, *Ap. J.*, **283**, 90.

Low *et al.* 1984, *Ap. J. (Letters)*, **278**, L23.

MacLow, M., and McCray, R. 1988, *Ap. J.*, **324**, 776.

Maeder, A., 1987, *Astr. Ap.*, **173**, 243.

Malkan, M. A., and Sargent, W. L. W. 1982, *Ap. J.*, **254**, 22.

Marshall, H. L. 1985, *Ap. J.*, **299**, 109.

Martin, C. and Bowyer, S. 1989, *Ap. J.*, **338**, 677.

Martin, C. and Bowyer, S. 1990, *Ap. J.*, **350**, 242.

Martin, C., and Friedman, P.G. 1993.
to be submitted to *Rev. Sci. Instr.*

Martin, C., Hurwitz, M., and Bowyer, S. 1990, *Ap. J.*, **354**, 220.

McGraw 1979, *Ap. J.*, **229**, 203.

McKee. C. F., and Ostriker, J. 1977, *Ap. J.*, **218**, 148.

Miller, G. E., and Scalo, J. M. 1979, *Ap. J. Suppl.*, **41**, 513.

Mirabel, I. F., and Sanders, D. B. 1989, *Ap. J. (Letters)*, **340**, L53.

Miralda-Escude, J., and Ostriker, J. P. 1990, *Ap. J.*, **350**, 1.

Mochkovich, R., Olive, K. A., and Silk, 1986, reprint.

Moller, P., and Jakobsen, P. 1989.

*Astr. Ap.*

Munakata, H., Kohyama, Y., and Itoh, N. 1985, *Ap. J.*, **296**, 197.

Mushotsky, R. F., Holt, S. S., Smith, B. W., Boldt, E. A., and Serlemitsos, P. J. 1981, *Ap. J. (Letters)*, **244**, L47.

Norgaard-Nielsen, H. U., Jorgenson, H. E., and Hansen, L. 1984, *Astr. Astrophys.*, **135**, L3.

Oort, J. H. 1974, in *The Formation and Dynamics of Galaxies*, IAU Symp. No. 58, ed. J. R. Shakeshift, p. 375 (Dordrecht: Reidel).

Ostriker, J. P., and Cowie, L. L. 1981, *Ap. J.*, **243**, L127.

Paresce, F., McKee, C. F., and Bowyer, S. 1980, *Ap. J.*, **240**, 387.

Patterson, J. 1984, *Ap. J. Suppl.*, **54**, 443.

Petre, R., Shipman, H. L., and Canizares, C. R. 1986, *Ap. J.*, **304**, 356.

Raymond, J. C., Blair, W. P., Fesen, R. A., and Gull, T. R. 1983, *Ap. J.*, **275**, 636.

Read, P.D., Carter, M.K., Patchett, B.E., and van Breda, I.G. 1992.

*Proc. of Conf. on Photoelectronic Image Devices, London* 57

Rees, M. J. 1984, *A.R.A.A.*, **22**, 471.

Sanders, D. B., Scoville, N. Z., Sargent, A. I., and Soifer, B. T. 1988, *Ap. J. (Letters)*, **324**, L55.

Schmidt, M. and Green, R. F. 1983, *Ap. J.*, **269**, 357.

Searle, L., Sargent, W. L. W., and Bagnuolo, W. G. 1973, *Ap. J.*, **179**, 427.

Shakura, N. I.,and Sunyaev, R. A. 1973, *Astr. Ap.*, **24,**, 337.

Shaya, E., and Federman, S. 1987, *Ap. J.*, **319**, 76.

Shull, J. M., and McKee, C. F. 1979, *Ap. J. Suppl.*, **227**, 131.

Siegmund, O. H. W., Lampton, M., and Raffanti, R. 1989, *SPIE EUV, X-Ray, and Gamma-Ray Instrumentation for Astronomy and Atomic Physics*, **1159**, 476.

Siegmund, O. H. W., and Stock, J. 1991, *SPIE EUV, X-Ray, and Gamma-Ray Instrumentation for Astronomy II*, **1549**, 81.

Silk, J. 1988, in *Galactic and Extragalactic Star Formation*, ed. R. E. Pudritz and M. Fich, p. 503 (Dordrecht: Reidel).

Slater, D. C., and Timothy, J. G. 1991, *SPIE EUV, X-Ray, and Gamma-Ray Instrumentation for Astronomy II*, **1549**, 68.

Snowden, S. 1992, private communication.

Sobottka, S. E. and Williams, M. B. 1988, *IEEE Trans. Nucl. Sci.*, **35**, 348.

Terebey, S. and Fich, Michel 1986, *Ap. J. (Letters)*, **309**, L73.

Timothy, J.G. 1989, *SPIE Ultraviolet Technology III*, **1158**, 104.

Timothy, J.G. 1991a.

*SPIE Space Astronomical Telescopes and Instruments* 1494

Timothy, J.G. 1991b, *SPIE EUV, X-Ray, and Gamma-Ray Instrumentation for Astronomy II*, **1549**, 221.

Tinsley, B. M. 1972, *Ap. J. (Letters)*, **173**, L93.

Tinsley, B. M. 1972a, in *Scientific Results from the Orbiting Astronomical Observatory*, ed. A. D. Code (NASA SP-310), p. 575.

Tinsley, B. M. 1972, *Ap. J. (Letters)*, **173**, L93.

Tully, R. B., and Fisher, J. R. 1987, *Nearby Galaxy Atlas*, (Cambridge: Cambridge University Press).

Turnshek, D. A., Foltz, C. B., Grillmair, C. J., and Weymann, R. J. 1988, *Ap. J.*, **325**, 651.

Tylenda, R. 1981, *Acta Astron.*, **31**, 127.

Tyson, J. A. 1981, *Ap. J. (Letters)*, **248**, L89.

Tyson, A. 1988, *A.J.*, **96**, 1.

Tytler, D. 1982, *Nature*, **298**, 427.

Tytler, D. 1987, *Ap.J.*, **321**, 49.

van Breugel, W. J. M., Heckman, T. M, and Miley, G.K. 1984, *Ap. J.*, **276**, 79.

Vauclair, G. and Liebert, J., 1987, in *Exploring the Universe with the IUE Satellite*, ed. Y Kondo, p. 355. (Dordrecht: Reidel).

Wagoner, R. V., Fowler, W. A., and Hoyle, F. 1967, *Ap. J.*, **148**, 3.

Wesemael, F. 1980, *Ap. J. Suppl.*, **45**, 177.

Wesemael, F. 1981, *Ap. J. Suppl.*, **43**, 159.

Winget, D.E., Hansen, C.J., van Horn, H.M., Fontaine, G., Nather, R.E., Kepler, S.O., and Lamb, D.O. 1987, *Ap. J.*, **315**, L77.

Winget, D. E., Kepler, S. O., Robinson, E.L., Nather, R. E., and O'Donoghue 1985, *Ap. J.*, **292**, 606.

Witt, A. N., Bohlin, R. C., and Stecher, T. P. 1984, *Ap. J.*, **279**, 698.

Witt, A. N., Bohlin, R. C., and Stecher, T. P. 1981, *Ap. J.*, **244**, 199.

Witt, A. N., Walker, G. A. H., Bohlin, R. C., and Stecher, T. P. 1982, *Ap. J.*, **261**, 492.

Wolfe, A. M. 1988, in *QSO Absorption Lines*, Space Telescope Science Institute Symposium Series, ed. J. C. Blades, D. Turnshek, and C. A. Norman, p. 297 (Cambridge; Cambridge University Press).

Zombeck, M. V. and Fraser, G. W. 1991, *SPIE EUV, X-Ray, and Gamma-Ray Instrumentation for Astronomy II*, **1549**, 90.